

UNIVERSITÀ DEGLI STUDI DI PAVIA
Facoltà di Ingegneria
Ph.D. School of Electronics, Computer Science and Electrical
Engineering
CICLO XXXI
a. a. 2015-2018

Advanced Techniques for Steerable Antennas

DOCTORAL THESIS OF
GIUSEPPE SICILIANO

TUTOR: PROFESSOR LUCA PERREGRINI

2018

To my
wonderful family

Contents

Introduction	9
1 Optimization of planar array antenna lattice for space debris detection	11
1.1 The Space Situational Awareness (SSA) programme	13
1.1.1 SSA Infrastructure	14
1.1.2 Track-While-Scan (TWS) Radar	17
1.1.3 Phased Arrays in Radars	18
1.2 Array Antennas	20
1.2.1 Introduction	20
1.2.2 Array Theory	21
1.2.3 Planar Arrays	25
1.3 Array Lattice Optimization for Rectangular Scanning	27
1.3.1 A Multi-Array System	29
1.3.2 Grating Lobes	36
1.3.3 Grating-Lobe Mapping into UV-Space	40
1.4 Design of an Optimal Lattice	44
1.5 Standard Lattice Optimization	44
1.5.1 UV Mapping of a Rectangular FoV	46
1.5.2 Optimal lattice	48
1.6 Alternative Lattice Optimization	51
1.6.1 Determination of the lattice parameters	53
1.6.2 Application of the general formulas to notable cases	56
1.6.3 Effect of the single-element radiation pattern	58
1.6.4 Validation example	59
1.7 Array Aperture Truncation and Random Phase Errors	66
1.7.1 Effects of array truncation	66

1.7.2	Effects of phase errors	71
1.8	Conclusions	73
	References	75
2	A Beam-Wave-Guide Antenna for THz Imaging of Moving Standoff Personnel	81
2.1	Introduction	81
2.2	100 GHz reflector antenna scanning system	85
2.3	System architecture	88
2.4	Choice of the system magnification	92
2.5	Location of the illuminator	99
2.6	The confocal region	102
2.7	Considerations on power budgets	109
2.7.1	Metal-plate target	111
2.7.2	Perfect-scatterer target	115
2.8	Scanning system	119
2.9	Conclusions	127
	References	128
3	Dielectric-Based and Mechanically Steered Antenna for Satellite Communications On-The-Move	131
3.1	Introduction	132
3.2	Presentation of the idea	138
3.2.1	Theory	142
3.2.2	Numerical validation	144
3.2.3	Comments	147
3.3	Effect of the dielectric properties	147
3.3.1	Effect of wedge dielectric constant	148
3.3.2	Impact of wedge losses	153
3.4	Dual band coating	154
3.4.1	Design of the dual band coating	155
3.4.2	Application of the theory to practical cases	161
3.4.3	Double-coated medium	162
3.5	Scanning architecture based on Risley prisms	168
3.5.1	Normal incidence analysis	168
3.5.2	Oblique Incidence Analysis	171
3.6	Analysis of a realistic up-down Risley prism system	175

3.6.1	Normal incidence	180
3.6.2	Oblique incidence	188
3.6.3	Comments	191
3.7	Full-wave validation of the dual-band anti-reflection coating	192
3.7.1	Simulation workflow	193
3.7.2	Full-wave extraction of the reflection coefficient	194
3.8	Future work	197
3.9	Conclusions	202
	References	203
4	An Error Model Analysis for ESA Monopulse Tracking Antennas	207
4.1	Tracking	208
4.2	Monopulse Tracking	209
4.2.1	4-horn monopulse	212
4.3	Multi-mode monopulse	213
4.3.1	Circular waveguide modes	213
4.3.2	Radiation features of the circular waveguide modes	214
4.3.3	Approximate expressions around boresight	218
4.3.4	Tracking information extraction	222
4.4	Tracking in ESTRACK stations	235
4.4.1	Tracking problems	239
4.5	A MATLAB error model	240
4.6	Results of the error simulations	242
4.7	Conclusions	248
	References	249
A	Dual band coating calculations	251
B	Mode couplers	255
B.1	Positioning of the mode-coupler ports	255
B.2	Coupling to higher order modes	256
	Conclusion	261

Abstract

This document presents the activities carried out during the three years of my Doctorate of Philosophy. All chapters refer to separate topics fitting in the main subject of this Ph.D., whose focus is on *techniques for steerable antennas*.

There are two main kinds of beam steering technologies: mechanical and electronic steering. The former is based on moving mechanical parts of the antenna or motions of the whole antenna itself, while the latter is accomplished by changing some electrical parameters of the antenna, without physically moving it. In this Ph.D., both technologies were investigated.

In **Chapter 1**, a phased array antenna for space debris detection is studied. The antenna lattice is optimized to minimize the number of array elements, and in turn, the cost of production, while, at the same time, preventing grating lobes from being visible. The project, done in cooperation with the European Space Agency (ESA), leads to a totally analytical procedure to find out the best array lattice based on a few input parameters such as the size of the sky window the array should scan and the antenna electrical size. A methodology is developed to compute the optimal lattice parameters controlling, at the same time, the level of grating lobes.

In **Chapter 2**, a beam-wave-guide antenna architecture is presented to accomplish mm-wave imaging of standoff targets for weapon detection. A scanning method based on a small rotating mirror allows the antenna beam to scan a prescribed field of view, where the target is expected to be located. The idea of the system is to dynamically scan moving targets in a complex open environment with multiple moving human beings. In this Ph.D., a feasibility study of the system is presented with preliminary electromagnetic simulations and theoretical calculations. The limitations of this antenna architecture were highlighted with considerations on the achievable power budgets in the round trip way of the electromagnetic wave

from the transmitter to the target and back to the receiver.

In **Chapter 3**, a simple scanning mechanism based on a double dielectric wedge placed above a flat-panel array antenna for satellite communications on the move (SOTM) is described. The dielectric superstrate is analyzed and designed to have a low profile, according to the application. The dielectric wedges are covered with an anti-reflection coating, which is designed in a completely analytical way, finding closed-form expressions for the electromagnetic and geometrical parameters of the coating layers. The beam scanning functionality and the anti-reflectivity of the coated wedge are simulated on MATLAB according to the transmission matrix theory and on commercial full-wave electromagnetic simulation softwares. Results show a proper operation of the system, with the possibility to manufacture a prototype by using 3D printing technology.

Eventually, in **Chapter 4**, an error model of a multi-mode monopulse tracking receiver is built up to study the problems of tracking performance degradation seen in many ground stations belonging to ESA tracking network (ESTRACK). These antennas scan the beam in a mechanical way using elevation and azimuth motors to keep the antenna on the target direction. The radiation characteristics of the circular waveguide fundamental and a few higher-order modes are deeply understood and the operation of a multimode monopulse receiver is analytically described in detail. An error model is built up through a MATLAB script, developed on purpose, based on the scattering parameters of ideal and simulated microwave components composing the monopulse chain. Amplitude and phase unbalance factors are also introduced in the model to see the effect of such non-idealities on the tracking performance. Results prove that some unbalances can, indeed, produce the same effects as measured in ESA stations.

Introduction

The problem of antenna beam steering finds applications in various technological fields.

In the field of radar systems, beam steering allows to point at certain directions and detect targets that may be located there. In this case the electromagnetic energy, generated by a transmitter, is focused on a narrow cone of emission, travels some distance, hits a reflective target and bounces back at the receiver, usually co-located or located nearby the transmitter. The target leaves a sort of “signature” on the reflected signal which can help the receiver for location and identification purposes. Aircraft or satellite surveillance and tracking and ground mapping are representative cases of radar technology, where beam steering is the key function behind their proper operation.

In communication systems, beam steering allows to concentrate the electromagnetic energy toward specific directions, where the interacting targets are located, in order to enhance the quality of the signals exchanged between transmitters and receivers. Satellite communications are a representative example of this technology, where steadily earth-orbiting spacecrafts or deep-space probes need a constant line-of-sight link with earth stations, usually accomplished by physically rotating a parabolic-dish antenna.

In this Ph.D. thesis both aforementioned major applications of beam steering are investigated and solutions to some major problems are proposed and analyzed.

In the field of radar detection, the problem of space debris, harmful out-of-control earth-orbiting objects, is addressed in Chapter 1, proposing an electronically scanned radar antenna system devised for surveillance and tracking purposes with the minimum set of equipments to ensure the same electromagnetic performance at reduced manufacturing costs. To achieve that, a novel theory is proposed in this thesis allowing to design a phased

array antenna with the minimum number of radiating elements, while preventing spurious radiation from being received through unwanted directions. A combination of analytical and simulation tools is adopted to sort out such a major problem.

In the field of radar imaging, the problem of stand-off target imaging at mm-wave frequencies for security applications (e.g. concealed metal and non-metal weapon detection) is addressed in Chapter 2. A complex reflector antenna system is analyzed, where a scanning strategy based on small flat mirror allows for a quick beam steering over a person-sized field of view at a given range.

In the field of satellite communications, the problem satellite line-of-sight communications with ground moving platforms (e.g. aircrafts, helicopters, off-road vehicles, ships) for high-data-rate links is addressed in Chapter 3. A novel scanning mechanism, based on a dielectric superstrate to be installed on top of an azimuth-over-elevation-actuated flat-aperture array antenna, is proposed in order to solve the major problem of keyhole, forcing such mechanically steered antennas to operate over a limited range of elevation steering angles. The analytical approach is combined with full-wave analyses in order to achieve the desired system functionality.

Eventually, in the field of satellite tracking, the problem of target misalignment errors in monopulse ground-station antennas is addressed in Chapter 4. Here, the receiving chains of some ESA ground stations, based on multi-mode monopulse antennas, is cut down into fundamental device units, that are characterized in terms of their non-idealities, analyzed and cascaded by means of a MATLAB tool developed on purpose. Again, the analytical approach, used to understand and characterize the various microwave and RF components, is combined with simulation, in order to explain the undesired misalignment errors affecting such monopulse systems.

Chapter 1

Optimization of planar array antenna lattice for space debris detection

Space debris, better explained afterwards, are out-of-control earth-orbiting objects which may cause severe damages in case of collision with operational satellites. For space debris located at low-earth orbits (LEO), phased array radar systems [1]–[3] are usually employed, offering superior benefits in terms of number of simultaneous beams and scanning speed [4]. In addition, phased arrays are well suited for scalable implementations where efforts and costs are spread over several years, gradually increasing the number of elements over time [5]. However, to achieve the required aperture dimension, a large number of radiators is required, with evident impact on budget and complexity. For this reason, the array lattice should be designed to minimize the number of elements, by maximizing the element spacing [6] (with the extra advantages of a better integration of the active systems, a more efficient cooling of the transmitters, and a reduction of the mutual coupling), while maintaining a grating-lobe-free radiation pattern over the entire sky region under surveillance, often referred to as Field of Regard (FoR) [7], [8]. Thinned or sparse arrays are often used whenever the reduction of the number of elements is addressed [9]–[14]. However, the element arrangement as well as the excitation function depends on the array aperture shape and size, which change over time for scalable systems. Therefore, this class of arrays is not the preferred solution for this application, where the com-

plete system is supposed to be composed of a number of identical replicated blocks. Furthermore, sparse arrays are not recommended as transmitting antennas in space debris applications, because of the huge power required in transmission. On the other hand, uniform arrays homogeneously distribute the power over the entire aperture, thus reducing the fraction of the total power a single radiating element has to handle. They also provide a uniform coverage of the u-v space and are suited for scalable solutions, which can be conveniently implemented on the ground using tiled arrays [15]–[23].

This chapter is devoted to the design of an optimal regular-latticed array antenna aimed at the detection of space debris objects crossing a prescribed rectangular-shaped window in the sky, called *field of regards* (FoR). The lattice is optimum in the sense it leads to an array with the minimum number of elementary radiators, with clear advantages in terms of cost reduction and ease of integration of active element electronic equipment. The optimization, of course, has to take into account the level of grating lobes, which should stay below a specified amount. This topic is addressed in a number of past works [24]–[27] with the development of either graphical or recursive methods. Whereas, in this work a systematic theory is presented [28], with the elaboration of analytical array-lattice-parameter expressions [29] including the effect of the array beam-width and element pattern, and introducing a four-dimension representation (4D) of the radiation pattern to control grating lobes (a sort of time-space optimization). In the work presented here, an analytical formulation is devised leading to a few equations relating the FoR specifications (elevation and size) and the desired grating lobe level to the array lattice geometrical parameters. Given such analytical formulation, the novelty of the proposed approach lies in the lack of any dependency on recursive or iterative methods, that are a normal practice in array lattice design. At the end of the chapter, array aperture truncation and phase errors will be addressed, as well. Results of this Ph.D. research topic were published in conference and journal papers [29]–[33].

In this chapter, the first sections are introductions to the problem of space debris, the European Space Agency space-debris programme, and the theory of array antennas. The last section contains the theory presented in this Ph.D. work.

1.1 The Space Situational Awareness (SSA) programme

Space debris represents a serious threat for all artificial satellites orbiting around the Earth, including current manned missions, namely the International Space Station and the Sojuz vehicle [34]. Space debris include large objects, such as non-operational spacecrafts and parts of launchers, as well as small fragments resulting from intentional and unintentional explosions and/or collisions. A recent example was the collision between the operative Iridium 33 satellite and the out-of-control Kosmos 2251 satellite in 2009, resulting into the complete destruction of both and the generation of around 1000 debris larger than 10 cm [35]. Even smaller space debris, travelling at a speed that may approach 10 km/s, could cause important damages. For this reason, satellites often implement a collision-avoidance system to reduce the probability of a critical impact. As an example, statistics updated at the end of 2015 indicate that the International Space Station has performed 25 collision-avoidance maneuvers [36]. Collision avoidance systems require a detailed knowledge of the space debris orbit parameters. An important role to create such a database is traditionally played by microwave steerable radars for Low-Earth-Orbit (LEO) debris, while Medium-Earth-Orbit (MEO) and Geostationary-Earth-Orbit (GEO) debris are often tracked using optical systems. Major advantages of microwave radars include proven tracking strategies and all-weather capabilities. They are often confined to the upper limit of LEO altitudes, 2000 km, due to limitations on the link budget, especially for debris in the order of 10-cm size or smaller [37].

ESA's Space Situational Awareness (SSA) Programme was formally launched on 1 January 2009 [38]. Its objective is to support Europe's independent utilization of space through the provision of timely and accurate information and data regarding the space environment, and particularly regarding hazards to infrastructures in orbit and on the ground. Such hazards stem from space debris, as said in the previous section, and other natural objects, such as earth-orbit-crossing asteroids. SSA means that Europe will know what goes on in space by acquiring the independent capability to watch for objects and natural phenomena that could harm satellite infrastructure. To date, Europe's access to such information has relied on non-European organizations. However, to promote its own independence, ESA needs an

autonomous SSA capability.

1.1.1 SSA Infrastructure

The SSA programme is active in three main areas:

A. Survey and tracking of objects in Earth orbit

comprising active and inactive satellites, discarded launch stages and fragmentation debris that orbit the earth;

B. Monitoring space weather

comprising particles and radiation coming from the sun that can affect communications, navigation systems and other networks in space and on the ground;

C. Watching for NEOs¹

comprising natural objects that can potentially impact the earth and cause damage, and assessing their impact risk and potential mitigation measures.

SSA is managed directly by ESA, in cooperation with European national and regional authorities, national space agencies and national research establishments. ESA also entertains a long-standing cooperation with NASA, US organizations such as NOAA and the US Defence Department, and other international agencies.

The SSA Programme will help to ensure:

- reliability and security of European space-based applications;
- peaceful uses of outer space in cooperation with international partners;
- benefits for the European industry through the development of SSA infrastructure and capabilities.

The SST System

In order to avoid the consequences of space debris objects, we need to know where they are and which trajectories they are following, so that prompt action can be taken in event of potential impact. Therefore, technologies

¹Near Earth Objects.

related to surveillance radars and telescopes are needed. The future perspective includes making use of satellite laser ranging and optical surveillance techniques, but in the present work radar techniques at the microwave frequencies are only studied.

As part of the European SSA Programme, ESA is designing a system to track debris, namely the Space Surveillance and Tracking system (SST). It aims at developing the ability to detect and forecast the movement of space debris in orbit around the earth at LEO altitudes.

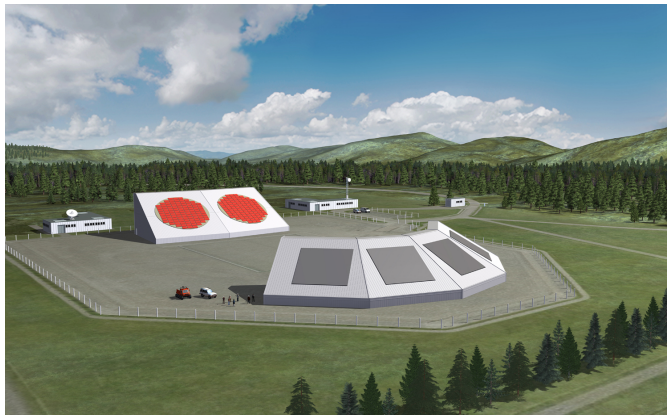


Figure 1.1: Artist's impression of a future SSA radar system.

The SST system is a collection of ground- and space-based sensors acquiring data regarding new and catalogued debris objects. Radars and telescopes look at the sky with the aim of detecting debris objects, determining their trajectories and estimating their size. An example of radar SST system is provided in Fig. 1.1.

The SST Segment

Every detected object is included in a catalogue, containing the fundamental parameters to accurately describe its motion around the earth. In order to generate this catalogue, it is necessary to:

- A. reconstruct object orbits from the data that are produced by the sensors (orbit determination);
- B. check to see if this object has already been seen and is already in the catalogue (correlation);

- C. monitor the data in the catalogue so that sensors can be tasked to update the information when needed.

The system will be automated to calculate the possibilities of collision between thousands of objects in the catalogue and then warn satellite operators of any potential risks. Based on this knowledge, satellite operators will be able to base their design considerations and make decisions on shielding materials to protect their infrastructure, maneuvering out of the way, saving fuel and extending the satellite lifetime.

Another utility of the catalogue is to predict when large pieces of space debris reenter the atmosphere. If these pieces are large enough, they could even hit the earth's surface, posing a risk to people, industry and public infrastructure. Warning governments of the risks related to such threats can help to take a balanced response and ensure the proper level of safety.

The SST Sensors

The SST sensors can be divided into two main types:

Surveillance Sensors. These sensors look, at once, at a large “window” up in the sky, trying to detect any object (within some given size requirements) passing over it. They behave rather passively, in that they don't actively look for any specific object, but just those that get into their visibility region. Some surveillance sensors, instead of monitoring an entire window at once, decompose it into small beams and actively scan the beams to cover it entirely. Once an object is detected, the sensor tries to compute some orbital parameters for the piece of debris and, in case of possible collision with a working satellite, yields a warning which asks the tracking system to acquire better data about the object.

Tracking Sensors. Tracking Sensors usually have a very small field of view² because their objective is to accurately determine the angular position and the range of the target. This data is used to precisely recalculate the orbit of the object which had been roughly estimated by the surveillance sensors.

²The Field of View, generally shortened to FoV, is the angular region a sensor is surveying.

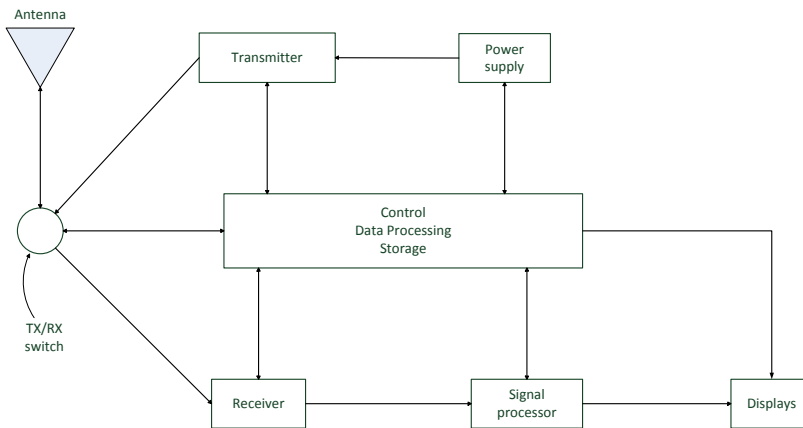


Figure 1.2: Radar block diagram [39].

A tracking sensor alone is not enough to build up a complete space-debris catalogue. In fact, its field of view is so small that only a few objects at one time can be detected. Moreover, the time while a detected object is observed is too short, with the first orbit guess having very large errors. Therefore, for the development and maintenance of a catalogue, an effective system also needs a surveillance sensor.

1.1.2 Track-While-Scan (TWS) Radar

A special radar used for both surveillance and tracking is the Track-While-Scan (TWS) radar. Its working principle is summarized below:

- The TWS scans a certain fence in the sky, through the beam-steering capability provided by a phased-array antenna.
- Every detectable³ object passing through the fence is detected by the radar and the measurement is passed to a computer and stored in its memory.
- At every subsequent acquisition, the radar has to decide whether it

³Object detectability depends on the SNR connected to the received target's echo.

belongs to a new object or to another one already present in the catalogue. The radar makes such decision through correlation between the new measured target's parameter and the estimate of the same parameter (e.g. angular position and range) based on past measurements.

- Tracking plots related to each object in the catalogue can be generated by some processing performed over its sample measurements stored in the computer's memory.

The general radar architecture is depicted in Fig. 1.2 [39]. Design of the entire radar system is out of the scopes of this work. We will rather concentrate on one part of the TWS radar's equipment, the phased-array antenna.

1.1.3 Phased Arrays in Radars

Phased array antennas provide the capability of electronically scanning the antenna beam, without any mechanical motion. They allow for a much more rapid scanning than mechanical steering, because beam steering is accomplished by changing some electronic parameters, with no need for moving the antenna itself. Electronic steering, however, suffers from gain loss, which limits the maximum angular size of the FoV, and costs of production. Despite these few issues, phased arrays lend themselves to automatic high-speed scanning and make up the best candidate technology to be employed in a surveillance and tracking radar system. In particular, phased arrays allow to acquire at the same time angle-separated beams, i.e. several objects at the same time can be tracked.

Phased Arrays: General Architecture

A phased array is a group of identical small antennas, referred to as array elements, equally oriented, distributed over a certain space region. A schematic model of a phased array is depicted in Fig. 1.3. The functional blocks are:

- The **tapering function** (labelled as a sum block), in charge of redistributing the power received from a transmitter to all different elements (transmitting array) or combining, in some way, the signals received from the elements and deliver the obtained signal to a receiver (receiving array).

- The **phase shifters**, providing different phase shifts across the various paths.
- The **radiating elements**, that are all identical small antennas.

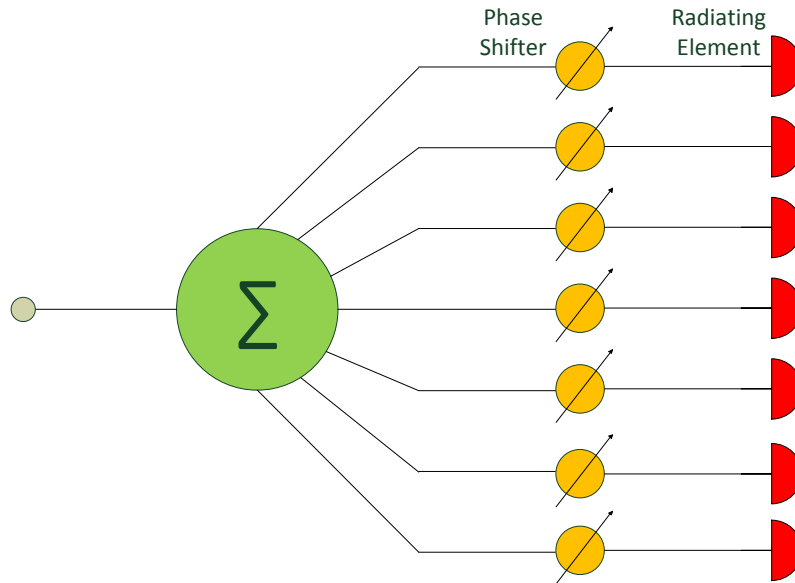


Figure 1.3: General circuit model of a phased array.

All these blocks have certain requirements and undergo specific designs. The part of the network including the tapering function and phase shifters is called *beam-forming network*. It can reach very high levels of complexity and is usually the most expensive part of the design of a phased array. The beam-forming network can either be analog or digital: in the first one, the phase shifting and the tapering (or amplitude weighting) functions are applied to the analog signals, before downconversion to baseband; in the second one, the signals are digitized immediately behind the array element (or after a downconversion to an intermediate frequency, according to the operational frequency band of the analog-to-digital converters), and the weighting and phase shifting functions are applied in the digital domain. It is straightforward why digital beamforming potentially has superior performance than analog beamforming, with the very first advantage of providing instantaneous multi-target tracking. In this work, we will not deal with the

beam-forming network, but we will only focus on the geometrical design of the array, so the arrangement of elements in space. Next section is devoted to the theory behind array's operation.

1.2 Array Antennas

This section will provide an overview of arrays. The first subsections show how to obtain the array factor for a general array topology and in particular for a planar array. Some examples of array factors for uniform arrays are provided, as well.

1.2.1 Introduction

Usually, the radiation pattern of a single element is relatively wide, resulting in a low value of gain (directivity). In order to achieve narrower beams and therefore higher directivities, it is necessary to enlarge the electrical size of the antenna. The main beam can be, for e.g., narrowed by increasing the physical size of the single element, but it generally results in the appearance of unwanted grating lobes. It is well known that if the length of a dipole exceeds half wavelength, side lobes begin to appear, and above one wavelength grating lobes also turn up. An alternative strategy permits to increase directivity without changing the single element size. It consists of taking identical and equally oriented copies of the single element and arrange them in a geometrical lattice, with each element simply shifted with respect to a reference position. Such an antenna system is called *array*[8]. The array elements can be distributed over a line, a surface or a volume, leading to linear, planar or 3-dimensional arrays. Because of linearity of Maxwell's equations, the total electromagnetic field at a given point in space is simply given by the vector sum of the fields produced by each element with amplitude and phase depending on the excitation and position of the array elements. However, this approximation is based on the assumption that the current flowing in each element is not influenced by the neighbour elements and does not itself affects the currents in the neighbour elements. This condition imposes no mutual coupling between the array elements. In other words, the current through an element in presence of all the others is the same as that of the isolated element, if the single-element excitation is unchanged.

A high directivity can be achieved if all fields produced by the elements of

the array sum up constructively in a small angular region and destructively in the remaining space regions. Practically, such radiation patterns are not possible, but can only be approached. In an array of identical elements, there are at least five controls that can be used to shape the overall pattern of the antenna:

1. the geometrical configuration (e.g. linear, planar, spherical, or arbitrary);
2. the spacing between the elements;
3. the amplitude excitation of each individual element;
4. the phase excitation of each individual element;
5. the radiation pattern of the individual element.

1.2.2 Array Theory

From a mathematical point of view, a general theory for arrays has been developed [40], with some fundamental outcomes being reported here. The theory is developed for time-harmonic fields, where the $e^{j\omega t}$ factor is suppressed.

Looking at Fig. 1.4, let \mathbf{E}_0 be the field that would be generated at the point P by an arbitrary element chosen as reference (with the coordinate system xyz centered at a reference point inside the array region). Then \mathbf{E}_0 can be expressed as:

$$\mathbf{E}_0 = \hat{\mathbf{p}}(\theta, \phi) F_0(\theta, \phi) \frac{e^{-j \frac{2\pi}{\lambda} r}}{r}, \quad (1.1)$$

where $\hat{\mathbf{p}}$ is the polarization unit vector, F_0 is a function only dependent on angular coordinates and related to the radiation intensity of the reference element, and r is its distance from the point P. Under the assumption that no mutual coupling occurs between the elements of the array, the fields generated by the other radiators of the array differ from that of the reference element only for their positions in space and their excitations. Therefore, the field generated by the n -th element is represented by:

$$\mathbf{E}_n = W_n \hat{\mathbf{p}}(\theta_n, \phi_n) F_0(\theta_n, \phi_n) \frac{e^{-j \frac{2\pi}{\lambda} r_n}}{r_n} \quad (1.2)$$

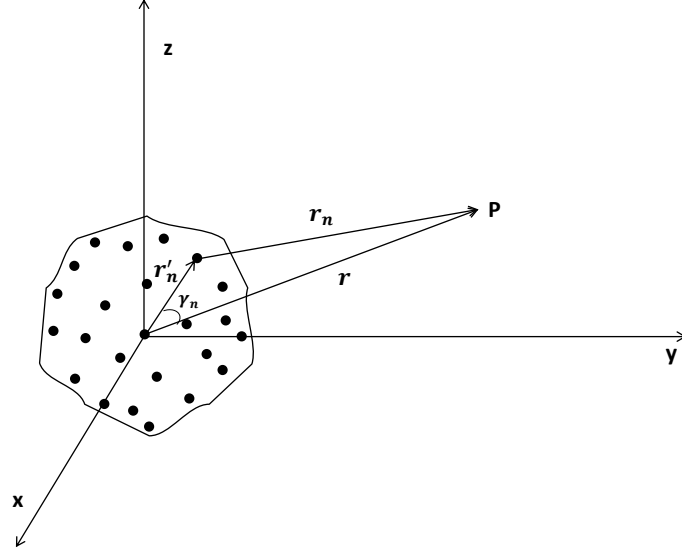


Figure 1.4: General array theory.

where θ_n, ϕ_n are the look angles under which the n -th element sees the point P, measured in a coordinate system centered at the n -th element, and r_n is the distance of the point P from the n -th element. W_n is an excitation coefficient, defined as the ratio between the excitation of the n -th radiator and the reference excitation. It can be expressed in terms of a modulus A_n and a phase δ_n ,

$$W_n = A_n e^{j\delta_n} .$$

Since the point of observation is assumed to be in the far field, vectors \mathbf{r}_n and \mathbf{r} are practically parallel, then $\theta_n \approx \theta$ and $\phi_n \approx \phi$. Moreover, $\frac{1}{r_n} \approx \frac{1}{r}$ and

$$e^{-j \frac{2\pi}{\lambda} r_n} \approx e^{-j \frac{2\pi}{\lambda} (r - r'_n \cos \gamma_n)} = e^{-j \frac{2\pi}{\lambda} r} e^{j \frac{2\pi}{\lambda} \mathbf{r}'_n \cdot \hat{\mathbf{u}}_r} .$$

With these approximations, the field generated by the n -th element becomes:

$$\mathbf{E}_n = W_n e^{j \frac{2\pi}{\lambda} \mathbf{r}'_n \cdot \hat{\mathbf{u}}_r} \hat{\mathbf{p}}(\theta, \phi) F_0(\theta, \phi) \frac{e^{-j \frac{2\pi}{\lambda} r}}{r} = W_n e^{j \frac{2\pi}{\lambda} \mathbf{r}'_n \cdot \hat{\mathbf{u}}_r} \mathbf{E}_0 . \quad (1.3)$$

For an array with N elements, the total electric field \mathbf{E} is given by the sum

of the electric fields due to each element:

$$\mathbf{E} = \sum_{n=0}^{N-1} \mathbf{E}_0 W_n e^{j k \mathbf{r}'_n \cdot \hat{\mathbf{u}}_r} = \mathbf{E}_0 \cdot AF \quad (1.4)$$

where AF is called *Array Factor* and is equal to:

$$AF = \sum_{n=0}^{N-1} W_n e^{j k \mathbf{r}'_n \cdot \hat{\mathbf{u}}_r} \quad (1.5)$$

Expression 1.5 is very general and can be applied to any array geometry.

In conclusion, the total electric field produced by an array is given by the multiplication of the electric field generated by the single element and a quantity, the array factor, which is a function of the array geometry and the excitation (amplitude and phase) of each element.

As far as the radiation intensity ($K(\theta, \phi)$) is concerned, since it is a function of the square modulus of the electric field⁴, it can be easily proven that:

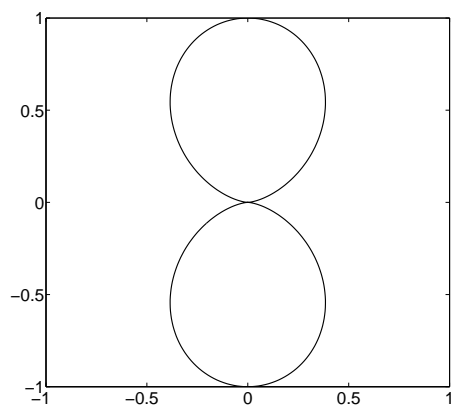
$$K(\theta, \phi) = K_0(\theta, \phi) \times |AF|^2$$

with K_0 being the radiation intensity of the single element. This result is very interesting. It shows that the radiation pattern of an array can be found by multiplying the radiation pattern of the single element by the square modulus of the array factor. Hence, we can quite reasonably refer to $|AF|^2$ as the *array-factor pattern*. Everytime one wants to compute the array radiation pattern, it's sufficient to follow these steps:

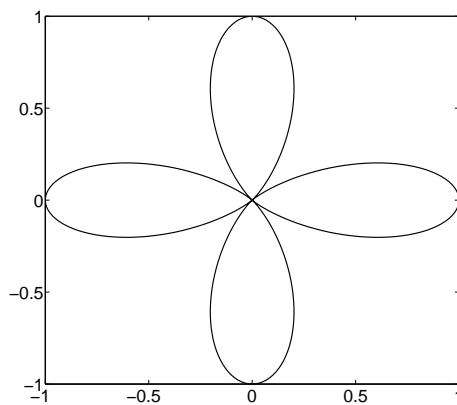
1. take the reference-element pattern;
2. calculate the array-factor pattern;
3. find the overall radiation pattern by multiplying the previous two patterns.

This procedure is also known as *Krauss Rule* [41]. Fig. 1.5 on the following page shows how the overall array radiation pattern can be obtained according to Krauss Rule. Fig. 1.5(a) shows the reference-element pattern, Fig. 1.5(b) the array-factor pattern, and Fig. 1.5(c) the overall pattern obtained by multiplication of the other two.

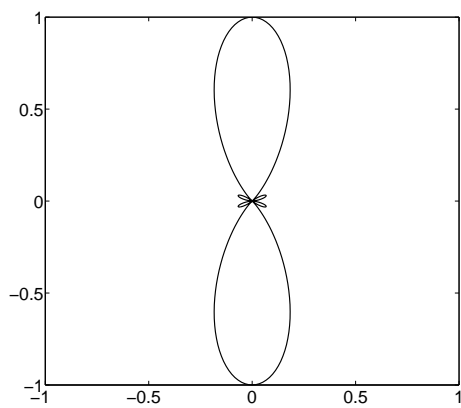
⁴The radiation intensity is given, by definition, as $K = r^2 \frac{|E|^2}{2\eta_0}$. K does not depend on r since the electric field in far field is a function of $\frac{1}{r}$



(a) Radiation pattern of the reference element, S_e .



(b) Square modulus of the array-factor pattern (i.e. $|AF|^2$).



(c) Overall radiation pattern of the array:
 $S_e \times |AF|^2$

Figure 1.5: Example. Application of Krauss Rule for finding the overall array pattern.

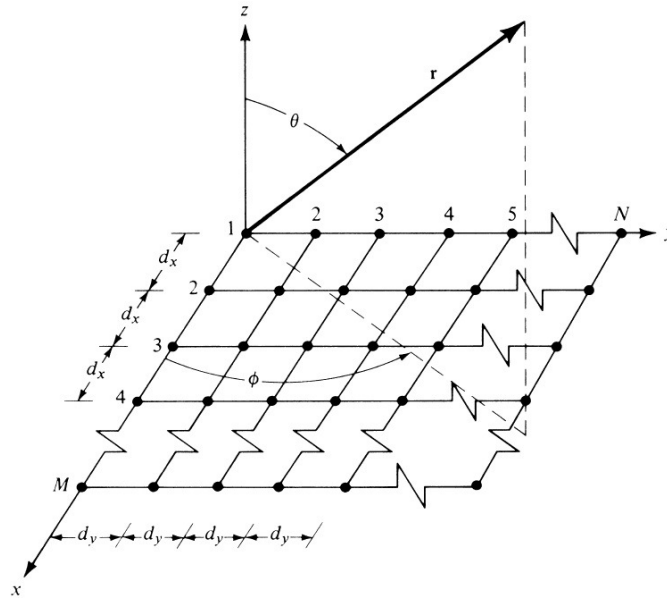


Figure 1.6: A planar array.

1.2.3 Planar Arrays

A planar array is an array whose elements are distributed over a plane (see Fig. 1.6 from [40]). Here, we provide the general theory for planar arrays. For more details concerning specific array topologies, the reader may refer to some textbooks on Planar Arrays, such as [42] and [40].

Planar arrays are versatile, because they provide sufficient variables for shaping the radiation pattern in both orthogonal planes, with the possibility of obtaining symmetrical patterns. In addition, they can be used to scan the beam in every direction in space. Applications include tracking radars, surveillance radars, remote sensing, communications and many others.

Planar arrays differ from each other for their lattices, i.e. the arrangement of their elements, and for their boundaries, i.e. the shape of the aperture. There are regular and irregular grids: the former are characterized by a regular cluster that repeats itself throughout the aperture, like the regular arrangement of particles in crystals; the latter don't have such regularity. We will only discuss about arrays of the former kind, whose grid is regular. In a regular grid, the array elements have a constant spacing along x , d_x , and along y , d_y . The most common lattices are the rectangular, triangu-

lar, and hexagonal one, this being a particular case of the triangular one⁵. Boundaries may be rectangular, circular or any other shape; however, the rectangular and circular ones are preferred because of some useful properties of their radiation pattern, and, of course, because they are easier to build up.

Array Factor of Planar Arrays

Consider a general planar array of N elements and let P_x^n and P_y^n be respectively the x - and y -position of the n -th element in the xy -plane. From Fig. 1.4 and Fig. 1.6, \mathbf{r}'_n , the vector-position of the n -th element of the array, can be written as

$$\mathbf{r}'_n = \hat{\mathbf{x}} \cdot P_x^n + \hat{\mathbf{y}} \cdot P_y^n + \hat{\mathbf{z}} \cdot 0 ,$$

where the hat symbol $\hat{\cdot}$ is used to indicate the axis unit vector. The unit vector $\hat{\mathbf{u}}_r$, representing the observer's direction is simply [41]

$$\hat{\mathbf{u}}_r = \hat{\mathbf{x}} \cdot \sin \theta \cos \phi + \hat{\mathbf{y}} \cdot \sin \theta \sin \phi + \hat{\mathbf{z}} \cdot \cos \theta .$$

Substituting the previous two expressions into 1.5 on page 23, the array factor, for planar arrays, becomes

$$AF = \sum_{n=0}^{N-1} W_n e^{jk(P_x^n \sin \theta \cos \phi + P_y^n \sin \theta \sin \phi)} \quad (1.6)$$

Uniform Planar Arrays

A uniform planar array is a planar array whose elements are all excited with the same amplitude. For these arrays, the only parameters which are used to shape the radiation pattern are the lattice topology and the phase of each element. Uniform arrays find applications as transmitting antennas, especially whenever large power is required to be radiated. This is due to their higher efficiency (and gain) compared with non-uniform arrays. However, uniform arrays suffer from non-negligible sidelobe levels⁶ with respect

⁵Hexagonal arrays are a subset of triangular arrays, where $\gamma = 60^\circ$ and $d_y = \frac{\sqrt{3}}{2} d_x$. It's called hexagonal, because the entire grid can be seen as a repetition of smaller hexagonal clusters.

⁶The sidelobe level of uniform arrays is also affected by their aperture shape [42]. For e.g., rectangular apertures have a sinc-like radiation pattern, thus exhibiting -13.26 dB first-sidelobe level referred to the maximum, while circular apertures have a behavior like the bessel function J_1 , thus showing -17.57 dB first sidelobes.

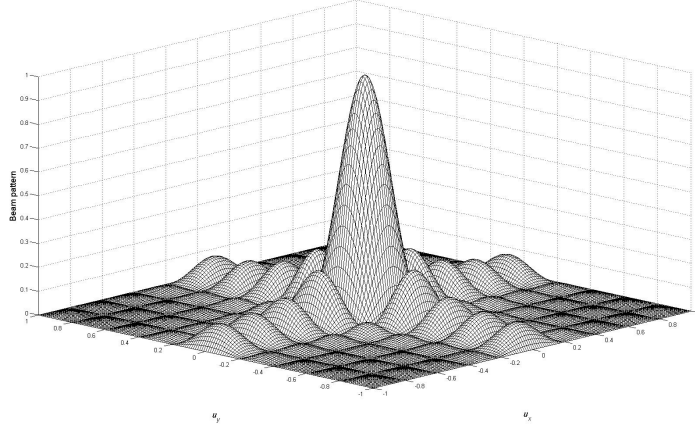


Figure 1.7: Beam pattern of a rectangular array with 10×10 elements ($u_x = \sin \theta \cos \phi$ and $u_y = \sin \theta \sin \phi$).

to the maximum. The expression of the array factor for a rectangular array is reported here, as well as its array-factor pattern.

The modulus of the normalized array factor of a uniform **rectangular** array with N elements along x direction and M elements along y direction is:

$$|AF| = \left| \frac{1}{N} \frac{\sin(N \cdot \Psi_x/2)}{\sin(\Psi_x/2)} \right| \left| \frac{1}{M} \frac{\sin(M \cdot \Psi_y/2)}{\sin(\Psi_y/2)} \right|, \quad (1.7)$$

where

$$\Psi_x = k d_x \sin \theta \cos \phi,$$

$$\Psi_y = k d_y \sin \theta \sin \phi.$$

The broadside patterns for a square array (Fig. 1.6) with 10×10 elements and distance $d_x = d_y = \lambda/2$ is depicted in Fig. 1.7.

1.3 Array Lattice Optimization for Rectangular Scanning

To select the optimal Field of Regard⁷ of the space surveillance radar system under consideration, an extensive study has been conducted by ESA and a contractor company. The analysis has considered the radar deployment within an ESA Member State in continental Europe (Spain). First, a

⁷Sky window the radar will have to scan

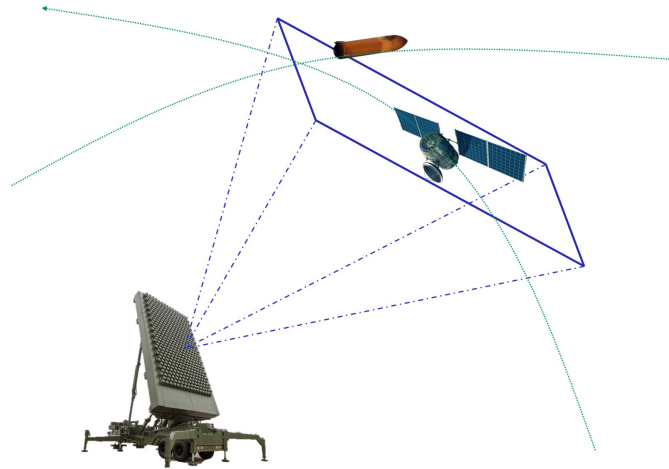


Figure 1.8: Concept of FoR radar surveillance for space debris detection.

Table 1.1: DEFINITION OF THE FIELD OF REGARD.

Field of Regard		
	min	max
Deflection angle A	-45	45
Deflection angle B	20	40

geometrical analysis was performed, in order to determine the observability for the objects forming the catalogue. Then, a quantitative simulation was done to calculate the detectability for the objects.

The site considered has been assumed to be located in Spain:

- Latitude: $40^{\circ}27'29''$ N.
- Longitude: $3^{\circ}29'48''$ W.

The **Field of Regard** has been defined in Table 1.1. It is described by a rectangular section defined by two angles in a local coordinate system, namely deflection angle A and deflection angle B , with the \mathbf{z} -axis normal to the array surface (see Fig. 1.9). The idea behind the microwave space debris detection, is to have a surveillance radar architecture continuously scanning the FoR, while detecting debris objects during their daily pass. This concept is graphically represented in Fig.1.8.

In this deflection-angle coordinate system (Fig. 1.9), the direction of a point P is given by two angles A and B . A is measured between the z -axis

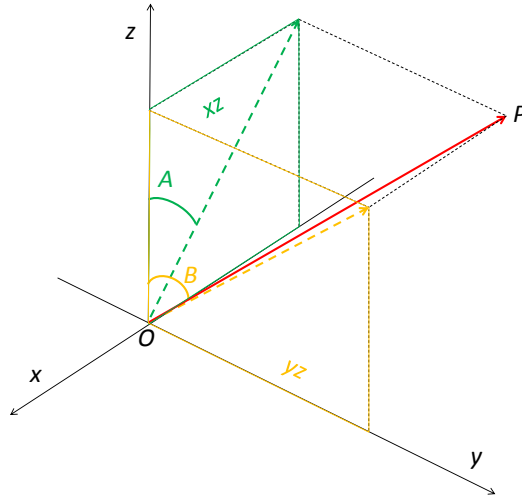


Figure 1.9: Definition of deflection angles A and B.

and the projection of the vector \vec{OP} onto xz plane. B is similarly measured between z and the projection of \vec{OP} onto yz plane.

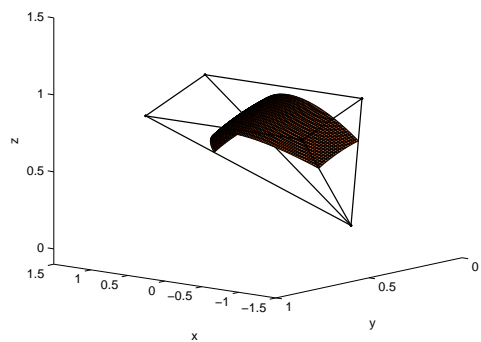
Fig. 1.10 shows the projection of the Field of Regard as defined in Table 1.1 onto the unit sphere. The deflection angle limits of the FoR draw a pyramidal section, represented in Fig. 1.10, as well.

1.3.1 A Multi-Array System

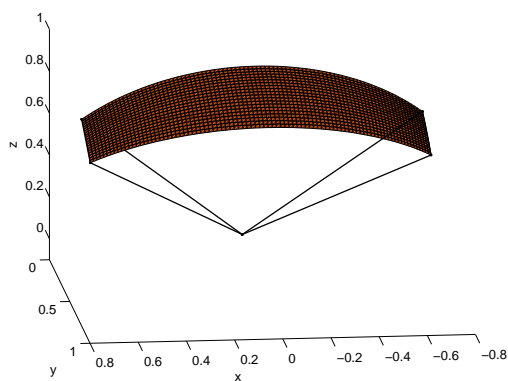
It is possible to notice that, due to constant range assumption, the FoR suffers from a distortion in the borders. This effect is clearly mitigated when two arrays are considered, as you can see by comparing Fig. 1.10(b) with Fig. 1.10(c). In this case, in fact, the FoR is divided into 2 subsectors, each assigned to a different array⁸. Thus, each array has to scan a smaller sector, also leading to lower gain losses⁹ at the borders. It is important to understand that the gain loss is not a property of the array factor, which is a periodic function of the angular coordinates, but it is a property of the elementary radiator's radiation pattern. It is, then, natural that when only the array factor pattern is visualized, in presence of grating lobes, it

⁸Please note that in practical applications there could be a certain degree of overlap between subsectors, but such problem will not be interest of this work.

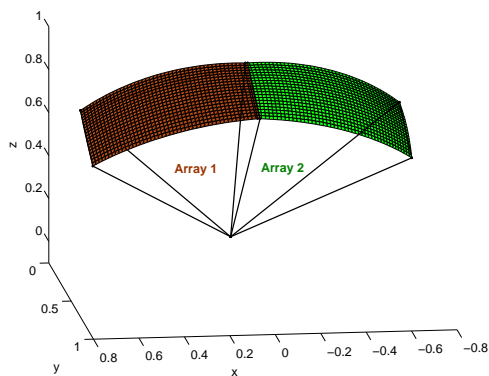
⁹When the beam is steered off broadside, the antenna suffers from a gain reduction which goes with the cosine of the off-boresight angle ([8] pp. 19-26). Thus, a scan angle of $\pm 60^\circ$ leads to a gain loss of around 3 dB



(a)



(b)



(c)

Figure 1.10: Pyramidal section subtended by the FoR (a). FoR when one sensor is employed (b) and when two sensors are employed (c).

should not surprise that the grating lobe level is the same as the main beam. Instead, the introduction of the elementary radiator pattern does affect the level of grating lobes, reducing it especially at the border of the hemisphere ($\pm 90^\circ$).

In this Ph.D. activity, we studied a multi-array system. Each array will yield a narrow beam and will scan its assigned FoR subsector. The single-array orientation was calculated in a local coordinate system and each array was geometrically optimized in order to scan its assigned subsector without grating lobes and with the least number of elements. Thus, no grating lobes should enter the visible region¹⁰ of the array during beam steering.

Multi-Array Orientation

For a system with N arrays, the FoR is divided into N subsectors, as depicted in the example of Fig. 1.11. The FoR is located at a certain elevation in a local coordinate system shown in the Figure. The FoR axis, i.e. the vector crossing the FoR centre, lies in the yz plane and forms an angle $\delta = \pi/2 - \text{EL}$ with respect to the z axis, where EL is the elevation of the FoR axis.

As said previously, given a sectorization of the FoR, each sub-sector will be scanned by a separate planar array whose normal unit vector is oriented perpendicularly to a separate FoR sub-sector. An artist impression of a 2-array system is given in Fig. 1.12, where each array axis orientation is calculated as a function of the usual polar angles θ, ϕ in the local coordinate system.

Let's assume the overall FoR is subtended by an angle equal to $2A'$ in the azimuth direction and $2B'$ in the elevation direction, as depicted in Fig. 1.13. The process to determine each array orientation was structured in the following two steps:

- First, the entire FoR was supposed to be located at 90° elevation, while the direction of each array axis vector was obtained performing a rotation about the y axis;
- Second, the entire FoR, as well as the array axis vectors, were rotated about the x axis to orient the FoR at the right elevation EL.

¹⁰All directions under which the array can receive signals make up the visible region. In this case, the array is planar and radiates only in one hemisphere, so the visible region can be considered the hemisphere toward the positive side of the array axis

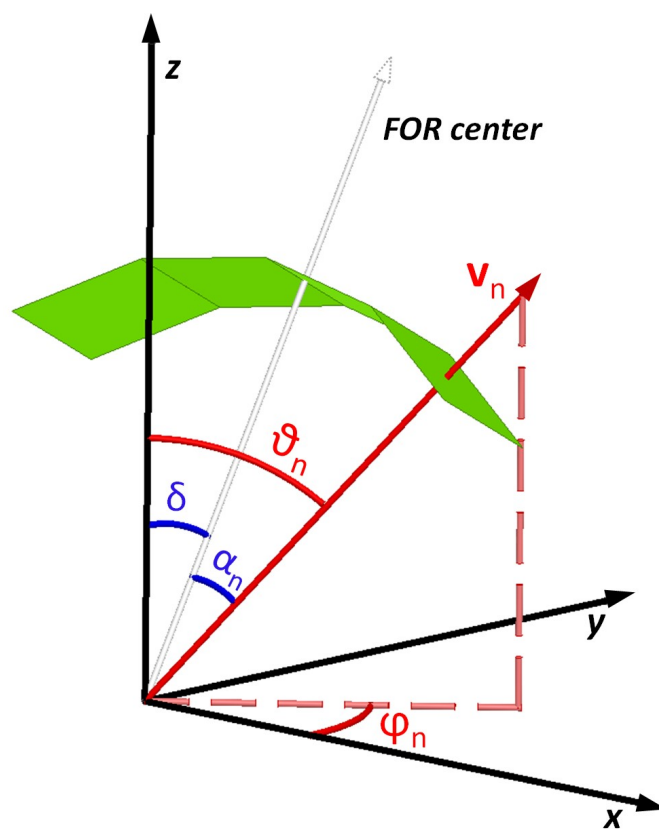


Figure 1.11: FoR divided into N sectors. In this example, $N = 4$.

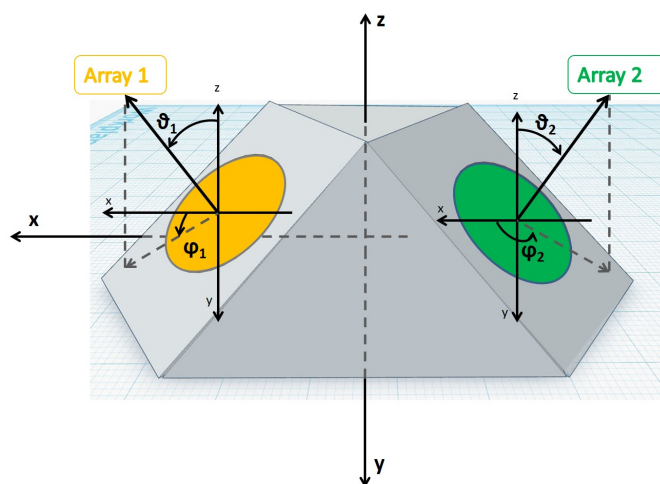


Figure 1.12: Artist impression of a 2-array-antenna radar system for the scanning of a FoR divided into 2 sectors.

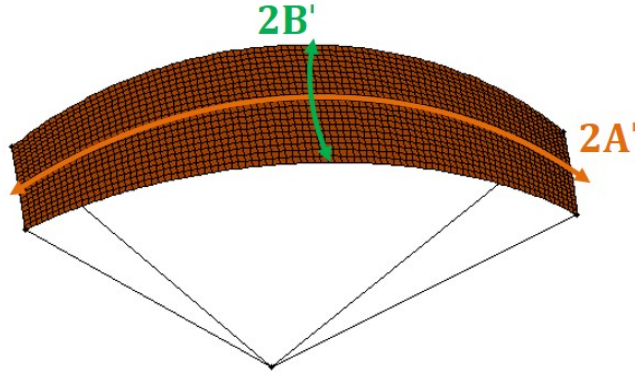


Figure 1.13: Angular extension of the entire field of regard.

To go through the first step, we shall consider Fig. 1.14, where the FoR is for simplicity located at 90° elevation. In this case, the calculation of each array orientation is simply given by a rotation about y axis of a vector initially aligned with the z axis. If the FoR, of overall angular size $2A'$, is divided into N sectors, then the size of each sub-FoR is $\frac{2A'}{N}$. Looking at Fig. 1.14, if array 1 is the first array on the left, toward the negative x axis, its vector angle α_1 with respect to the z axis would be

$$\alpha_1 = -A' + \frac{A'}{N}$$

The axis vector of array 2 would, instead, form an angle with respect to z equal to

$$\alpha_2 = \alpha_1 + 2\frac{A'}{N}$$

Thus, in general, the n -th array vector would form an angle with respect to z equal to

$$\alpha_n = -A' + \frac{A'}{N} + 2(n-1)\frac{A'}{N}$$

Generally, as said previously, in the local coordinate system, the FoR is located at an elevation of $\delta = \pi/2 - \text{EL}$, measured between the FoR's axis (Fig. 1.11) and the xy plane. Additionally, in our coordinate system, the FoR is centered so that y axis divides it into two halves. To properly orient the FoR at the right elevation, it has to be rotated by an angle δ from the z axis in the yz plane (i.e. apply a rotation about x). Each array vector orientation can be calculated starting from a vector equally oriented to z , say $\mathbf{v}_0 = (0 \ 0 \ 1)^T$, and rotate it twice, firstly by an angle α_n about y

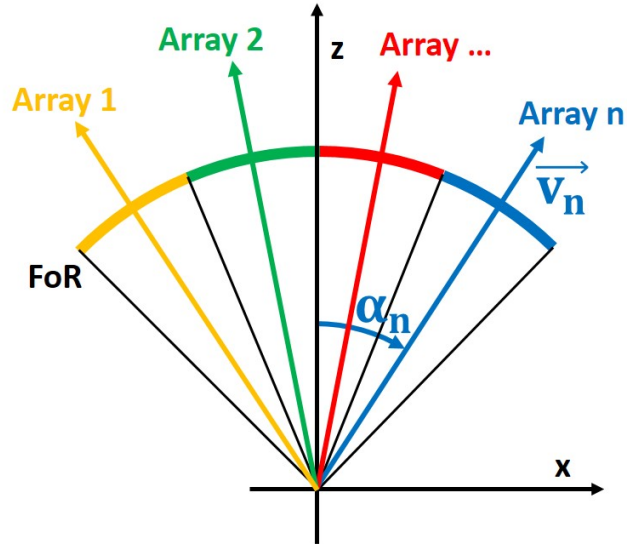


Figure 1.14: Definition of deflection angles A and B.

axis and secondly by an angle δ about x axis. The corresponding rotation matrix is:

$$\mathbf{R} = \mathbf{R}_x \times \mathbf{R}_y$$

where

$$\mathbf{R}_x = \begin{bmatrix} 1 & 0 & 0 \\ 0 & \cos \delta & \sin \delta \\ 0 & -\sin \delta & \cos \delta \end{bmatrix} \quad (1.8)$$

$$\mathbf{R}_y = \begin{bmatrix} \cos \alpha_n & 0 & \sin \alpha_n \\ 0 & 1 & 0 \\ -\sin \alpha_n & 0 & \cos \alpha_n \end{bmatrix} \quad (1.9)$$

Then, the normal vector \mathbf{v}_n of the n -th array, as drawn in Fig. 1.15, can be obtained as:

$$\mathbf{v}_n = \mathbf{R} \times \mathbf{v}_0 = \begin{bmatrix} \sin \alpha_n \\ \cos \alpha_n \sin \delta \\ \cos \alpha_n \cos \delta \end{bmatrix} \quad (1.10)$$

Now, we observe that the x -component of \mathbf{v}_n is given by $|\mathbf{v}_n| \sin \theta_n \cos \phi_n$, the y -component of \mathbf{v}_n is given by $|\mathbf{v}_n| \sin \theta_n \sin \phi_n$, and the z -component is

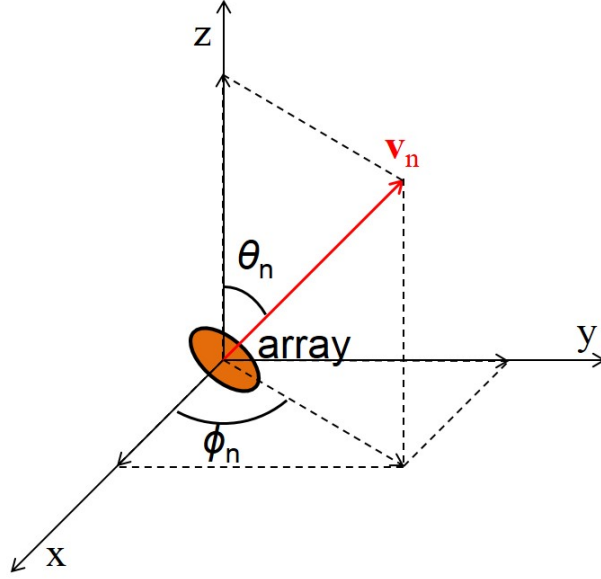


Figure 1.15: Orientation of the normal vector to the n-th array.

given by $|\mathbf{v}_n| \cos \theta_n$, with $|\mathbf{v}_n| = 1$. Thus, from Eq. 1.10, it is straightforward to obtain the following expressions:

$$\begin{aligned}\cos \theta_n &= (\mathbf{v}_n)_z \\ \tan \phi_n &= \frac{(\mathbf{v}_n)_y}{(\mathbf{v}_n)_x}\end{aligned}$$

Solving for θ_n and ϕ_n , we get:

$$\theta_n = \cos^{-1}(\cos \alpha_n \cos \delta) \quad (1.11)$$

$$\phi_n = \begin{cases} \tan^{-1} \left(\frac{\cos \alpha_n \sin \delta}{\sin \alpha_n} \right) + \pi & \text{if } -\frac{\pi}{2} \leq \alpha_n < 0 \\ \frac{\pi}{2} & \text{if } \alpha_n = 0 \\ \tan^{-1} \left(\frac{\cos \alpha_n \sin \delta}{\sin \alpha_n} \right) & \text{if } 0 < \alpha_n \leq \frac{\pi}{2} \end{cases} \quad (1.12)$$

Expressions 1.11 and 1.12 provide the orientation of all arrays making part of a system of a general number of arrays, each scanning an assigned sub-sector of the entire FoR.

Now, given each array and its sub-sector, the aim of the work is to define an optimal array geometry to perform the scanning of the whole sub-sector

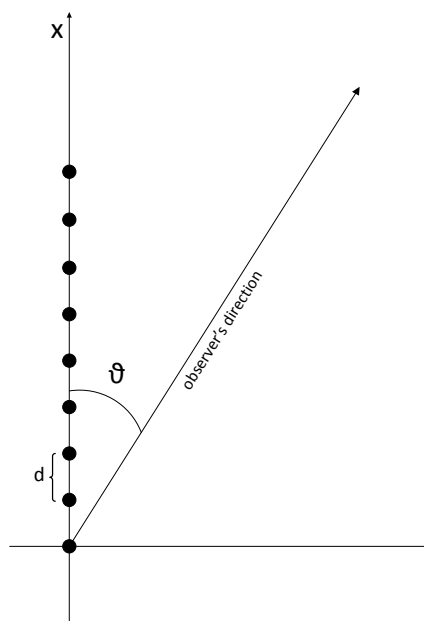


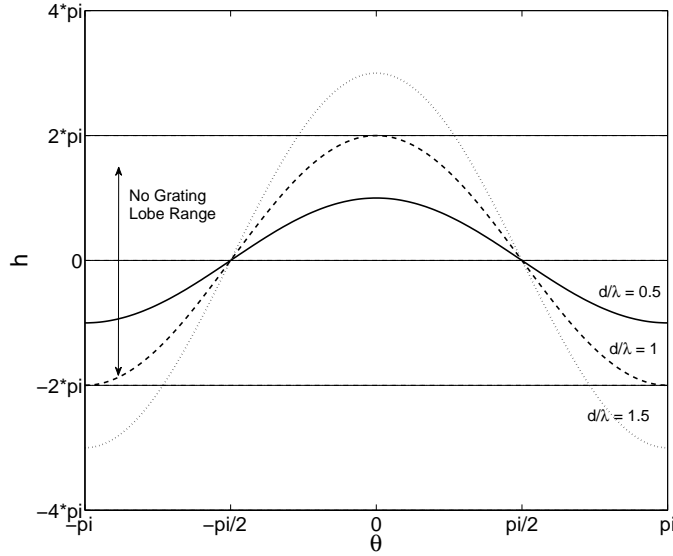
Figure 1.16: Linear array with uniform spacing.

while avoiding the appearance of grating lobes. Next sections will introduce the problem of grating lobes, the representation of the radiation pattern of planar arrays in a more convenient coordinate system, called UV space, and the geometrical analysis carried out to minimize the number of elementary radiators.

1.3.2 Grating Lobes

In a radiation pattern, a grating lobe is a lobe whose strength is equal to that of the main lobe. Grating lobes are generated when there is a maximally constructive interference of the waves radiated by the elements in a different direction from the main lobe. The array factor of a regular planar array¹¹ is periodic in the UV space, leading to the appearance of such lobes in the visibility region. As an example, consider the array factor of a broadside N-element uniform linear array [Fig. 1.16] oriented along one direction, say

¹¹In a regular planar array, the element spacing in the two coordinates x and y is the same for the whole array aperture


 Figure 1.17: Plot of $h = 2\pi/\lambda d \cos \theta$ versus θ .

x axis, whose expression is given by [40]

$$AF(\theta) = \sum_{n=0}^{N-1} e^{j \frac{2\pi}{\lambda} n d \cos \theta} , \quad (1.13)$$

with d the element-spacing and θ the angle between \mathbf{x} axis and observer's direction. We see that, introducing a new variable

$$h = \frac{2\pi}{\lambda} d \cos \theta ,$$

the array factor becomes

$$AF(h) = \sum_{n=0}^{N-1} e^{j n h} , \quad (1.14)$$

which, as a function of h , has a periodicity of 2π . In the broadside direction ($\theta = \pi/2$), $h = 0$. But we know that AF has also maxima for

$$h = \pm 2\pi, \pm 4\pi, \dots$$

It is clear that the appearance of grating lobes depends on how fast the variation of h with respect to the variation of θ is. A plot of h versus θ is given in Fig. 1.17 for three different values of d/λ . As you can see, depending on this ratio, the ranges of oscillation of h change. Everytime the curve of

h intersects one of the $\pm 2k\pi$ -lines, with $k = 1, 2, 3, \dots$, the array pattern has a grating lobe. If h lies in between the two lines -2π and 2π for every possible value of theta, the radiation pattern will be free of grating lobes. Having said that, from a grating lobe viewpoint, the element spacing, in an array, has a strong influence on the radiation pattern. For a planar array, the directions of the grating lobes are strictly connected to the element spacing along x , that along y , and the skew angle γ (see Fig. 1.23 on page 45).

Definition of UV Space

Referring to a planar array, lying on the xy plane, with z axis passing through its center, it is possible to pass from the angle space, where each direction is defined in terms of θ and ϕ angles, to the so called *UV space*, where each direction is represented by two coordinates u and v , where

$$u = \sin \theta \cos \phi, \quad (1.15)$$

$$v = \sin \theta \sin \phi. \quad (1.16)$$

This space represents the projection of a point $P(r = 1, \theta, \phi)$ onto the xy -plane. This means that two points that are symmetrical about the xy plane are mapped onto the same point in the UV space. For this reason, it's convenient to use the UV space only focussing on either $z > 0$ or $z < 0$. From Eq. 1.15, every point (u, v) in the UV space is subject to the conditions:

$$u^2 + v^2 = \sin^2 \theta, \quad (1.17)$$

$$\frac{v}{u} = \tan \phi. \quad (1.18)$$

Looking at the previous two equations, not all points in the UV space represent real values for θ and ϕ . The first condition indicates that points of constant θ and varying ϕ are mapped onto circles of radius $|\sin \theta|$. This means that, since $0 \leq |\sin \theta| \leq 1$, the set of points in the UV space representing physical angles all lie inside the unit circle. The second condition shows that ϕ is the angle formed between the radius of a point in the UV plane and the u axis (see Fig. 1.18). For e.g., the broadside direction of a planar array (z axis) is mapped into the origin of the uv plane ($\theta = 0, \forall \phi$). As a second e.g., the angle $(\theta, \phi) = (30^\circ, 90^\circ)$ is mapped into the point $(u, v) = (0, 0.5)$.

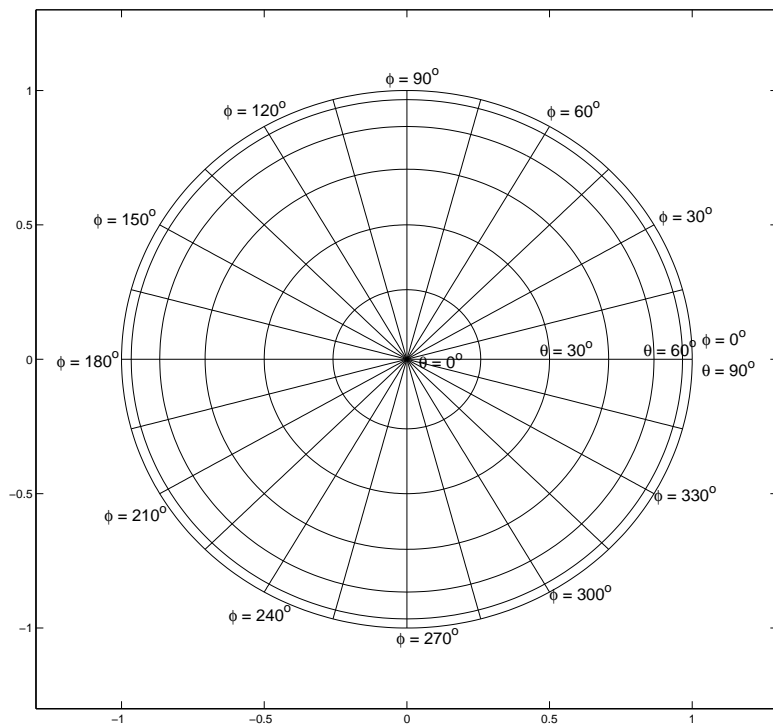


Figure 1.18: Mapping of the angle space onto the UV space.

1.3.3 Grating-Lobe Mapping into UV-Space

To study the grating lobes generated by a planar array, the UV space can provide a better way to understand where they are located and how they can be cancelled.

Consider the array factor of an $N \times M$ rectangular array, with a beam steered to the direction (θ_s, ϕ_s) . Its expression is given by [42]

$$AF = e^{-j\left(\frac{N-1}{2} \frac{2\pi}{\lambda} d_x (\sin \theta \cos \phi - \sin \theta_s \cos \phi_s) + \frac{M-1}{2} \frac{2\pi}{\lambda} d_y (\sin \theta \sin \phi - \sin \theta_s \sin \phi_s)\right)} \cdot \sum_{n=0}^{N-1} \sum_{m=0}^{M-1} w_{nm} e^{j \frac{2\pi}{\lambda} [n d_x (\sin \theta \cos \phi - \sin \theta_s \cos \phi_s) + m d_y (\sin \theta \sin \phi - \sin \theta_s \sin \phi_s)]}, \quad (1.19)$$

where d_x and d_y are the element spacings along the two directions of the plane of the array. By using the relationships 1.15, the array factor can be written as

$$AF = e^{-j\left(\frac{N-1}{2} \frac{2\pi}{\lambda} d_x (u - u_s) + \frac{M-1}{2} \frac{2\pi}{\lambda} d_y (v - v_s)\right)} \cdot \sum_{n=0}^{N-1} \sum_{m=0}^{M-1} w_{nm} e^{j \frac{2\pi}{\lambda} [n d_x (u - u_s) + m d_y (v - v_s)]}, \quad (1.20)$$

where $u_s = \sin \theta_s \cos \phi_s$ and $v_s = \sin \theta_s \sin \phi_s$. Let's assume, at the outset, that the beam is steered to the broadside, i.e. $u_s = 0$ and $v_s = 0$. It is straightforward that the maximum of this array factor will occur at $(u, v) = (0, 0)$, but it also has a periodicity in uv such that grating lobes will occur at the *positions*

$$\begin{aligned} u_{GL} &= \pm p \frac{\lambda}{d_x} & \text{with } p = 1, 2, 3, \dots \\ v_{GL} &= \pm q \frac{\lambda}{d_y} & \text{with } q = 1, 2, 3, \dots \end{aligned} \quad (1.21)$$

Visualizing grating lobes in the UV space is much more convenient than in the angle space, because they make up a sort of regular lattice where horizontal and vertical distances between two neighbour grating lobes are constant. Fig. 1.19 shows an example of uv grating-lobe mapping for a broadside square array with $d_x = d_y = 0.8\lambda$. In this situation, grating lobes (GL) are all outside the unit circle, meaning that the array pattern is GL-free.

However, what happens if the main beam is steered to the point (u_s, v_s) ? Then the main beam will be shifted in the UV space by a certain vector,

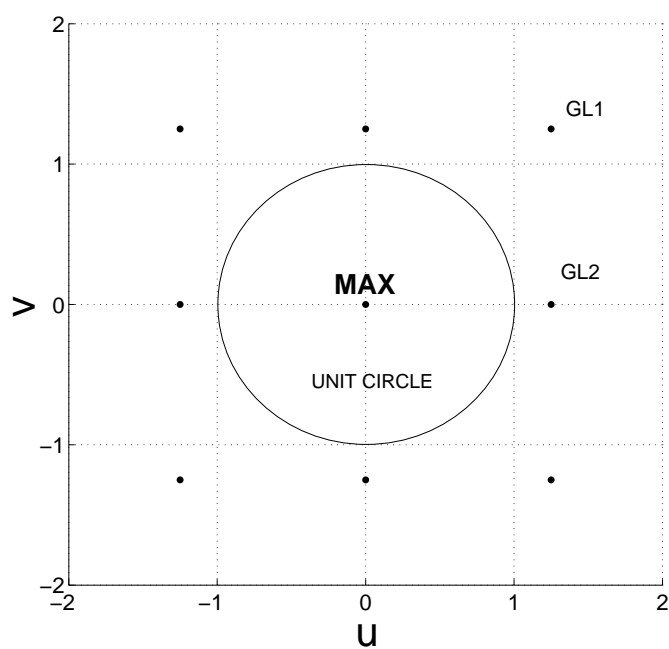


Figure 1.19: Grating-lobe mapping into UV space [43]. The main lobe lies in the origin.

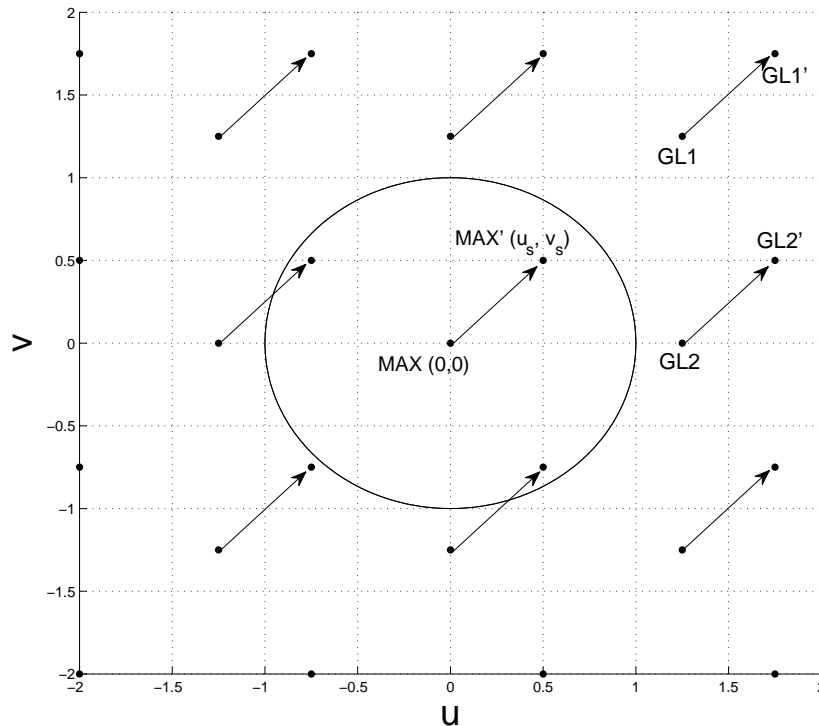


Figure 1.20: Example of grating lobe migration due to beam steering.

pointing from $(0, 0)$ to (u_s, v_s) (as shown in Fig. 1.20). Then, grating-lobe positions will also change into

$$\begin{aligned} u_{GL} &= u_s \pm p \frac{\lambda}{dx} & \text{with } p = 1, 2, 3, \dots \\ v_{GL} &= v_s \pm q \frac{\lambda}{dy} & \text{with } q = 1, 2, 3, \dots \end{aligned} \quad (1.22)$$

Grating lobes will, thus, experience the same vector shift as the main beam. This phenomenon is known as *Grating-Lobe Migration*, as depicted in Fig. 1.20. In this example, there are two grating lobes coming inside the unit circle. These GLs will pop up in the array pattern. So, as one can see, due to beam steering, grating lobes may appear in the visibility region, making it necessary to carefully design the array lattice for GL-avoidance.

Of course, general designs will not require an array to scan the unitary circle in the UV space, but only some smaller sector. It does make sense, then, to consider the behaviour of the array depending on a certain arbitrary

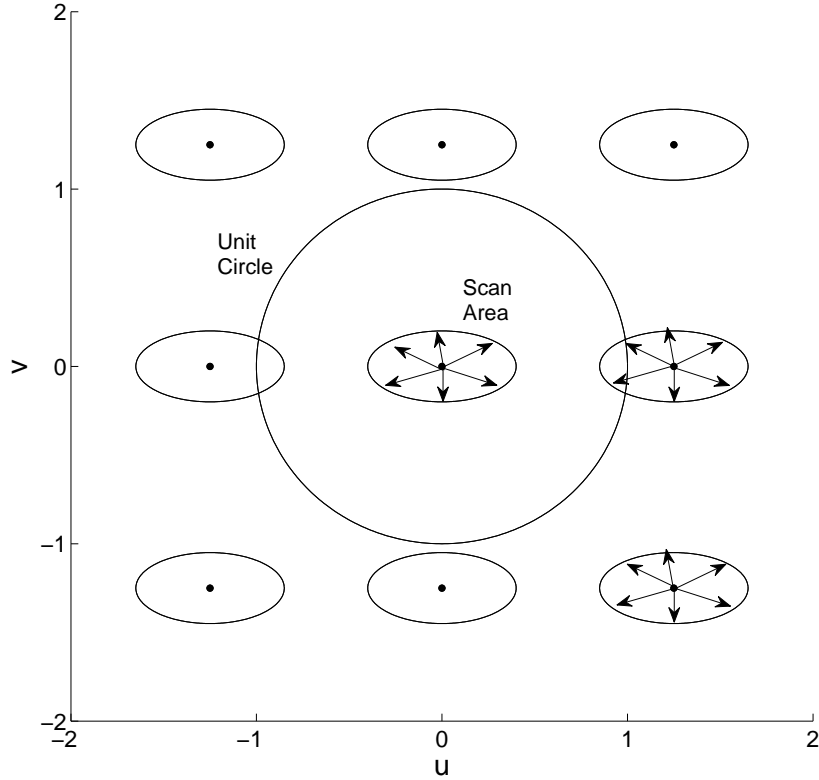


Figure 1.21: Grating-lobe contours for an elliptical scan area in the UV space.

area to be scanned. We will refer to that area as the *scan area*. Every feasible scan area has, naturally, a representation in the UV space. For sake of simplicity, assume a symmetrical scan area around the origin of the UV space, as depicted in Fig. 1.21. As the main beam is scanned throughout the scan area, it will experience several possible vector-shifts all lying within the scan-area contour. This fact will, in turn, induce all grating lobe to migrate by the same vector-shifts. The final result is that the grating lobe all lie within the same contour as the scan region centered around each GL. Fig. 1.21 shows such contours around GLs.

At this stage, it is clear that a condition for GL-avoidance during beam-steering is that all grating-lobe contours should lie outside the unit circle, the limit condition occurring when the contours are exactly tangent to the unit circle.

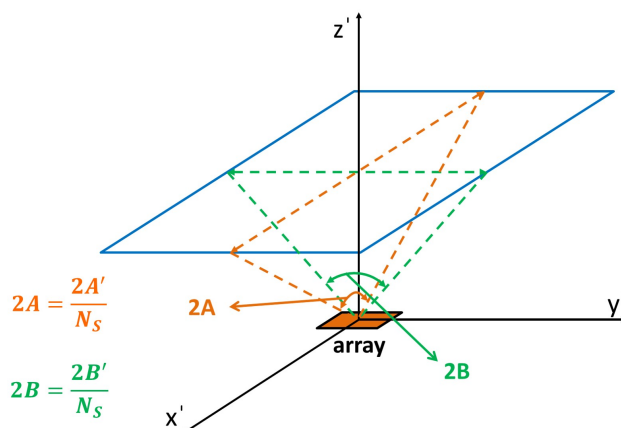


Figure 1.22: FoR sub-sector (subFoR) with its assigned array. The array axis crosses the subFoR exactly in the centre. A' and B' are the elevation and azimuth size of the entire FoR, as defined in Fig. 1.13 on page 33.

1.4 Design of an Optimal Lattice

As shown in Subsection 1.3.1 on page 29, in this multi-array system, each planar array has to scan a prescribed FoR sub-sector (subFoR). This implies that the geometrical optimization, as stated in Subsection 1.3.3 on page 40, should consider a scan area whose extension is equal to a FoR sub-sector, with angle size $2A$ and $2B$, as shown in Fig. 1.22.

Thus, the following section is devoted to the determination of the geometrical parameters of a planar array, given a rectangular subFoR, defined in terms of a couple of angles A and B . The array lattice optimization criterion is the minimization of the number of elements while avoiding grating lobes.

1.5 Standard Lattice Optimization

Consider the general array lattice depicted in Fig. 1.23, where a is the element spacing directed along \mathbf{x} , b is the element spacing directed along \mathbf{y} , and γ is the skew angle. It can be proven [44] that for this general array

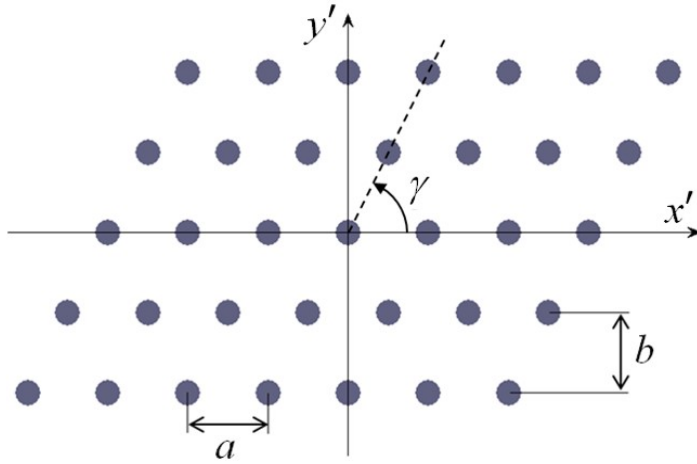


Figure 1.23: General array lattice.

lattice, grating lobes centres will occur, in the uv space, at the positions

$$\begin{aligned} u_{GL}^p &= p \frac{\lambda}{a} \\ v_{GL}^{p,q} &= q \frac{\lambda}{b} - \frac{u_{GL}^p}{\tan \gamma} \end{aligned}, \text{ with } p, q = 0, \pm 1, \pm 2, \dots \quad (1.23)$$

Fig. 1.24 shows the UV mapping of a pyramidal scan as defined in Table 1.1. In Fig. 1.26 on page 49, GL-contours are also plotted. As the element spacing increases, GL contours move towards the unit circle (visibility region), possibly getting inside. The opposite effect occurs if the element spacing decreases. To achieve an optimal situation, the array lattice should be such that GL contours, at the most, are tangent to the unit circle, i.e. the following two conditions should be met [28]:

1. All the left-hand side grating lobe contours should be moved upward and the right-hand side contours downward. The parameter to be changed is the skew angle γ .
2. After the definition of the skew angle, both left-hand side and right-hand side grating lobe contours should be moved horizontally to be tangent to the unit circle (visible region).

For a symmetrical scan region about the origin, condition 1 is obtained when grating lobe $GL2$ in Fig. 1.26 on page 49 and $GL3$ are at the same distance

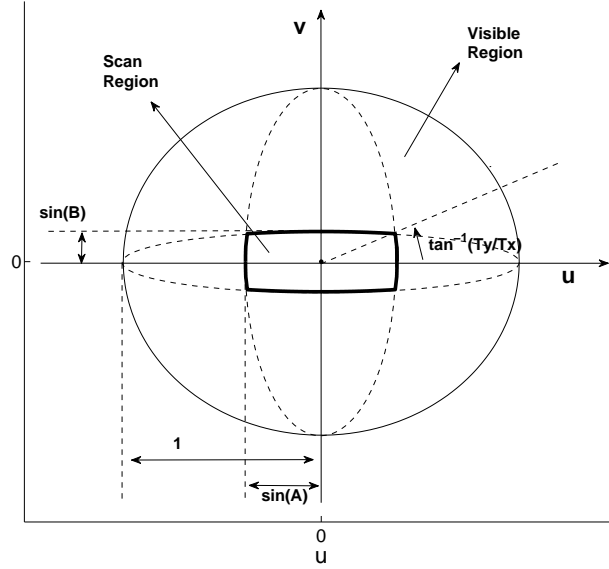


Figure 1.24: Mapping of a rectangular FoV in the UV space.

from u axis, i.e. if

$$\frac{\lambda}{2b} = v_{GL2}.$$

From Eq. 1.23,

$$\begin{aligned} v_{GL2} = (v_{GL})_{1,1} &= \frac{\lambda}{b} - \left[\frac{\lambda/a}{\tan \gamma} \right] \\ &= \lambda \left[\frac{1}{b} - \frac{1}{a \tan \gamma} \right]. \end{aligned}$$

Hence, condition 1 is accomplished if

$$\gamma = \tan^{-1} \left(\frac{2b}{a} \right). \quad (1.24)$$

As a first achievement, the optimal parameter γ has been determined. The next steps will allow to find the optimal values of element spacings a and b in the case of a rectangular FoV.

1.5.1 UV Mapping of a Rectangular FoV

Consider the rectangular FoV given in Fig. 1.25, defined by angles A and B . Without loss of generality, a rectangular surface at $z = 1$ and perpendicular

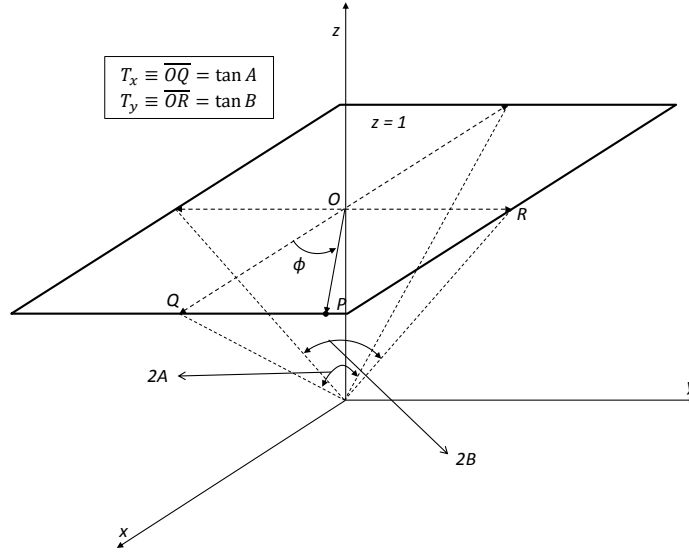


Figure 1.25: Rectangular FoV.

to the z axis is mapped onto the UV plane. Because of the symmetry of that surface, only the region corresponding to $0^\circ \leq \phi \leq 90^\circ$ is mapped and the remaining map can be constructed by symmetry. Any point P, lying on the boundary of the rectangular surface, can be represented by

$$(x, y, z)_P = \begin{cases} (T_x, T_x \tan \phi, 1) & \text{if } 0^\circ \leq \phi \leq \tan^{-1} \left(\frac{T_y}{T_x} \right) \\ (T_y \cot \phi, T_y, 1) & \text{if } \tan^{-1} \left(\frac{T_y}{T_x} \right) \leq \phi \leq 90^\circ \end{cases},$$

where $T_x = \tan A$ and $T_y = \tan B$. It can be shown [28] that mapping of a rectangular FoV onto the UV space is given by

$$(uv)_{\text{pyramidal scan}} : \begin{cases} \left(\frac{u}{\sin A} \right)^2 + v^2 = 1, & \text{if } 0^\circ \leq \phi \leq \tan^{-1} \left(\frac{T_y}{T_x} \right) \\ u^2 + \left(\frac{v}{\sin B} \right)^2 = 1, & \text{if } \tan^{-1} \left(\frac{T_y}{T_x} \right) \leq \phi \leq 90^\circ \end{cases}. \quad (1.25)$$

Interestingly, the corresponding contour, as depicted in Fig. 1.24, represents the intersection of two mutually orthogonal ellipses centered at the origin. The horizontal ellipse has semi-major axis equal to 1 and semi-minor axis equal to $\sin B$; the vertical ellipse has semi-major axis again equal to 1 and semi-minor axis equal to $\sin A$.

1.5.2 Optimal lattice

Fig. 1.26(a) shows the mapped rectangular FoV in the UV space with the addition of grating lobe contours. The optimal value for b is such that the contour of $GL1$ is tangent to the unit circle, that is:

$$\frac{\lambda}{b_{opt}} - \sin B = 1 .$$

Hence,

$$b_{opt} = \frac{\lambda}{1 + \sin B} . \quad (1.26)$$

The other array lattice parameter a depends on the two critical points $CP2$ and $CP3$, as shown in the more detailed view of Fig. 1.26(b). After choosing γ according to 1.24, the critical points $CP2$ and $CP3$ become symmetrical about u axis. Thus, the optimal value for a is obtained when either of the two critical points is touching the unit circle. Now, it's a matter of calculating, for e.g., the coordinates of the point $CP2$ and impose that its distance from the origin be equal to 1.

We will calculate point $CP2$ by first calculating the coordinates of the point $P1$ [Fig. 1.26(b)] and then shifting it by the coordinates of grating lobe $GL2$. We shall pose $T_\phi = \tan \phi$, consequently:

$$T_\phi = \frac{\tan B}{\tan A} .$$

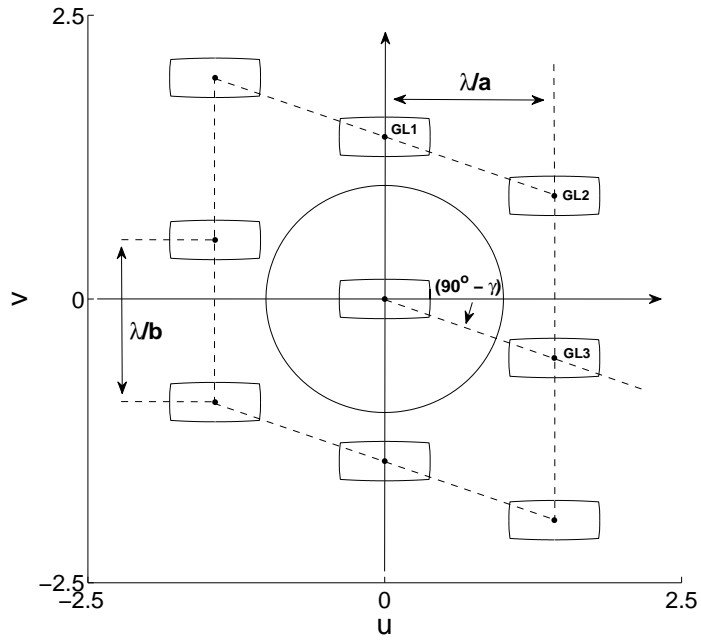
Point $P1$ may be obtained by the intersection of the straight line $v = T_\phi u$ and the horizontal ellipse, i.e. by solving the system

$$(u, v)_{P1} : \begin{cases} v = T_\phi u \\ \left(\frac{u}{S_A}\right)^2 + v^2 = 1 \end{cases} , \quad (1.27)$$

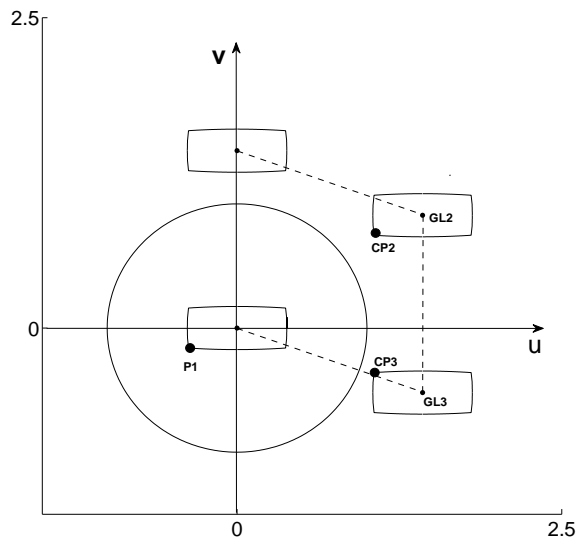
where $S_A = \sin A$. The solutions to this system are extremely easy to obtain:

$$\begin{cases} u = \pm \sqrt{\frac{S_A^2}{1 + (S_A T_\phi)^2}} \\ v = \pm T_\phi \sqrt{\frac{S_A^2}{1 + (S_A T_\phi)^2}} \end{cases} .$$

Since point $P1$ lies in the third quadrant of the UV plane, the right solution



(a) Grating-lobe mapping in UV space.



(b) Critical points for the rectangular FOV.

Figure 1.26: Rectangular FoV and grating lobes in the UV space.

to the system is:

$$P1 : \begin{cases} u_{P1} = -\sqrt{\frac{\sin^2 A}{1 + (\sin A T_\phi)^2}} \\ v_{P1} = -\frac{\tan B}{\tan A} \sqrt{\frac{\sin^2 A}{1 + (\sin A T_\phi)^2}} \end{cases} . \quad (1.28)$$

The coordinates of the point $CP2$ are, then, given by

$$CP2 : \begin{cases} u_{CP2} = u_{P1} + u_{GL2} \\ v_{CP2} = v_{P1} + v_{GL2} \end{cases} , \quad (1.29)$$

where u_{G2} and v_{G2} are the coordinates of grating lobe $G2$, and are equal to

$$\begin{aligned} u_{GL2} &= \frac{\lambda}{a} \\ v_{GL2} &= \frac{\lambda}{2b} \end{aligned} .$$

The distance of $CP2$ from the origin is

$$d_{CP2} = \sqrt{u_{CP2}^2 + v_{CP2}^2} .$$

For $CP2$ to touch the unit circle, this distance must be equal to 1, and we can analytically compute the optimum value for a as follows:

$$\begin{aligned} \sqrt{u_{CP2}^2 + v_{CP2}^2} &= 1; \\ (u_{P1} + u_{G2})^2 + (v_{P1} + v_{G2})^2 &= 1; \\ \left(u_{P1} + \frac{\lambda}{a}\right)^2 + \left(v_{P1} + \frac{\lambda}{2b}\right)^2 &= 1; \\ \left(u_{P1} + \frac{\lambda}{a}\right) &= \sqrt{1 - \left(v_{P1} + \frac{\lambda}{2b}\right)^2}; \\ \frac{\lambda}{a} &= \sqrt{1 - \left(v_{P1} + \frac{\lambda}{2b}\right)^2} - u_{P1}. \end{aligned}$$

From the previous calculations, the optimal parameter a is given by

$$a_{opt} = \frac{\lambda}{\sqrt{1 - \left(v_{P1} + \frac{\lambda}{2b}\right)^2} - u_{P1}} . \quad (1.30)$$

Summarizing all previous arguments, given a pyramidal FoR, symmetrical about the array axis (z axis), and defined by a couple of deflection angles A and B , the optimal array lattice parameters can be obtained through the following procedure

1. Calculate u_{P1} and v_{P1} according to 1.28 on the preceding page.
2. Calculate b_{opt} according to 1.26 on page 48 and a_{opt} according to 1.30.
3. Calculate the skew angle γ according to 1.24 on page 46.

The process to determine the optimum lattice parameters with this alternative approach is recapped in Table 1.2¹².

1.6 Alternative Lattice Optimization

The standard lattice optimization was carried out without considering the beamwidth of the array into account. In fact, the tangency condition of GL contours to the unit circle ensures that the GL centres are exactly at the boundary of the visibility region when the array beam is scanned to the maximum critical angles. The same condition does not ensure at all that the whole lobes belonging to the GLs lie out of the unit circle. It is, thus, necessary to take the lobe-width into account in order to really get rid of any residual grating lobe. Another aspect not considered in the previous approach is the array element pattern, which can further decrease GL level. The alternative optimization here described is called *alternative* in the sense that the optimal lattice parameters will also depend on the array beamwidth and the single-element radiation pattern. Since this optimization will again be carried out in the UV space, a very good property of this space can be exploited [40]: i.e. the GL width is exactly the same as the main beam¹³. As the alternative approach is used, on the one hand, the element spacing will inevitably decrease to compensate for the GL width, with a consequent increase of the number of radiators (assuming to fill a prescribed finite array aperture); on the other hand, a proper selection of the elementary radiator can have an opposite effect, i.e. the possibility of increasing the element spacing¹⁴. It is important to explain that the alternative approach

¹²To recap, the space debris radar has to scan a certain field of regards (FoR). To do that, the FoR will be divided into N_s identical sectors (Fig. 1.11). Each sub-FoR, with size $2A \times 2B$, is assigned to a separate array, oriented orthogonally to the sub-sector (Fig. 1.22).

¹³In a polar coordinate system, the width of the grating lobes changes depending on their angular position, with a widening as the position tends to the horizon.

¹⁴For e.g., consider an array with some GLs at the boundary of the visible region with -10 dB portion of the GL peak amplitude inside the UV-plane unit circle. If, for

Table 1.2: OPTIMUM LATTICE PARAMETERS - STANDARD APPROACH.

Symbol	Parameter	Expression
a	horizontal spacing	$\frac{\lambda}{\sqrt{1 - \left(v_{P1} + \frac{\lambda}{2b}\right)^2} - u_{P1}}$
b	vertical spacing	$\frac{\lambda}{1 + \sin B}$
γ	skew angle	$\arctan \frac{2b}{a}$
u_{P1}	u-coordinate of P1 (Fig. 1.27)	$-\sqrt{\frac{\sin^2 A}{1 + (T_\phi \sin A)^2}}$
v_{P1}	v-coordinate of P1	$-T_\phi u_{P1}$
T_ϕ		$\frac{\tan B}{\tan A}$
A	subFoR azimuth extension	$\frac{A'}{N_s}$
B	subFoR elevation extension	$\frac{B'}{N_s}$
N_s	number of FoR sub-sectors	application-dependent

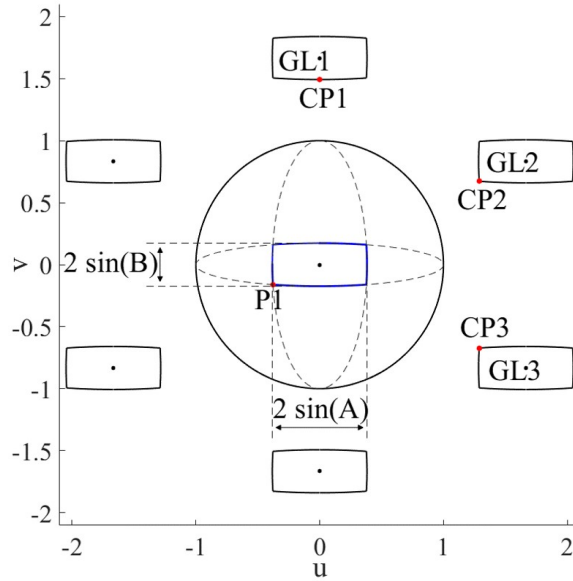


Figure 1.27: Representation in the UV plane of the rectangular subFoR (blue contour) created by the interception of two mutually orthogonal ellipses (dashed lines), the unit circle, and the first six grating-lobe replicas.

as compared with the standard one should not be assumed as the best one in terms of number of elementary radiators, but as the most complete and refined approach which considers other aspects previously neglected.

1.6.1 Determination of the lattice parameters

Again, the determination of the proper lattice parameters starts by considering the mapping of the rectangular subFoR onto the UV space along with the representation of the replicas centered around the GLs, see Fig. 1.27. Let us consider an array with a radiation pattern where the main lobe at a given taper can be described in the UV space using a circular footprint defined by a radius R_{BW} ¹⁵, as shown in Fig. 1.28.

This kind of radiation pattern is rigorously generated by an array with a circular extension and uniform excitation. However, it also represents

instance, it is desirable to further reduce this GL level, a possibility is to reduce the element spacing; another possibility is to choose a single-element radiation pattern which shows an attenuation at the boundary. In the second choice, you don't have to act on the number of elementary radiators, but only on the shape of the single-element pattern.

¹⁵As said, in the UV space, there is no deformation of a circular symmetric beam, even when it is considered at the horizon

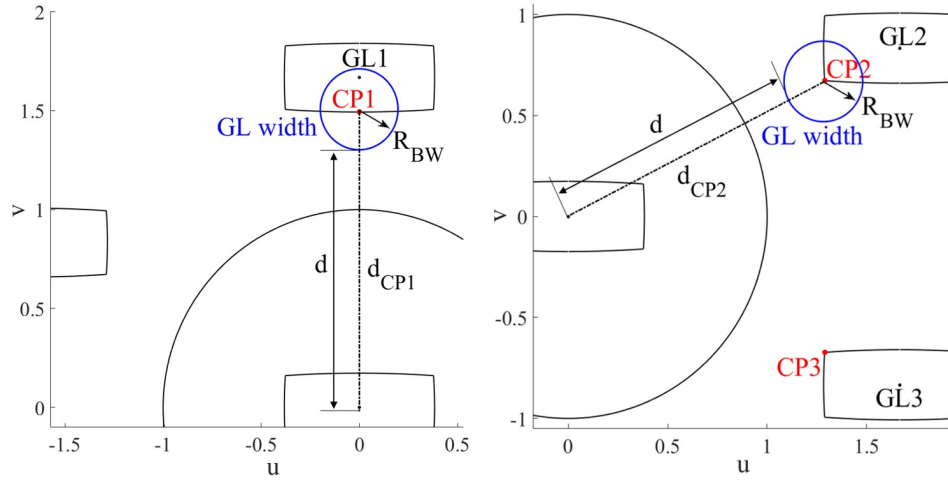


Figure 1.28: Enlarged view of Fig. 1.27 showing the calculation schema for points CP1 and CP2 for the alternative approach.

a fair approximation in other situations of some relevance to space debris applications, most notably arrays with hexagonal extension (one of the preferred shapes when implementing scalable arrays). It is also worth to notice that the circular footprint holds for any point of the scanned sub-FoR in the UV space, where scanning angles different from zenith appear as rigid translations, and not as beam distortions as in the $\theta\phi$ domain. Let us first determine the optimum condition for the vertical spacing b . This is calculated by imposing the tangency condition for the critical point CP1 shown in Fig. 1.28, which is related to the grating lobes defined by $(p = 0, q = 1)$ from Eq. 1.23 on page 45, and taking into account the main lobe radial extension R_{BW} :

$$d = d_{CP1} - R_{BW} = v_{CP1} - R_{BW} = 1 \quad (1.31)$$

where v_{CP1} is the v -component of the critical point CP1 in the UV space, which, looking at Figs. 1.27 and 1.28, can be found as:

$$v_{CP1} = v_{GL}^{0,1} - \sin B = \lambda/b - \sin B \quad (1.32)$$

where the vertical displacement $v_{GL}^{0,1}$ of the grating lobe replica defined by $(p = 0, q = 1)$ is calculated using Eq. 1.23 on page 45, $\sin B$ represents the semi-minor axis of the horizontal ellipse defined by Eq. 1.25 and depicted in Fig. 1.27. Substituting Eq. 1.32 into Eq. 1.31, we get:

$$\lambda/b - \sin B - R_{BW} = 1 \quad (1.33)$$

Solving for b , we obtain the equation for the vertical element spacing:

$$b = \frac{\lambda}{1 + \sin B + R_{\text{BW}}} \quad (1.34)$$

Let us now determine the optimum condition for the horizontal spacing a . This is calculated by imposing the tangency condition for the critical point CP2 shown in Fig. 1.28, which is related to the grating lobe defined by ($p = 1, q = 1$), and taking into account the main lobe radial extension R_{BW} :

$$d = d_{\text{CP2}} - R_{\text{BW}} = 1 \quad (1.35)$$

where

$$(d_{\text{CP2}})^2 = (u_{\text{CP2}})^2 + (v_{\text{CP2}})^2 \quad (1.36)$$

and

$$\begin{aligned} u_{\text{CP2}} &= u_{\text{P1}} + u_{\text{GL}}^1 \\ v_{\text{CP2}} &= v_{\text{P1}} + v_{\text{GL}}^{1,1} \end{aligned} \quad (1.37)$$

Using Eq. 1.23 into 1.37 and plugging the UV coordinated of CP2 into 1.36 and then back into 1.35, we obtain:

$$\sqrt{\left(u_{\text{P1}} + \frac{\lambda}{a}\right)^2 + \left(v_{\text{P1}} + \frac{\lambda}{b} - \frac{\lambda/a}{\tan \gamma}\right)^2} - R_{\text{BW}} = 1 \quad (1.38)$$

Again, since the optimum lattice also in this case satisfies the relation $\tan \gamma = 2b/a$ (which guarantees a symmetrical distribution of GLs around the unit circle), we have that $\frac{\lambda/a}{\tan \gamma} = \lambda/2b$. So, we can solve the previous equation for a , obtaining the horizontal element spacing:

$$a = \frac{\lambda}{\sqrt{(1 + R_{\text{BW}})^2 - \left(v_{\text{P1}} + \frac{\lambda}{2b}\right)^2} - u_{\text{P1}}} \quad (1.39)$$

To sum up, the procedure to compute the optimum geometrical lattice parameters can be structured in the following steps:

1. Calculate u_{P1} and v_{P1} according to 1.28 on page 50;
2. define R_{BW} depending on the desired attenuation of GL level¹⁶;

¹⁶ R_{BW} is the beamwidth in the UV plane. The choice of this value directly affects the amount of GL appearing in the visible region (or entering the unit circle). If, for instance, it is defined as the first-null beamwidth, this condition ensures the GLs completely stay out of the unit circle; if it is defined as the half-power beamwidth, at most the 3 dB value of GLs are inside the unit circle.

3. calculate b according to Eq. 1.34 and a according to 1.39;
4. calculate the skew angle γ according to 1.24 on page 46.

The process to determine the optimum lattice parameters with this alternative approach is recapped in Table 1.3¹⁷.

1.6.2 Application of the general formulas to notable cases

It is important to notice the role played by R_{BW} . The choice of this value is strictly dependent on the array beamwidth. But, the beamwidth can be defined in several ways (e.g. half-power and first-null beamwidth) [40], according to the designer needs. We are used to defining it as the half-power (or 3 dB) beamwidth (HPBW), that is the width at which the beam power is half the peak value. But, what happens if this value is set and lattice parameters are calculated? To answer this question, we don't have to compute all parameters; it is sufficient to look at Fig. 1.28. The calculation of the lattice parameters according to the alternative method presented here imposes the tangency condition of the small beam circles with radius R_{BW} with the unit circle. In case of HPBW definition for R_{BW} , all points lying in the small circumference represent values equal to -3 dB of the GL peak value. Thus, the tangency condition imposes that along the boundary of the unit circle, there is a non-zero GL amplitude, and in particular there are 6 points where GL values is equal to -3 dB. Each of these 6 GLs of course appear whenever the beam is scanned to the 6 critical scan points in the subFoR.

It is now clear how the choice of R_{BW} is fundamental for the GL attenuation. To appreciate this, we will study some notable cases:

- a. **Standard approach**, where R_{BW} is zero, i.e. the beamwidth is totally neglected;
- b. **-3 dB approach**, where R_{BW} is set to the HPBW;
- c. **first-null (FN) approach**, where R_{BW} is set to the FNBW, i.e. the width at which the beam value reaches its first zeros.

¹⁷To recap, the space debris radar has to scan a certain field of regards (FoR). To do that, the FoR will be divided into N_s identical sectors (Fig. 1.11). Each sub-FoR, with size $2A \times 2B$, is assigned to a separate array, oriented orthogonally to the sub-sector (Fig. 1.22).

Table 1.3: OPTIMUM LATTICE PARAMETERS - ALTERNATIVE APPROACH.

Symbol	Parameter	Expression
a	horizontal spacing	$\frac{\lambda}{\sqrt{(1 + R_{\text{BW}})^2 - \left(v_{\text{P1}} + \frac{\lambda}{2b}\right)^2}} - u_{\text{P1}}$
b	vertical spacing	$\frac{\lambda}{1 + \sin B + R_{\text{BW}}}$
γ	skew angle	$\arctan \frac{2b}{a}$
R_{BW}	UV-space beam radius	antenna-dependent
u_{P1}	u-coordinate of P1 (Fig. 1.27)	$-\sqrt{\frac{\sin^2 A}{1 + (T_\phi \sin A)^2}}$
v_{P1}	v-coordinate of P1	$-T_\phi u_{\text{P1}}$
T_ϕ		$\frac{\tan B}{\tan A}$
A	subFoR azimuth extension	$\frac{A'}{N_s}$
B	subFoR elevation extension	$\frac{B'}{N_s}$
N_s	number of FoR sub-sectors	application-dependent

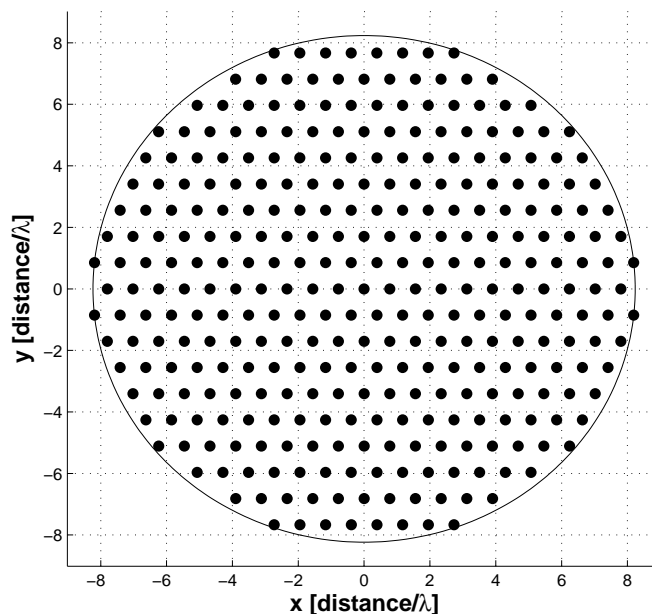


Figure 1.29: Example of circular-aperture array with triangular lattice designed according to the methodology exposed in this chapter.

A natural choice for the array antenna aperture shape is circular one, in order to generate a perfect circular beam and exploit Taylor taper function to have very low sidelobes. An example of such an array is reported in Fig. 1.29. In this case, an approximated closed-form expression to describe the radial extension R_{BW} for both cases b and c is given by [40]:

$$R_{BW} = \sin \left(X \frac{\lambda}{R_A} \right) \quad (1.40)$$

where R_A is the radius of the uniformly excited circular array and X is a parameter equal to 14.60° or to 34.95° for the case of the -3 dB contour and for the case of the first-null contour, respectively.

1.6.3 Effect of the single-element radiation pattern

Another relevant aspect is represented by the single-element radiation pattern. Both the standard approach providing expressions 1.30, 1.26, and 1.24 and the advanced approach providing 1.39, 1.34, and 1.24 implicitly assume an isotropic radiation pattern. In practical cases, this can be a rough assumption, especially for large angles, which is where grating lobes may occur.

As an example of radiating element suitable for space debris applications, rectangular patch antennas are addressed in this work. In particular, the angular dependence of the radiation intensity on the E-plane and H-plane can be approximately described as [40]:

$$\begin{aligned} K_0 &= [\text{sinc}(Q \cos \theta) \cos(P \sin \theta)]^2 && \text{E-plane} \\ K_0 &= [\cos \theta \text{sinc}(Q \cos \theta) \text{sinc}(W \sin \theta)]^2 && \text{H-plane} \end{aligned} \quad (1.41)$$

Parameters Q , P , and W are related to the physical dimensions of the patch antenna and to the working frequency f [40]. Therefore, while for arrays with isotropic elements, the radiation patterns are calculated using the array factor, for arrays with non-isotropic elements, the radiation patterns are calculated also taking into account the contribution of the element radiation intensity (e.g., described by Eqs. 1.41 for rectangular patch antennas), according to standard practice for arrays.

1.6.4 Validation example

Once the optimum array lattice is calculated, using the equations provided in this chapter, and the element radiation intensity K_0 is known (e.g. using Eqs. 1.41), the array radiation intensity K is obtained multiplying the element radiation intensity K_0 by the square modulus of the array factor AF. With the aim of validating the proposed equations, an example based on the current assumptions for the surveillance radar under development for the European Space Agency is discussed. The key parameters of the example are reported in Table 1.4.

The subFoR exhibits an angular extension of $30^\circ \times 20^\circ$ (achieved dividing the sky region under surveillance (FoR), $90^\circ \times 20^\circ$, into three sub-sections). The final array diameter is expected to be in the order of 24 m to provide adequate signal-to-noise ratio for targets as far as 2000 km and as small as 10 cm in diameter [4]. However, as said previously, to spread manufacturing cost effort over several years, the arrays have a regular lattice, so as to provide the antenna aperture with the flexibility to change its dimension. For this reason, an initial array extension $R_A = 2.4$ m is considered in this work. This array is expected to provide adequate signal-to-noise ratio for target as far as 2000 km and as small as 50 cm in diameter. The problem of designing the array lattice with the minimum number of elements, while avoiding grating lobes, is studied and solved using either the standard ap-

Table 1.4: ESA SURVEILLANCE RADAR - MAIN PARAMETERS.

Symbol	Parameter	Value
f	working frequency	1.25 GHz
λ	free-space wavelength	24 cm
	FoR under surveillance	$90^\circ \times 90^\circ$
	number of sectors	3
A	subFoR angular extension	15°
B	subFoR angular extension	10°
R_A	array radius	2.4 m
Q	patch geometrical factor	$\pi/20$
P	patch geometrical factor	$\pi/2$
W	patch geometrical factor	$\pi/2$

proach, or the alternative approach, the latter specialized for two different contours of the main lobe, namely -3 dB and first-null (FN).

Table 1.5 reports the results obtained. As expected, the number of elements calculated using the standard approach is smaller compared to the alternative approach. In particular, the number of elements is increased by around 5% and 12% for the alternative approach at -3 dB and FN, respectively. However, the apparent disadvantage represented by the higher number of elements is outweighed by improved radiation patterns in terms of grating lobes. In particular, the analysis on the radiation patterns is performed considering both isotropic elements and the rectangular patch presented in Subsec. 1.6.3. The latter is also validated using a full-wave Ansys HFSS model, taking into account the mutual coupling. In particular, the patch antenna element is simulated using a Rogers RT/duroid 5880 substrate ($\epsilon_r = 2.2$, $\tan \delta = 0.0009$), with a $50\text{-}\Omega$ coaxial feed excitation. The effect of mutual coupling is taken into account by simulating the unit cell of an indefinitely large array with the periodic lattice specified by the three array geometrical parameter a , b , and γ (according to data reported in Table 1.5), as shown in Fig. 1.30. The infinite-array approximation is very good owing to the big size of the array apertures under consideration, and it has revealed an unsevere impact of mutual coupling on the array input matching. The final patch antenna dimensions were $L_p = 6.7$ cm, $W_p = 12$ cm, and $H_p = 1.2$ cm for all cases reported in Table 1.5. From Fig. 1.30,

Table 1.5: ESA SURVEILLANCE RADAR - VALIDATION EXAMPLE
Full-wave values in brackets

Parameter	Standard approach	-3 dB approach	first-null (FN) approach
a	0.860 λ	0.844 λ	0.822 λ
b	0.852 λ	0.834 λ	0.810 λ
γ	63.23°	63.17°	63.09°
# elements	425	445	477
max secondary lobe isotropic elements	0 dB	-2.8 dB	-17.3 dB
max secondary lobe patch elements	-17.3 dB (-17.8 dB)	-20.4 dB (-21.3 dB)	-32.3 dB (-33.8 dB)
main lobe reduction isotropic elements		0 dB	
main lobe reduction patch elements		-0.92 dB (-1.08 dB)	

it can be appreciated that, due to the relatively large separation between the elements (more than 0.8 λ for all cases reported in Table 1.5), which contributes to reduce the effects of mutual coupling, the input matching at -10 dB, while reduced with respect to the case of the stand-alone antenna, still remains large enough to accommodate the design frequency (1.25 GHz) with no re-design. Finally, the array radiation intensity K is calculated using either the analytical procedure, where the element radiation intensity K_0 is determined using expressions 1.41, or the full-wave approach, where it is determined simulating the element active gain [45].

Comparison with hexagonal and rectangular array lattices

It is interesting to notice that, independently of the utilized approach of Table 1.5, a certain reduction of the number of elements always occurs if the proposed array lattice is compared with a traditional hexagonal or rectangular lattices. Just to show an example, in this paragraph the presented formulas refer to the case where GLs are considered, in the worst case, tangent to the visible region, likewise the standard approach treated in the previous sections.

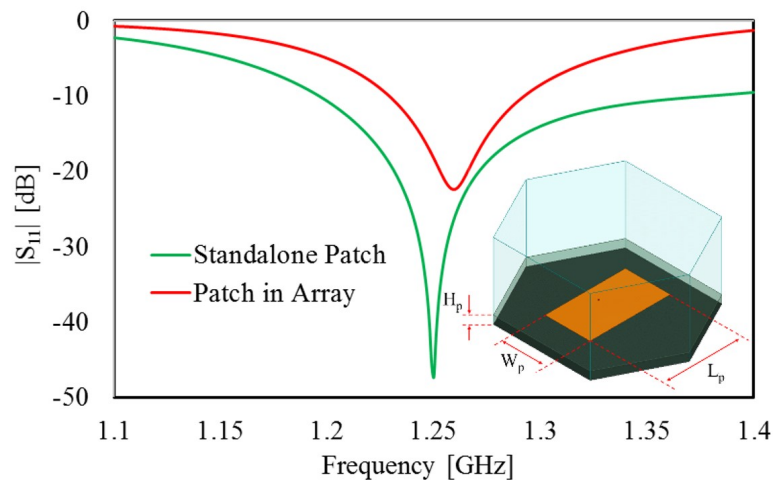


Figure 1.30: Full-wave (Ansys HFSS) simulation results for the input matching of the patch antenna shown in the inset, used as the unit cell for the periodic array lattice, showing the effect of the mutual coupling (red curve) against the case of the standalone antenna (green curve).

For a hexagonal lattice, the maximum allowed element spacing is given by the well known formula [44]:

$$d_{\max} = \frac{2\lambda}{\sqrt{3}(1 + \sin \theta_{\max})}$$

Given the rectangular pyramidal scan region ($A = 15^\circ$, $B = 10^\circ$) under study, the maximum scan angle θ_{\max} is roughly 18° , which gives $d_{\max} = 0.88\lambda$. Using this spacing, the total number of elements required to fill the same circular array aperture of Table 1.4 is about 475.

For a rectangular lattice, assuming the maximum allowed element spacings in the horizontal direction a and in the vertical direction b are [44]

$$a_{\max} = \frac{\lambda}{(1 + \sin A)}$$

$$b_{\max} = \frac{\lambda}{(1 + \sin B)}$$

which, for the prescribed scan region, gives $a_{\max} = 0.79$ and $b_{\max} = 0.85$. The total number of elements required to fill the circular array aperture is about 467.

Remembering that the proposed method, derived in this thesis, gives a total number of elements of 425, it is possible to notice a reduction of about

10% with respect to hexagonal lattice and 9% with respect to a rectangular lattice.

Usually, we are used to the hexagonal lattice being preferred over the rectangular lattice, but here it seems to happen the contrary. The reason lies in the shape of the scan region, which, being rectangular, better adapts to a simple rectangular lattice, while the hexagonal lattice would show its potential only if the scan region were conical. Instead, the lattice proposed in this thesis performs better than both hexagonal and rectangular lattices.

“Time-Space” Representation

The array radiation intensity K is studied according to a sort of four-dimension (4D) representation of the entire FoR, shown from Fig. 1.31a to Fig. 1.31f (time-space representation), where the radiation patterns relative to the most critical scan angles of the sub-FoR are overlapped. The “4D” diagrams report the magnitude of the array radiation pattern, using a color scale, in the UV plane. The UV plane is a representation of the radiation pattern in the space domain, while the various critical scan angles (assuming that scanning occurs over time) are seen as sequentially overlapped in time, hence “time-space”. The term “Time-Space” shall not be considered as a transcendental time- or space-domain transform, but just as a way of representing in just one graph all critical scan angles with related grating lobes. In the figures, six extreme scan points along the subFoR contour (the solid black line depicted in Fig. Fig. 1.31a) are identified and labeled in Fig. 1.31a using the symbols S1 to S6 (the subFoR contour and the labeling is not reported in subsequent figures for simplicity). Each scan point generates a number of grating lobes, labeled in Fig. 1.31a using the symbols $GLn - m$, where $n = 1$ to 6 identifies the scan point S_n which the grating lobe stems from, and $m = 1, 2$ identifies the grating-lobe sequential number (for instance, scan points S2 and S5 generate one grating lobe only, while all other scan points generate two grating lobes). Thus, the use of the 4D diagrams allows for evaluating the array radiation pattern while the main beam is scanned within the subFoR¹⁸. As we can observe from Fig. 1.31a,

¹⁸Another example may help understand the notation in Fig. 1.31a. If the main beam is scanned to point S3, the associated GLs appearing in the radiation pattern are those labeled with number 3, so GL3-1 and GL3-2, where GL3-1 is the first grating lobe and GL3-2 is the second grating lobe associated to scan point S3.

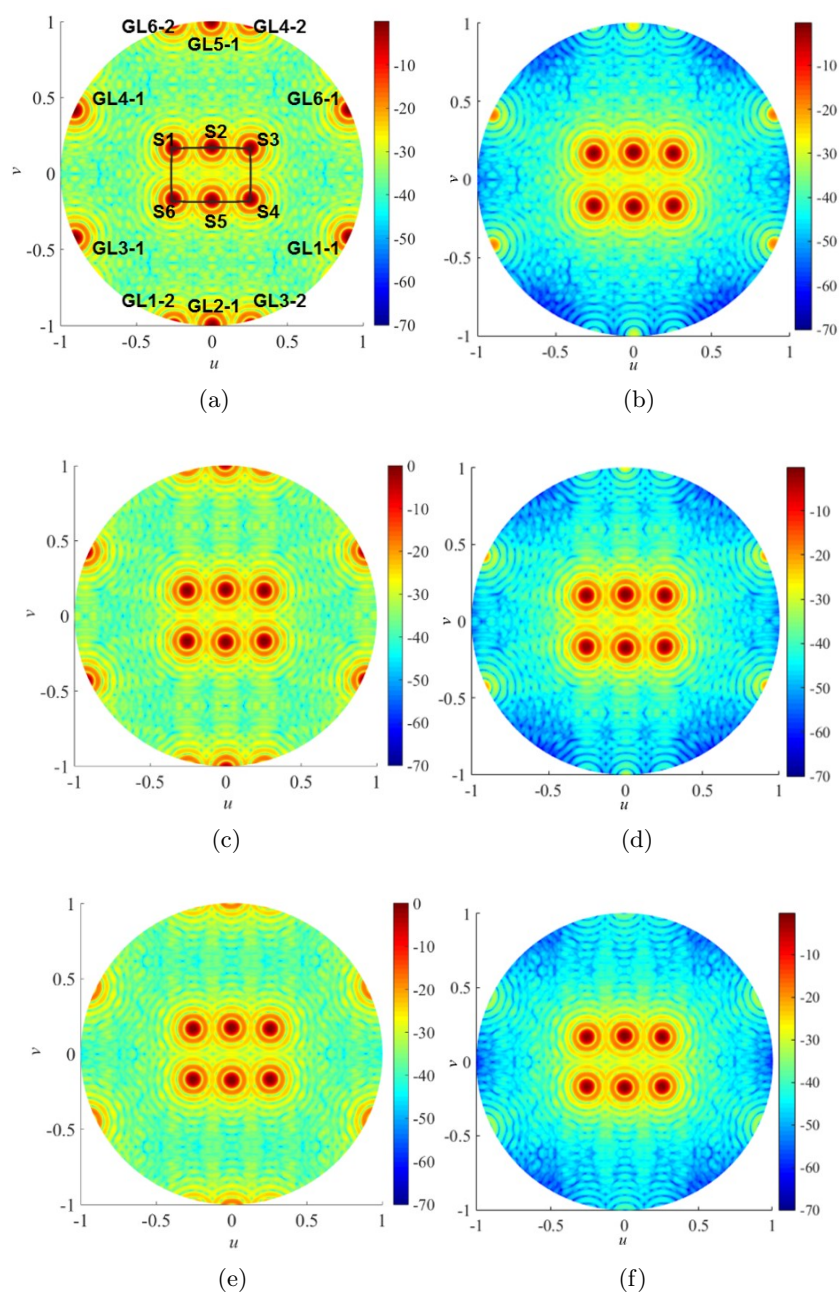


Figure 1.31: Time-space (4D) diagrams for the array radiation pattern. Color scale in dB. On the left-hand side, patterns generated using isotropic elements. On the right-hand side, patterns generated using rectangular-patch elements. Results for the standard approach are shown in the first row - cases (a) and (b); for the -3 dB approach, in the mid row - cases (c) and (d); and for the first-null approach, in the third row - cases (e) and (f).

the 6 critical scan points of the subFoR generate 6 major GLs having a risk of popping up in the radiation pattern. Then, the grade of impairment caused by those GLs depends on whether the standard, the -3 dB or the FN approach is used. In particular, taking into account isotropic elements, grating lobes as high as the main lobe (i.e., 0 dB, Fig. 1.31a) and around 3 dB lower (Fig. 1.31c) occur using the standard approach and the -3 dB approach, respectively, as expected. On the other hand, using the FN approach, grating lobes are completely canceled (Fig. 1.31e). However, in Fig. 1.31e, one may also observe the presence of some peripheral half-rings with an amplitude of around -17 dB below the main beam peak. These are due to the array factor periodicity in UV space, which replicates the sidelobe rings around the main lobe also around grating lobes, thus raising the amplitude of the radiation pattern to the same value as can be observed around the main lobe, i.e. to about -17 dB (typical of uniformly tapered arrays with circular aperture [8]). Table 1.5 summarizes all these results, reporting the highest value of the secondary lobe amplitude, which can be either grating lobe or sidelobe, according to the discussion above. Table 1.5 clearly identifies a horizontal trend. Indeed, the maximum secondary lobe decreases moving from the standard to the other two approaches, the largest improvement being obtained with the FN approach. Taking into account rectangular-patch elements, the same horizontal trend still holds, and each case is further improved by the element radiation pattern (vertical trend in Table 1.5), which is attenuated towards the boundary of the unit circle. As mentioned before, these results are obtained using either the approximated element pattern Table 1.41 or the full-wave simulated active element pattern. However, the difference can be considered as negligible. The improvement on the maximum amplitude of secondary lobes given by the use of a non-isotropic element pattern is clearly highlighted using the 4D diagrams. It can also be appreciated that the use of non-isotropic element patterns inevitably causes a reduction of the main beam due to the scan losses. In any case, this loss is around 1 dB for the example under analysis (neglecting mutual coupling and scan blindness effects). From a general perspective, it is thus worth noting that using the alternative approach presented in Section 1.6 and the 4D diagrams, the array lattice parameters can be designed and optimized according to the given specification in terms of maximum secondary lobe, with the minimum number of elements.

1.7 Array Aperture Truncation and Random Phase Errors

Besides the problem of defining an optimum lattice for ESA space debris radar, addressed in the previous sections, this section is devoted to some sources of errors which may degrade the radiation pattern of the antenna. In fact, any inaccuracy in the determination of the radiation pattern, either due to array truncation and/or feeding errors, may result in a wrong detection.

To calculate the array radiation pattern, the patch active element pattern [45] was used in Sec. 1.6, simulating an indefinitely large array. Although this approximation is quite accurate for large arrays, it may lead to inaccuracies for moderate-sized arrays, where edge effects due to the finite aperture dimension can arise, degrading the radiation performance, in particular in terms of gain reduction and sidelobe level increase. For this reason, truncation effects have been analyzed, by adopting a separate radiation pattern for the boundary elements at the edge of the array and keeping the infinite-array active element pattern for the internal array elements.

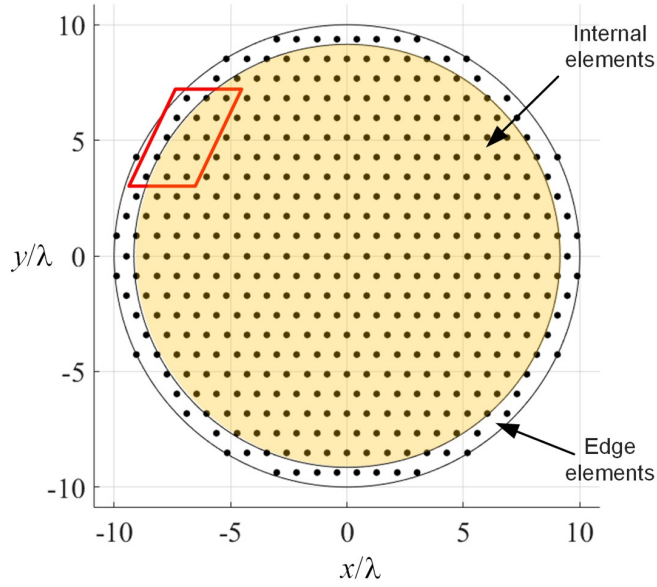
Beside array truncation, another source of inaccuracy is the element feed phase error, which leads to a degradation of the array factor pattern in terms of gain reduction, pointing error, and sidelobe level increase. To this regard, a Monte Carlo analysis on the perturbed array factor compared to the ideal one is presented hereafter pointing out some interesting statistical quantities about the main degradation effects.

1.7.1 Effects of array truncation

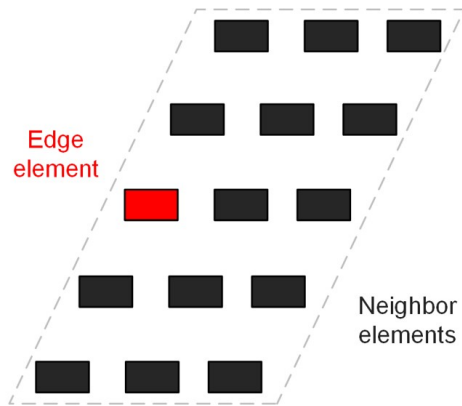
In the case of very large aperture, the radiation intensity (expressed in W/sterad) of the array can be very well approximated by the formula:

$$K = K_0 \times |\text{AF}|^2 \quad (1.42)$$

where K_0 is the active element radiation intensity and AF is the array factor. This expression was used in Sec. 1.6, but because of the moderate size of the array under study (see Fig. 1.32), it may lead to inaccuracies. Therefore, edge effects are addressed in this subsection. The analysis of truncation effects for finite arrays of patches has been extensively analyzed [46], [47]; here this effect has been evaluated by using ANSYS HFSS simulation tool. To introduce in first instance such effects, the edge elements (i.e., the elements



(a)



(b)

Figure 1.32: The array under study: (a) the full array including 425 patch elements of dimensions $12\text{ cm} \times 6.7\text{ cm}$, and lattice parameters $a = 0.86\lambda = 20.64\text{ cm}$, $b = 0.852\lambda = 20.45\text{ cm}$, $\gamma = 63.23^\circ$ (Fig. 1.23 on page 45); (b) the portion of the array boundary (shown in red in Fig. 1.32a) simulated on HFSS for the evaluation of the radiation pattern of the edge elements.

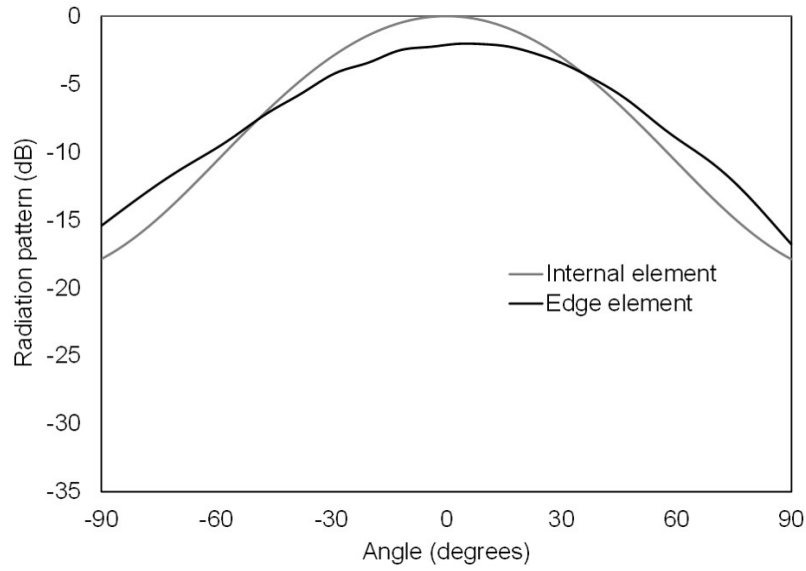
at the boundary of the array, Fig. 1.32a) have been simulated surrounded by some other more internal neighbor elements (Fig. 1.32b). The simulated radiation pattern of an edge element is compared with the one of the internal element (i.e., calculated under the infinite-array approximation) in Fig. 1.33a and Fig. 1.33b for the H-plane and E-plane, respectively. The radiation patterns are normalized to the internal element pattern. Fig. 1.33 shows several differences between the two patterns: modifications in the shape of the radiation pattern (especially in the E-plane) and reduction from 2 dB to 3 dB of the gain compared with the internal element pattern. The radiation patterns of the internal and edge elements are used together with the array factor to calculate the effect of the array truncation. In particular, two array factors are generated, namely AF_{int} and AF_{edge} , which take into account only the internal and only the edge elements, respectively (Fig. 1.32a). Assuming $\mathbf{E}_{0,\text{int}}$ and $\mathbf{E}_{0,\text{edge}}$ are the electric field generated by the internal and edge elements, respectively, the electric field \mathbf{E} , of the overall array, can be obtained by

$$\mathbf{E} = \mathbf{E}_{0,\text{int}} \times AF_{\text{int}} + \mathbf{E}_{0,\text{edge}} \times AF_{\text{edge}} \quad (1.43)$$

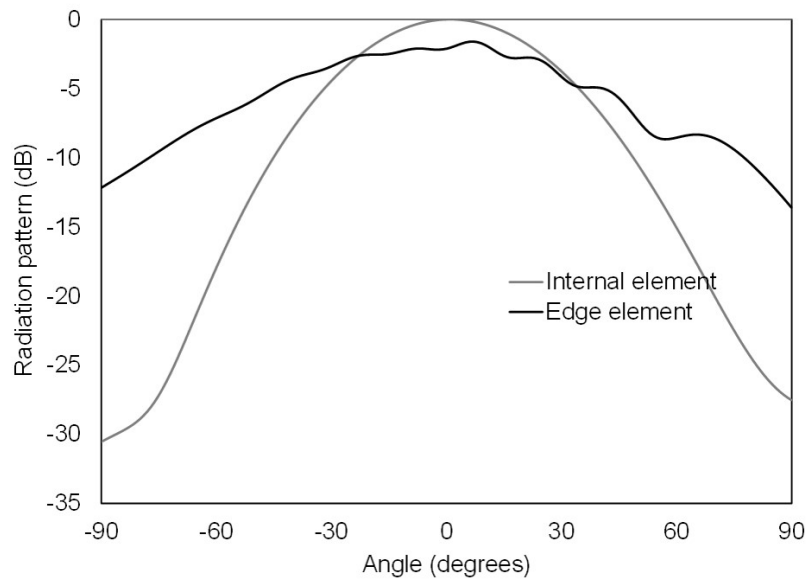
Therefore, the radiation intensity of the overall array results

$$K = \frac{r\mathbf{E}}{2\eta_0} \quad (1.44)$$

where r is the distance at which \mathbf{E} is calculated, and η_0 is the characteristic impedance of vacuum. The normalized array radiation pattern with no truncation effects (infinite array) and with truncation effects (truncated array) are depicted in Fig. 1.34a and Fig. 1.34b, for the H-plane and E-plane, respectively. The differences around the main lobe can be appreciated in the insets. The maximum array gain experiences a reduction of 0.32 dB, revealing that for this moderate-sized array, truncation effect is worth to be further investigated. In fact, in the present study, we just considered one specific radiation pattern for all the edge elements. However, this could be further investigated specializing the pattern for different groups of edge elements, depending on the surrounding environment. For sake of simplicity, the results have been presented under the assumption of uniform array tapering. Although this assumption is consistent as long as the antenna is used in transmission, it may not in reception where tapered illumination (e.g. Taylor 25 dB [48]) is usually implemented. However, this assumption

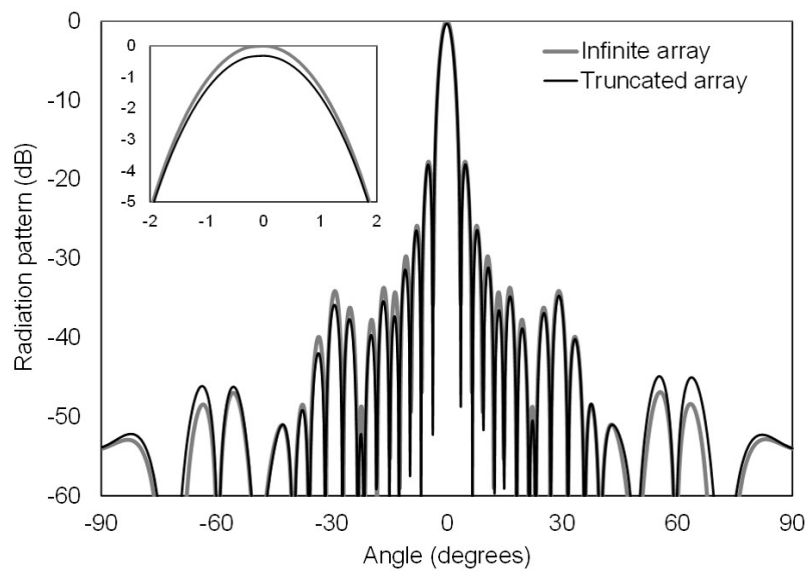


(a)

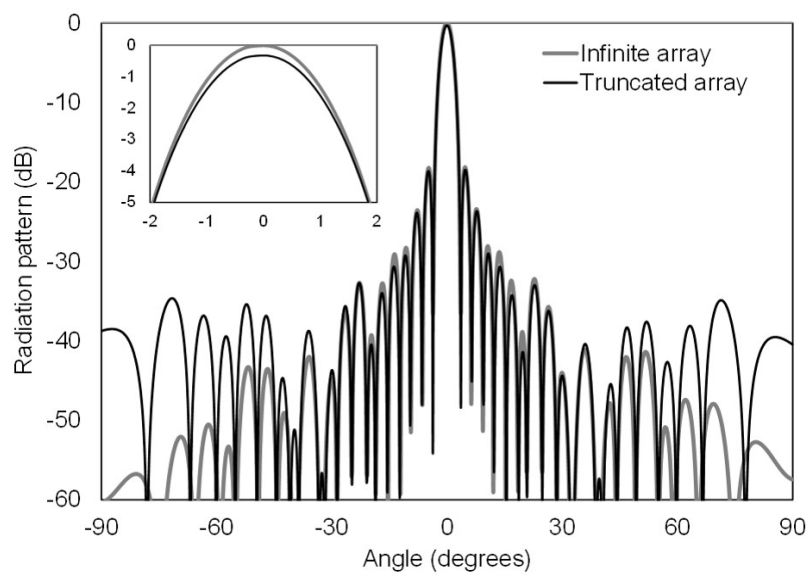


(b)

Figure 1.33: Radiation pattern of an edge element and of an internal element of the array: (a) H-plane; (b) E-plane.



(a)



(b)

Figure 1.34: Radiation pattern of the array considering all identical elements (black line) and specific elements for the array edge (gray line). The insets show a close-up of the main beam: (a) H-plane radiation pattern; (b) E-plane radiation pattern.

will not cause any loss of generality for the evaluations proposed in this work.

1.7.2 Effects of phase errors

To achieve the desired array factor pattern, all elements should be properly excited both in amplitude and phase. This analysis only focuses on phase errors, which are usually much more problematic than amplitude errors. Phase errors are treated in a number of previous works (e.g., [49], [50]), and a simple way to evaluate them is to consider the excitation phase of each element in the array as a Gaussian random variable Φ_{err} with zero mean and standard deviation σ_{err} . The array factor (see Eq. 1.5 on page 23), in case of uniform amplitude tapering, can be written as:

$$\text{AF} = \sum_n e^{jkr'_n \cdot \hat{\mathbf{u}}_r} \quad (1.45)$$

where $k = 2\pi/\lambda$ is the wave number, \mathbf{r}'_n is the vector radial position of the n th element of the array, and $\hat{\mathbf{u}}_r$ is the unit vector of the pointing direction. A Matlab routine has been run 10 000 times recalculating the AF given such a random distribution of phase errors, obtaining a Monte Carlo analysis, with the possibility to work out some interesting statistical quantities regarding gain reduction, sidelobe level variation, and pointing error. The choice of the standard deviation of such Gaussian phase error is based on the expected values in real scenarios. According to [51], [52], if a phased array antenna is used in reception, phase errors can be corrected in closed loop by a correlator up to a residual error of 7° , but if it is used in transmission, no closed loops can be exploited, thus pushing the phase errors up to around 30° . However, the system under study at ESA will be equipped with a proper calibration and element-phase-monitoring system, which would also be able to reduce transmitter-side phase errors down to around 5° . Nevertheless, to test the array performance in an extreme-case scenario, 30° phase errors will be assumed hereafter, even for a reception system. Since 99.7% of the values of a Gaussian random variable fall below 3σ from the mean value, it is reasonable to set $3\sigma_{\text{err}}$ equal to 30° , i.e. σ_{err} equal to 10° . Fig. 1.35 shows a result of a Monte Carlo analysis obtained with Matlab iterations, where the red curve represents the ideal array factor. Table 1.6 presents synthetic statistical results on the principal array performances, which better permits to appreciate the effect of phase errors. In particular, the pointing error is

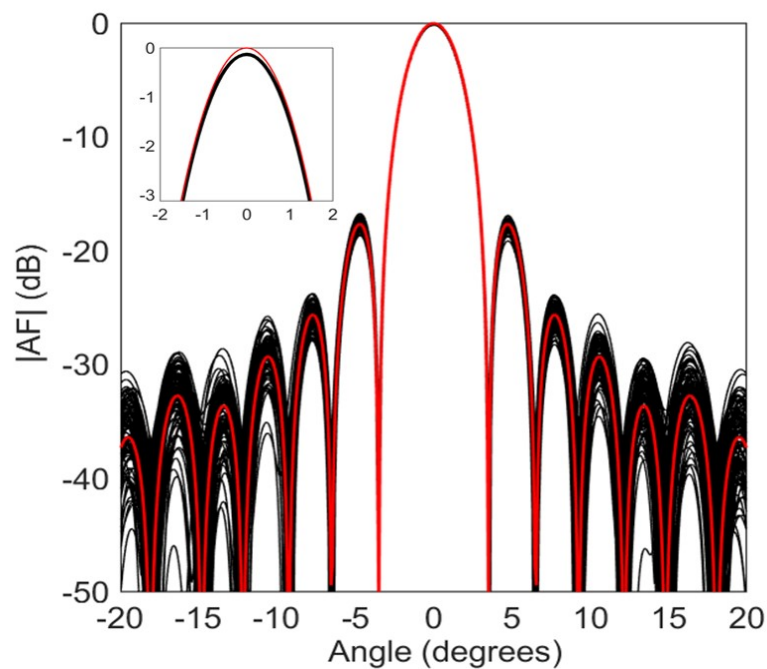


Figure 1.35: Monte Carlo analysis of the broadside array radiation pattern with normally distributed random phase errors. The red curve is the nominal radiation pattern in case of no phase error, while black curves are the results of the Monte Carlo simulation. The inset shows close-up view around the main beam.

Table 1.6: MONTE CARLO STATISTICS AFTER PHASE ERRORS

Statistical quantity	Mean value	Standard deviation	Maximum value
Pointing error	0°	1.15°	3.61°
Gain reduction	-0.13 dB	0.009 dB	-0.17 dB
Pointing error	-17.46 dB	0.23 dB	-16.24 dB

expected to be less than 2.3° with a probability of 95.45%¹⁹, which, due to the large distances of the target objects, may result into unacceptably large inaccuracies in the estimation of the position of the debris object. As far as the gain is concerned, such phase errors lead to an average reduction of 0.13 dB with small variations around this value. This value is lower than the one due to the array truncation, however it may represent an issue because the gain degradation due to truncation can be mitigated during the design phase, while the phase error affects the operation performance of the array. Finally, the maximum sidelobe level is also affected by random phase errors, with an average value of -17.46 dB, very close to the ideal array case, and variations within 0.46 dB from the mean value with 95.45% probability. Naturally, assuming the 5° phase error of ESA phased array system, such effects may be further mitigated until reaching acceptable levels.

1.8 Conclusions

A multi-array-antenna system for parallel scanning of a certain field of regard, aimed at space debris detection, has been designed in the framework of the European Space Agency Space Situational Awareness program, providing the orientation of each array in a local coordinate system.

In this Ph.D. work, a complete procedure to calculate the optimal array-lattice geometrical parameters, given some rectangular pyramidal scan specifications, has been developed. The optimization has been performed through the analysis of grating lobes versus scan specifications in the UV space. Analytical expressions for the three array parameters have been developed, in contrast to purely graphical techniques relying on iterative optimization procedures. In particular, closed-form analytical expressions to determine the optimum lattice geometrical parameters for regular arrays scanning rectangular sky regions were derived and presented, including the effects of the array main lobe beamwidth and the single element pattern. This allowed for minimizing the number of elements, while avoiding grating lobes. Different design strategies were discussed, introducing the use of time-space (4D) diagrams for the radiation patterns, which permitted to visualize the array performance, in particular in terms of secondary lobes, in one single graph

¹⁹A property of the Gaussian distributions. 95.45% of the values taken by the random variable fall within an interval of $\pm 2\sigma$ centered around the average.

for the entire scanned region. The results achieved with this methodology were applied and validated, using full-wave simulations including mutual coupling effects, to an example based on the current developments of the European Space Agency in the field of surveillance radars, aimed at monitoring objects flying at low Earth orbits.

The effects of inaccuracies in phased arrays for space debris detection have been investigated, as well. In particular, the finite size of the array as well as the inaccuracies of the phase excitation of the array elements have been addressed. The finite size of a phased array has been studied by considering a more realistic radiation pattern for the edge elements. Results showed significant differences between the patch elements at the center and at the edge of the array, which in turn reflects onto a degradation of the radiation pattern, especially in the E-plane. The element excitation phase errors have been studied through a Monte Carlo analysis for an extreme-case scenario. The results showed a degradation of the array radiation performances, with limited gain reduction and sidelobe level increase, and with non-negligible pointing error. However, such effects could also be considerably mitigated in a more realistic scenario where a proper phase-monitoring system is adopted.

The results achieved in this Ph.D. activity, published in conference and journal papers [29]–[33], will be used by ESA as design guidelines for a European space debris radar architecture which will allow for the detection, size estimation, and monitoring of space debris objects. The data will be used to generate a European catalogue of debris objects with daily updated trajectories and orbital parameters, a fundamental database to rapidly send out warning messages to the operative satellite population for actuating collision avoidance maneuvers in short times.

References

- [1] M. Geissler, F. Woetzel, M. Bottcher, S. Korthoff, A. Lauer, M. Eube, and R. Gieron, “Innovative phased array antenna for maritime satellite communications”, in *2009 3rd European Conference on Antennas and Propagation*, Mar. 2009, pp. 735–739.
- [2] A. B. Smits and P. van Genderen, “The apar multifunction radar - system overview”, in *IEEE International Symposium on Phased Array Systems and Technology, 2003.*, Oct. 2003, pp. 241–246.
- [3] G. H. C. van Werkhoven and R. H. van Aken, “Evolutions in naval phased array radar at thales nederland b.v.”, in *Proceedings of the Fourth European Conference on Antennas and Propagation*, Apr. 2010, pp. 1–4.
- [4] J. G. G. Trujillo, S. Halte, M. S. Perez, and P. Besso, “On the design of a planar phased array radar antenna architecture for space debris situational awareness”, *7th European Conference on Antennas and Propagation (EuCAP)*, Gothenburg, Sweden, April 8-12, 2013.
- [5] E. S. Agency, *Declaration on the space situational awareness (ssa) preparatory programme*, European Space Agency Council, ESA/C(2008)192, Att.: ESA/C/SSA-PP/VII/Dec. 1 (Final), Paris, Dec. 8, 2008.
- [6] R. C. Hansen, *Phased Array Antennas*, Second Edition. Hoboken, New Jersey, USA: John Wiley & Sons, 2009.
- [7] H. S. Lui, H. T. Hui, and M. S. Leong, “A note on the mutual-coupling problems in transmitting and receiving antenna arrays”, *IEEE Antennas and Propagation Magazine*, vol. 51, no. 5, pp. 171–176, 2009.
- [8] R. J. Mailloux, *Phased Array Antenna Handbook*, Second Edition. Norwood, MA: Artech House, 2005.
- [9] H. Unz, “Linear arrays with arbitrarily distributed elements”, *IRE Trans. on Antennas and Propagation*, vol. 8, no. 2, pp. 222–223, 1960.
- [10] R. L. Haupt, “Thinned arrays using genetic algorithms”, *IEEE Transactions on Antennas and Propagation*, vol. 42, no. 7, pp. 993–999, 1994.
- [11] W. P. M. N. Keizer, “Large planar array thinning using iterative fft techniques”, *IEEE Transactions on Antennas and Propagation*, vol. 57, no. 10, pp. 3359–3362, Oct. 2009.

-
- [12] G. Prisco and M. D’Urso, “Maximally sparse arrays via sequential convex optimizations”, *IEEE Antennas Wireless Propag. Lett.*, vol. 11, pp. 192–195, 2012.
- [13] G. Toso and P. Angeletti, “Array tracing: A graphical-deterministic procedure for the synthesis of linear sparse arrays”, in *2015 9th European Conference on Antennas and Propagation (EuCAP)*, Apr. 2015, pp. 1–4.
- [14] F. Namin, J. S. Petko, and D. H. Werner, “Analysis and design optimization of robust aperiodic micro-uav swarm-based antenna arrays”, *IEEE Transactions on Antennas and Propagation*, vol. 60, no. 5, pp. 2295–2308, May 2012.
- [15] Y. Mancuso, “Components and technologies for t/r modules”, *IEEE A&E Systems Magazine*, Oct. 2010.
- [16] T. Hoffmann, C. Fulton, M. Yeary, A. Saunders, D. Thompson, B. Murmann, B. Chen, and A. Guo, “Impact - a common building block to enable next generation radar arrays”, *2016 IEEE Radar Conference (RadarConf)*, May 2016.
- [17] L. Infante, A. D. Luca, and M. Teglia, “Low-profile ultra-wide band antenna array element suitable for wide scan angle and modular sub-array architecture”, *2010 International Symposium on Phased Array Systems and Technology (ARRAY)*, Oct. 2010.
- [18] S. S. Holland and M. N. Vouvakis, “The planar ultrawideband modular antenna (puma) array”, *IEEE Transactions on Antennas and Propagation*, vol. 60, no. 1, Jan. 2012.
- [19] J. S. Herd and M. D. Conway, “The evolution to modern phased array architectures”, *Proceedings of the IEEE*, vol. 104, no. 3, Mar. 2016.
- [20] R. W. Lyon, A. M. Kinghorn, G. D. Morrison, A. Stonehouse, G. Byrne, and M. Dugan, “Active electronically scanned tiled array antenna”, *2013 International Symposium on Phased Array Systems and Technology (ARRAY)*, Oct. 2013.
- [21] A. W. Mast, “Multi-tiled configured phased array antenna architecture”, US. Patent 6 166 705, Dec. 2000.

-
- [22] P. Rocca, G. Oliveri, R. J. Mailloux, and A. Massa, “Unconventional phased array architectures and design methodologies - a review”, *Proceedings of the IEEE*, vol. 104, no. 3, pp. 554–560, Mar. 2016.
- [23] T. G. Spence and D. H. Werner, “Design of broadband planar arrays based on the optimization of aperiodic tilings”, *IEEE Trans. Ant. Prop.*, vol. 56, no. 1, Jan. 2008.
- [24] G. H. Knittel, “Choosing the number of faces of a phased-array antenna for hemisphere scan coverage”, *IEEE Transactions on Antennas and Propagation*, vol. 13, no. 16, pp. 878–882, Jun. 1965.
- [25] J. L. Kmetzo, “An analytical approach to the coverage of a hemisphere by n planar phased arrays”, *IEEE Transactions on Antennas and Propagation*, vol. 15, no. 3, pp. 367–371, Mar. 1967.
- [26] L. E. Corey, “A graphical technique for determining optimal array geometry”, *IEEE Transactions on Antennas and Propagation*, vol. 33, no. 7, pp. 719–726, Jul. 1985.
- [27] A. Jablon and A. Agarwal, “Optimal number of array faces for active phased array radars”, *2004 IEEE Antennas and Propagation Society Int. Symposium (APS-2004)*, Monterey, CA, USA, June 20-26, 2004.
- [28] S. R. Zinka, I. B. Jeong, J. H. Chun, and J. P. Kim, “A novel geometrical technique for determining optimal array antenna lattice configuration”, *IEEE Transactions on Antennas and Propagation*, vol. 58, no. 2, pp. 404–412, Feb. 2010.
- [29] G. Siciliano, M. Mendijur, P. Besso, M. Pasian, and L. Perregrini, “A multi-array antenna system with optimal lattice for rectangular pyramidal scanning of space debris”, *10th European Conference on Antennas and Propagation (EuCAP)*, Davos, Switzerland, April 10-15, 2010.
- [30] —, “Lattice optimization for a multi-array antenna system aimed at space debris surveillance”, *Riunione Nazionale per l'Elettromagnetismo (RINEM 2016)*, Parma, Italy, September 12-14, 2016.
- [31] —, “Effects of finite aperture and random phase errors for a space debris radar antenna array”, *2017 European Microwave Conference (EuMC), European Microwave Week (EuMW)*, Nurnberg, Germany, October 07-13, 2017.

-
- [32] ———, “Time-space optimization of uniform array lattices for space debris radars”, *IEEE Transactions on Antennas and Propagation*, vol. 66, no. 5, pp. 2673–2677, May 2017.
- [33] G. Siciliano, “Aperture truncation and excitation error analysis for a space debris radar antenna array”, *Riunione Nazionale per l’Elettromagnetismo (RINEM 2018)*, Cagliari, Italy, September 3-6, 2018.
- [34] United Nations, “Technical report on space debris”, United Nations, Tech. Rep., 1999.
- [35] F. Laghezza, F. Berizzi, A. Capria, E. Dalle Mese, G. Pupillo, S. Montebugnoli, E. Salerno, and M. Di Martino, “Italian bistatic radar system for surveillance of space debris in low earth orbit”, *2010 IEEE Radar Conference*, 2010.
- [36] N. Aeronautics and S. Administration, “<http://www.nasa.gov>”, (accessed March 2016).
- [37] B. Yağlıoğlu, A. Utku, Ö. Yilmaz, and B. G. Özdemir, “Surveillance of space: An overview and a vision for turkey’s roadmap”, *2013 6th International Conference on Recent Advances in Space Technologies (RAST)*, 2013.
- [38] European Space Agency, “<http://www.esa.int/Our-Activities/Operations/Space-Situational-Awareness/About-SSA>”, (accessed April 2015).
- [39] J. C. Toomay, *Radar Principles For The Non-Specialist*, Second Edition. New York: Van Nostrand Reinhold, 1989.
- [40] A. C. Balanis, *Antenna Theory Analysis and Design*. Hoboken, New Jersey, U.S.A.: John Wiley & Sons, 2005.
- [41] G. Conciauro and L. Perregini, *Fondamenti di Onde Elettromagnetiche*. Milan, Italy: Mc Graw-Hill Education, 2003.
- [42] H. L. V. Trees, *Optimum Array Processing. Part IV of Detection, Estimation, and Modulation Theory*. John Wiley & Sons, 2002.
- [43] N. Amitay, V. Galindo, and C. P. Wu, *Theory and Analysis of Phased Array Antennas*. New York, NY, USA: Wiley Interscience, 1972.
- [44] A. K. Bhattacharyya, *Phased Array Antennas, Floquet Analysis, Synthesis, BFNs, and Active Array Systems*. Hoboken, New Jersey, U.S.A.: John Wiley & Sons, 2006.

-
- [45] D. M. Pozar, “The active element pattern”, *IEEE Trans. Ant. Propag.*, vol. 42, no. 8, Aug. 1994.
- [46] —, “Finite phased arrays of rectangular microstrip patches”, *IEEE Transactions on Antennas and Propagation*, vol. AP-34, no. 5, May 1986.
- [47] A. K. Skrivervik and J. R. Mosig, “Analysis of finite phased arrays of microstrip patches”, *IEEE Transactions on Antennas and Propagation*, vol. 41, no. 8, Aug. 1993.
- [48] T. T. Taylor, “Design of circular apertures for narrow beamwidth and low sidelobes”, *IRE Transactions on Antennas and Propagation*, vol. 8, pp. 17–22, Jan. 1960.
- [49] C. A. Greene and R. T. Moller, “The effect of normally distributed random phase errors on synthetic array gain patterns”, *IRE Transactions on Military Electronics*, vol. MIL-6, no. 2, pp. 130–139, Apr. 1962.
- [50] A. Quazi and A. Nuttall, “Effects of random shading, phasing errors and element failures on the beam patterns of line and planar arrays”, *Acoustics, Speech, and Signal Processing, IEEE International Conference on Acoustics, Speech and Signal Processing*, pp. 290–293, 1979.
- [51] M. Bozzi, M. Cametti, M. Fornaroli, P. Maguire, S. Marti, and M. Pasian, “Future architectures for european space agency deep-space ground stations”, *IEEE Antennas and Propagation Magazine*, vol. 54, no. 1, Feb. 2012.
- [52] M. Pasian, M. Cametti, M. Bozzi, and L. Perregrini, “Efficiency of arrays composed of high-gain reflector antennas”, *IET Microwaves, Antennas & Propagation*, pp. 1636–1642, 2012.

Chapter 2

A Beam-Wave-Guide Antenna for THz Imaging of Moving Standoff Personnel

In this chapter, the preliminary design of a beam-wave-guide antenna with fast mechanical beam steering is presented. The system is aimed at mm-wave imaging of standoff targets for detecting weapons under clothes. The activity represents a feasibility study, from an antenna point of view, in the framework of a contract with a Chinese company interested in developing a complete THz imaging system for security applications. The intention of this study was to provide a preliminary antenna architecture. For this reason, the results presented in this chapter are limited to preliminary simulations, while manufacturing, testing, and design of electronic equipment were left for a subsequent development phase.

(COMPLETARE O RISCRIVERE QUESTA PARTE ALLA FINE!!!)

2.1 Introduction

Today, the most common imaging systems used for the detection of concealed weapons are *metal detectors* [1] and *full-body scanners* [2]. The former (Fig. 2.1a), quite well known, is based on the magnetic interaction of metal objects with a short induced magnetic field; the latter (Fig. 2.1b) can be of two different kinds: mm-wave scanner or backscatter scanner. Both kinds of full-body scanners aim at discerning a concealed object from the

human skin. The mm-wave scanner is based on the skin reflection of a high-frequency radio wave (up to 300 GHz). It adopts low-power and non-ionizing electromagnetic waves and it is nowadays quite accurate in producing a 3D image of the human body, with a good localization of the concealed weapon. The backscatter scanner is based on very low-intensity X-rays which are reflected out of the human skin. Of course the amount of reflected energy is directly affected by the possible presence of a concealed object. For both full-body scanners, the exposure to radio waves is comparable with normal environmental electromagnetic radiation.

The aforementioned scanning systems (walk-through metal detector and body scanner) can detect contraband concealed on human bodies, but they require the sensors and the targets to be in close proximity. So, these systems are excellent for areas with controlled accesses, like security control zones in airports or in other sensitive public buildings. But, when it comes to remote surveillance of large areas with multiple and possibly moving targets, weapon detection with the previous systems is extremely difficult to achieve.

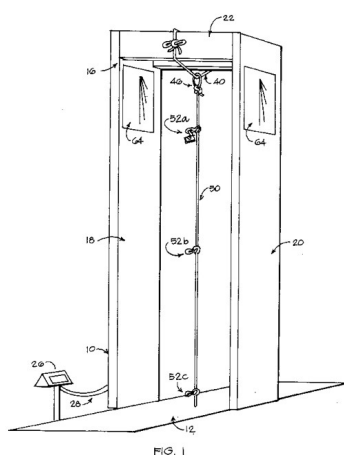
The detection of metal target such as ships, military vehicles or airplanes at long ranges has always been accomplished through the use of radars. Vast majority of radars operate at X band (around 10 GHz), i.e. at microwave frequencies. There has been a huge technological progress in the detection of fix and moving targets with a current trend toward multiple target tracking at the same time. However, at microwave frequencies and with reasonable antenna sizes, imaging of targets is not possible, due to the large beam the antenna can produce. The beamwidth¹ a certain antenna aperture can generate is approximately given by

$$\text{BW} = 70 \frac{\lambda}{D} . \quad (2.1)$$

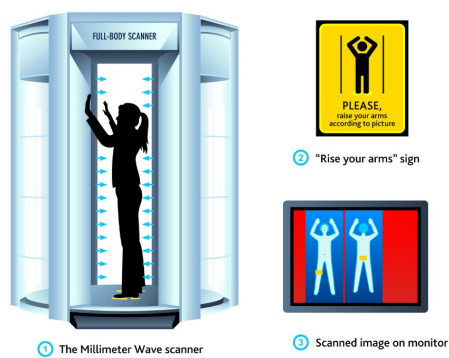
where λ is the free-space wavelength and D is the diameter of the antenna aperture. At 10 GHz ($\lambda = 3$ cm), an antenna with a reasonable diameter of 1 m can generate a beam as large as 2.1° , which at a ranges of 10-20 m, for instance, translates on a beam spot on the target as wide as 40 cm in diameter, more or less. With these numbers, it is of course extremely difficult to acquire an image of a target located at far distances. To have narrow spots on the target, higher frequencies should be selected, that's why in the optical domain, we can take so beautiful pictures. Then, why

¹In this case, the half-power beamwidth (in degrees) is considered.

U.S. Patent Jun. 16, 1987 Sheet 1 of 2 4,672,837



(a)



(b)

Figure 2.1: (a) An artist's impression of a full-body scanner; source: www.thehealthyhomeeconomist.com. (b) A drawing of a walk-through metal detector, taken from a US patent.

not choosing optical wavelengths? Because of garments opacity. Clothes are not transparent at those frequencies and the radio wave cannot penetrate through them and show up conceal weapons. At all parts of the band from 100 GHz to 1 THz, there are differences in the optical properties of skin, explosives and metals which can enable detection of weapons and IEDs² [3], [4]. As we go up in frequency, the attenuation in clothing and the atmosphere tends to increase. For active imaging³, the signature is determined by small differences in reflectivity across the band. For passive imaging⁴, the contrast mechanism will change as frequency increases. At 100 GHz, it will tend to be dominated by the reflectivity of the items and their geometrical relationship to the body. At frequencies of 500 GHz and above, it will be dominated by the emissivity of the items and their physical temperature.

Recent technological advancement in the field of high-frequency solid-state electronic circuits allows to produce radars with very good signal-to-noise ratios (SNR) meant for standoff target imaging and detection of contraband in the frequency domain between 100 GHz and 1 THz, otherwise also called THz domain [5]. For e.g., already 10 years ago (in 2007-2008) a radar imaging system developed by Jet Propulsion Laboratory (JPL)⁵ was capable of achieving an SNR of nearly 67 dB assuming a target with -20 dB backscattering coefficient (isotropically reflecting 1% of the incident radio wave) and an integration time of 10 ms. These results are quite promising for investing time and research resources in the development of THz radar imaging systems. Hopefully, in the near future such systems could be installed in very sensitive areas or even in public places in order to prevent terrorist attacks and/or suspicious thugs. And the current research is moving toward the development of imaging systems able to acquire simultaneous images of multiple moving targets [6], [7]. Naturally, the aim is always to detect concealed weapons or explosives (even metal-free ones).

²IED: improvised explosive devices, commonly used as roadside bombs.

³Active imaging employs transmitters and receivers and is mainly based on the reflectivity properties of materials.

⁴Passive imaging is based on the natural emissivity of materials.

⁵JPL used Schottky diodes with more than 2 mW coherent output power and Schottky mixers with an overall system noise temperature of around 40,000 K.

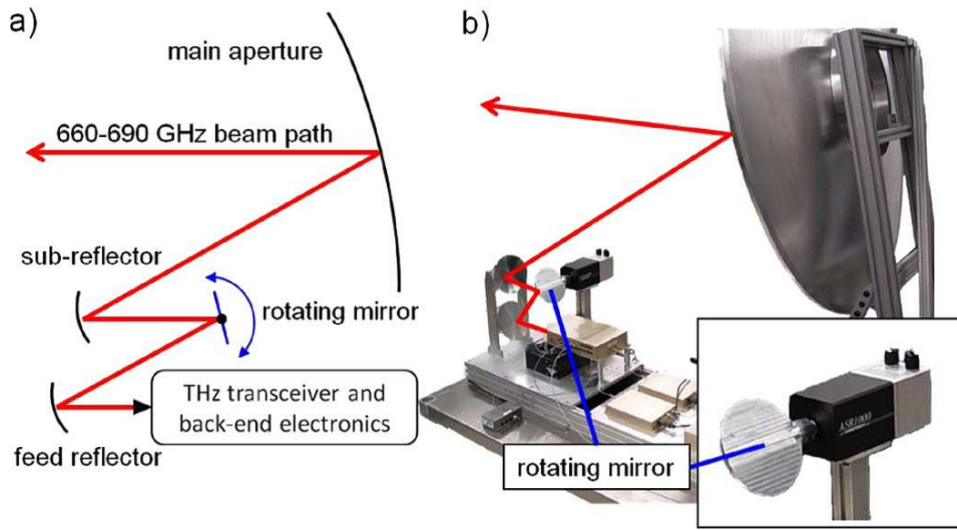


Figure 2.2: Imaging system adopted by JPL.

2.2 100 GHz reflector antenna scanning system

This Ph.D. activity scope was to design a preliminary scanning system intended for the image acquisition of a target at around 10-12 m range.

The architecture is based on the imaging system adopted by JPL [8], [9], shown in Fig. 2.2, where the beam is produced by a source located at a focal point and is then magnified by a set of mirrors; a movable mirror is used to squint the beam. However, in this implementation, the system will operate at a lower frequency and at a different target range, and in the future an array of receivers will be adopted for acquiring simultaneous beams (or spots in the target) at the same time. The objective was to scan a field of view (FoV) as large as 1 m \times 2 m (width \times height), as shown in Fig. 2.3, intended to cover the whole human body. Such a wide FoV is expected to cause several problems especially in terms of beam distortion. A question this study wanted to answer was whether it is possible to scan such a large FoV. In this chapter, several beam analyzes will be presented trying to answer this question.

Because the presented system is intended to be equipped with a transmitting (or receiving) array of antennas, simultaneous beams can be generated on the prescribed FoV, so different image acquisition strategies can be envisaged.

Fig. 2.4 shows three different scanning strategies, where colors represent

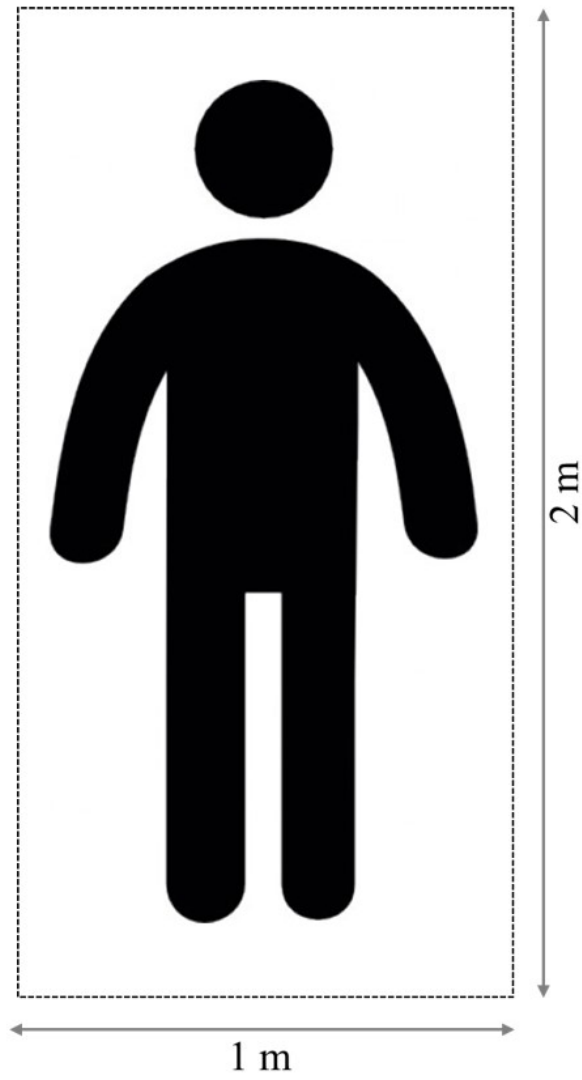


Figure 2.3: Dimension of the field of view (FoV).

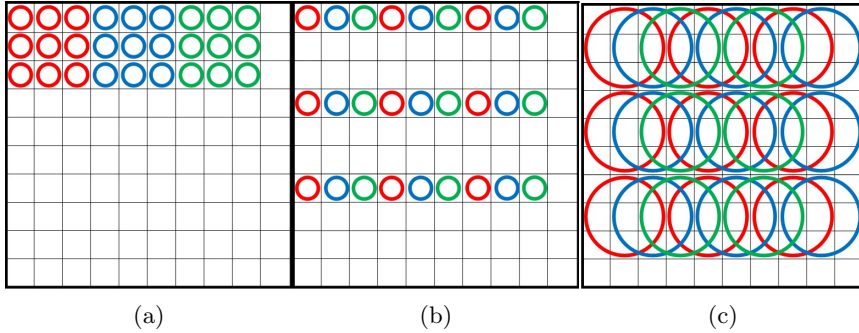


Figure 2.4: Different possible focusing strategies: circles represent the spots seen by the various receivers and colors identify different time steps (red = t_0 , blue = $t_0 + \Delta t$, and green = $t_0 + 2\Delta t$).

different time steps. Fig. 2.4a requires a compact array of receivers, with a large angular scan to cover the entire FoV, having to move the set of beams from the red position directly to the blue one, and so on. This implementation has the advantage of allowing for a compact array and consequently the receivers are located close to the focal point, but it suffers from a large angular swing of the movable mirror; moreover, if the mirror is static (the beam is not scanned), only a small portion of the field of view is visible.

Fig. 2.4b requires an array of largely spaced receivers, which see spots scattered throughout the field of view. The advantage is that the angular swing of the movable mirror is smaller than in case of Fig. 2.4a. The large separation between the array elements is beneficial whenever transmission features is added⁶, and also with respect to thermal dissipation efficiency. The disadvantages are that the array is larger, with some receivers located far from the focal point, and in the static version (not scanned), an under-sampled view is obtained.

In the solution of Fig. 2.4c, larger pixels are adopted and partially overlap over subsequent time steps. In this case, the big size of such beams can be compensated through the use of super-resolution techniques, which increase the resolution of the image after post-processing [10]. The system benefits from being able to acquire a low-resolution image of the entire field of view, in the event of static mirror (unscanned case). But, it suffers from a more intense post-processing required for achieving super-resolution.

⁶There is more space to locate transmitters.

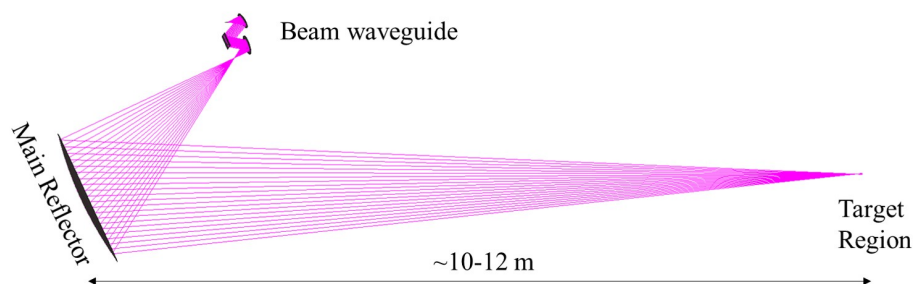


Figure 2.5: Sketch of the system architecture under analysis.

2.3 System architecture

The system architecture which has been analyzed is depicted in Fig. 2.5, Fig. 2.6, and Fig. 2.7. It was inspired by several published works and particularly by JPL THz Imaging system [11]–[15]. The idea is to design an antenna system which is intended to accommodate a radar technology where the target is illuminated by a transmitter and the reflected RF energy is collected by a big dish (main) reflector M_m (Fig. 2.5 and 2.6), and via a beam waveguide⁷, focused into the receiver. The path of RF energy can be described, for instance, in the reverse direction (from the source to the target), as depicted in Fig. 2.6 and 2.7. The initially spherical-front beam departs from the feed and hits a parabolic mirror M_f , which transforms the beam front into a planar wave. Reflected by the planar reflector M_r , the beam is re-focused by a parabolic (sub-main) reflector and magnified onto M_m . Reflector M_m is an ellipsoidal mirror, with one focal point coinciding with the sub-main focal point and the other located at the target region. Mirror M_r is allowed to rotate in the two directions in order to implement the scanning of the beam spot on the target region. The function of the rotating mirror is to defocus the beam so as to let the beam to be radiated in a different

⁷A beam wave guide (BWG) is a system composed of multiple reflective surfaces or lenses keeping the radio-wave beam always confined [16]. It is commonly adopted in radio astronomy or in space communications in place of traditional dish+feed antennas. It can be used to guide the radio-wave, focalize or de-focalize it, turn it to a plane or spherical wave, etc. The advantage of using a BWG instead of a traditional parabolic dish with the feed in front of it is that the feed with all complex, heavy, and bulky electronic/cooling equipment can be located somewhere else, for instance at the bottom of the antenna. In this case, the wave emitted by the source is guided through a set of small reflectors up to the main dish, from which it is then radiated to the free space. A good property of BWG antennas is the very limited losses as compared with traditional cables.

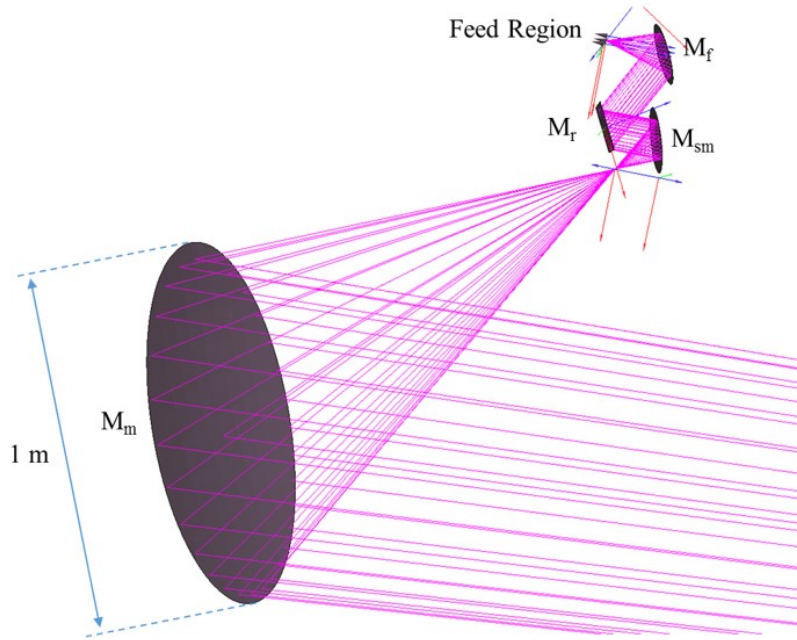


Figure 2.6: Arrangement of the system reflectors.

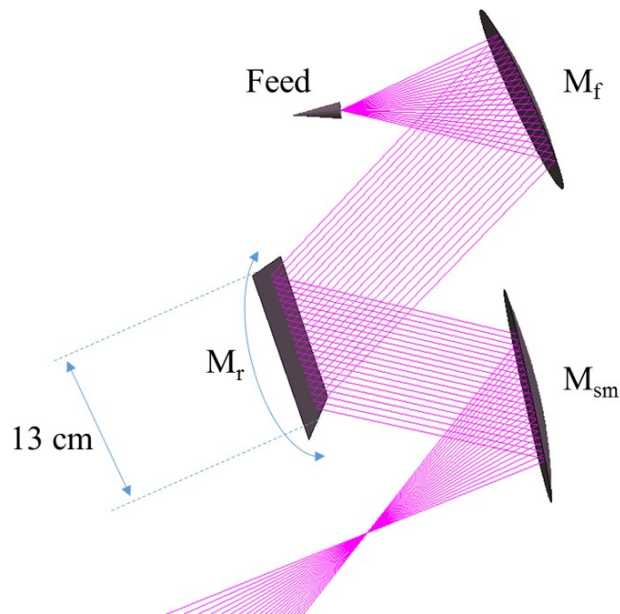


Figure 2.7: Magnified view of the beam waveguide system.

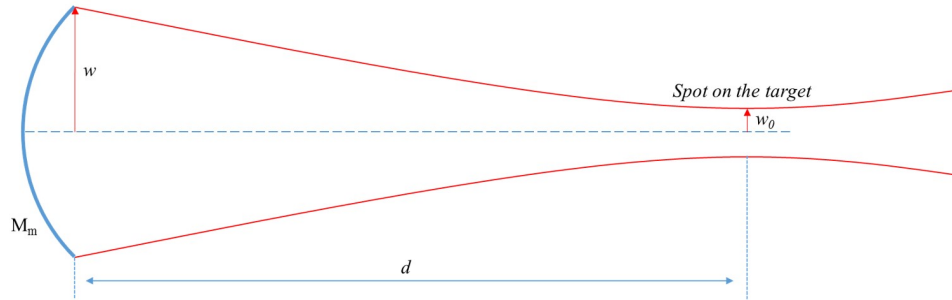


Figure 2.8: Definition of the beam radius for the system under analysis.

direction. As the rotating mirror is rotated, the illuminated portion of the sub-main reflector surface changes as well. For this reason, the sub-main reflector should be oversized, to accommodate the beam deflection caused by the flat mirror M_r . The main reflector has an ellipsoidal shape. Why not a parabolic shape? The reason for the choice of an ellipsoidal surface is that this geometrical object has two foci. In particular, all rays emitted by the one focus and reflected from the ellipsoidal surface converge again into the second focus. This ensures the system is maximally focalized, with a consequent very small spot size on the target FoV. Looking at Fig. 2.5, it is evident the presence of the two foci of the ellipsoid: one is located in the source region and is shared between the main reflector and the sub-main reflector M_{sm} (Fig. 2.6); the other is located in the target region, i.e. in the FoV. The dimension of the main reflector is upper bounded to 1 m diameter. Its size affects the spot size on the target, given the specified ~ 10 m range. This estimation can be carried out with the aid of Gaussian-beam propagation theory [17], whose background is provided in Appendix A. In fact, because the wave is continuously guided through all mirrors and eventually focalized onto the target, the system can be considered as a beam waveguide and the propagation of the wave from the source to the target can be studied with the theory of Gaussian beams. This theory is able to predict the size of the beam after being reflected by the main reflector and focused on the target. If we call w_0 the spot radius on the target and w the radius of M_m , as seen from Fig. 2.8, the relationship which permits to calculate the required diameter D_m ($2w$) for M_m in order to have a certain spot radius on the target is:

$$D_m = 2w = 2w_0 \sqrt{1 + \left(\frac{\lambda d}{\pi w_0^2} \right)^2} \quad (2.2)$$

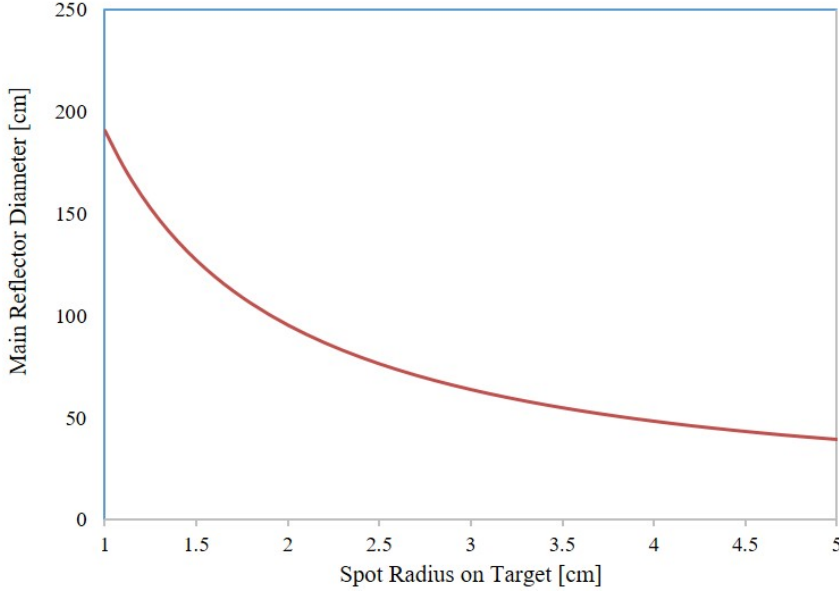


Figure 2.9: Main-reflector diameter as function of the spot radius on the target.

where λ is the free-space wavelength and d is the distance between the main reflector and the target (or, say, the focal region). Fig. 2.9 graphically shows the required main reflector diameter as a function of the spot radius on the target, at 10-m range, at 100-GHz frequency. One may observe that for this system specification on the target range, D_m should be ~ 2 m for having a spot radius of 1 cm, but, in our case, D_m has an upper bound of 1 m, so the minimum achievable spot radius is 2 cm. This means that some post-processing techniques, (for instance, super-resolution algorithms [10], [18]), to enhance the image resolution may be required, but this is not object of this work. The system magnification M , defined as the ratio of the main reflector focal distance f_m to the sub-main reflector focal distance f_{sm} , clearly affects the system compactness in two ways:

1. The distance between M_m and M_{sm} (Fig. 2.6) is related to the system magnification, once f_{sm} is fixed⁸;

⁸Usually, it is better to have mirrors with a larger radius of curvature, because they are less susceptible to de-pointing or de-focusing. Since the radius of curvature of a parabolic mirror goes down with the decreasing focal distance, there is somehow a lower limit for the focal length f_{sm} . In fact, a large system magnification implies a less compact system, having to locate the main reflector at a longer distance.

2. Once D_m is fixed, the sub-reflector diameter D_{sm} depends on M through:

$$D_{sm} = \frac{D_m}{M} \quad (2.3)$$

Since the size of all reflectors in the BWG is almost the same, having a small system magnification forces to increase the size of the BWG mirrors.

So, based on the previous arguments, the system magnification seems to be a very important parameter, whose value has a significant impact on the compactness of the overall system. Since the imaging system is assumed to operate in a public area, probably in a limited space, its whole size is important.

2.4 Choice of the system magnification

Since the system magnification directly affects the sub-main reflector size (and consequently all other reflectors in the beam waveguide), it is also crucial in a number of issues:

- Scan speed. The larger the size of the rotating mirror M_r (Fig. 2.7), the larger its momentum of inertia, hence the lower the achievable rotation acceleration, which may considerably reduce the scan speed of the system⁹;
- Mirror rotation range. According to [14], a rotation Ψ of the mirror M_r corresponds to a deviation $\alpha = 2\Psi$ of the wave impinging on the sub-main reflector (Fig. 2.10). Due to the system magnification, a beam angle deviation of α corresponds to a deviation of the wave reflected from M_m (Fig. 2.11) equal to [14]:

$$\theta_s = \frac{\alpha}{M} = 2\frac{\Psi}{M} \quad (2.4)$$

⁹The flat rotating mirror has to be mounted on a precision rotation stage, which can reach very fast rotation accelerations and speed, but strongly dependent on the momentum of inertia of the mirror. A large and bulky mirror will inevitably limit the maximum achievable rotation acceleration, with a huge impact on the time required to complete an entire scanning of the field of view.

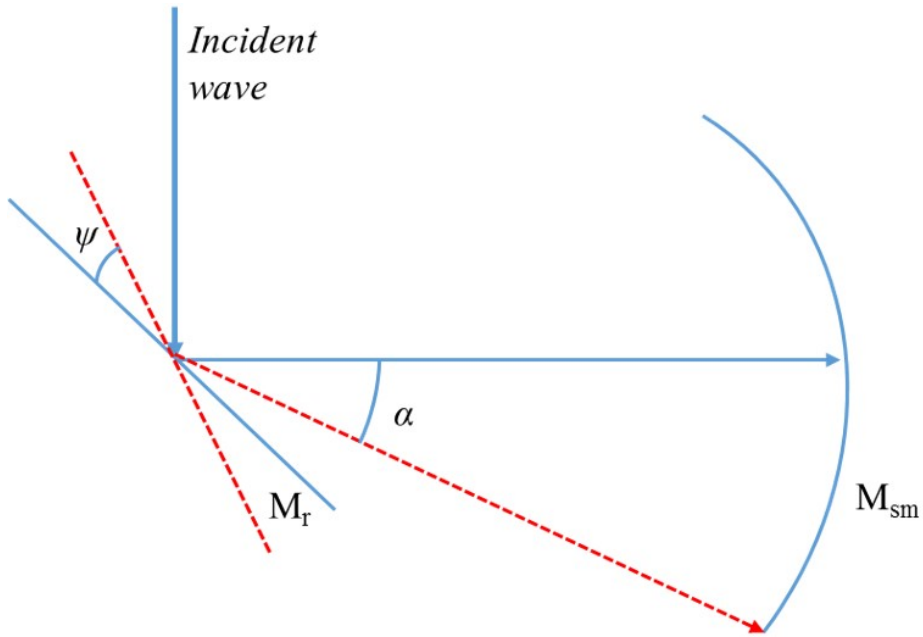


Figure 2.10: Beam deviation angle from the flat mirror (M_r) to the sub-main reflector (M_{sm}).

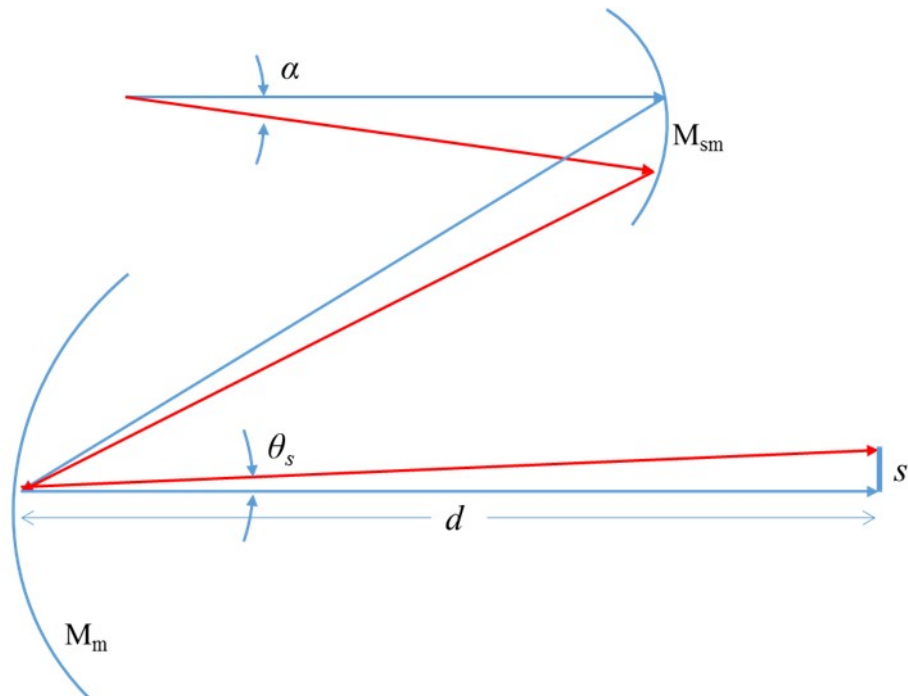


Figure 2.11: Picture of the scanning architecture.

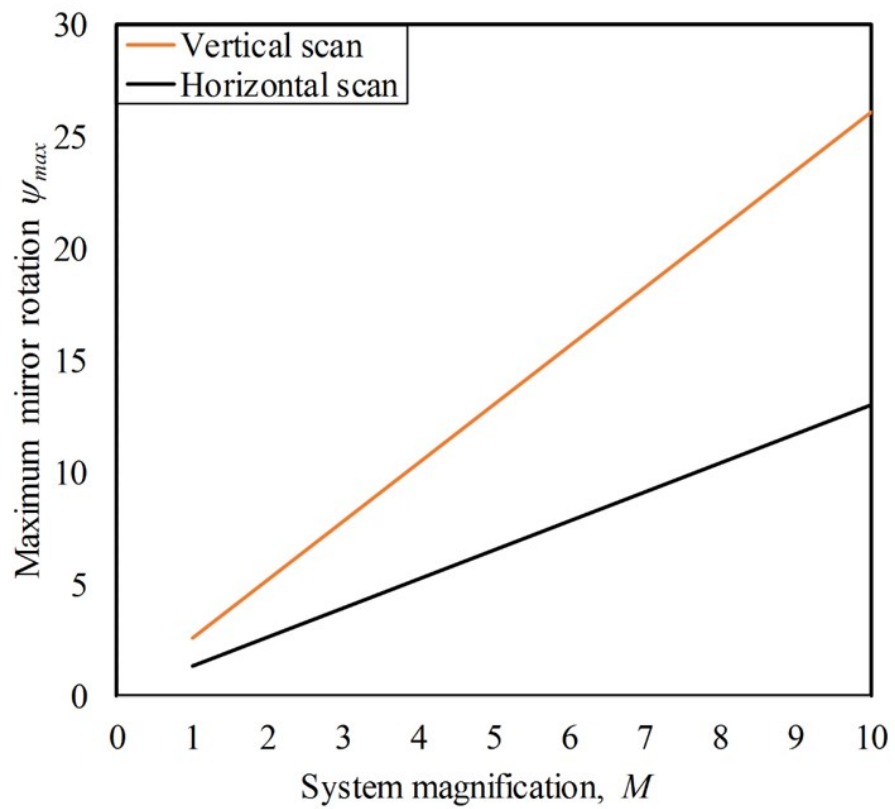


Figure 2.12: Maximum mirror rotation angle as function of system magnification at 11-m target range to achieve a maximum theoretical FoV of 1 m \times 2 m.

Table 2.1: MAXIMUM MIRROR ROTATION TO SCAN THE ENTIRE FoV (1 M×2 M).

Magnification (M)	Max horizontal scan (Ψ_{\max})	Max vertical scan (Ψ_{\max})
10	$\pm 13^\circ$	$\pm 26^\circ$
5	$\pm 6.5^\circ$	$\pm 13^\circ$
2	$\pm 2.5^\circ$	$\pm 5^\circ$

The previous analysis reveals that, assuming $d \gg D_m$ (Fig. 2.8), which is usually the case, the beam scan trace s at the plane of the target is (Fig. 2.11):

$$s \simeq \theta_s d = 2 \frac{\Psi}{M} d \quad (2.5)$$

This means that, assuming a maximum rotation angle Ψ_{\max} for M_r , the theoretical maximum extension of the FoV (Fig. 2.3 on page 86), considered in the geometrical optics study, is given by:

$$\text{FoV}_{\max}[m] = 2s_{\max} = 4 \frac{\Psi_{\max}}{M} d \quad (2.6)$$

Fig. 2.12 shows the maximum required mirror rotation angle as a function of the extension of the FoV, with target range fixed to 11 m. Fig. 2.12 clearly shows that a very small system magnification is required in order to scan the prescribed FoV with limited excursions of the mirror rotation angle. From Table 2.1, which reports some examples of required maximum mirror rotation at different system magnifications, if $M = 10$, the maximum mirror rotation is $\Psi = \pm 13^\circ$ for horizontal scan and $\Psi = \pm 26^\circ$ for vertical scan; if $M = 5$, then $\Psi = \pm 6.5^\circ$ for horizontal scan and $\Psi = \pm 13^\circ$ for vertical scan; and, finally, if $M = 2$, $\Psi = \pm 2.5^\circ$ for horizontal scan and $\Psi = \pm 5^\circ$ for vertical scan. Of course, M cannot be set arbitrarily small, because it also affects the size of the rotating-mirror diameter, as highlighted in Fig. 2.13. In fact, the diameter D_r of the rotating mirror, which, if no scan is implemented, is comparable with the sub-main's diameter D_{sm} , is

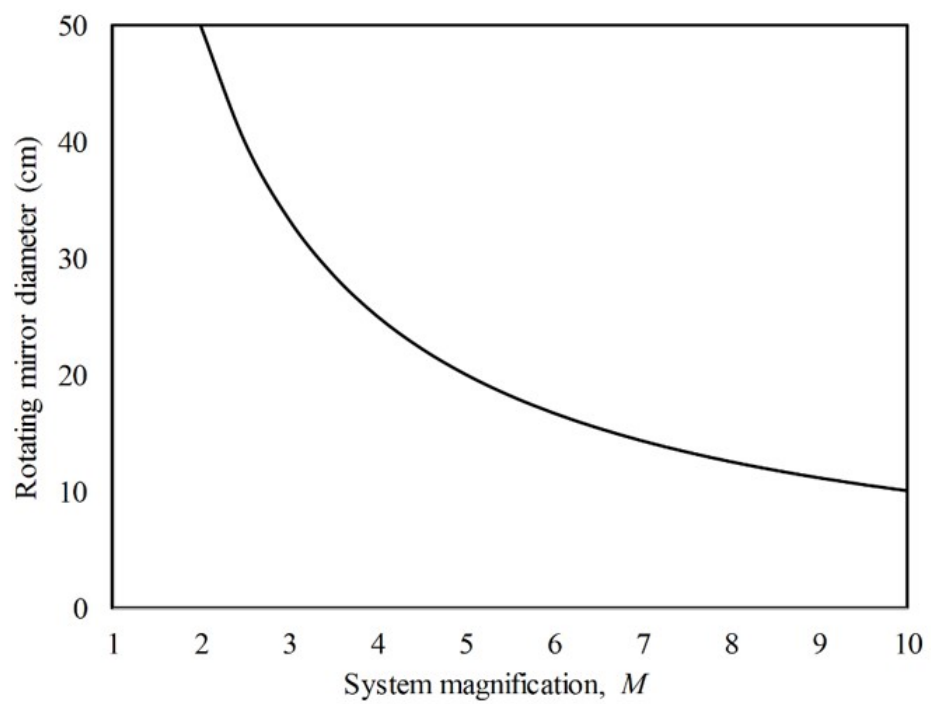


Figure 2.13: Rotating mirror diameter as function of system magnification, with main reflector diameter fixed to 1 m.

given by:

$$D_r \simeq \frac{D_m}{M} \quad (2.7)$$

From Fig. 2.13, we see that if we want to set an upper limit for the rotating mirror diameter to 20 cm¹⁰, a magnification factor (or system magnification) greater than 5-6 has to be selected. The choice of $M = 6$, according to Fig. 2.12, will set the maximum required mirror rotation angle to $\Psi_{\max} = \pm 15^\circ$ (for vertical scan). This mirror rotation may be still too big and may lead to several collateral effects which may significantly degrade the system imaging performance, namely ray path length errors due to asymmetries and beam broadening (or narrowing) on the target due to the different illumination of the main reflector while scanning [9]. For e.g., these effects are shown in Fig. 2.14. In this picture, the system is offset in the xz plane and mirror M_r is rotated in that plane by an angle $\Psi = -5^\circ$ in the direction $x \rightarrow z$ and $\Psi = +5^\circ$ in the direction $z \rightarrow x$; while $\Psi = 0^\circ$ indicates the mirror is in the all-focused nominal orientation (no scan). As anticipated before, for some scan angles, the main reflector is under-illuminated, whilst for others it is well-illuminated or possibly over-illuminated. For the aforementioned reasons, new scanning techniques are required, for e.g. relying on sectorization of the FoV, demanding the scan of the sectors to multiple offset feeds each pointing at a distinct sector of the FoV. But such investigations are not matter of this study. With $M = 6$, the system will reasonably be compact, contained within a region whose extension does not exceed the specifications.

¹⁰Leading to a reasonable compactness of beam wave guide

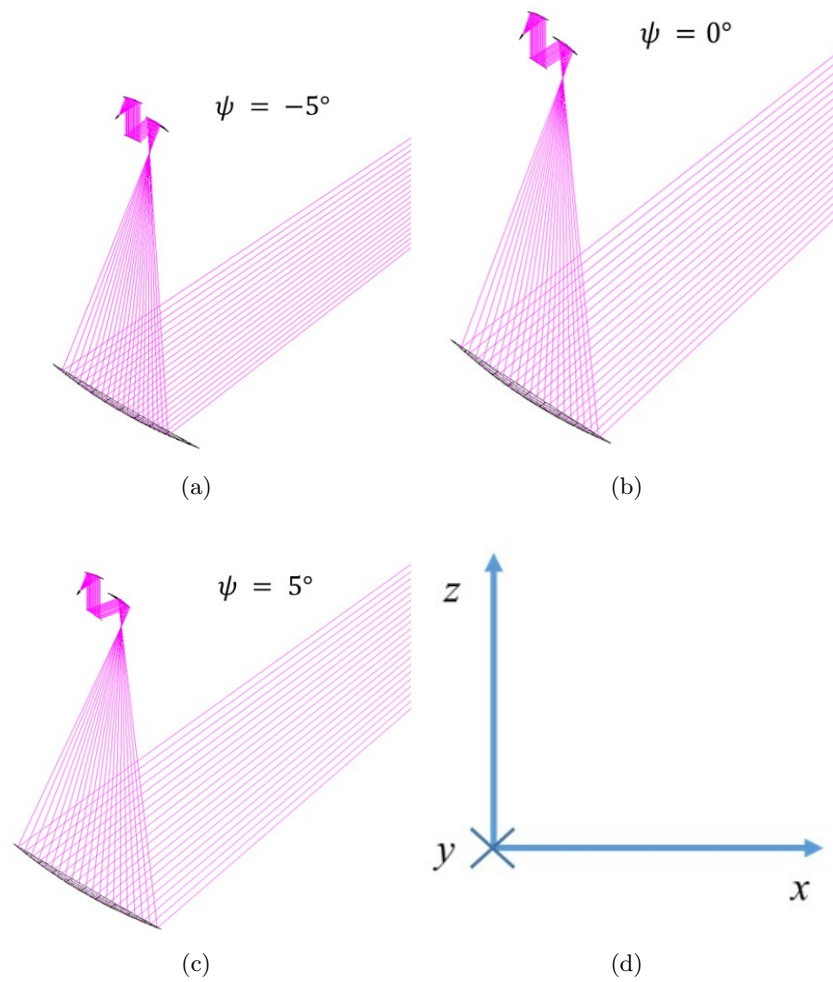


Figure 2.14: Ray path plot with mirror M_r rotated by -5° (a), 0° (b), and $+5^\circ$ (c) in the xz plane of the reference coordinate system (d).

2.5 Location of the illuminator

To illuminate the field of view, where the target is, different strategies have been evaluated for a possible implementation:

- Entire target illumination. A horn transmitting TX antenna can be used in order to produce a beam whose solid angle encloses the entire FoV;
- Single Pixel illumination. The TX antenna illuminates pixels one by one. Both the TX and RX antenna may share the same beam waveguide, for e.g. using a beam splitter¹¹ [19]–[21].

In the case of entire target illumination, two different topologies are proposed:

1. Out-Flash TX. As illustrated in Fig. 2.15a, the transmitter is placed near the main reflector edge;
2. In-Flash TX. As illustrate in Fig. 2.15b, a hole is cut in the center of the main reflector and the transmitter is placed right there.

The reason for the term “flash” is that in this configuration, the TX illuminates, like a camera flash, the whole target. This means that the signal emitted by the source reaches every “pixel” in the target region, which in turn scatters a portion of the impinging signal back. But since the receiver architecture is focalized through the beam waveguide system, the receiver will only “catch” the signal scattered from the pixel which it is pointing at. The term “out” or “in” refers to the position of the transmitter: either outside the main reflector or inside. For both solutions, we have investigated whether there could be some direct interference produced by the transmitter which is transferred to the receiver. Thus, we have simulated the amount of cross-coupling between the TX and the RX antenna to assess which solution performs better. Cross-coupling may occur because part of the transmitted wave induces some currents in the sub-main reflector surface and then back at the receiver. However, since the TX horn is illuminating the FoV (imagine a cone of emission enclosing the FoV), only the very-low-amplitude tail

¹¹A beam splitter is a mirror which spatially separates orthogonally polarized impinging waves. It can be used, for instance, to let the same beam wave guide system be shared among a transmitter and a receiver located in two different positions.

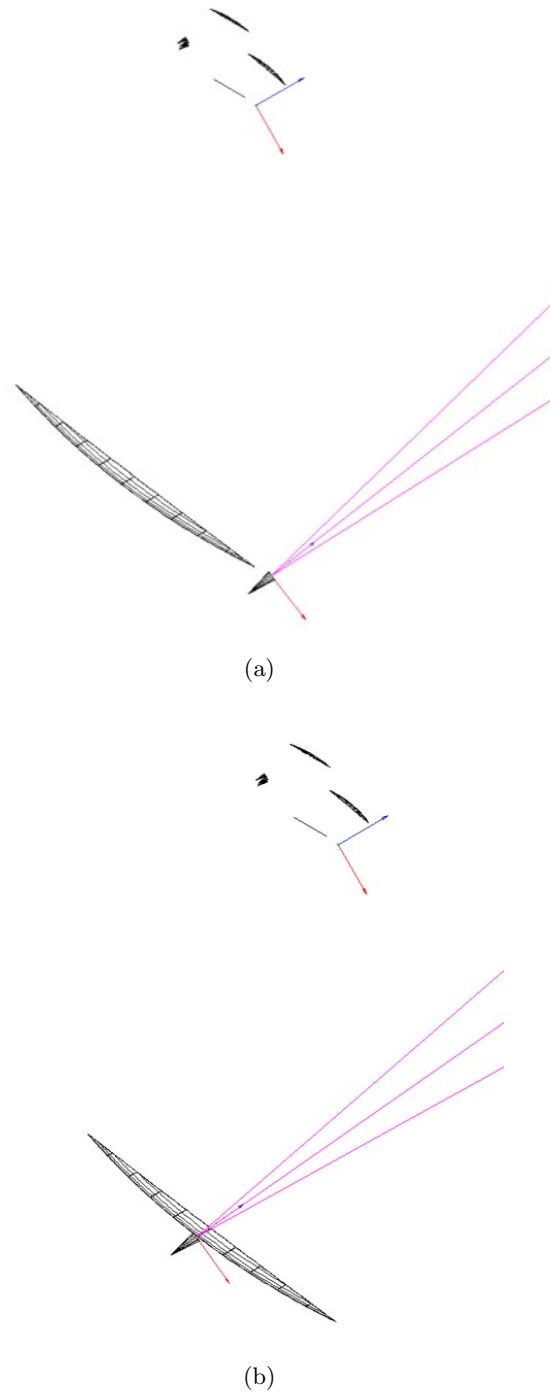


Figure 2.15: Possible location of the transmitter: (a) out-flash TX configuration and (b) in-flash TX configuration.

of the transmitted wave is intercepted by the sub-main reflector (which is weakly intersected by transmitted cone of emission), so the TX-to-RX cross-talk is expected to be very weak. Indeed, both the In-Flash and Out-Flash configurations exhibit a negligible cross-coupling with respect to the levels of back-scattered signals expected to be received by the radar, thus both solutions do not represent any relevant issue and either of them can be undertaken.

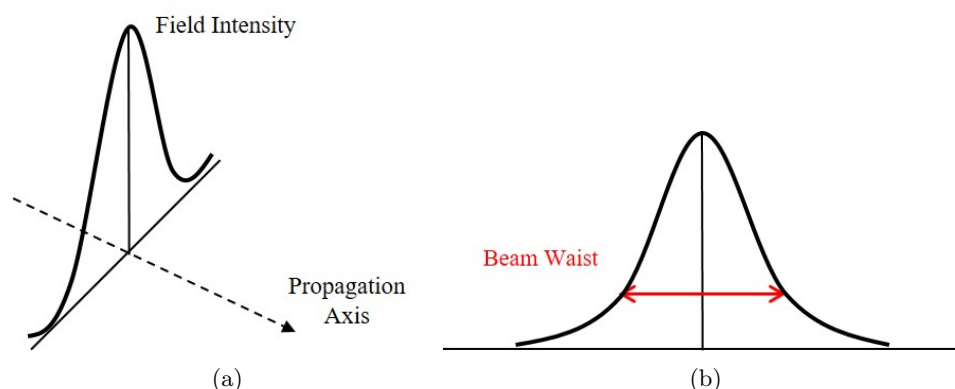


Figure 2.16: (a) Field intensity and (b) waist of a Gaussian beam.

2.6 The confocal region

As mentioned previously, the system currently under study consists of a beam waveguide, i.e. a series of reflectors confining the radio wave energy in a beam with limited cross-section. Such kind of propagation regime is very well described by the so-called paraxial-limit approximation, which provides a full description of the beam shape and field intensity distribution through very simple equations [17]. The beam also takes the name of Gaussian beam because the function describing the amplitude of the electric field in the cross-section around the beam axis has a Gaussian-like shape (Fig. 2.16a). There are two quantities which can be used to describe a Gaussian beam:

- The waist radius w (Fig. 2.16b). It is the distance from the propagation axis where the field amplitude is above the 10 dB level, with 0 dB being the maximum field intensity (at the propagation axis);
- The radius of curvature R (Fig. 2.17): is the radius of curvature of the spherical wave front of the Gaussian beam.

The beam parameters change along the propagation axis. In particular, there is a region, called *confocal region*, where the beam waist is minimum and the wave front is planar. Instead, beyond a certain distance (Rayleigh distance), the beam waist gets larger and the wave front becomes spherical with radius of curvature very close to the distance from the focal region (Fig. 2.17).

The system under study is a confocal Gregorian reflector system (Fig. 2.5 on page 88), where the beam is focalized onto a small spot at the target

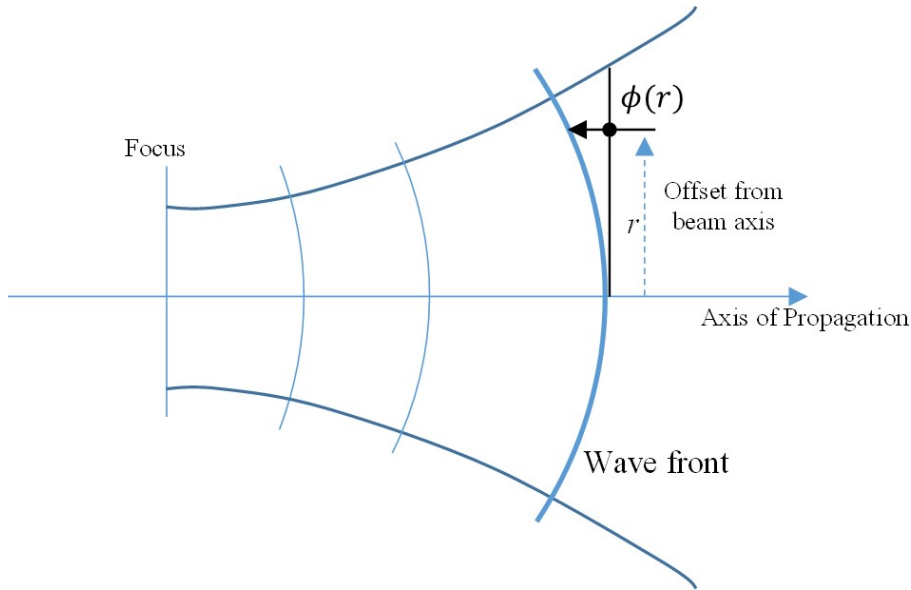


Figure 2.17: Radius of curvature of Gaussian-beam wave fronts.

region. Thus, the target is supposed to be placed in the confocal region of the beam radiated by the main reflector M_m (Fig. 2.6 on page 89). If the target were static, it would always be possible to place the target in the confocal region and the system would always be perfectly focused. However, in our case, the target is expected to be dynamic and the scanning of the target be performed during its natural motion. Now, if the target escapes from the confocal region, the beam waist starts increasing, degrading the image resolution. Consequently, it is fundamental to ensure that the target should be entirely scanned before it leaves the confocal region. For our system, the confocal region length on the target, depicted in Fig. 2.18, is given by [17]

$$\Delta d = 2 \left(\frac{\pi w_0^2}{\lambda} \right) \quad (2.8)$$

where w_0 is the beam waist radius at the focal point (on the target), as shown in Fig. 2.8, i.e. the pixel radius. For the 2 cm pixel radius achievable with this system, as said in Sec. 2.3, Δd is equal to 84 cm (± 42 cm from the focus). If we call d_f the distance from the focus point as defined in Fig. 2.19, then the beam waist radius w_f and the radius of curvature R_f at that distance are given by [17]:

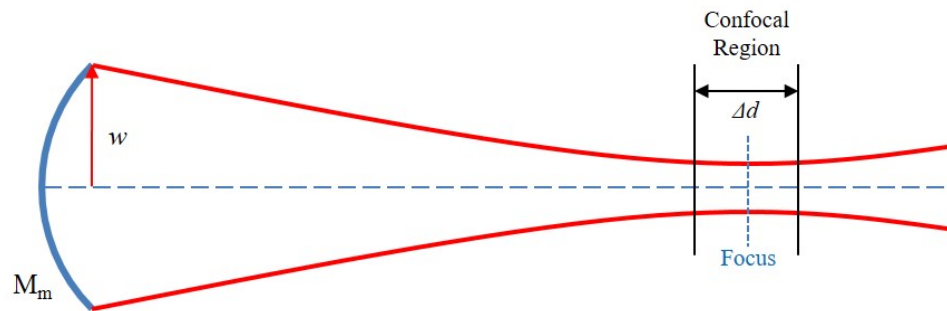


Figure 2.18: Extension of the confocal region on the target. M_m is the main reflector (Fig. 2.5 on page 88).

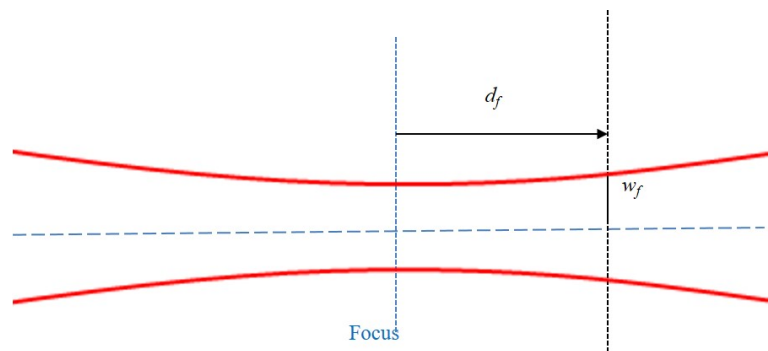


Figure 2.19: Definition of distance from the focus point.

$$w_f = w_0 \sqrt{1 + \left(\frac{\lambda d_f}{\pi w_0^2} \right)^2} \quad (2.9)$$

$$R_f = z_f + \frac{z_c^2}{z_f} \quad (2.10)$$

where z_c is the Rayleigh distance and is equal to

$$z_c = \frac{\pi w_0^2}{\lambda} \quad (2.11)$$

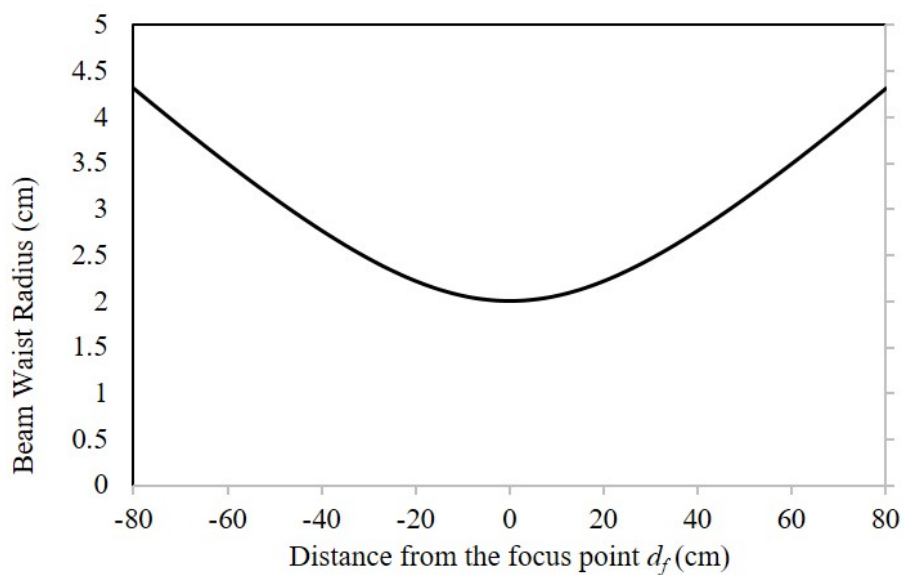
Thus, according to Eq. 2.9, the beam waist radius, at the extremes of the confocal region ($d_f = \Delta d/2$) increases up to 2.8 cm which could be acceptable to some limited extent. Fig. 2.20a and Fig. 2.20b show the beam waist radius and the radius of curvature, respectively, as function of the distance from the focus point (d_f). We observe that around the focus point the radius of curvature is quite high, reflecting into a planar wave front, while, moving away from the focus point, it decreases until it asymptotically equals d_f . Within the confocal region, the wave can be approximated as a plane wave, but attention must be paid to the beam waist which should not grow too much. Another way to evaluate the planarity of the wave front at a distance d_f from the focus point is considering the phase delay of a point on the beam cross-section at an offset distance r from the beam axis. This phase delay $\Phi(r)$ is the phase difference between a point on the beam cross-section and a point on the beam spherical wave front at the same distance from the focus (Fig. 2.21) and is defined as:

$$\Phi(r) = \frac{\pi r^2}{\lambda R_f} \quad (2.12)$$

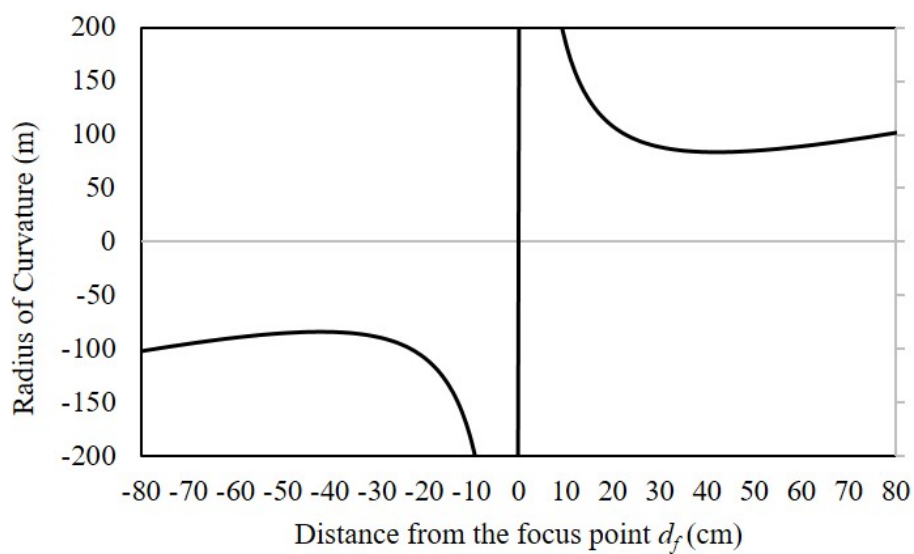
In particular, if we take $r = 2$ cm, at the extremes of confocal region (± 42 cm), $|R_f| = 83$ cm and $|\Phi(r)| \simeq 30^\circ$. In Table 2.2, the parameters evaluated until now are presented at two different distances from the focus point. The table suggests that a reasonable extension for the confocal region should not be higher than ± 42 cm. As mentioned previously, in a moving-target environment, the confocal region extension tells how fast the imaging system should be. In particular, the entire target should be scanned within a time $t < t_{\max}$, with

$$t_{\max} = \frac{\Delta d}{v_{\text{tg}}} \quad (2.13)$$

where v_{tg} is the average target velocity and Δd is the extension of the confocal region. For instance, for ± 42 cm confocal region ($\Delta d = 84$ cm),



(a)



(b)

Figure 2.20: (a) Beam waist radius and (b) radius of curvature as a function of the distance from the focus point.

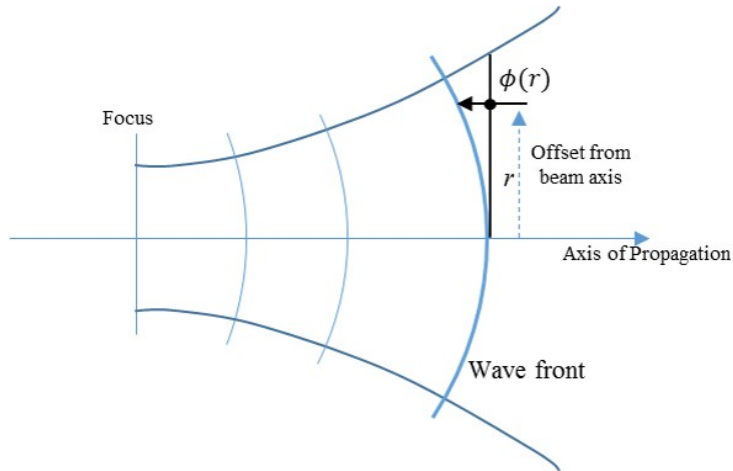


Figure 2.21: Phase delay $\Phi(r)$ of spherical wave front relative to plane wave at a certain offset distance r from the beam axis.

Table 2.2: SOME PARAMETERS OF THE BEAM AT DIFFERENT DISTANCES FROM THE FOCUS POINT.

Distance from focus point	Radius of curvature	Beam waist radius	Phase delay at 2 cm offset distance from the beam axis
42 cm	83 cm	2.8 cm	30°
20 cm	108 cm	2.2 cm	22°

assuming a typical target velocity of 4.5 km/h, the maximum scan time should be 670 ms. This number will determine the system performance not only in terms of scan speed, but also in terms of signal-to-noise ratio, because the SNR depends on the radar integration time per single pixel, which is the time the radar has to dedicate to each single pixel. For instance, to have a rough estimation of the single-pixel scan time, with a pixel size of 2 cm and a FoV of 1 m×2 m, about 50 spots in the horizontal and 100 spots in the vertical direction are required to cover the whole FoV. Thus, approximately 5,000 spots are necessary to cover the FoV entirely, leading to a single-pixel time of 134 μ s (670/5,000). This number can be considered as the radar integration time for each pixel, which may be too small for an adequate SNR. That's the reason why an feed architecture with an array of receivers simultaneously scanning multiple pixels of the FoV should be pursued, so that the integration time can be increased and a good SNR accomplished¹².

¹²For a radar architecture with very low received signal levels, integration time is extremely important [22]. The noise collected by a radar is time-uncorrelated; so, summing up (or integrating) subsequent copies of it is equivalent to making an average of it. Conversely, signal is strongly time-correlated; so, integrating it over time is equivalent to increasing its level more and more, until it emerges out of the noise floor.

2.7 Considerations on power budgets

The imaging system under study operates by transmitting a Terahertz-frequency radio wave toward a target placed at about 10 m range (distance). The radio wave interacts with the target body: clothing, skin, and other concealed objects. Every material reacts differently to the impinging radio wave [3] and three classes of materials can be identified:

- Reflective materials: objects whose principal behavior is to reflect the radio wave. The direction of reflection depends on their shape and the direction of incidence of the wave.
- Absorbing materials: objects whose main behavior is to absorb the impinging wave. They are very bad materials because their effect is twofold. On the one hand, they reflect very small signals back to the receiver (i.e. they are of difficult detection); on the other hand, they stop the radio wave, hiding all other layers underneath.
- Transparent materials: objects which mainly let the radio wave pass through. Clothes at the THz band behave almost as such.

All other objects present an intermediate behavior among these three separate classes. To evaluate the performance of the system, in this preliminary work, two extreme cases have been investigated: perfect-mirror target and perfect-scatterer target (Fig. 2.22). In the following discussion, the system of Fig. 2.5 to 2.7 on page 89 is considered, under the assumption that both the transmitter and the receiver are placed in the feed region. The power budget in a two-way path is tried to be evaluated, from the source to the target and back from the target to the source. In the case of metal-plate target (Fig. 2.22a), the target is a perfect reflective material, modelled as a loss-less metal plate oriented orthogonally to the direction of incidence of the wave. In this situation a high proportion of the transmitted power is expected to be reflected back to the source, giving a power budget of around 0 dB relative to the transmitted power. In the other case, which considers a perfect-scatterer target (Fig. 2.22b), the incident power is absorbed by the target and evenly scattered in all directions; then only a fraction of the scattered wave is expected to be finally collected by the receiver. Thus, in this situation, a power budget much lower than 0 dB is expected. The results presented in this Section have been obtained by using TICRA GRASP

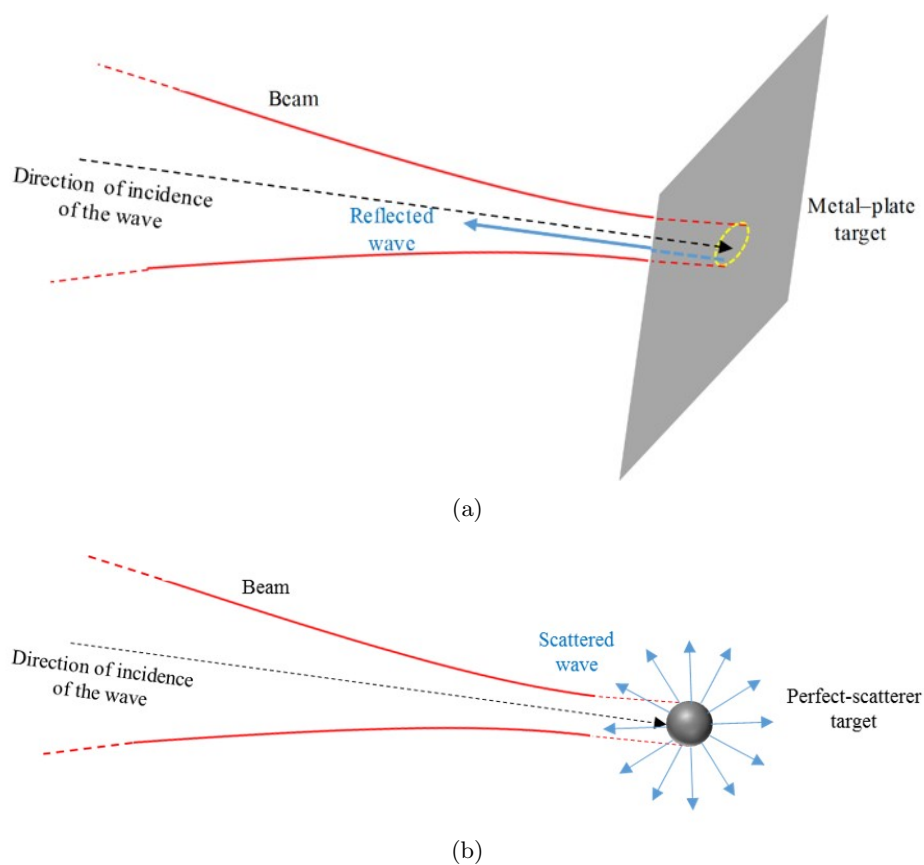


Figure 2.22: (a) Metal-plate target oriented orthogonally to the direction of incidence of the wave, or, alternatively the pointing direction of the antenna system; (b) perfect-scatterer target, completely absorbing the impinging wave and scattering it back in all directions. In the first situation, a high proportion the transmitted power is expected to be reflected back to the receiver; in the second, only a small fraction of the transmitted power is expected to be detected by the receiver.

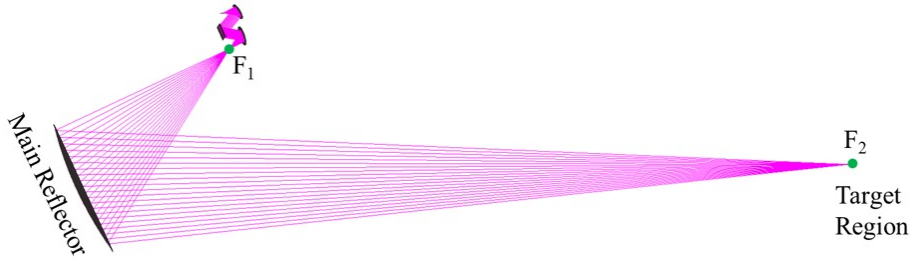


Figure 2.23: Location of the foci of the main ellipsoidal reflector. Focus F_1 is shared with the sub-main reflector M_{sm} (Fig. 2.6) and focus F_2 is placed in the target region.

simulation tool¹³.

2.7.1 Metal-plate target

As anticipated in Sec. 2.7, a metal-plate target (Fig. 2.22a) has been simulated on Ticsra GRASP. The system has been first analyzed in the all-focused situation, with the rotating mirror M_r (Fig. 2.7) in its nominal orientation. The source has been modeled as a horn antenna generating a Gaussian-beam radio wave, placed in the feed of the system (Fig. 2.7). We remind that the system is focalized; in particular, the main reflector is an ellipsoid and, thus it has two foci, F_1 and F_2 (Fig. 2.23): the first focus is shared with the sub-main reflector M_{sm} (Fig. 2.6) and the second focus is placed in the target region. This means that the target, from a radiation point of view, is placed in the near field of the antenna system. Thus, to evaluate the power patterns at the target, a near-field calculation has to be performed. On GRASP, the near-field analysis gives as a result the amplitude and phase

¹³Ticsra GRASP is an asymptotic solver, which is based on the physical optics theory and the theory of diffraction. In recent versions, a method of moment (MoM) has also been implemented. GRASP allows to simulate electromagnetic propagation in systems which are large compared with the wavelength. Radiation problems of beam wave guides are afforded efficiently in relatively short simulation times. The mechanism behind GRASP's calculation is quite simple. The field emitted from a source is first propagated with the theory of physical optics to calculate the field far from the source; the currents induced by the electromagnetic field over object surfaces in the model are computed; the field radiated from these currents are calculated by using a sort of transformation which performs an integration of those currents multiplied by some field functions; eventually, the field so computed can be re-propagated and the process repeated depending on the presence of other scattering objects (mirrors, dielectrics, etc.).

of the electric field at a selected distance from the reference system. The electric field displayed by GRASP is expressed in normalized GRASP units. If $\bar{\mathbf{E}}$ is the actual electric field in the International System of Units and \mathbf{E} the same field in GRASP units, then:

$$\bar{\mathbf{E}} = \frac{1}{k\sqrt{2\eta_0}} \mathbf{E} \quad (2.14)$$

where $k = 2\pi/\lambda$ is the wave number and $\eta_0 = \sqrt{\mu_0/\epsilon_0}$ is characteristic impedance of vacuum¹⁴ (equal to 377 Ω). Since in the target region, the wave is approximately a plane wave, the Poynting vector [23] (in W/m^2) has the same direction as the direction of incidence of the wave and can be calculated as:

$$S = \frac{E^2}{2\eta_0} = k^2 \bar{E}^2 \quad (2.15)$$

where all quantities (not in bold) represent the moduli of the corresponding vectors. Furthermore, GRASP computes such fields setting a source input power of 4π W, i.e. 12.6 W.

The fields were calculated over a plane orthogonal to the direction of incidence of the wave (Fig. 2.24) and, assuming the beam to be a fundamental Gaussian beam, i.e. symmetric around the beam axis, the field amplitude is independent of the angular coordinate ϕ being only a function of the radial distance r from the beam axis. If $E(r)$ is the amplitude of the electric field over the plane in Fig. 2.24, and $S(r)$ the associated power flux (amplitude of the Poynting vector), then the power collected by a circular region of radius $r = R$ is given by:

$$P = \int_0^R \int_0^{2\pi} S(r) r dr d\phi = 2\pi \int_0^R S(r) dr \quad (2.16)$$

Fig. 2.25a shows the power flux over the plane at the target position expressed in dB, i.e. $10 \log_{10} S$, as a function of the radial distance r from the beam axis. Most of the power is concentrated in a spot of 4 cm (diameter). The source radiates 12.6 W, of which 12.2 W are radiated toward the target (integration performed over a circle of radius $R = 40$ cm), 7.7 W collected by a 4-cm spot. Now, if we place the metal-plate target of Fig. 2.22a, the radio wave is reflected back to the feed. We can calculate again the

¹⁴ μ_0 and ϵ_0 are, respectively, the magnetic permeability and the electric permittivity of vacuum, and are equal to $4\pi \times 10^{-7} H/m$ and $8.854 \times 10^{-12} F/m$.

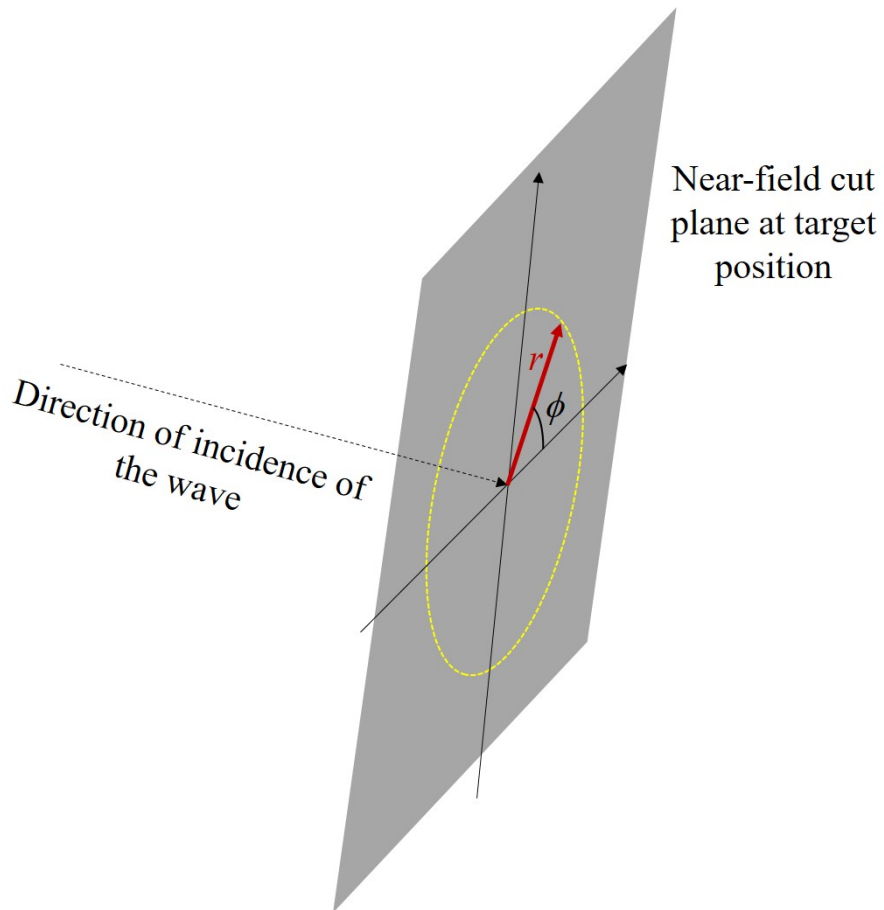
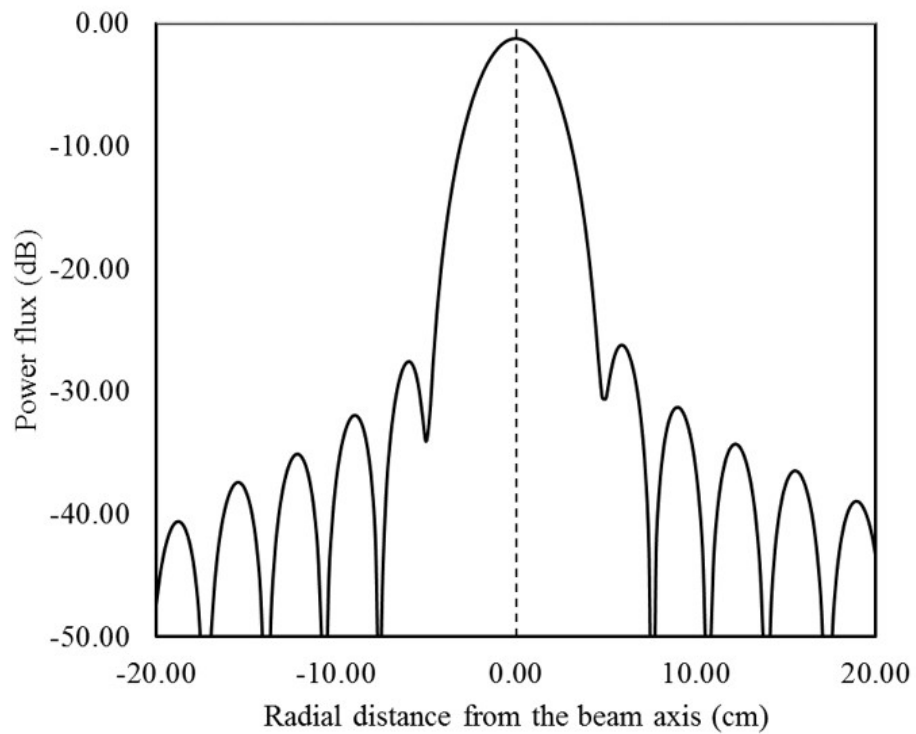
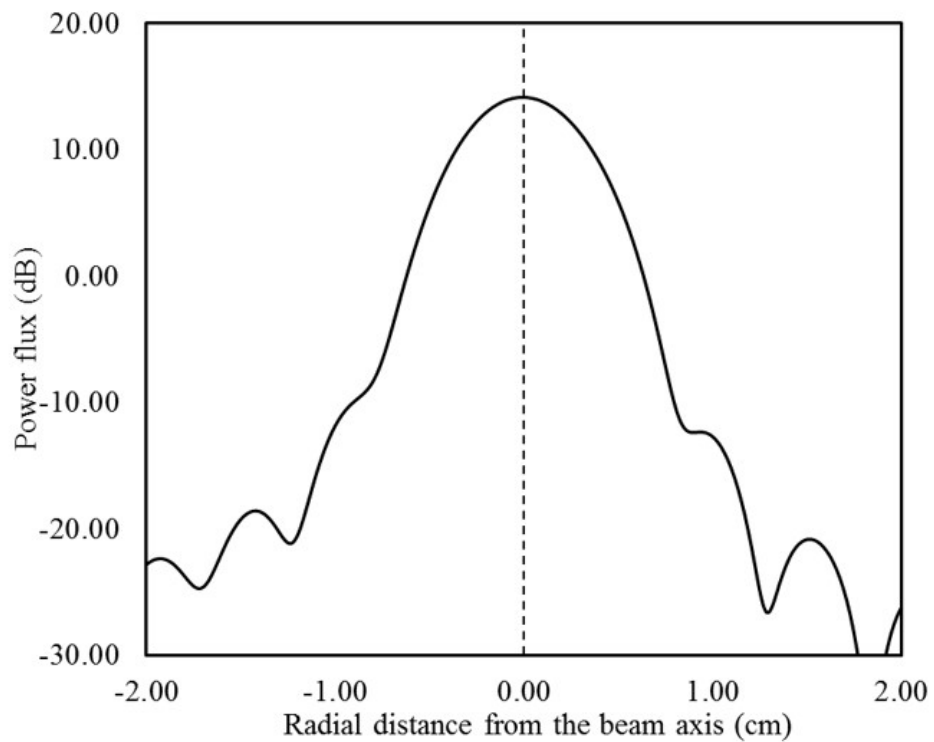


Figure 2.24: Near-field cut plane where the fields are calculated. The plane is located at the focus point (expected target position) orthogonally to the direction of incidence of the radio wave. The beam is assumed to be a fundamental Gaussian beam, i.e. the field is symmetric around the axis of propagation, being an only function of the radial distance r from the beam axis.



(a)



(b)

Figure 2.25: Power flux ($10 \log_{10} S$) as a function of the radial distance r from the beam axis over a plane placed (a) at the target position (Fig. 2.24) and (b) at the feed after reflection of the radio wave from a metal-plate target.

Table 2.3: POWER CALCULATIONS FOR A SOURCE OUTPUT POWER OF 12.6 W (DEFAULT GRASP)

Power intercepted by the metal-plate target	Power intercepted by a spot of 2-cm radius	Power reflected by the metal-plate target back to the feed
12.2 W	7.7 W	10.4 W
-0.14 dB	-2.14 dB	-0.83 dB

power flux over a plane at the feed position, with the plane oriented orthogonally to the direction of incidence of the wave. Such power flux is shown in Fig. 2.25b. The power which is reflected back to the source is approximately 10.4 W (integration performed at the source position over a circle of radius $R = 1.2$ cm, almost equal to the theoretical feed aperture). As expected, the fraction of the transmitted power (12.6 W) which is received at the feed is high, precisely -0.83 dB. These results are reported in Table 2.3, for immediate consultation.

2.7.2 Perfect-scatterer target

A perfect-scatterer target will be examined in this subsection, with reference to Fig. 2.22 on page 110b. The case of perfect-scatterer target represents an extreme case where the pixel on the target completely absorbs the incident wave and scatters it back in all directions. In the real situation, the incident wave is reflected more similarly to what is depicted in Fig. 2.26, with the power scattered in many directions but mostly concentrated in specific directions. However, a perfect scatterer is a good choice for our power budget evaluation purpose, owing to its simplicity. Since a perfect scatterer does not exist in nature, the power budget calculations have been performed analytically. We have assumed that all the power hitting the plane placed at the target's position is absorbed and scattered as a spherical wave (Fig. 2.27). So, of this amount of power only the fraction captured by the solid angle subtended by the main reflector (Fig. 2.27) is collected by the source. To

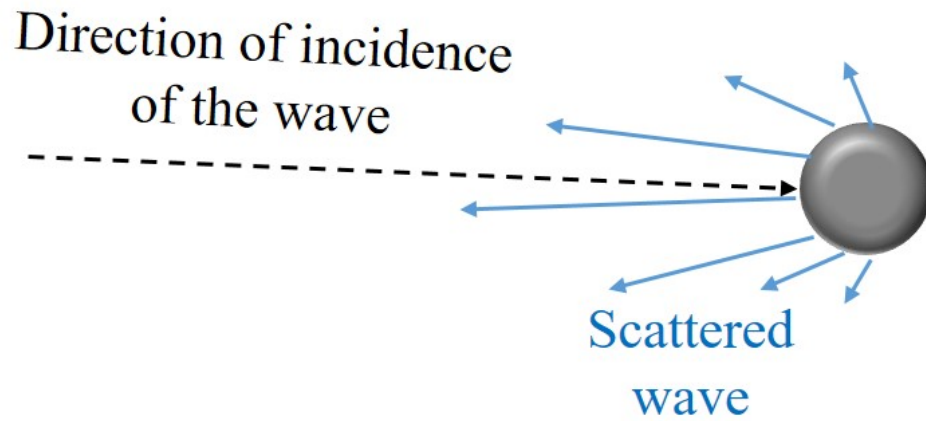


Figure 2.26: More common types of reflection pattern for scattering objects. The incident radio wave is scattered mainly in some directions and less in others.

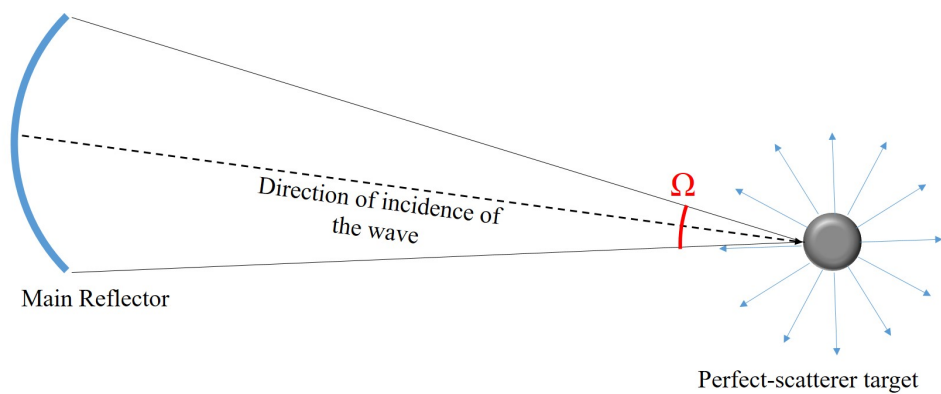


Figure 2.27: Solid angle subtended by the main reflector (Fig. 2.5 on page 88) with standpoint located at the focus point (target position), i.e. focus F_2 in Fig. 2.23.

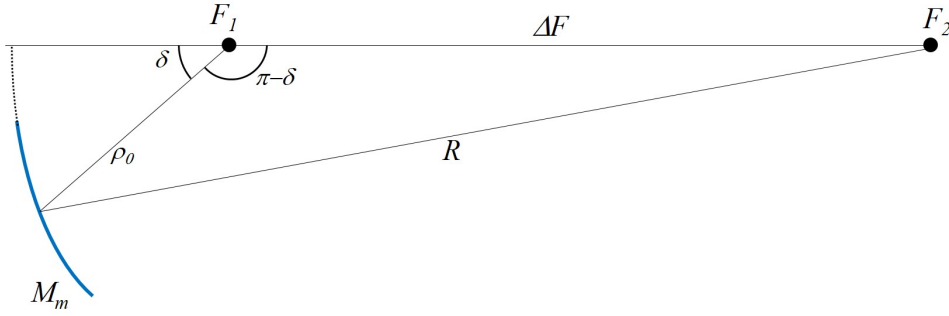


Figure 2.28: Geometry used to calculate the distance between the centre of the main reflector M_m and the focus F_2 where the perfect scatterer is placed.

calculate the solid angle, we need to know the distance R between the main reflector and the scatterer target (Fig. 2.28).

In Fig. 2.28, some other useful quantities are depicted: the distance between focus F_1 and the centre of the main reflector (ρ_0), the foci distance (ΔF), the semi vertex distance ($\Delta V/2$), and the angle between ρ_0 and the axis of the main reflector δ . Given the foci distance and the vertex distance, the eccentricity of the ellipsoidal shape of the main reflector is equal to:

$$\xi = \frac{\Delta F}{\Delta V} \quad (2.17)$$

Then, the distance between focus F_1 and the centre of the main reflector M_m is given by [24]:

$$\rho_0 = \frac{\Delta V}{2} \frac{1 - \xi^2}{1 - \xi \cos \delta} \quad (2.18)$$

R is part of a general triangle, with two known edges, ΔF and ρ_0 , and the angle comprised by them equal to $(\pi - \delta)$. Thus, from the law of cosines, we have:

$$R^2 = \rho_0^2 + \Delta F^2 - 2\rho_0\Delta F \cos(\pi - \delta)$$

from which the value of R is derived:

$$R = \sqrt{\rho_0^2 + \Delta F^2 + 2\rho_0\Delta F \cos \delta} \quad (2.19)$$

Given R and the diameter of the main reflector D_m (Fig. 2.6 on page 89), the angle α subtended by the main reflector as seen from a standpoint placed at focus F_2 can be approximated as:

$$\alpha \simeq \frac{D_m}{R} \quad (2.20)$$

Then, the solid angle Ω subtended by the cone in Fig. 2.27 is:

$$\Omega = 2\pi \left(1 - \cos \frac{\alpha}{2}\right) \simeq \frac{2\pi \left(\frac{\alpha}{2}\right)^2}{2} = \frac{\pi\alpha^2}{4} \quad (2.21)$$

Where the cosine term has been replaced by its first-order Taylor expansion, because α is very small in the system under study.

As a consequence of the previous calculations, the amount of power (P_r) collected by the main reflector is the portion of the scattered spherical wave which falls within the solid angle Ω (Fig. 2.27):

$$P_r = P_t \frac{\Omega}{4\pi} = P_t \frac{\alpha^2}{16} \quad (2.22)$$

where P_t is the transmitted power. The fraction of power received, in case of perfect-scatterer target, neglecting spill-over effects and diffraction at the edges of the reflectors, is approximately equal to:

$$\frac{\Omega}{4\pi} \simeq \frac{1}{2000}$$

because Ω , for the system under study, is roughly equal to 6×10^{-3} steradians. So, the power budget, in case of perfect scatterer is roughly:

$$10 \log_{10} \frac{1}{2000} \simeq -33 \text{ dB}$$

This concludes the evaluation of the power budget in the case of a perfectly focus system with two extreme types of targets, metal-plate and perfect-scatterer. It is possible to observe that, given an input power of 1 mW, almost -33 dBm are received back by the source. This level of power is typical in any radar system, so reasonable SNR can be expected even in a bad case like the perfect scatterer which has been here examined.

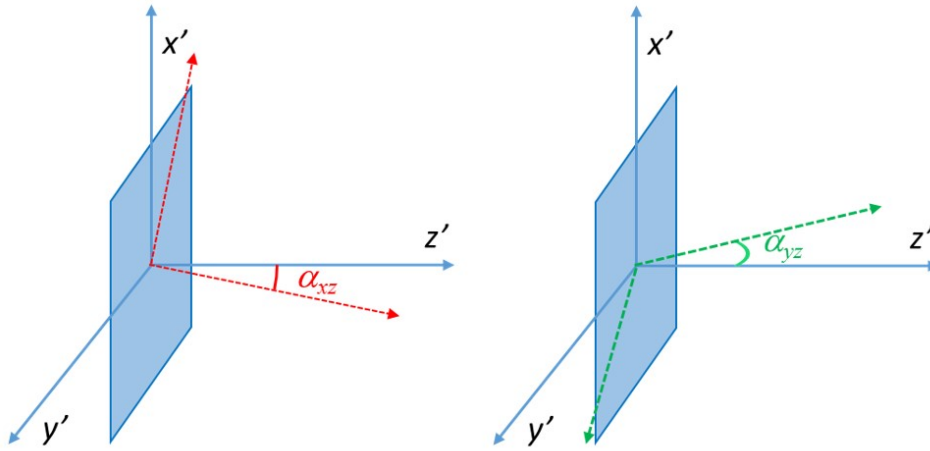


Figure 2.29: Definition of the mirror rotation angles: α_{xz} and α_{yz} stand for a rotation in the $x'z'$ plane and in the $y'z'$ plane, respectively.

2.8 Scanning system

The imaging system under study provides an image of the target by mechanically rotating a low-inertia flat mirror in the two directions, as represented in Fig. 2.29, in a with the z' axis coinciding with the normal to the surface of the mirror. The rotation of the mirror, as seen in one direction, corresponds to a deflection of the beam reflected by the main reflector, Fig. 2.11 on page 93. The reason for this beam scan can be understood after looking at a simplified system which is equivalent to our beam waveguide system. In particular, the effect of the beam waveguide is to virtually turn the point where the feed is physically located (Fig. 2.6 on page 89) into the focus point of the main reflector, i.e. it is as if the feed were virtually placed at the main reflector focal point F_1 (Fig. 2.23 on page 111). So, the simplified equivalent system is made up of a single-reflector feed system. It is well known from literature [25] that an offset of the feed with respect to the focus point of the reflector produces a deflection of the beam relatively to its nominal pointing direction. The effect of the rotating mirror is simply that of shifting the virtual feed of the equivalent system off the main reflector focus point, thus scanning the beam. However, a non-focused system, as mentioned previously, suffers from some drawbacks, such as beam astigmatism due to the different illumination of the main reflector (Fig. 2.14 on page 98) and asymmetry in the beam shape relative to its axis due to phase errors induced by

the different ray-path lengths [19]. In the following section, some results on power pattern at the target plane will be provided for a set of mirror rotation angles. As anticipated in previous sections, the mirror rotation translates into the steering of the main beam, to an extent depending on the system magnification factor M , treated in Sec. 2.4:

$$\theta_s \simeq \frac{2\Psi}{M} \quad (2.23)$$

with Ψ defined as the mirror rotation angle (Fig. 2.10) either in the horizontal or the vertical dimension. Some system parameters are studied hereafter, depending on the mirror rotation. In the current experiment, the maximum allowed mirror rotation is set to $\pm 5^\circ \times \pm 5^\circ$ horizontally and vertically ($\alpha_{xz} = \pm 5^\circ$ and $\alpha_{yz} = \pm 5^\circ$, as seen in Fig. 2.29). The corresponding measured focus-point offset on the target (Fig. 2.11 on page 93) is only about 17-20 cm over the cross section. To show what happens when scanning the beam, several power patterns at different mirror rotation angles are shown in Fig. 2.30- 2.33, referring to the power reaching the target FoV and going back to the feed after reflection from a metal plate target (Fig. 2.22a) oriented orthogonally to the direction of incidence of the wave. A list of system parameters is provided in Table 2.4- 2.7 for different scan situations. In particular, Table 2.4 and 2.5 refer to a mirror rotation only performed up-ward, down-ward, left-ward, and right-ward; while Table 2.6 and 2.7 refer to rotations performed up-leftward, up-rightward, down-leftward, and down-rightward. Correspondingly, Fig. 2.30 and 2.31 refer to the rotations of the mirror reported in Table 2.4 and 2.5; while Fig. 2.32 and 2.33 refer to the rotations reported in Table 2.6 and 2.7. The beam patterns depicted in these plots were used to compute the quantities represented in the tables.

As it is possible to observe from Tables 2.4 to 2.7, as the mirror is rotated, the power intercepted by the 2-cm pixel greatly varies, result of the change in the position of the focal region (which changes with the beam scan). Conquently to the change of the focal region, the beam waist also changes, the wavefront is not planar anymore on the target. So, the amount of power flux reaching the target varies, and the collected power varies as well. A different situation appears for the metal-plate target. In this case, the metal plate is quite large, so the beam waist is always evenly intercepted. That's the reason why the power scattered back to the feed is almost the same for all mirror rotation angles.

Table 2.4: SPOT SIZE ON THE TARGET AT DIFFERENT MIRROR ROTATION ANGLES, AND POWER COLLECTED BY A SPOT OF RADIUS 2 CM AT THE TARGET REGION. MIRROR ROTATION PERFORMED ONLY IN ONE PLANE AT THE SAME TIME

Rotation angles $\alpha_{yz} \times \alpha_{xz}$ (deg \times deg)	-3 dB spot diameter (cm)	Power collected by 2-cm spot radius (W)	Power collected by a 2-cm spot radius as fraction of the transmitted power
0×5 (up)	3.8	6.5	51.8
0×-5 (down)	4.2	7.4	58.8
0×0 (focused)	4.0	7.7	61.5
-5×0 (left)	4.4	9.5	75.5
5×0 (right)	3.8	6.6	52.9

Table 2.5: POWER RECEIVED BY THE FEED AFTER FULL REFLECTION FROM A METAL-PLATE TARGET. THE TRANSMITTED POWER IS 12.6 W. MIRROR ROTATION PERFORMED IN ONE PLANE AT THE SAME TIME.

Rotation angles $\alpha_{yz} \times \alpha_{xz}$ (deg \times deg)	Received power (W)	Received power as fraction of the transmitted power (%)
0×5 (up)	10.9	86.8
0×-5 (down)	11.0	87.3
0×0 (focused)	10.4	82.5
-5×0 (left)	11.2	89.4
5×0 (right)	11.2	89.4

Table 2.6: SPOT SIZE ON THE TARGET AT DIFFERENT MIRROR ROTATION ANGLES, AND POWER COLLECTED BY A SPOT OF RADIUS 2 CM AT THE TARGET REGION. MIRROR ROTATION PERFORMED IN THE TWO PLANES AT THE SAME TIME.

Rotation angles $\alpha_{yz} \times \alpha_{xz}$ (deg \times deg)	-3 dB spot diameter (cm)	Power collected by 2-cm spot radius (W)	Power collected by a 2-cm spot radius as fraction of the transmitted power
-5×5 (up left)	3.7	5.7	45.1
5×5 (up right)	3.8	6.2	49.5
0×0 (focused)	4.0	7.7	61.5
-5×-5 (down left)	4.4	6.7	53.6
5×-5 (down right)	4.2	6.7	53.6

Table 2.7: POWER RECEIVED BY THE FEED IN PRESENCE OF A METAL-PLATE TARGET, IN THE WORST CASES. THE TRANSMITTED POWER IS 12.6 W. MIRROR ROTATION PERFORMED IN THE TWO PLANES AT THE SAME TIME.

Rotation angles $\alpha_{yz} \times \alpha_{xz}$ (deg \times deg)	Received power (W)	Received power as fraction of the transmitted power (%)
-5×5 (up left)	10.6	84.3
5×5 (up right)	10.6	84.1
0×0 (focused)	10.4	82.6
-5×-5 (down left)	10.7	85.0
5×-5 (down right)	10.4	82.5

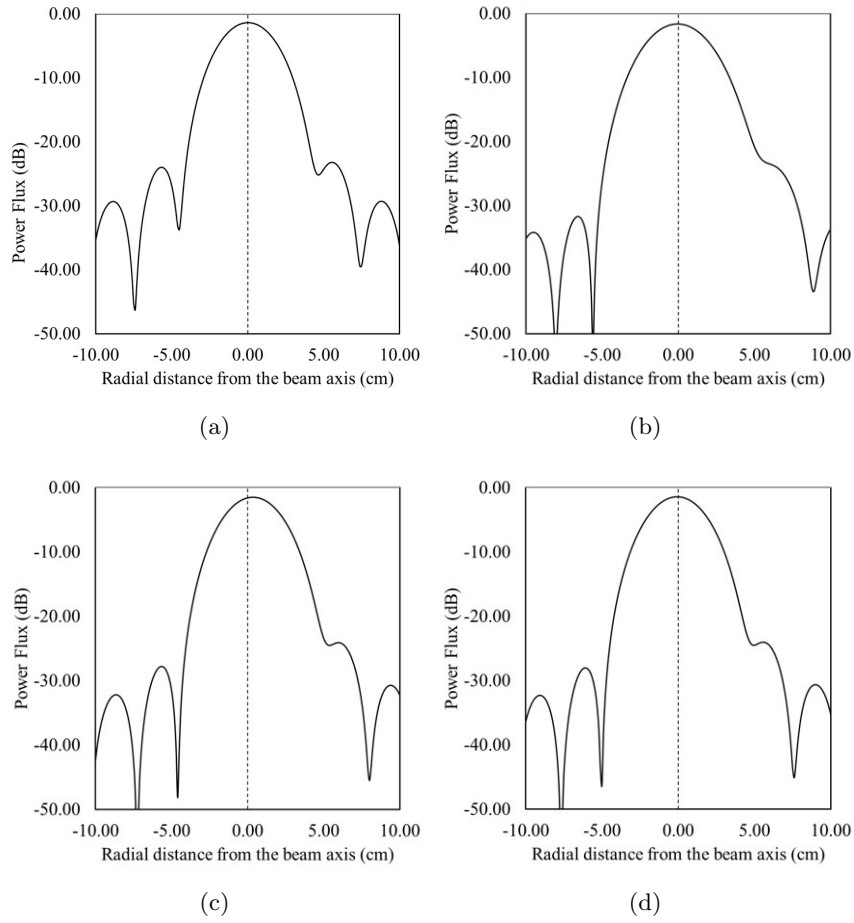


Figure 2.30: Power flux in the target region as function of the radial distance from the beam axis (Fig. 2.24). The power flux is here defined as the dB-amplitude of the Poynting vector ($10 \log_{10} |S|$). Mirror rotated (a) upward, (b) downward, (c) leftward, and (d) rightward by an amount equal to 5° .

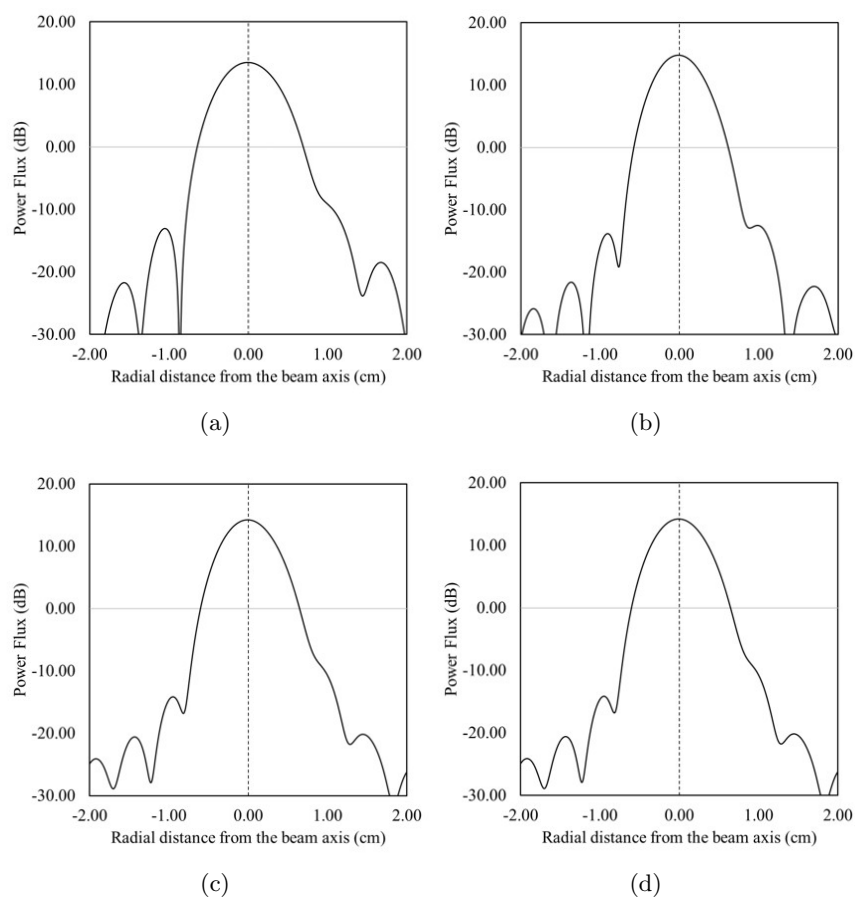


Figure 2.31: Power flux in the feed region as function of the radial distance from the beam axis (Fig. 2.24), after reflection from a metal-plate target oriented orthogonally to the direction of incidence of the wave. The power flux is here defined as the dB-amplitude of the Poynting vector ($10 \log_{10} |S|$). Mirror rotated (a) upward, (b) downward, (c) leftward, and (d) rightward by an amount equal to 5° .

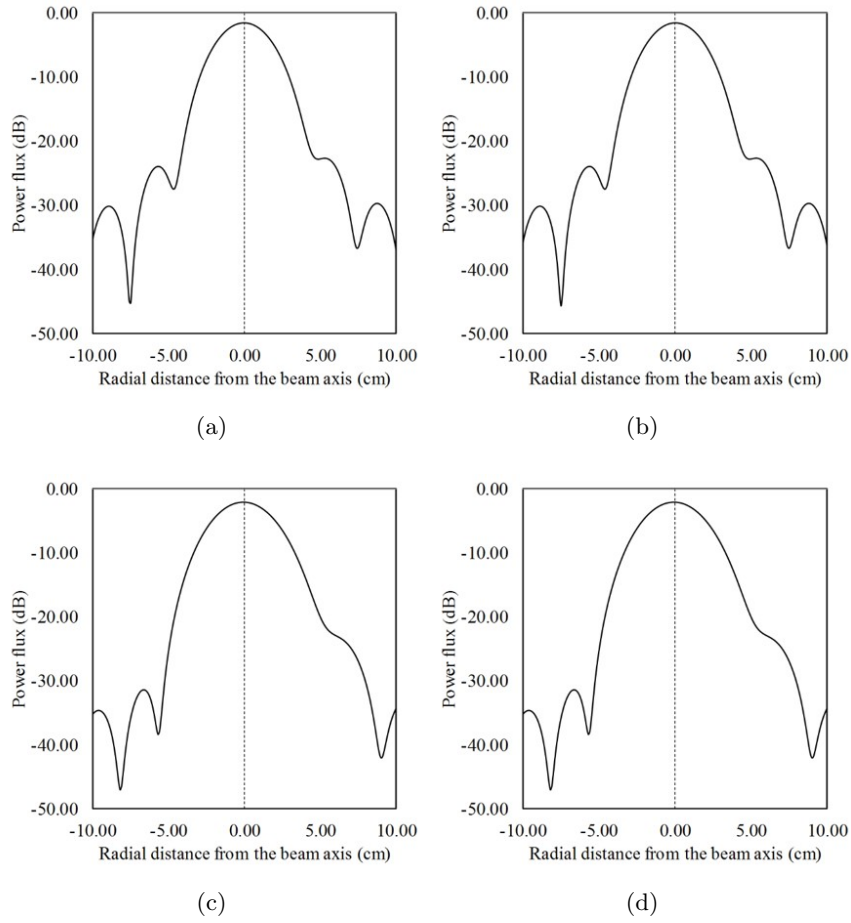


Figure 2.32: Power flux in the target region as function of the radial distance from the beam axis (Fig. 2.24). The power flux is here defined as the dB-amplitude of the Poynting vector ($10 \log_{10} |S|$). Mirror rotated (a) up-leftward, (b) up-rightward, (c) down-leftward, and (d) down-rightward by an amount equal to 5° .

2.9 Conclusions

As part of this Philosophy Doctorate, the general architecture of a mechanically scanned beam-wave-guide antenna for standoff target imaging was designed and preliminarily analyzed. The proposed system was intended to operate at mm-wave frequencies, and in particular at 100 GHz. The architecture was based on a confocal gregorian reflector antenna, with a main ellipsoidal reflector illuminated after a set of mirrors used to magnify the beam and scan it through the use of a movable flat reflector. The system promises to reach fast scan speed as long as an array of receivers is used. An initial target scene, also called field of view (FoV), with the same size as a human being was intended to cover by scanning the beam throughout it. However, covering such a large FoV may be quite critical because of significant system performance degradation, in terms of beam aberration and moving focal point, for large rotations of the mirror. In this preliminary study, the maximum scanned portion of the FoV was almost a square with 20 cm edge, achieved with a maximum mirror rotation of 5° . The beam aberration can be considered acceptable with such limited beam scans, but it may become high for large rotations. Beam aberration could be mitigated if the target range were increased significantly, with a consequent cost in terms of SNR, but technology is advancing in this field, so in the near future, it is likely to find some antenna architecture like this fully operating in a real scenario.

In terms of power budget, the system under analysis has proven to perform quite well both with very good scatterers and with very bad scatterers, leading to pretty good expected levels of received signals. This topic was part of a preliminary design phase, in the framework of a collaboration with a Chinese company interested in developing a body scanner for open environments and imaging of multiple moving person. However, the project was suspended due to a change of the company strategic plans, so no further investigations have been pursued and no experimental results are available. Having said that, the topic was of great interest for this Ph.D., because well fitted in its main topics and created a know-how in this previously untouched field. A master thesis at the Microwave Laboratory of Pavia was also produced based on this Ph.D. results, with further analyzes in terms of system scanning capabilities [26].

References

- [1] J. P. KarbowskiMark and W. Rohde, “Walk-through metal detector”, US. Patent 4 906 973, Mar. 1990.
- [2] Transportation Security Administration, *Imaging technology*, “www.tsa.gov”, (accessed August 2018).
- [3] R. Appleby and H. B. Wallace, “Standoff detection of weapons and contraband in the 100 ghz to 1 thz region”, *IEEE Transactions on Antennas and Propagation*, vol. 55, no. 11, Nov. 2007.
- [4] H. B. Wallace, “Analysis of rf imaging applications at frequencies over 100 ghz”, *Applied Optics*, vol. 49, no. 19, Jul. 2010.
- [5] K. B. Cooper, R. J. Dengler, N. Llombart, T. Bryllert, G. Chattopadhyay, E. Schlecht, J. Gill, C. Lee, A. Skalare, I. Mehdi, and P. H. Siegel, “Penetrating 3-d imaging at 4- and 25-m range using a submillimeter-wave radar”, *IEEE Transactions on Microwave Theory and Techniques*, vol. 56, no. 12, Dec. 2008.
- [6] E. Gandini and N. Llombart, “Toward a real time stand-off submillimeter-wave imaging system with large field of view: Quasi-optical system design considerations”, *Proceedings of SPIE - The International Society for Optical Engineering*, vol. 9462, May 2015.
- [7] E. Gandini, J. Svedin, T. Bryllert, and N. Llombart, “Optomechanical system design for dual-mode stand-off submillimeter wavelength imagers”, *IEEE Transactions on Terahertz Science and Technology*, vol. 7, no. 4, pp. 393–403, Jul. 2017.
- [8] K. Cooper, R. Dengler, N. Llombart, B. Thomas, G. Chattopadhyay, and P. Siegel, “Thz imaging radar for standoff personnel screening”, *IEEE Transactions on Terahertz Science and Technology*, vol. 1, no. 1, pp. 169–182, Sep. 2011.
- [9] N. Llombart, K. Cooper, R. Dengler, T. Bryllert, and P. Siegel, “Confocal ellipsoidal reflector system for a mechanically scanned active terahertz imager”, *IEEE Transactions on Antennas and Propagation*, vol. 58, no. 6, pp. 1834–1841, Jun. 2010.
- [10] V. Lakshminarayanan, M. L. Calvo, and T. Alieva, *Mathematical Optics: Classical, Quantum, and Computational Methods*. U.S.A.: CRC Press, 2012.

-
- [11] J. Martinez-Lorenzo, A. Garcia-Pino, B. Gonzalez-Valdes, and C. Rappaport, “Zooming and scanning gregorian confocal dual reflector antennas”, *IEEE Transactions on Antennas and Propagation*, vol. 56, no. 9, Sep. 2008.
- [12] N. Llombart, R. Dengler, and K. Cooper, “Terahertz antenna system for a near-video-rate radar imager”, *IEEE Antennas and Propagation Magazine*, vol. 52, no. 5, Oct. 2010.
- [13] H. Quast and T. Loffler, “Towards real-time active thz range imaging for security applications”, in *2009 International Conference on Electromagnetics in Advanced Applications*, Sep. 2009, pp. 501–504.
- [14] A. García-Pino, N. Llombart, B. Gonzalez-Valdes, and O. Rubiños-López, “A bifocal ellipsoidal gregorian reflector system for thz imaging applications”, *IEEE Transactions on Antennas and Propagation*, vol. 60, no. 2, Sep. 2012.
- [15] Y. Imaizumi, Y. Suzuki, Y. Kawakami, and K. Araki, “A study on an onboard ka-band phased-array-fed imaging reflector antenna”, in *IEEE Antennas and Propagation Society International Symposium*, vol. 4, Jun. 2002, pp. 144–147.
- [16] J. E. Degenford, M. D. Sirkis, and W. H. Steier, “The reflecting beam waveguide”, *IEEE Transactions on Microwave Theory and Techniques*, vol. 12, no. 4, pp. 445–453, Jul. 1964.
- [17] P. F. Goldsmith, *Quasioptical Systems - Gaussian Beam, Quasioptical Propagation and Applications*. New York, NY, U.S.A.: IEEE Press, 1998.
- [18] S. Farsiu, D. Robinson, M. Elad, and P. Milanfar, “Fast and robust multi-frame super-resolution”, *IEEE Transactions on Image Processing*, vol. 13, no. 2, pp. 1327–1344, Oct. 2004.
- [19] A. García-Pino, B. Gonzalez-Valdes, O. Rubiños, J. Grajal, A. Badolato, B. Mencia-Oliva, P. Soidán, and J. Besada-Sanmartín, “Bifocal reflector antenna for a standoff radar imaging system with enhanced field of view”, *IEEE Transactions on Antennas and Propagation*, vol. 62, no. 10, Oct. 2014.

-
- [20] N. Llombart, K. B. Cooper, R. J. Dengler, T. Bryllert, G. Chattopadhyay, and P. H. Siegel, “Time-delay multiplexing of two beams in a terahertz imaging radar”, *IEEE Transactions on Microwave Theory and Techniques*, vol. 58, no. 7, pp. 1999–2007, Jul. 2010.
- [21] J. L. Hirshfield, P. D. Kolchin, N. V. Kuzikov, and V. I. Petelin, “Quasi-optical antenna duplexer”, in *25th International Conference on Infrared and Millimeter Waves (Cat. No.00EX442)*, Sep. 2000, pp. 405–406.
- [22] M. A. Richards, J. A. Scheer, and W. A. Holm, *Principles of modern rada*. Raleigh, NC, U.S.A.: SciTech Publishing, 2010.
- [23] G. Conciauro and L. Perregrini, *Fondamenti di Onde Elettromagnetiche*. Milan, Italy: Mc Graw-Hill Education, 2003.
- [24] E. H. Lockwood, *A Book of Curves*. Cambridge, England: Cambridge University Press, 1967.
- [25] S. K. Sharma, S. Rao, and L. Shafai, *Handbook of Reflector Antennas and Feed Systems*. Artech House, 2013.
- [26] F. M. Fasolo, “Antenna a fascio guidato a 300 ghz con scansione meccanica per applicazioni di imaging”, master thesis, Correlators Giuseppe Siciliano and Prof. Luca Perregrini, Microwave Lab, University of Pavia, Dec. 2017.

Chapter 3

Dielectric-Based and Mechanically Steered Antenna for Satellite Communications On-The-Move

This chapter presents the theoretical design and validation through software simulations of a Ka-band flat-panel antenna, based on array technology, with mechanical azimuth/elevation scanning and with the introduction of a further scanning capability accomplished by the addition of a mechanically actuated wedge-shaped dielectric superstrate. In this way, the keyhole problem affecting a traditional azimuth/elevation scanning antenna can be overcome by introducing a sort of third-axis steering. The dielectric superstrate is designed to be properly matched with the radiowave propagation and not perturb the operation of the underlying array. The array has a dual-band operation and the same aperture is used for both uplink and downlink, so the dielectric superstrate is matched in two separate frequency bands. The matching of the superstrate is the most difficult part of the project, as evident from subsequent sections of the chapter.

This study makes part of a collaboration with the European Space Operations Centre, in the framework of the NPI initiative, and A.D.S. International s.r.l., a company based in Lecco (Italy), working in the field of

telescope, radiotelescope and astronomical instruments design and production. The results of theoretical analyses and simulations are here presented to demonstrate the utility and the limits of this approach. Among the future developments, a prototype of the antenna may be realized by using 3D printing technology and eventually tested.

3.1 Introduction

The satellite industry has grown over the last decade well beyond the global economy. In 2016 the total amount of revenues reached \$ 260.5 B with an overall growth of about 25% over the previous 5 years. The number of operative satellites passed from 994 in 2012 to 1459 in 2016, with a growth of nearly 60%. Out of all operational satellites, over 35% are used for commercial communications. Consumer satellite mobile industry, totalizing an overall global revenue of \$ 3.6 B (in 2016), is growing, as well, of nearly 5% on an annual basis, in the last years [1]. In this framework of global growth, emerging companies, as well as international state governments are investing considerable resources on a new market which seems to be quite promising in the near future, i.e. satellite communications on-the-move (SATCOM On-The-Move) [2].

While on the ground the communication infrastructure is steadily growing, with the Internet being the major source of profit, satellite internet infrastructure is still limited due to several constraints companies need to cope with. The reason is that, conversely to applications on the ground, satellite communications have to deal with very large distances the signals have to cover to go from the transmitter to the receiver. Larger distances mean heavier propagation losses, leading to the need for high-gain links in order to ensure sufficient SNR for wideband applications, like the Internet. Having said that, though internet connectivity is excellent on the ground, when users move to remote areas of the planet or take a flight or a ship, connectivity is inevitably lost, due to the lack of mobile communication infrastructure in the sea or in the sky, as well as in desertic areas. Satellites, instead, are devoted to offer services where global coverage is not a problem, rather it is the reason-of-life of any satellite, as shown in Fig. 3.1. In principle, satellites are able to offer connectivity to mobile users in any place and at any time. Passengers on super-fast trains, or ships, or airplanes demand



Figure 3.1: In-flight satellite connectivity. Source <http://www.writeopinions.com/air-traffic-management>.

constant connectivity to keep in touch with their companies, friends, freely surf on the Internet, watching videos, reading, post on social media, and so on. Ship personnel may benefit from crew connectivity with the latest maritime information such as chart updates, engine monitoring, and weather routing broadcast.

SATCOM is always delivered through a modulated RF carrier having to travel from a TX antenna to an RX antenna through an absorptive atmosphere. The antenna is the most important device to ensure proper operativity of the radio link. There are specific requirements the antennas have to fulfill, such as [3], [4]:

- High gain. An antenna with a high gain is efficient in focusing the radiowave energy over a small solid angle. This means that more power density (in W/m^2) can invest the satellite (if, for e.g., the TX is the mobile equipment and the RX is the satellite).
- Low system noise. This parameter is important and strictly correlated to the capability of the system to collect more signal than disturbance. Every antenna should have a radiation pattern minimizing the noise collected from undesired directions.

- Low sidelobes. The level of sidelobes should be low enough to reduce the interference, coming from unwanted directions, with other satellites or mobile antennas or other terrestrial radiowave sources.

Satellite applications are mainly concentrated in the frequency spectrum ranging from L/S band (used for global navigation systems, satellite tracking, telemetry and telecommand TT&C), to X band (used especially for military purposes, or earth observation missions), Ku band (used for satellite communications, television broadcast), and Ka band (used for scientific missions and emerging broadband communications). Since Ku band is currently the most crowded by satellite communication services, Ka band is quite promising for next-generation SATCOM on-the-move applications. Fewer satellites are currently using this frequency band, with a clear advantage in terms of higher data rates and payload¹ size.

The antenna does not only have to fulfill requirements in terms of gain, sidelobes and noise temperature, but also other crucial aspects:

- Beam scanning. The satellite and the terrestrial antenna must always keep line-of-sight (LOS), so scanning capability is definitely a fundamental requirement. Furthermore, the mobile terminal could be installed on ships, airplane, off-road vehicles, as shown in Fig. 3.2. All of these are moving platforms whose any pitching and rolling make lose the LOS, which of course must be compensated by the antenna beam scan.
- Polarization. The antenna should be circularly polarized to make the radio link performance polarization-alignment-independent.
- Low profile. The antenna may be mounted on the skin of an airplane or over a terrestrial vehicle, so depending on the context, it must be fulfill strict profile requirements, like aerodynamics, for instance.

Table 3.1 shows a variety of companies proposing several SATCOM antennas, some of which are available today in the market, while some are under research [2]. From the table, it is possible to classify 3 main kinds of antenna architectures: reflector (or dish) antennas, phased arrays, and hybrid antennas.

¹In a satellite, the payload is the functional body of the satellite, including the antenna, the electronic equipment, the set of sensors, making it operational.



(a)



(b)

Figure 3.2: SATCOM on-the-move antenna mounted (a) on a military off-road vehicle, source <https://www.xsens.com/> and (b) on a ship from the US navy, source <https://www.satellitetoday.com/>

Table 3.1: SOME SATCOM ANTENNAS IN THE MARKET OR UNDER RESEARCH.

Product	Technology	Freq.	Polariz.	G/T (dB/K)	EIRP (dBW)	Diam.	H	EL \times AZ coverage	Application
ViaSat 2532	Horn array	Ka	Any	11.3	43.5	80.8 cm	23.1 cm	$[0^\circ-75^\circ] \times 360^\circ$	Aircrafts
ViaSat 5230	Dish	Ka	LHCP & RHCP	10.2	46.5	34.5 cm	8.64 cm	$[5^\circ-75^\circ] \times 360^\circ$	In-flight connectivity
TTI 2021	Hybrid Electronic Mechanical	K	any	5	-	80 cm	30 cm	$[0^\circ-85^\circ] \times 360^\circ$	Vehicle connectivity
ThinkKom Ka1000	Flat Panel	Ka	LHCP & RHCP	11.5	44.5	66 cm	16.5 cm	$[-10^\circ-90^\circ] \times 360^\circ$	In-flight connectivity
TTI KU08A	Hybrid Electronic Mechanical	Ku	Dual Linear	11	42	1.4 m	20 cm	$[20^\circ-70^\circ] \times 360^\circ$	Vehicle connectivity
SANTEL-165	Flat Panel	Ku	Linear	14	-	1.3 m	30 cm	$[0^\circ-90^\circ] \times 360^\circ$	Vehicle connectivity
QUEST Q-EPA	Phased Array	Ku/Ka	-	-	-	-	10 cm	-	Under Research
PHASOR (no product)	Phased Array	Ku	-	> 20	> 70	-	~ 3 cm	$[0^\circ-70^\circ] \times 360^\circ$	Any mobile platform
RaySat ESA/PAA	Phased Array	Ku Ka	Linear Circular	max 8 max 7	max 50 max 45	max 52.3 cm max 32.5 cm	~ 5 cm	$[0^\circ-70^\circ] \times 360^\circ$	In-flight connectivity
RaySat ER6000-A	Flat Panel	Ku Ka	Dual linear LHCP/RHCP	12.4 15.4	45.8 48.7	95.7 cm	23.8 cm	$[0^\circ-90^\circ] \times 360^\circ$	In-flight connectivity
C-COM iNetVu	Dish	Ka	LHCP/RHCP	13.5	43	1.3 m	52 cm	$[10^\circ-90^\circ] \times 360^\circ$	Vehicle connectivity

Reflectors [5], [6] are very simple, low-cost, high-performance antennas, but they are bulky and do not easily lend themselves to airborne applications where aerodynamics counts a lot; furthermore, they are usually based on elevation-azimuth scan mechanisms, which suffer from a well-known problem called *key-hole*² which de-facto poses a limit on the full-performance elevation coverage for all angles comprised between 0° and 10° [7].

Phased arrays [8]–[11] are much more complex and expensive than reflectors, but offer superior scanning speed, do not suffer from the keyhole problem and, above all, are very low profile, so thin to become even conformable to the platform skin (e.g. aircraft fuselage) [12]. However, their elevation coverage is usually to $\pm 70^\circ$ ³ about the aperture axis, restricting their range of applicability, limited to all situations where the satellites relatively to the platform fly above 20°-elevation.

Hybrid antennas here represent those antennas where the scan mechanism is a combination of different techniques, for e.g. electronic and mechanical steering. For instance, there can be antennas with electronic steering in elevation and mechanical steering in azimuth, or antennas with electronic

²The *keyhole* is a problem affecting the performance at very high elevations of all elevation-azimuth scanning antennas. To understand this problem, it is better to consider some operative scenarios. First of all, there are no problems if the satellite (or, in general, the target) is only moving in azimuth, relatively to the antenna; the problems arise when the satellite moves in elevation with the antenna pointed at very high elevations (close to 90°). In the best situation, where the antenna is pointing at low elevations, if the satellite moves upwards with a certain angular speed, the antenna can track it with by rotating with same speed. Now, let's consider the worst case, when the antenna is pointing at high elevation, say, 85°; if the satellite moves toward and then overcomes 90°, say it reaches an angle of 95° (which is again 85°-elevation but in the opposite side), the antenna (which cannot rotate overhead), has to perform a very fast rotation of 180° in azimuth in a short time to keep tracking the satellite, while it's passing overhead. Such rotations can become so fast that the antenna is not able to follow them, hence the keyhole problem. This means that, at zenith, even when the satellite spans very small elevation angles in a certain time, the antenna has to span very large azimuth angles in the same time. The result of the keyhole is that, when the antenna, mounted on a vehicle, ship or airplane, is pointing at high elevations, the normal attitude changes of the platforms (due to rolling, pitching, or dirt roads) result in very fast and caotic rotations of the antenna).

³When the beam produced by a phased array is scanned, the radiation performance of the antenna degrades as long as the off-boresight angle increases. This degradation is due to a problem known as *scan loss*. Scan loss is caused by the natural attenuation of the single-element gain far from the boresight and it usually goes with the cosine (or some similar function) of the off-boresight angle. If that angle is 70°, scan loss is about 5 dB, which is normally considered as a limit.

Table 3.2: ADVANTAGES AND DISADVANTAGED OF REFLECTOR, PHASED ARRAY, AND HYBRID ANTENNA TECHNOLOGIES FOR SOTM.

Technology	Advantages	Drawbacks
Reflector	Simple and low cost, full-performance scan	Bulky and tall keyhole problem
Phased array	Fast scan speed, very low profile, and easy scalability	Complex and expensive, limited coverage, and scan loss
Hybrid	Fast scan speed, good performace and reduced profile	A little complex, a little bulky, limited scan loss

steering covering a certain conical region and mechanical steering covering the remaining region, or antennas with mechanical azimuth/elevation steering in one region and mechanical elevation/cross-elevation⁴ steering in the remaining region. These antennas take some advantages and drawbacks from both reflector and phased array technology. They have a size which is in the middle between both technologies, they have less scan loss problems than phased arrays, and they don't suffer from the keyhole. Among hybrid technologies, there are also metamaterial-based antennas, usually having a very low profile, but being more complex [13], [14]. In Table 3.2, the main advantages and drawbacks of these three technologies for SATCOM On-The-Move (SOTM) are summarized.

This chapter presents design evaluations on a hybrid antenna technology based on a double mechanical steering, one accomplished with a conventional azimuth/elevation scanning and the other accomplished with a dielectric-based scanning [15].

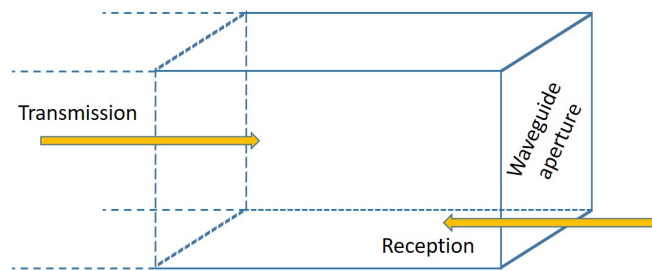
3.2 Presentation of the idea

The idea is to introduce a further beam scan capability on the beam produced by a planar-aperture array antenna already equipped with an azimuth/elevation scan mechanism. The additional beam scanning will help

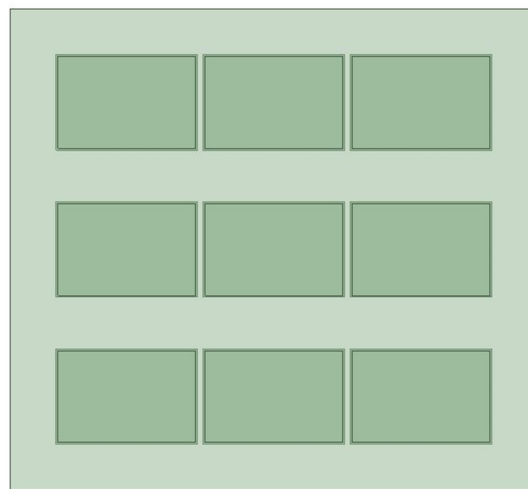
⁴Elevation and cross-elevation steering is a type of scan mechanism where the antenna rotates in two orthogonal planes about the boresight. It is also called XY steering.

mitigate the keyhole problem, by providing an independent beam scan functionality around the array boresight. In this case, when the antenna is tracking (or communicating with) low-elevation targets, the normal azimuth/elevation mode will remain active; instead, when it is tracking high-elevation targets (or targets around the zenith), the additional beam scan function will be activated, thus preventing the normal mode of operation from being limited by the keyhole problem.

The array antenna under study has been developed by A.D.S. International s.r.l. and, for obvious commercial reasons, cannot be described in technical and deep-level detail. However, regardless of the technology behind the antenna, the purpose of this Ph.D. was to study and analyze the effect of introducing an additional beam scan functionality independently of the technological information on the antenna. To do that, the radiation pattern of the antenna only matters, and the array can be just modeled as a very simple planar-aperture array of truncated waveguides. Fig. 3.3a shows an isolated waveguide and Fig. 3.3b a corresponding 3×3 array as seen from the top. One way proposed here to deviate the beam produced by a waveguide antenna array is to introduce a dielectric superstrate immediately above the antenna, as shown in the lateral view of Fig. 3.4. This superstrate should be composed of a cut portion of sphere, which we call *bowl* because of its shape, able to slide in all directions like a rocking cradle. The effect of the cradling is shown in Fig. 3.5 The dielectric superstrate is practically equivalent to a wedge, as shown in Fig. 3.6 whose slope depends on the bowl sliding. If the wedge is placed at a distance d such that the wave emitted by each truncated waveguide has a planar wavefront, the refraction of the rays through the wedge can be studied according to the standard theory of refraction of light hitting a planar interface between different media. In this specific case, without the wedge the rays would be directed along the zenith (z -axis) of the antenna. The presence of the wedge produces a deflection of the rays, as shown in Fig. 3.6, to an extent that depends on the index of refraction (and consequently on the real part of the relative electric permittivity ϵ') of the material composing the wedge and the slope of the wedge.



(a)



(b)

Figure 3.3: (a) Side view of an isolated truncated waveguide and (b) front view of an array of truncated waveguides.

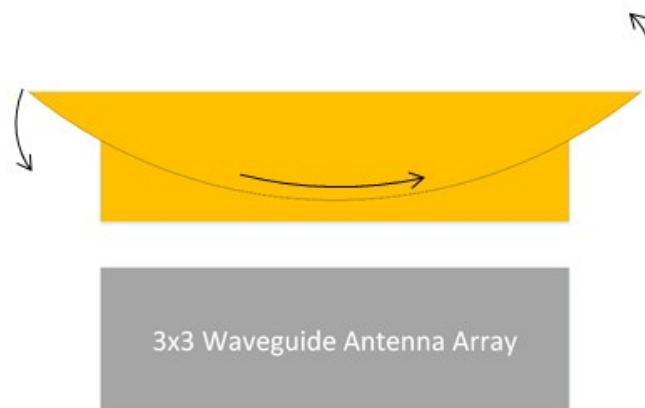


Figure 3.4: Scanning strategy based on the sliding of a dielectric bowl.

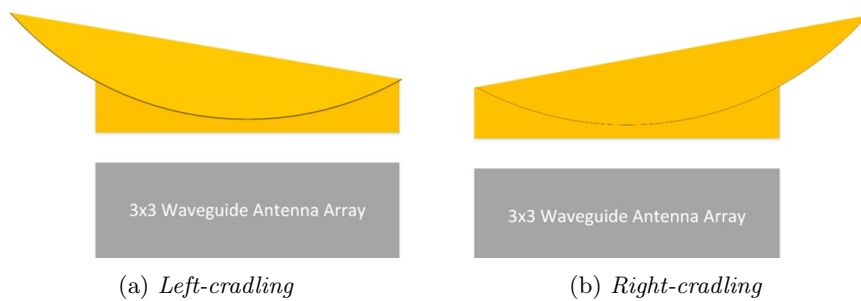


Figure 3.5: Effect of the bowl cradling.

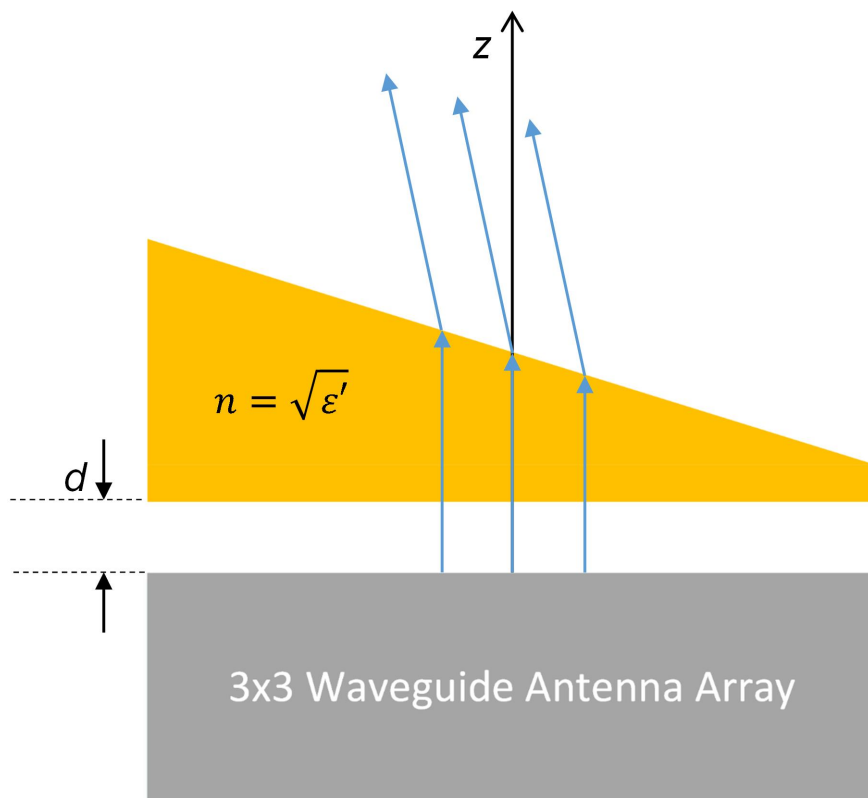


Figure 3.6: Wedge-based beam scanning.

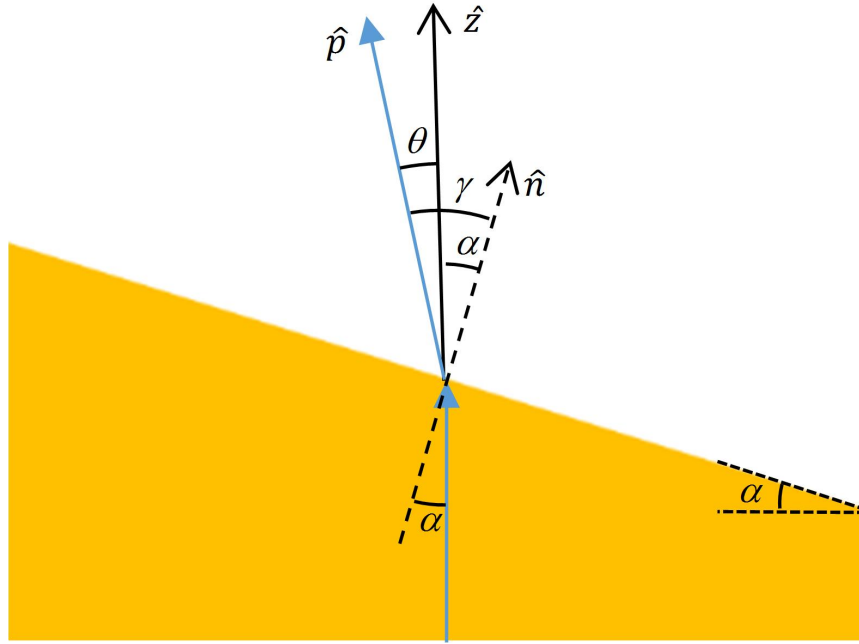


Figure 3.7: Wedge-based beam scanning.

3.2.1 Theory

To study the beam scanning based on a dielectric wedge, Snell's laws of refraction will be exploited [16]. Let's consider a single ray emitted by the source. Referring to Fig. 3.7 Such a ray will initially hit the first air-to-dielectric interface without being deflected; then it will hit the second dielectric-to-air interface, whose slope is α with respect to the horizontal plane. This means that the normal unit vector to the second interface creates an angle α with the z -axis. When hitting the second interface, the ray forms an angle α with respect to the normal vector to the interface \hat{n} . From the Snell's laws, the refracted ray will form an angle γ with respect to the normal, given by:

$$n \sin \alpha = 1 \cdot \sin \gamma = \sin (\theta + \alpha) \quad (3.1)$$

where $n = \sqrt{\varepsilon'}$ is the index of refraction of the dielectric wedge. From Eq. 3.1, we can retrieve the beam scan angle as:

$$\theta = \arcsin (n \sin \alpha) - \alpha \quad (3.2)$$

Under the assumption of small angles, Eq. 3.2 can be approximated as:

$$\theta \simeq n\alpha - \alpha = (n - 1)\alpha \quad (3.3)$$

An interesting result comes if $\varepsilon' = 4$. In this situation $\theta \simeq \alpha$, revealing that small perturbations of the antenna platform attitude may be compensated by performing a rotation of the wedge by the same amount.

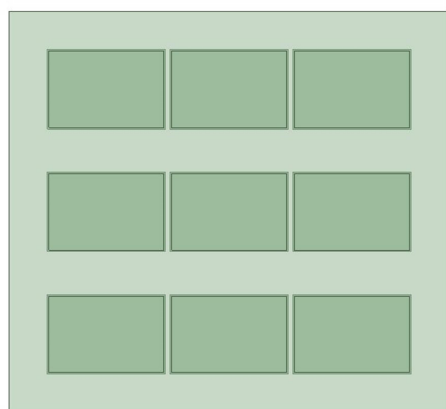
3.2.2 Numerical validation

In order to validate the theory presented in Subsec. 3.2.1, a structure has been simulated composed by a 3×3 waveguide antenna array (Fig. 3.8a) with a dielectric wedge placed above the antenna at a distance of 1 mm (Fig. 3.8b). Two matching layers have been added in order to reduce reflections at a centre frequency of 30 GHz. Matching a dielectric interface is equivalent to cancelling the reflections of the wave as it hits the interface. In this case, the interface is between air ($n_{\text{air}} = 1$) and the wedge material (n). The simplest single-frequency matching layer is a quarter-wavelength dielectric layer with index of refraction n_a equal to the $\sqrt{n_{\text{air}} \times n}$, i.e. $n_a = \sqrt{n}$. Of course, this matching strategy is narrow-band, but more complex structures exist which provide broad-band features. In Fig. 3.8b, n has been chosen to be equal to 2, i.e. matching is performed with:

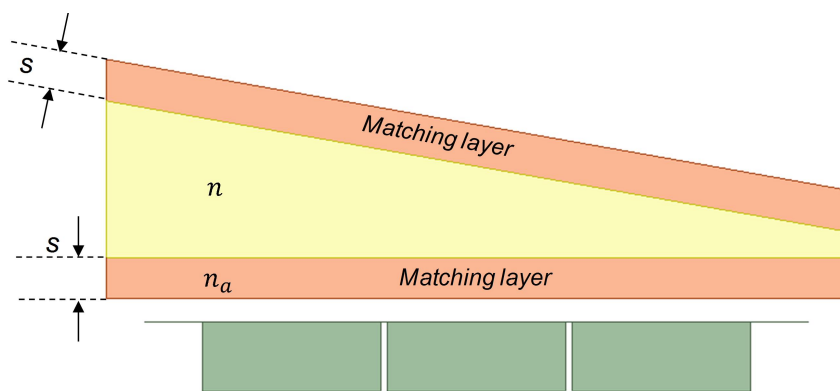
$$\begin{aligned} n_a &= \sqrt{2} \\ s &= \frac{\lambda}{4} = \frac{c}{4n_a f} \end{aligned} \tag{3.4}$$

where s is the matching layer thickness, c is the speed of light in vacuum ($\sim 3 \times 10^8$ m/s), and f the frequency. In this case, using the approximated formula from Eq. 3.3, we have that the beam scan angle $\theta \simeq \alpha$, where α is the wedge slope. Indeed, Ansys HFSS [17] results for $\alpha = 0^\circ$ and $\alpha = 10^\circ$, presented in Fig. 3.9, agree with the theory, leading to a beam scan of approximately 10^{55} .

⁵The array was modeled on HFSS as a series of short truncated pieces of rectangular waveguides, each one with a wave port applied. Then, a dielectric wedge, with tilt angle $\alpha = 10^\circ$ and dimension large enough to cover the entire array aperture, was placed above the array. The simulation was carried out at a centre frequency of 30 GHz.

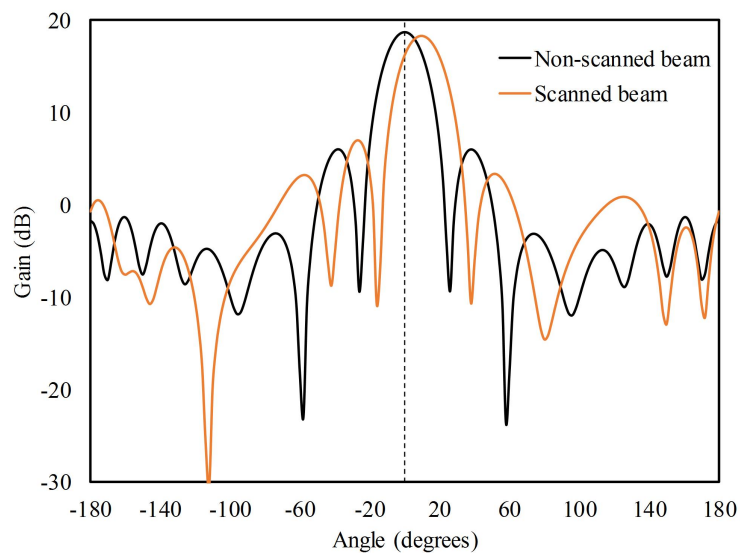


(a) *Waveguide array*

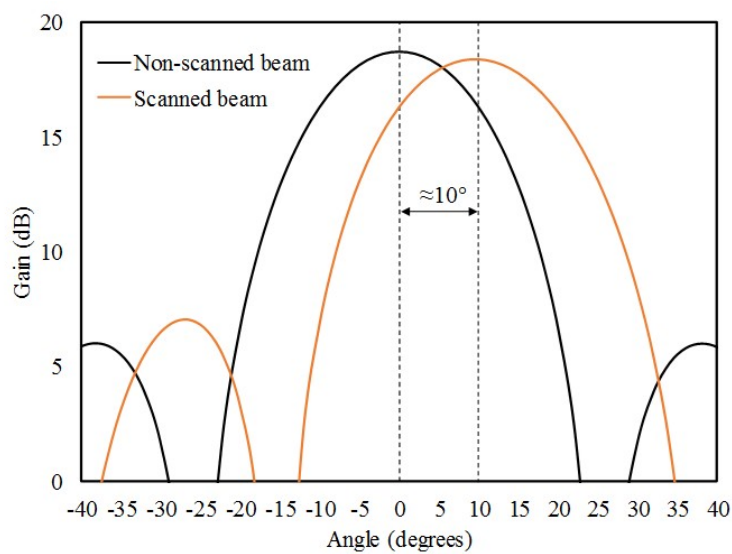


(b) *Dielectric superstrate*

Figure 3.8: HFSS models of the waveguide array with the dielectric superstrate.



(a) Overall view



(b) Closer view

Figure 3.9: Radiation pattern of the wedge-superstrate waveguide antenna array simulated on HFSS.

3.2.3 Comments

In this first section, the idea behind the dielectric-based scanning of a beam produced by an array has been shown. The idea may be implemented in a simple way to achieve the deflection of the beam generated by a waveguide antenna array (or in general by an antenna producing a planar wave front⁶). A possible structure could be based on a dielectric superstrate with a bowl-shaped portion made free to cradle in the two directions. The effect of the bowl cradling is to change the slope of the upper dielectric-to-air interface, thus causing the deflection of the planar wavefront generated by the antenna. This beam scan method is applicable in mechanically scanned Ka-band SATCOM flat-panel antennas (Table 3.1). In such antennas, a broadside planar array is usually physically rotated by an azimuth-elevation motor. As long as the antenna points at low elevations, the scanning operations run normally. But, as the antenna has to point directly toward the zenith, even small relative motions of the satellite around zenith reflect into very quick azimuthal rotations of the gimbals, a previously explained issue known as *keyhole*. In some cases, these rotations are too fast to be implemented. The solution presented in this Ph.D. work is to place a dielectric superstrate above the antenna aperture, so that, when the satellite passes through the zenith, the beam scan is actuated by the dielectric superstrate up to an angular extension of $\pm 10^\circ$. Out of the critical pointing at zenith, the beam scan is performed by the normal azimuth-elevation gimbals. In this way, the keyhole problem can be overcome or at least considerably mitigated.

The system has been here evaluated only from a theoretical and numerical point of view. However, the feasibility of a mechanical implementation of the system needs to be investigated, as well.

3.3 Effect of the dielectric properties

In this section, several analyses are presented varying some of the wedge dielectric properties, i.e. ϵ_r and $\tan \delta$. The former is the relative dielectric

⁶Here, the term *planar wave front* should be intended as a wavefront which is locally planar. In fact, in theory, a planar wave front is, by definition, a wavefront where the field amplitude and phase is constant over a plane orthogonal to the direction of propagation and extending to infinity

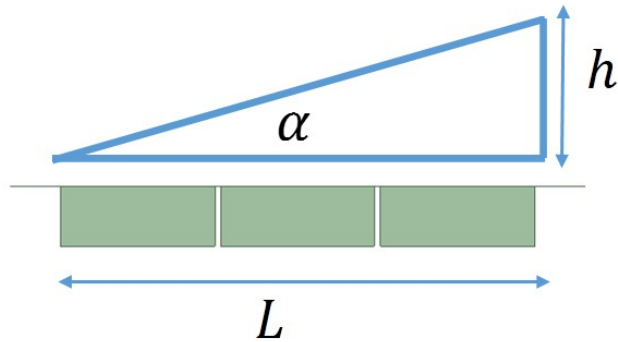


Figure 3.10: Lens thickness.

constant or relative permittivity and the latter is the loss tangent or dissipation factor. The dielectric constant has a direct impact on the lens thickness (as evident from Eq. 3.4, which also depends on the antenna surface⁷. From Eq. 3.3, the wedge tilt angle α necessary for yielding a certain beam squint θ is given by:

$$\alpha = \frac{\theta}{\sqrt{\varepsilon_r} - 1} \quad (3.5)$$

The minimum required wedge thickness, in each dimension, is

$$h = L \tan \alpha \simeq L\alpha = L \frac{\theta}{\sqrt{\varepsilon_r} - 1} \quad (3.6)$$

where h and L are the lens thickness and the antenna size in one dimension, as depicted in Fig. 3.10. As also seen in Section 3.2.1, in order to shrink the wedge thickness and make the dielectric bowl more low-profile, a large value of ε_r is required. In the next two subsections, two separate dielectric constants are compared and the impact of wedge losses on the antenna gain is shown.

3.3.1 Effect of wedge dielectric constant

The results presented in this subsection have been computed by using Ansys HFSS evaluating two different wedge dielectric constants: $\varepsilon_r = 4$ and $\varepsilon_r = 9$. In each case, a match layer has been designed in order to minimize reflections at the working frequency of 30 GHz. The match layer are simply quarter-wave

⁷Naturally, because of the wedge tilt angle, a larger antenna implies a taller wedge to cover it.

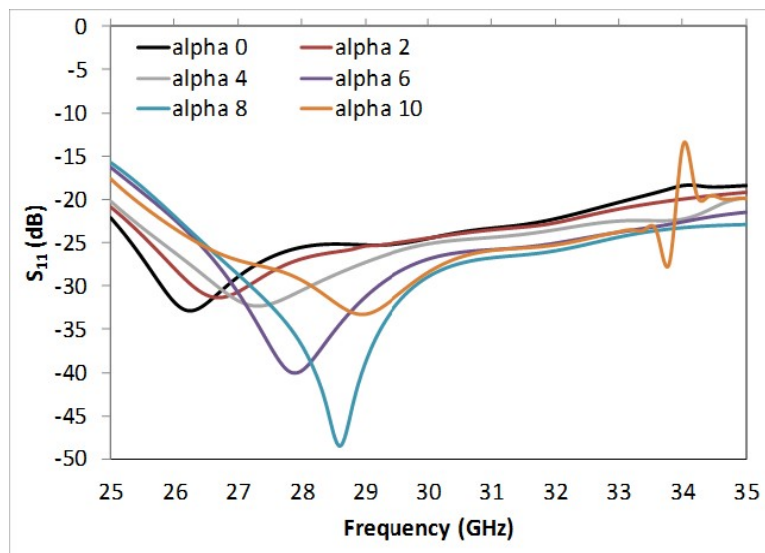
Table 3.3: Match layer dielectric constant.

Wedge (ε_r)	Match Layer (ε_{rs})
4	$\sqrt{2}$
9	$\sqrt{3}$

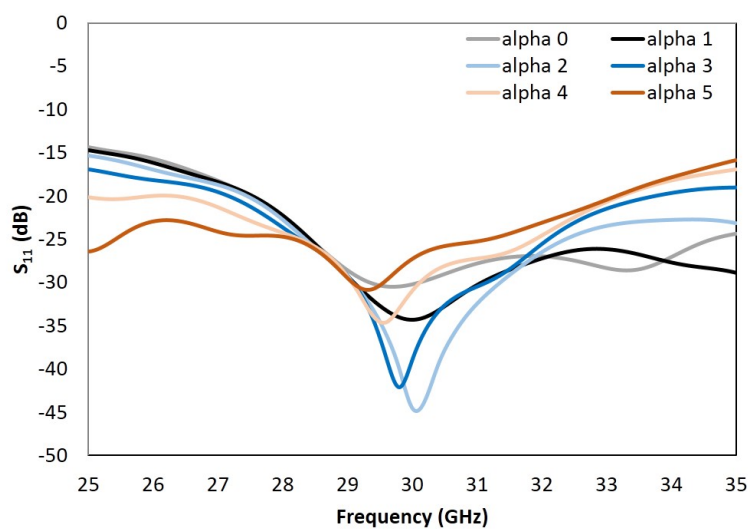
layers with refraction index:

$$n_s = \sqrt{n_0 n}$$

with $n_0 = 1$ and $n = \sqrt{\varepsilon_r}$ the refraction indexes of air and the wedge, respectively. The electric permittivity of the match layers in both cases are reported in Table 3.3. In the first couple of figures (Fig. 3.11), the input matching for the two cases are compared. The max beam squint is fixed at 10° and α is consequently ranged according to Eq. 3.3. In the second set of figures (Fig. 3.12), the gain at the maximum beam squint angle for both cases is depicted. We expect a max squint of 10° , but it is not exactly the case, because Eq. 3.3 was an approximation of the exact Eq. 3.2. However, what really matters is that a nearly 10° -squint occurs. In fact, for a system to operate, it is possible to build up a look-table where every squint corresponds to a certain wedge tilt. Fig. 3.13a shows a comparison of the scan angle (beam squint), beamwidth (assumed as the half-power beam width), and the scan loss (loss of gain with respect to the case with no squint), for the $\varepsilon_r = 4$, while Fig. 3.13b reports some quantities concerning $\varepsilon_r = 9$. It is evident that small losses under considerations lead to a very small degradation of the radiation performance. Finally, Fig. 3.14 presents the max gain assuming no wedge tilt at varying frequency. In the case of $\varepsilon_r = 4$, lossless wedge versus lossy wedge are compared, practically overlapping. In the case of $\varepsilon_r = 9$, the lossless wedge is only represented. Negligible changes are reported between the standalone and the lossless-wedge array. Instead, interestingly, for $\varepsilon_r = 4$, the lossy-wedge array gain is larger than the standalone array. But, unfortunately, the same effect does not identically repeat when $\varepsilon_r = 9$. The effect is certainly due to some diffraction effect which has a significant impact considering the limited size (in terms of wavelength) of the model analyzed via HFSS. In a larger model, this effect is expected to disappear, in place of a normal gain reduction as the beam squint increases.



(a)



(b)

Figure 3.11: Input matching as a function of frequency. (a) Wedge $\epsilon_r = 4$, with α ranging from 0° to 10° ; (b) wedge $\epsilon_r = 0$, with α ranging from 0° to 5° .

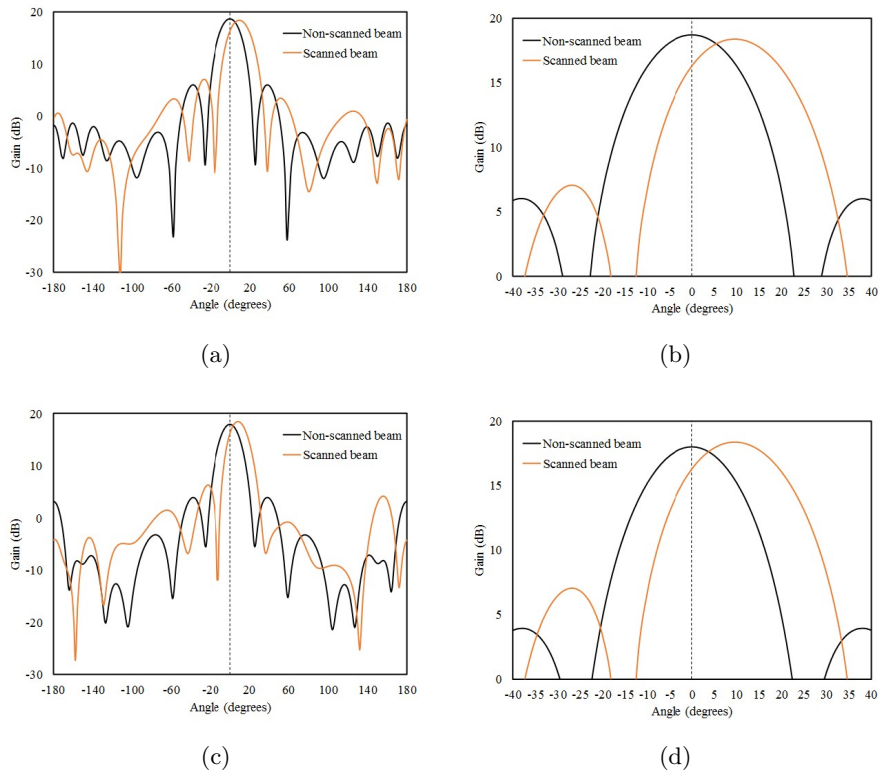


Figure 3.12: Gain as a function of theta, seen in the plane of squint, with no squint and with maximum squint. First case: wedge $\epsilon_r = 4$, (a) full θ -range (b) close-up view. Second case: wedge $\epsilon_r = 9$, (c) full θ -range (d) close-up view.

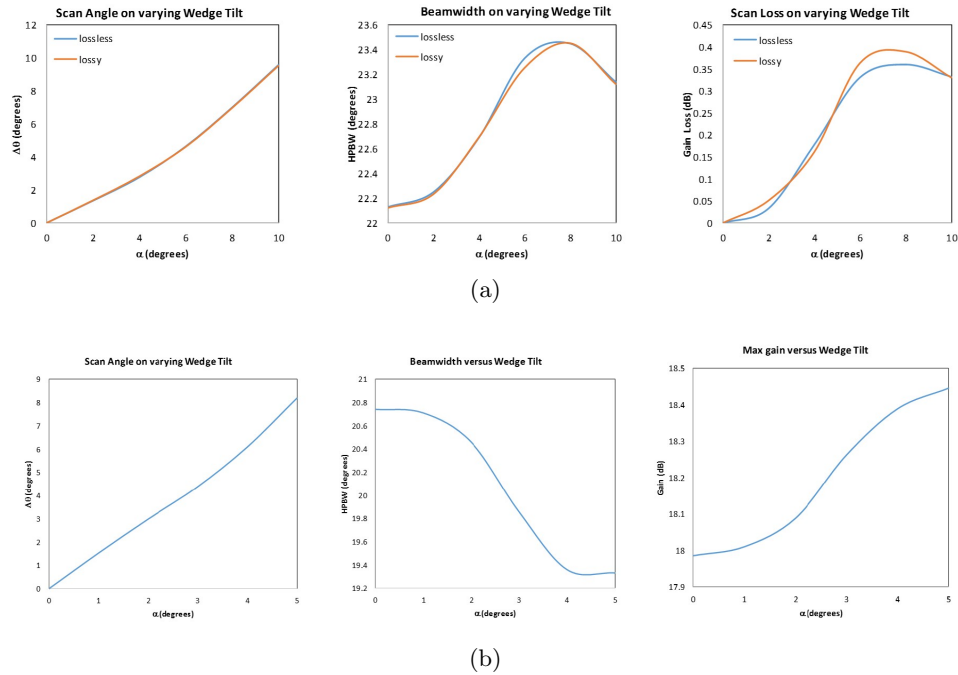


Figure 3.13: (a) Scan angle, beamwidth, and scan loss as a function of the wedge tilt, with $\epsilon_r = 4$, for lossless and lossy wedge; (b) scan angle, beamwidth, and max gain as a function of the wedge tilt, with $\epsilon_r = 9$, for lossless wedge. The lossy wedge $\tan \delta = 0.001$ and the match layer is lossless.

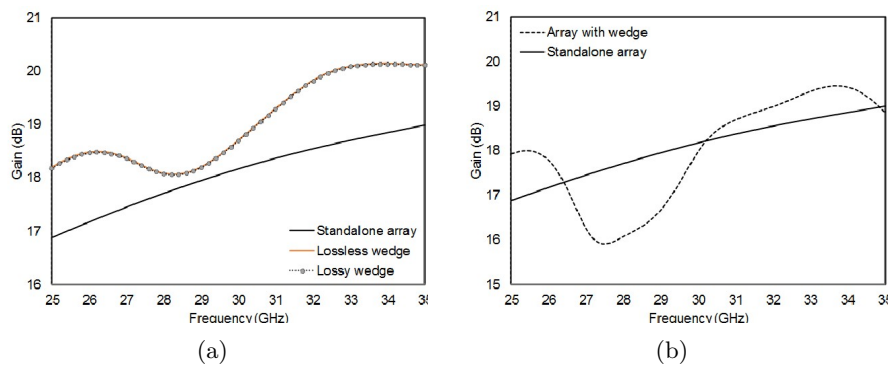


Figure 3.14: Gain as a function of frequency for the standalone antenna, the antenna with lossless wedge, and the antenna with lossy wedge. (a) $\epsilon_r = 4$ and (b) $\epsilon_r = 9$. The wedge $\tan \delta = 0.001$ and the match layer is lossless.

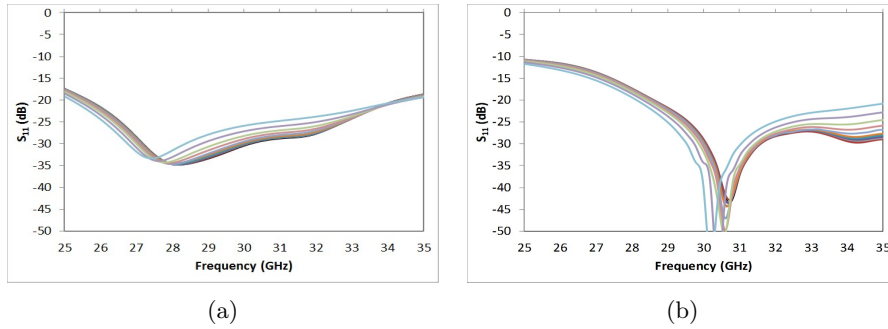


Figure 3.15: Input reflection coefficient with $\tan \delta$ ranging from 0.001 to 0.1 (Table 3.4). (a) $\varepsilon_r = 4$ and (b) $\varepsilon_r = 9$. The match layer is assumed to be lossless. The x-axis is on logarithmic scale.

Table 3.4: Values of $\tan \delta$ used in simulation.

$\tan \delta$
0.001
0.0016
0.004
0.0063
0.01
0.016
0.04
0.063
0.1

3.3.2 Impact of wedge losses

Wedge losses have an impact on the power transmission coefficient through the wedge. While the input matching is minimally affected by losses (Fig. 3.15), the magnitude of the transmission coefficient goes down, with a consequent reduction of the antenna gain as losses increase (Fig. 3.16). It is interesting to notice that for $\varepsilon_r = 9$, there is a specific interval of loss tangents where a discontinuous behavior occurs, probably due to some numerical error.

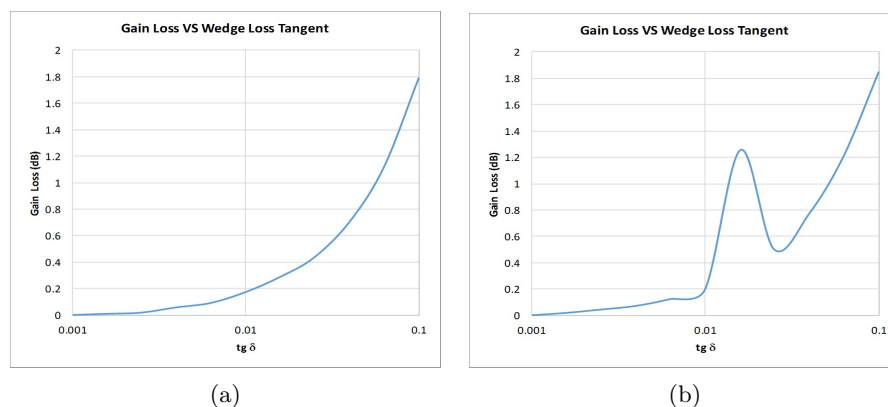


Figure 3.16: Gain loss with $\tan \delta$ ranging from 0.001 to 0.1 (Table 3.4). (a) $\varepsilon_r = 4$ and (b) $\varepsilon_r = 9$. The match layer is assumed to be lossless. The x-axis is on logarithmic scale.

3.4 Dual band coating

In the previous sections, a dielectric wedge was proved to deviate the beam produced by a flat-panel array antenna. The objective is to equip an azimuth-over-elevation mount antenna with a further beam squint functionality of $\pm 10^\circ$ about the antenna boresight in order to mitigate the keyhole problem. The wedge is capable of yielding a squint which approximates the function $(n - 1)\alpha$, where n and α are the wedge's index of refraction and tilt angle, respectively. Since the application is about satellite communications on-the-move (SOTM), where low-profile is a fundamental requirement, the dielectric superstrate should be as thin as possible. A way to reduce its footprint is by increasing its index of refraction or relative electric permittivity. For e.g., according to Eq. 3.3 on page 143, if $n = 3$, the achievable beam squint is

$$\theta \simeq 2\alpha$$

meaning that, a wedge tilt of only 5° is required to yield a beam squint of 10° . In principle, higher values of n will further reduce the wedge footprint. But, a value of $n = 3$ implies an $\varepsilon_r = 9$, which is already quite big. Moving to higher dielectric constants is possible, but dielectric constant tolerances reduce and losses normally increase. For this reason, this work has considered, for the moment, a wedge's ε_r of 9.

With such a high wedge's permittivity, it is important to introduce some

Table 3.5: BANDS OF INTEREST FOR THE SOTM ANTENNA UNDER STUDY.

Up-link		Down-link	
Center frequency f_0	Frequency band Δf	Center frequency f_0	Frequency band Δf
20 GHz	2 GHz	30 GHz	2 GHz

matching layers to reduce the reflections coming from the air-to-dielectric interfaces due to the presence of the wedge. In the previous sections, just for a demonstrative purpose, a mono-frequency match layer was designed. In that case, it was sufficient to only put a layer with permittivity and thickness given by Eq. 3.4 on page 144.

In this work, the system under study is intended to operate in two frequency bands, one for downlink and the other for uplink, whose frequency bands are reported in Table 3.5. There are two bands of interest: one is centered at 20 GHz and spans from 19 GHz to 21 GHz; the other is centered at 30 GHz and spans from 29 GHz to 31 GHz. Of course, the wedge should be reflectionless at both uplink and downlink frequency bands. A mono-layer matching is too narrowband to accommodate such a large frequency band from 19 GHz to 31 GHz. It is, then, more reasonable to pursue a design based on a dual-layer matching.

3.4.1 Design of the dual band coating

In this subsection, the design of a dual band coating for the waveguide antenna array based on a dielectric bowl sliding is presented. The dielectric bowl has an index of refraction equal to $n = \sqrt{\epsilon_r}$. The dielectric will be placed at a distance of about 1 mm (or a few millimeter) from the antenna aperture. This implies the reflectionless coating to be designed between air-to-wedge interface. If a simple quarter-wavelength coating were chosen, only zero reflectivity at a single frequency (and even multiples) would be possible. In the following discussion, we analyze whether it is possible to design a dual band coating by only using two quarter-wave dielectric slabs. Referring to Fig. 3.17a, let's assume that n_0 and n are the refraction indexes of the air and the lens respectively, and that n_1 and n_2 the refraction indexes of the two quarter-wave dielectric slabs. The problem will be tackled assuming

that on one side there is only air and on the other side of the interface there is only the dielectric lens, as shown in Fig. 3.17b; the coating is, naturally, interposed between air and lens. The two slabs are designed as quarter-wavelength at a frequency lying in between the two reflectionless frequencies. It has been proved [18] that the reflection coefficient of such coating is given by

$$\Gamma = \frac{\rho_0 + (\rho_1 + \rho_0\rho_1\rho_2)z^{-1} + \rho_2z^{-2}}{1 + (\rho_0\rho_1 + \rho_1\rho_2)z^{-1} + \rho_0\rho_3z^{-2}} \quad (3.7)$$

where ρ_i is the simple reflection coefficient of interface i and $z = \exp(j\pi f/f_0)$, with f_0 being the central frequency, equal to the arithmetic average of the two reflectionless frequencies f_1 and f_2 . We would like that $\Gamma = 0$ at our two frequencies f_1 and f_2 , so at $z_1^{-1} = e^{-j\pi f_1/f_0}$ and $z_2^{-1} = e^{-j\pi f_2/f_0}$. So, let's try to impose the nulling condition for Γ .

$$\Gamma = 0 \iff \frac{\rho_0}{\rho_2} + \frac{\rho_1 + \rho_0\rho_1\rho_2}{\rho_2}z^{-1} + z^{-2} = 0 \quad (3.8)$$

If we want Eq. 3.8 to have z_1 and z_2 as solutions, we have to impose the following conditions, from well-known mathematical second-order equations⁸:

$$\begin{cases} z_1^{-1}z_2^{-1} = \frac{\rho_0}{\rho_2} \\ z_1^{-1} + z_2^{-1} = -\frac{\rho_1 + \rho_0\rho_1\rho_2}{\rho_2} \end{cases} \quad (3.9)$$

⁸In a second-order equation of the kind $t^2 + bt + c = 0$, the roots t_1 and t_2 of the equation can be found by solving the system:

$$\begin{cases} t_1t_2 = c \\ t_1 + t_2 = -b \end{cases}$$

By solving the previous system, the well known formulas for the roots of the second-order equation are found:

$$t_1 = \frac{-b/2 + \sqrt{(b/2)^2 - 4c}}{2}$$

$$t_2 = \frac{-b/2 - \sqrt{(b/2)^2 - 4c}}{2}$$

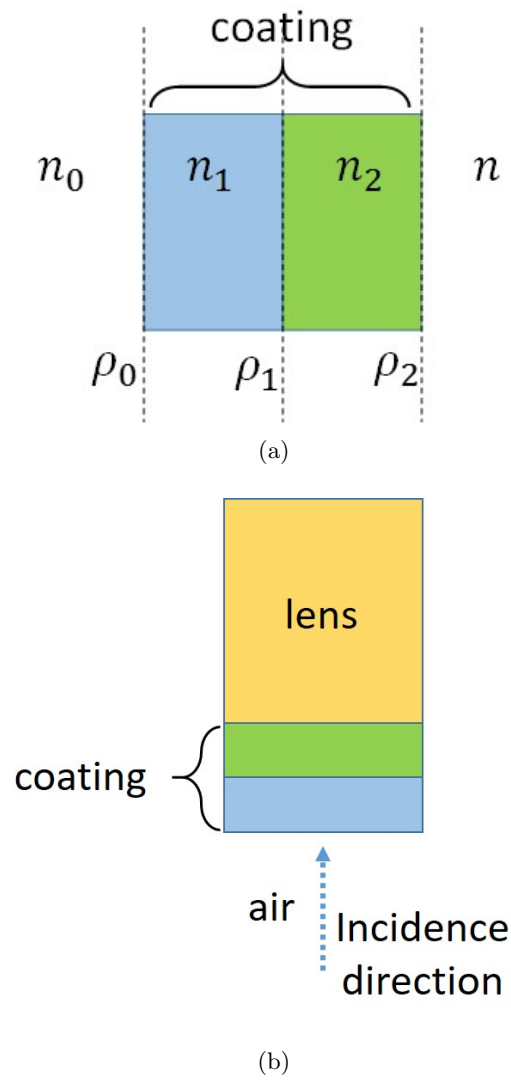


Figure 3.17: Coating using two dielectric slabs.

Now, writing the explicit form of z_1 and z_2 , we have:

$$\begin{cases} e^{-j\pi\left(\frac{f_1}{f_0} + \frac{f_2}{f_0}\right)} = \frac{\rho_0}{\rho_2} \\ e^{-j\pi\frac{f_1}{f_0}} + e^{-j\pi\frac{f_2}{f_0}} = -\frac{\rho_1 + \rho_0\rho_1\rho_2}{\rho_2} \end{cases} \quad (3.10)$$

Since the matching coating is supposed to gradually increase the permittivity to have matching between air and the wedge, we will have $1 < n_1 < n_2 < n$. This means that ρ_0 , ρ_1 , and ρ_2 are all negative reflection coefficients. This implies that

$$\frac{\rho_0}{\rho_2} > 0$$

Since all quantities on the right-hand side of the equalities of Eq. 3.10 are real, a first set of conditions to be satisfied a priori is:

$$\begin{cases} \pi\left(\frac{f_1}{f_0} + \frac{f_2}{f_0}\right) = 2\pi \\ -j\left[\sin\left(\pi\frac{f_1}{f_0}\right) + \sin\left(\pi\frac{f_2}{f_0}\right)\right] = 0 \end{cases} \quad (3.11)$$

The second condition imposes that the imaginary part of the left-hand side member of Eq. 3.10 is null. We immediately observe that the first condition of system 3.11 always holds as long as $f_0 = (f_1 + f_2)/2$, which is exactly our case. The second condition becomes, due to the properties of trigonometric functions:

$$\begin{aligned} \sin\left(\pi\frac{f_1}{f_0}\right) + \sin\left(\pi\frac{f_2}{f_0}\right) &= 2\sin\left(\pi\frac{f_1 + f_2}{2f_0}\right)\cos\left(\pi\frac{f_2 - f_1}{2f_0}\right) \\ &= 2\sin\pi\cos\left(\pi\frac{f_2 - f_1}{2f_0}\right) \\ &= 0 \end{aligned}$$

So, both conditions of 3.11 are satisfied. This is a good news, because it means that whatever frequency couple is chosen, a possibility to design a two-slab matching coating exists, provided that the slabs are quarter-wavelength at a frequency equal to the arithmetic mean between the two frequencies. In light of the previous results, conditions 3.10 become (neglecting the imaginary part of the second equation):

$$\begin{cases} 1 = \frac{\rho_0}{\rho_2} \\ \cos\left(\pi\frac{f_1}{f_0}\right) + \cos\left(\pi\frac{f_2}{f_0}\right) = -\frac{\rho_1 + \rho_0\rho_1\rho_2}{\rho_2} \end{cases} \quad (3.12)$$

Then, again, due to trigonometric properties:

$$\begin{aligned}\cos\left(\pi\frac{f_1}{f_0}\right) + \cos\left(\pi\frac{f_2}{f_0}\right) &= 2\cos\left(\pi\frac{f_1+f_2}{2f_0}\right)\cos\left(\pi\frac{f_2-f_1}{2f_0}\right) \\ &= 2\cos\pi\cos\left(\pi\frac{\Delta f}{2f_0}\right) \\ &= -2\cos\left(\pi\frac{\Delta f}{2f_0}\right)\end{aligned}$$

where Δf is the difference $f_2 - f_1$. Now, posing $\cos\left(\pi\frac{\Delta f}{2f_0}\right) = C$, a constant depending on the particular width of the frequency interval, Sys. 3.12 becomes:

$$\begin{cases} \rho_2 = \rho_0 \\ 2C\rho_2 = \rho_1 + \rho_0\rho_1\rho_2 \end{cases} \quad (3.13)$$

Remember that ρ_i is the simple reflection coefficient of i^{th} interface, so:

$$\begin{cases} \rho_0 = \frac{n_0 - n_1}{n_0 + n_1} \\ \rho_1 = \frac{n_1 - n_2}{n_1 + n_2} \\ \rho_2 = \frac{n_2 - n}{n_2 + n} \end{cases} \quad (3.14)$$

Substituting these relationships into 3.13 and following the mathematics shown in detail in Appendix B, we can find the solution for n_1 and n_2 , as reported in Table 3.6: An interesting aspect of this analysis is that the dual-band coating has been defined by means of a totally analytical procedure, finding the formulas that define the dielectric constants and the thickness of the two layers composing the coating.

Table 3.6: ANALYTICAL EXPRESSIONS FOR THE DUAL-BAND-COATING SLABS.

Parameter	Expression
n_1	$\sqrt{\frac{(1-C)n_0(n-n_0) + \sqrt{[(C-1)n_0(n-n_0)]^2 + 4(C+1)^2nn_0^3}}{2(C+1)}}$
n_2	$\frac{nn_0}{n_1}$
d_1	$\frac{c}{4n_1f_0}$
d_2	$\frac{c}{4n_2f_0}$
C	$\frac{f_2 - f_1}{2f_0}$
f_0	$\frac{f_1 + f_2}{2}$
f_1	Up-link centre freq. (Tab. 3.5)
f_2	Down-link centre freq. (Tab. 3.5)
n_0	Index of refr. of air (Fig. 3.17)
n	Index of refr. of the wedge (Fig 3.17)
c	Speed of light constant

Table 3.7: Design Specs (Example 1).

f_1	f_2	f_0	n_0	n
20 GHz	30 GHz	25 GHz	1	3

Table 3.8: Calculated parameters (Example 1).

n_1	n_2	d_1	d_2
1.36	2.21	2.21 mm	1.36 mm

3.4.2 Application of the theory to practical cases

In this section, we show some practical cases to design a dual band reflectionless coating. We would like, for instance, to design a coating to match the interface between air ($n_0 = 1$) and a dielectric medium ($n = 3$), called *Example 1*. The dielectric medium is assumed to extend indefinitely to the right-hand side, while the electromagnetic wave is travelling from left to right, from air toward the dielectric.

The method described in Sec. 3.4 provides two formulas for calculating the refraction indexes of the two quarter-wave layers constituting the reflectionless coating. With the aid of Table 3.6, we can go through the following steps:

1. Use the equation for n_1 to calculate the refraction index of the layer 1 (Fig. 3.17);
2. plug n_1 into the equation for n_2 to get the index of the layer 2;
3. use n_1 and n_2 to calculate the thickness of the quarter-wave layers d_1 and d_2 .

In this example, the input data is presented in Table 3.7, with $f_0 = (f_1 + f_2)/2$ being the design frequency of the quarter-wave layers. The output data, calculated according to the analytical procedure summarized in Table 3.6, is presented in Table 3.8. We shall consider now another practical case, called *Example 2*, with a different refraction index of the dielectric medium $n = 2$. The problem is again to design two matching layers composing a dual-band coating which has to make the air-to-dielectric interface reflectionless at the specified frequencies f_1 and f_2 , shown in Table 3.9.

Table 3.9: Design Specs (Example 2).

f_1	f_2	f_0	n_0	n
20 GHz	30 GHz	25 GHz	1	2

Table 3.10: Calculated parameters (Example 2).

n_1	n_2	d_1	d_2
1.21	1.65	2.48 mm	1.82 mm

By applying again the formulas devised in Sec. 3.4 and summarized in Table 3.6, it is possible to re-calculate the electrical and geometrical parameters of coating layer 1 and layer 2, as shown in Table 3.10. A plot of the reflection coefficients for Example 1 and 2, obtained by using the values provided in the Tables 3.8 and 3.10, is shown in Figs. 3.18 and 3.18, respectively. Interestingly, the reflection coefficient not only becomes null at the two design frequencies (20 GHz and 30 GHz), but it also stays more or less below -25 dB for the whole frequency band. So, in this specific case, what was born as a dual-band coating actually behaves as a wide-band coating. Naturally, we expect that by increasing the permittivity of the dielectric medium, the level of reflection coefficient will increase, as well. It is possible to appreciate from Figs. 3.18 and 3.18 that the matching coating has a dual band behavior, with deep nulls (zeros) centered at the two specified frequencies. These results confirm the theoretical formulas presented in Table 3.6.

3.4.3 Double-coated medium

The theory and results presented in the previous subsections were only based on matching layers designed for the particular case where there is air on one side and the dielectric medium on the other side. Actually, the real system consists in a dielectric material which is confined in a certain region, so that there is air in one side and air again in the other side of the medium. The electromagnetic wave propagation starts in air, crosses an air-to-dielectric interface, crosses again a dielectric-to-air interface, and finishes back in air. If only the first interface is coated for matching, the wave passes through that interface without any reflection; but as the wave impinges on the second (uncoated) interface, it encounters an unmatched interface which causes a

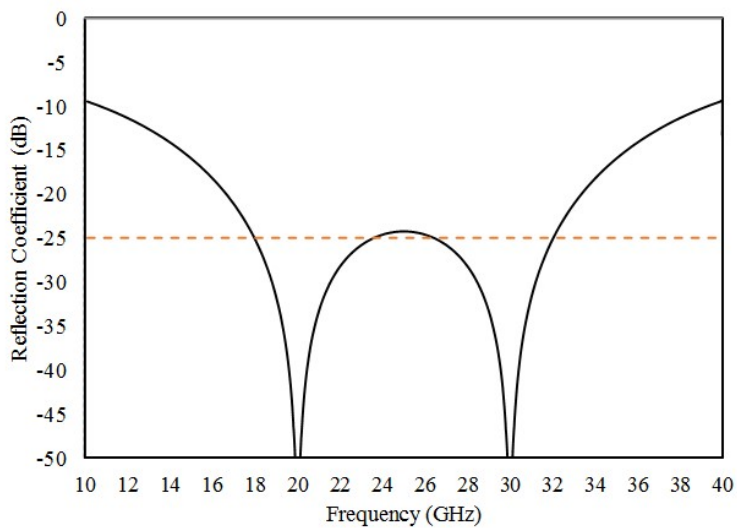


Figure 3.18: Example 1. Reflection coefficient after application of the designed coating.

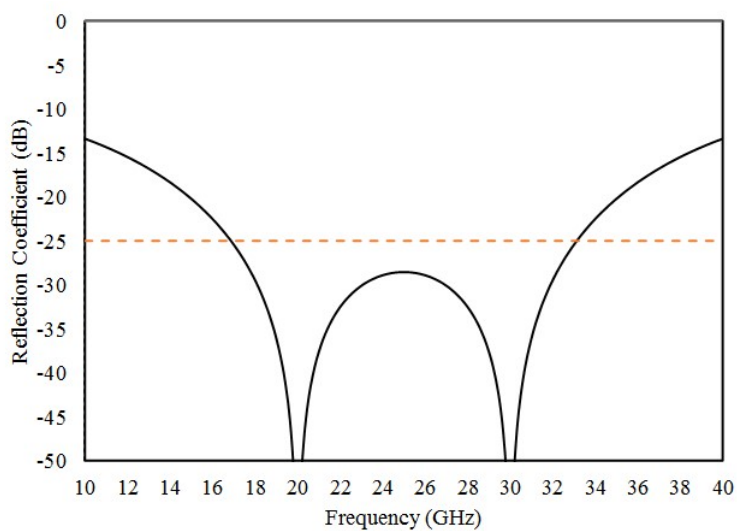


Figure 3.19: Example 2. Reflection coefficient after application of the designed coating.

back reflection.

The reflection-less coating must be, therefore, placed at both sides of the dielectric medium, so that both interfaces between air and medium are matched. The system so obtained can be studied with the transmission matrix theory as a cascade of multiple dielectric layers [19]. In particular, let $[A_n]$ be the 2 by 2 transmission matrix associated with a certain layer in a cascade. The expressions of its elements are:

$$a_n(1, 1) = a_n(2, 2) = \cos(k_n d_n) \quad (3.15)$$

$$a_n(1, 2) = j\eta_n \sin(k_n d_n) \quad (3.16)$$

$$a_n(2, 1) = j \frac{1}{\eta_n} \sin(k_n d_n) \quad (3.17)$$

where d_n is the thickness of the n-th layer, while the wave number k_n and the wave impedance η_n are expressed by:

$$k_n = \beta_n - j\alpha_n \quad (3.18)$$

$$\eta_n = \frac{\eta_0}{\sqrt{\varepsilon'_n}} \quad (3.19)$$

where $\eta_0 \simeq 377 \Omega$ is the wave impedance in vacuum, ε'_n the relative electric permittivity (real part) of the n-th layer, and the phase constant β_n as well as the attenuation constant α_n are expressed by:

$$\beta_n = \frac{2\pi f}{c} \sqrt{\varepsilon'_n} \quad (3.20)$$

$$\alpha_n = \beta_n \frac{\theta_e}{2} \quad (3.21)$$

with f the frequency, c the speed of light constant, and θ_e the dielectric loss angle⁹. The overall transmission matrix of N cascaded layers (Fig. 3.20) is simply the cascade of all single-layer matrices (matrix multiplication):

$$[A_{tot}] = [A_1] \times [A_2] \times \cdots \times [A_N] \quad (3.22)$$

From the elements of a transmission matrix, the reflection and transmission coefficients R and T are retrieved according to [19]:

$$R = \frac{a_{11}\eta_{rt} + a_{12} - \eta_f(\eta_{rt}a_{21} + a_{22})}{a_{11}\eta_{rt} + a_{12} + \eta_f(\eta_{rt}a_{21} + a_{22})} \quad (3.23)$$

⁹Losses in dielectric media are usually described by the loss tangent, $\tan \delta$, where $\delta \equiv \theta_e$.

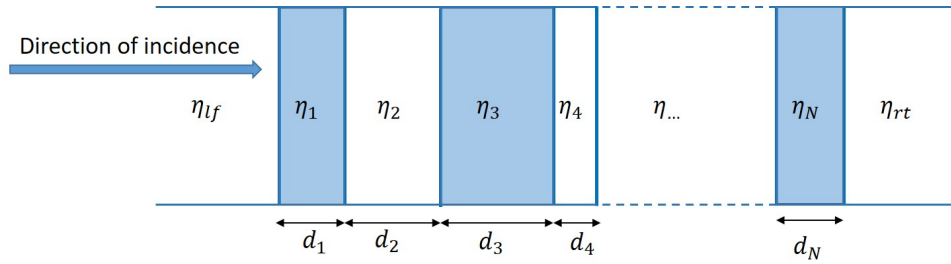


Figure 3.20: Cascade of N dielectric media.

$$T = \frac{2\eta_{rt}}{a_{11}\eta_{rt} + a_{12} + \eta_{lf}(\eta_{rt}a_{21} + a_{22})} \quad (3.24)$$

where η_{lf} and η_{rt} are the wave impedances of the materials on the left-hand and the right-hand side of the multi-layer cascade.

An interesting property of a cascade of homogeneous isotropic media is the reciprocity property of the cascade, i.e. the magnitude of the reflection and transmission coefficients of the cascade does not change if the direction of incidence is reversed. This property is extremely useful to match dielectric slabs. In our case, indeed, we have a dielectric medium immersed in air. Then, to fully match it, it is sufficient to take the coating used on the first interface (air-to-dielectric), reverse the order of the matching layers and replicate it on the second interface (dielectric-to-air).

Analysis of the dual-band coating with transmission matrices

As shown in Fig. 3.21a, the dual-band coating is replicated twice both at the bottom and at the top of the dielectric medium, to ensure a dual-frequency matching at both air-to-dielectric and dielectric-to-air interfaces. Please, notice that here the dielectric medium does not have a wedge-shape, apparently in contrast with our design (Fig. 3.6). But bear in mind that the wedge is a complex geometrical shape to be analyzed by means of analytical tools. However, since the wedge tilt angle is very small, the two interfaces are nearly parallel, leading to very small incidence angles at each interface. Furthermore, it is expected from experience that an anti-reflection coating designed for a certain incidence angle θ_i shows a similar performance for a range of angles of $\pm 30^\circ$ about θ_i [18]. Thus, it is reasonable to tackle the problem by studying the wedge anti-reflection coating as a normal incidence problem. The reflection coefficient computed according to the transmission

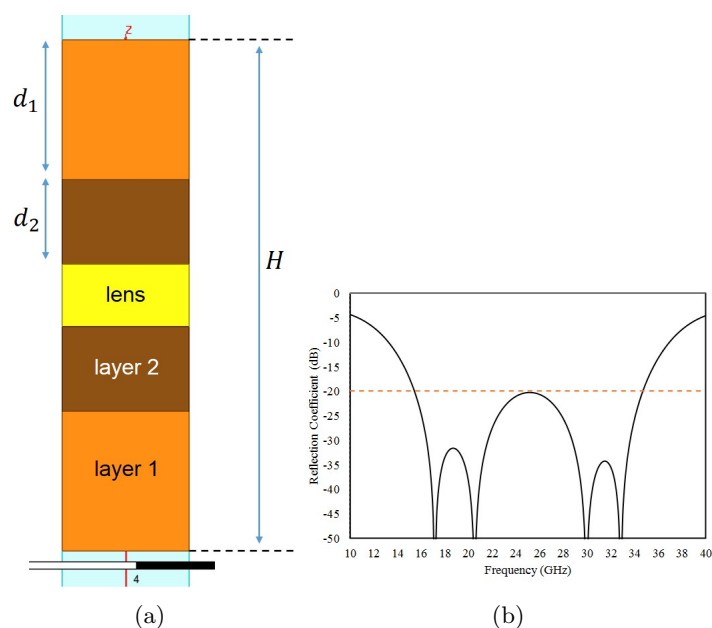


Figure 3.21: (a) CAD model of the lens with double coating (at the two sides); (b) MATLAB simulation of the two-side coating of the lens.

matrices is reported in Fig. 3.21b. From a comparison of Fig. 3.21b with previous MATLAB simulations considering only a one-side coating, some difference can be appreciated. In particular, 2 additional zeroes (one at 17 GHz and the other at 33 GHz) occur. Their appearance is directly related to the lens thickness. Matlab simulations revealed that the thicker the lens is the more zeroes turn up but the depth and position of the zeros at the desired frequencies are the same as the one-side-coating. For sake of clarity, Fig. 3.22 shows the reflection coefficient in case of infinite-size lens with one-side coating (Fig. 3.17b) and in case of finite-size lens with double-side coating (Fig. 3.21b). Of course, a very thick lens compared with the wavelength becomes equivalent to an infinite lens taking up all the volume on one side, making the reflection coefficient identical to the one-side-coating case.

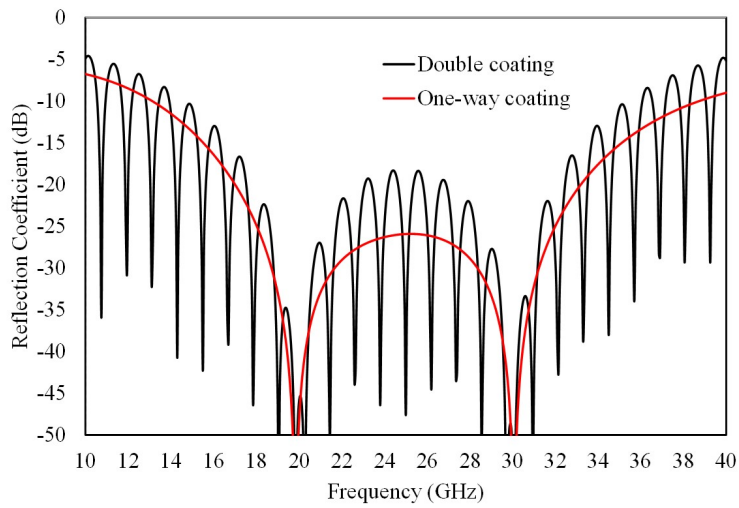


Figure 3.22: Amplitude of the reflection coefficient (dB) in case of infinitely long medium with one-side coating on the air-to-dielectric interface (red curve) and in case of finite medium thickness with double coating on both air-dielectric-air interfaces (black curve).

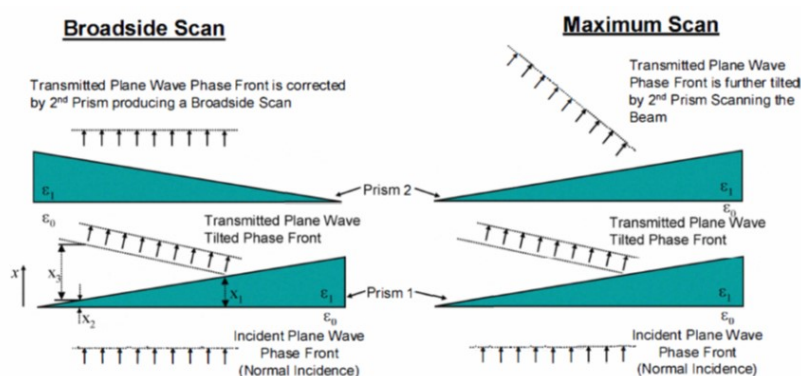


Figure 3.23: Qualitative description of the mechanism behind Risley-prisms-based scanning [20].

3.5 Scanning architecture based on Risley prisms

We have previously described a scanning antenna system based on a dielectric bowl sliding equivalent to a dielectric wedge that is tilted in elevation and rotated in azimuth. From a mechanical standpoint, the dielectric bowl sliding mechanism is not so trivial, requiring some *ad-hoc*-designed actuators. Another possibility to implement a dielectric-refraction-based beam scan is given by the so called Risley prisms [20], [21]. Instead of one wedge, two wedges are necessary to actuate the Risley scanning strategy, with a wedge rotating in the azimuth direction relative to the other one and the two wedges capable of jointly rotating in azimuth. The system is depicted in Fig. 3.23 picked from 3.5 and will be investigated in the framework of our SOTM¹⁰ antenna. The relative wedge rotation yields a beam squint in elevation (also causing a spurious azimuth scan), while the joint rotation yields a squint in azimuth (which can compensate for the spurious azimuth scan). This scan mechanism has been fully investigated [20] and analytical formulas have been found to calculate the $\theta\phi$ angles as functions of the relative and joint wedge rotations (Fig. 3.24).

3.5.1 Normal incidence analysis

Since Risley scanning mechanism is based on two identical wedges, the required number of reflectionless coatings is 4: 2 for the top and bottom of the first wedge, and 2 for the second wedge. In the Example 2 of Sec. 3.4,

¹⁰Satellite communications on-the-move.

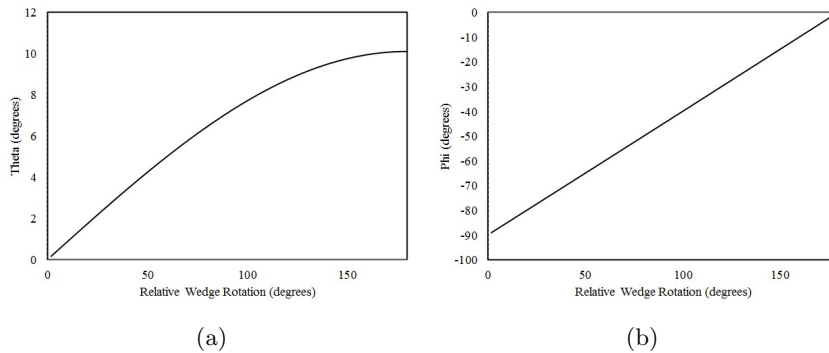


Figure 3.24: Connection between the relative wedge rotation and the elevation (a) and azimuth (b) scan.

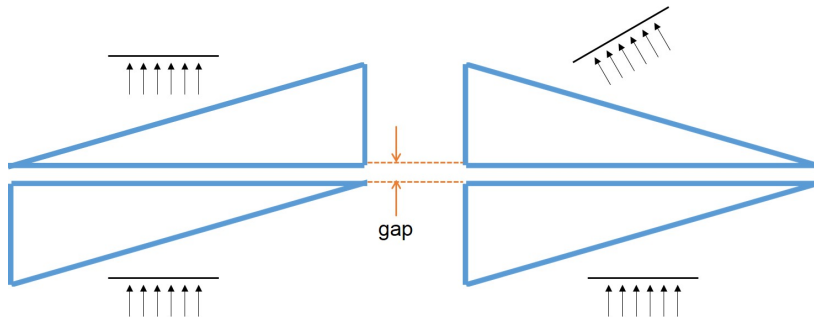


Figure 3.25: Qualitative description of the mechanism behind upside-down Risley-prisms.

each coating was about 3.5-mm thick. Having to place 4 coatings leads to an overall thickness of 14 mm which is only used for matching! Another possibility to reduce the number of coatings is to turn the lower wedge upside down and let their horizontal interfaces to touch, as illustrated in Fig. 3.25. We may call them *up-down Risley Prisms* or up-down RP.

Effect of the gap and lens thickness

Of course, in reality, the wedges cannot touch because they have to rotate one relative to the other, so some gap (possibly filled with a friction-less gel or compressed air) has to be left to allow the two interfaces to slide all round. The operation of the up-down RPs is pretty analogous to the standard Risley prisms, but, in contrast to those ones, they only need 2 coatings for matching.

The analysis of the up-down RPs can be carried out having recourse to the transmission matrices, including the effect of the gap. For the moment, the gap is supposed to be filled with air and its thickness is supposed to be much thinner than the wavelength. Under the assumption of infinitely thin gap, no difference can be seen in the reflection coefficient; but, as the gap thickness starts increasing and becomes comparable with the wavelength, the behavior of the reflection coefficient is expected to get altered.

As proof of these expectations, Fig. 3.26 shows the effect on the reflection coefficient of the air gap at different lens thicknesses. In the same figure, the effect of the lens thickness is also depicted. It is evident that both the lens thickness and the gap height affect the reflection coefficient. In general, we can say that the lens thickness (reading from up to down the column, in Fig. 3.26) does not change the zeroes located at the two reflection-less frequencies (in the example, 20 and 30 GHz) and does not increase the maximum level of the reflection coefficient within the two design frequencies. The gap height, instead, modifies the shape of the curve and shifts the position of the zeroes off the design frequencies (as can be seen by reading left to right along each row in Fig. 3.26). Interestingly, we cannot say that the increase of the gap height worsens the reflection coefficient in any case. In fact, curves (j) to (l), where lens thickness is 4 mm, in Fig.3.26, are clearly much better than curves (g) to (i), where lens thickness is 3 mm, and comparable in quality with curves (a) to (c), where lens thickness is 1 mm! Having said that, the gap height is expected to be not controllable because the two wedges of the Risley configuration will be put in direct contact for sliding on each other. As a consequence, it is necessary to make that gap short enough so that the reflection coefficient of the structure becomes unaffected by its presence.

3.5.2 Oblique Incidence Analysis

In the Subsec. 3.5.1, the performance of a matching coating was investigated by making use of the available theory of propagation matrices applied on multi-layer coatings. The important thing to bear in mind is that such formulation applies to normal incidence only. But what happens if the incidence angle is different from zero? Practice evidence shows that within a limited range of incident angles (say less than 30°), no re-design is required in that the reflection coefficient does not get so much altered. But, near and above 30°-angle incidence, a re-optimization may be necessary to restore the shape of the reflection coefficient. An all-angle optimization seems to be impossible for the system under study (two-layer coating). What is possible to do is to optimize the system to work at some angle lying in between the maximum and the minimum incident angle, hoping such design to be good for the whole angle range. For instance, if the incidence angle spans the range from 0° to 40°, what may be reasonable is to optimize the coating at 20°, so as to maintain an acceptable performance even at 0° and 40°.

We are now considering our system as depicted in Fig. 3.21a at **oblique incidence**. The rigorous theory aiding this analysis is well presented in [18], where a recursive formula of the reflection coefficient of a multi-layer film is presented for the two main components of the electric and magnetic fields, called TM and TE polarizations¹¹. In particular, for a coating with M layers, as depicted in Fig. 3.27, a and b denote the two extreme media to be matched, θ_i the direction of incident propagation in the layer i , with $i = a, 1, 2, \dots, M, b$, l_i the thickness of layer i , then the reflection coefficient can be obtained as:

$$\Gamma_i = \frac{\rho_i + \Gamma_{i+1}e^{-2j\delta_i}}{1 + \rho_i\Gamma_{i+1}e^{-2j\delta_i}}, \quad i = M, M-1, \dots, 1 \quad (3.25)$$

where

$$\delta_i = \frac{2\pi}{\lambda} n_i l_i \cos \theta_i$$

$$\rho_i = \frac{n_{T,i-1} - n_{Ti}}{n_{T,i-1} + n_{Ti}}, \quad i = 1, 2, \dots, M+1$$

¹¹We remind that for oblique incidence the electric field is conveniently decomposed into two polarizations (both orthogonal to each other and to the direction of propagation of the wave), where one is parallel to the plane of incidence, and is called TE (or *parallel*) polarization, while the other is orthogonal to the plane of incidence, and is called TM (or, for convenience, *perpendicular*) polarization.

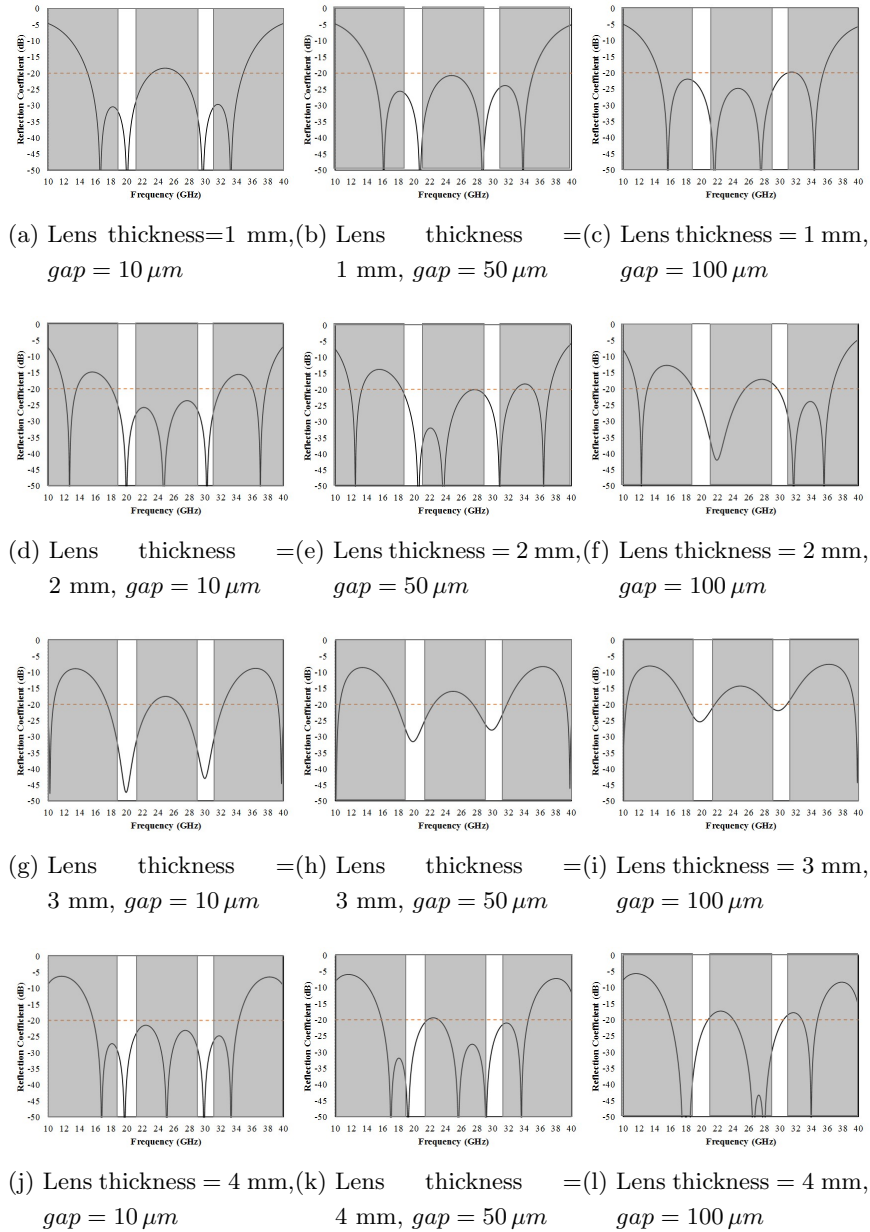


Figure 3.26: Reflection coefficient (S_{11}) under the assumption of normal incidence. Each column represents a specific lens thickness, which is changed from 1 to 4 mm. Each row shows the effect of varying the gap height from 10 to 100 μm .

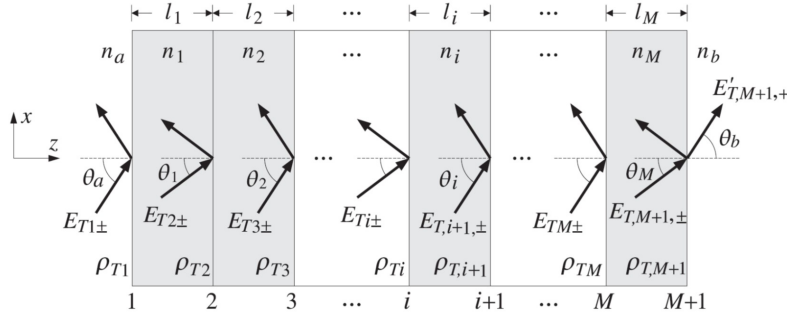


Figure 3.27: Oblique incidence on multilayer dielectric structure (courtesy of [18]).

Table 3.11: Lens coating parameters for normal incidence and oblique incidence.

	Normal Incidence	Oblique Incidence	
		Unoptimized	Optimized
n_1	2.21	2.21	2.24
n_2	1.36	1.36	1.33
d_1 (mm)	1.36	1.36	1.43
d_2 (mm)	2.21	2.21	2.32

$$n_{Ti} = \begin{cases} \frac{n_i}{\cos \theta_i}, & \text{TM polarization} \\ n_i \cos \theta_i, & \text{TE polarization} \end{cases}, \quad i = a, 1, 2, \dots, M, b$$

and Γ_{M+1} is initialized to ρ_{M+1} . Fig. 3.28 shows the plot of the reflection coefficient referred to Example 1 of Table 3.8 in the case of 30° -incidence angle (dashed line). After a re-design of the coating, the new modified layer parameters are reported in Table 3.11 and the related reflection coefficient is shown on the black continuous line of Fig. 3.28. Please notice that this picture refers to the one-way coating (Fig. 3.17b), assuming that after the coating, the rest of space is occupied by the lens. When the real system is analyzed, considering a double-side coating, as depicted in Fig.3.21a, the reflection coefficient changes in shape. For instance, for a lens thickness of 1 mm, the same reflection coefficients as Fig. 3.28 takes the shape illustrated in Fig. 3.29.

We may observe two deep zeroes at around 15 and 35 GHz in contrast to the two zeroes of Fig. 3.28. The explanation to this deviation is the effect of the finite lens thickness which, we remind, introduces additional zeroes at frequencies other than the design ones. In addition, some signifi-

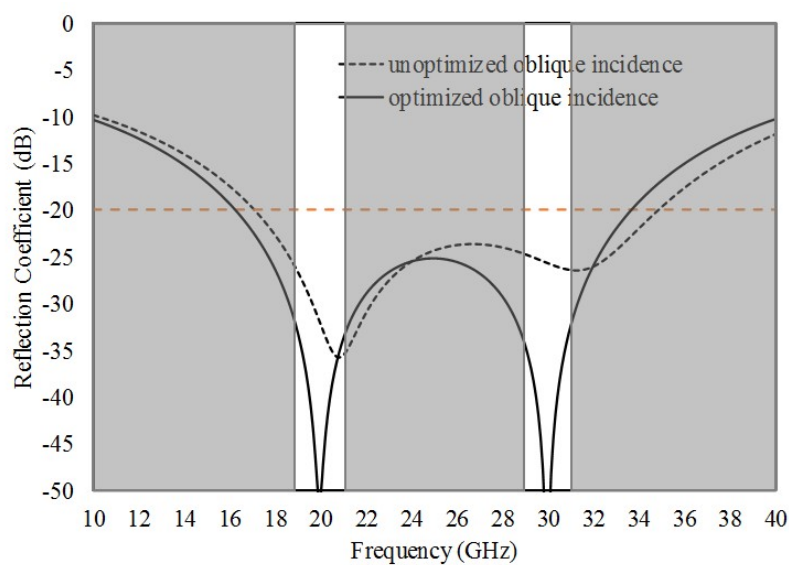


Figure 3.28: Reflection coefficient referred to Example 1 of Table 3.8 in the case of oblique incidence at 30° with no re-design (black dashed line) and with re-design (black continuous line). The reflection coefficient for normal incidence was illustrated in Fig. 3.19. Please notice that this picture refers to the one-way coating, assuming that after the coating, the rest of space is occupied by the lens.

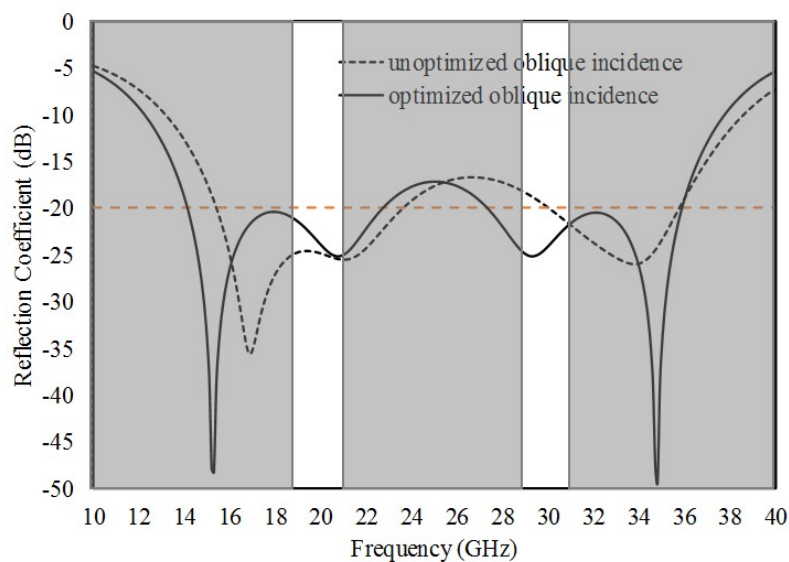


Figure 3.29: Reflection coefficient referred to Fig.3.28 assuming the realistic case of a double-coated lens (Fig. 3.21a) with 1 mm thickness.

cant changes in the reflection coefficient of the double-coated lens have been detected, meaning that further optimization will be required. It would be interesting to analyze these effects by running some HFSS simulations, as well. The problem of the finite lens thickness is not negligible. In fact, considering the two lenses of Fig. 3.25, the equivalent lens thickness in the right-hand-side picture modifies through the different vertical sections. This poses a serious problem if the matching coatings have a large performance variability depending on the lens thickness. So, the best situation would be that matching performance stays the same when changing the lens thickness parameter. In the next section, the dielectric superstrate will be actually designed and its size will be adapted to the size of the given array antenna. Then, some incidence analyses will be performed on the realistic system to assess the effect of several design parameters on the reflection coefficient.

3.6 Analysis of a realistic up-down Risley prism system

In this section, the actual array antenna size will be considered and the dielectric superstrate based on an up-down Risley prism (RP) configuration will be evaluated, accordingly. The relative permittivity ε' of the wedge dielectric was chosen to be 9, providing a refraction index n of 3, according to Example 1 of Subsec. 3.4.2. In this case, the computed refraction indexes and thicknesses of the layers composing the anti-reflection coating were reported in Table 3.8. A top view of the antenna footprint is depicted in Fig. 3.30a. Let's first consider the single-wedge topology, as shown in Fig. 3.30b, in order to make a comparison of the overall space taken by the single-wedge and the two-wedge (Risley) configurations. Looking at Fig. 3.30b, the diameter of the wedge (without considering the coatings) required to cover the whole antenna surface is equal to the antenna diagonal $L = 417$ mm. Thus, as seen in the lateral view of Fig. 3.30b, the wedge height, given its tilt angle α , is, from Eq. 3.6:

$$h = L \tan \alpha \simeq 37 \text{ mm}$$

where $\alpha = 5^\circ$ was calculated according to Eq. 3.5, using $n = 3$ and $\theta = 10^\circ$ ¹². If the up-down RP topology is now considered, as shown in Fig. 3.30c, the overall height seems to double. Actually, this is not true, because in a Risley

¹²Remember that θ is the desired beam squint, which for our system equals 10° .

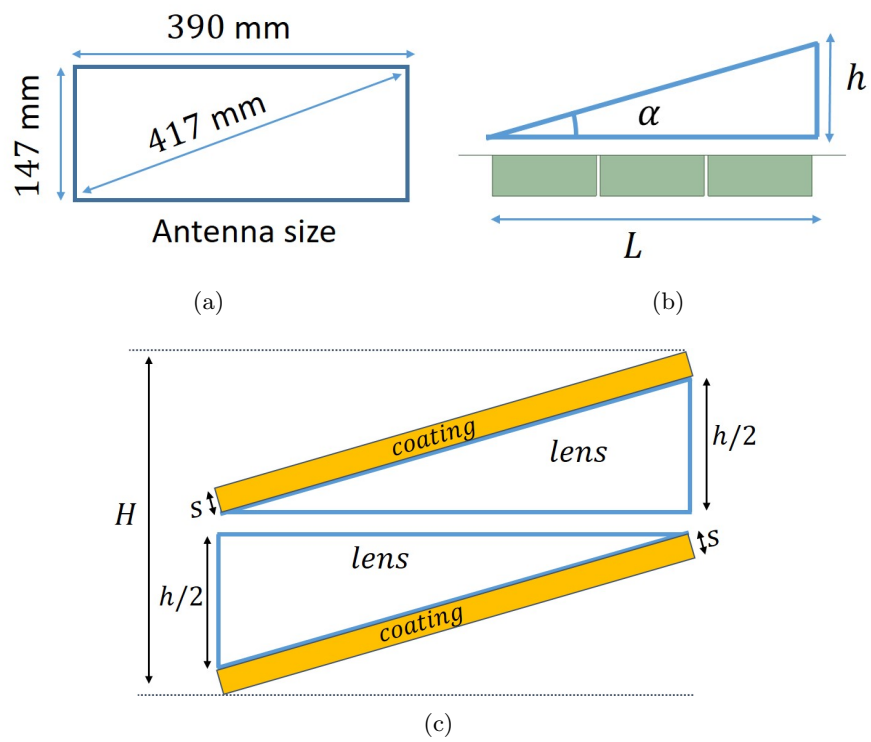


Figure 3.30: (a) Top view of the array antenna footprint; (b) side view of the antenna with single wedge configuration; and (c) side view of the up-down RP configuration.

configuration, the propagating wave experiences a double deviation, a first one due to the lower wedge and a second one due to the upper wedge. As a consequence, the tilt angle of each prism can be halved. This means that if 10°-beam squint is achieved by using a single wedge with tilt angle α , the same beam squint can be obtained by using a Risley topology with each prism tilt angle equal to $\alpha/2$. Now, looking at Fig. 3.30c, since each prism tilt angle is $\alpha/2$, the height of each prism is (provided that α is small):

$$L \tan(\alpha/2) \simeq L\alpha/2 = h/2$$

As far as the coating is concerned, as reported in Table 3.8, the thickness s of the coating, given by the sum of the two layers' thicknesses, is about 3.6 mm. So, the height of the up-down RP configuration of Fig. 3.30c is:

$$H = h + 2s = 37 + 2 \times 3.6 \sim 45 \text{ mm}$$

To summarize, the height of the dielectric medium composing the two prisms is on the order of 40 mm, while the addition of the anti-reflection coatings on the top and bottom of the structure increases the size by 7.2 mm, which is roughly 15% of the total height, not a big issue considering the precious function they play. Table 3.12 compares the single-wedge topology with the Risley one. As you can appreciate, although there is a difference in the tilt angle and height of each single wedge, the overall height of the structure adding the coatings remains, in principle, the same. The dielectric superstrate under analysis is intended to provide the antenna array with a further 10° maximum beam squint. According to Eq. 3.5 and Table 3.12, the required tilt angle for each wedge is about 2.5°. With such a small value of α , the incidence angles at the various interfaces that the wave experiences while it propagates through the whole structure are expected to be small as well. Indeed, in the best situation, when the two wedges are oriented like in Fig. 3.31a (this wedge relative orientation gives no beam squint with respect to the vertical line, so $\theta = \text{ang}0$), the incidence angle at the lower interface is $\beta_1 = \alpha = 2.5^\circ$, the incidence angle at the upper interface is $\beta_2 = \alpha = 2.5^\circ$, so the maximum incidence angle with respect to the normal to each interface is, in the best case, 2.5°. In the worst situation, when the two wedges are oriented like in Fig. 3.31b (this wedge relative orientation gives max beam squint with respect to the vertical line, so $\theta = \text{ang}10$), the incidence angle at the lower interface is $\beta_1 = \alpha = 2.5^\circ$, while the incidence angle at the

Table 3.12: Comparison between single-wedge and Risley topology.

Specifications	Coating parameters	Topology	Dimensions
Reflectionless frequencies: 20 GHz and 30 GHz ***	Layer 1 $n_1 = 1.36, d_1 = 2.21$ mm ***	Single-wedge	$L = 417$ mm $\alpha \simeq 5^\circ$ $h \sim 37$ mm $s \simeq 3.6$ mm (each coating) $H \sim 45$ mm (total)
Max beam squint $\theta = 10^\circ$ ***	Layer 2 $n_2 = 2.21, d_2 = 1.36$ mm		
Lens permittivity and refraction index $n = 3, \epsilon' = 9$		Risley	$L = 417$ mm $\alpha \simeq 2.5^\circ$ (each wedge) $h \sim 18.5$ mm (each wedge) $s \simeq 3.6$ mm (each coating) $H \sim 45$ mm (total)

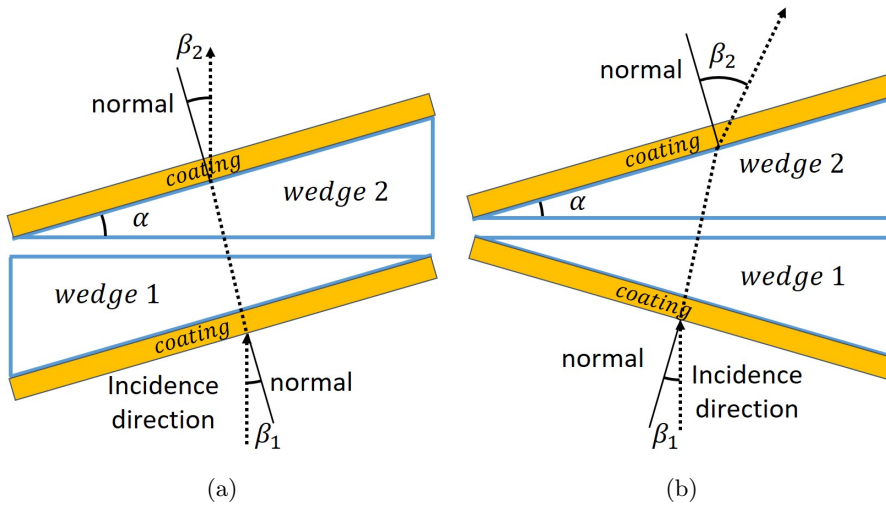


Figure 3.31: Up-down RP configuration. Expected path of the incident wave while it crosses the various interfaces of the structure, in the best case (a), with no beam squint with respect to the vertical line, and in the worst case (b), with maximum beam squint.

upper interface is $\beta_2 = \alpha + \theta = 12.5^\circ$, so the maximum incidence angle with respect to the normal to each interface is, in the worst case, 12.5° . In light of the previous considerations on the maximum incidence angle, to somehow have a clue on the performance of the system during best and worst case, it is reasonable to analyze the structure under the assumption of parallel interfaces¹³ in two different cases: normal and oblique incidence.

In the following subsections, the superstrate presented here will be simulated on MATLAB exploiting the transmission matrix methodology to see the effect of several factors on the reflection coefficient, for normal incidence and oblique incidence. The thickness of the wedge region ($n = 3$) is set to be 40 mm, a realistic one.

¹³In the designed up-down RP structure, all interfaces are not exactly parallel, but, because of the small involved incidence angles, they could be considered as nearly parallel.

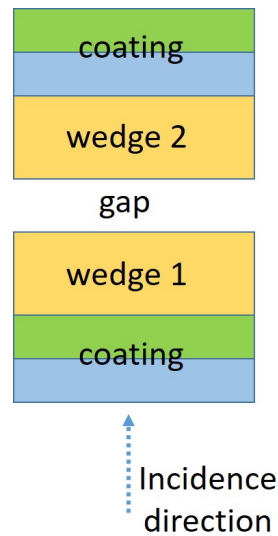


Figure 3.32: Parallel-interface structure in case of normal incidence.

3.6.1 Normal incidence

In this subsection, the reflection coefficient of the up-down Risley Prism structure (Fig. 3.30c) with dual band coating will be analyzed, under the assumption of normal incidence and parallel interfaces (Fig. 3.32), by varying two parameters:

- Gap permittivity, which is the relative electric permittivity of the material separating the two prisms (or wedges) that are put in contact to slide around.
- Gap thickness, which, as said previously, may have a detrimental impact on the reflection coefficient.

As said previously, this normal incidence analysis should provide some clues on the performance of the up-down RP superstrate in the best case of Fig. 3.31a, where the max incidence angle is very small, i.e. 2.5° .

Fig. 3.33 to Fig. 3.38 show the reflection coefficient at different fixed gap permittivities ($\epsilon'_{\text{gap}} = 1, 2, 4, 6, 8, 9$) by varying the gap thickness from $10 \mu\text{m}$ to $500 \mu\text{m}$. Each set of plots presents a variation of the gap thickness increasing while moving from plots (a) to (e).

As it is possible to notice from Fig. 3.33 to Fig. 3.38 is that if the gap thickness increases, the reflection coefficient at the bands of interest (the

bands of no interest are covered by grey boxes, so those ones of interest are within the blank spaces) becomes worse, becoming unacceptable for values as large as 200 or 500 μm . Instead, as the gap permittivity increases from 1 to 9, it is possible to see an improvement of the reflection coefficient, with the best result obtained for $\varepsilon'_{\text{gap}} = 9$. This should not surprise, since when the gap permittivity equals the lens permittivity, the gap does not introduce any discontinuity.

$\epsilon'_{\text{gap}} = 1$ by varying gap thickness

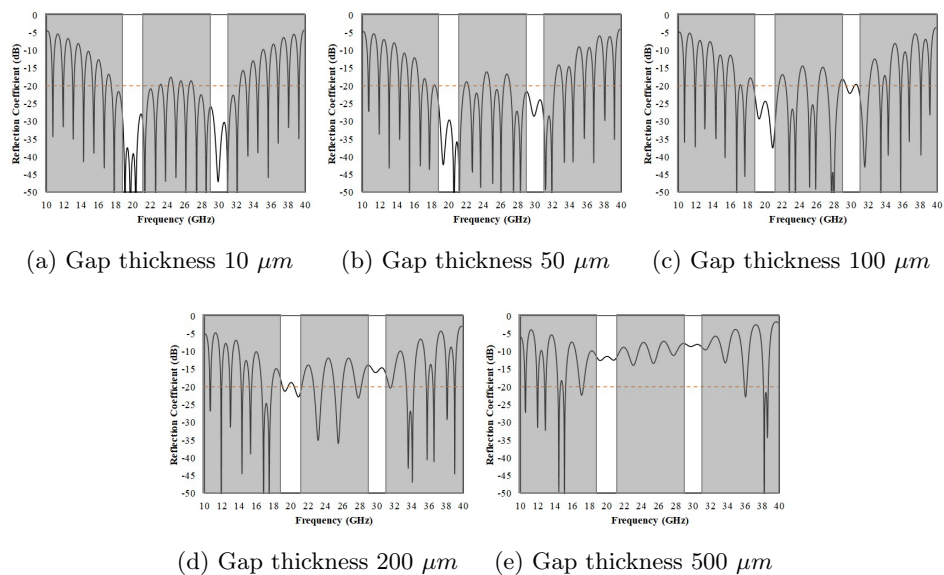


Figure 3.33: Reflection coefficient (S_{11}) under the assumption of normal incidence for the structure depicted in Fig. 3.32. The gap thickness is varied from 10 to $500 \mu\text{m}$, while the gap relative electric permittivity is fixed to 1.

$\epsilon'_{\text{gap}} = 2$ by varying gap thickness

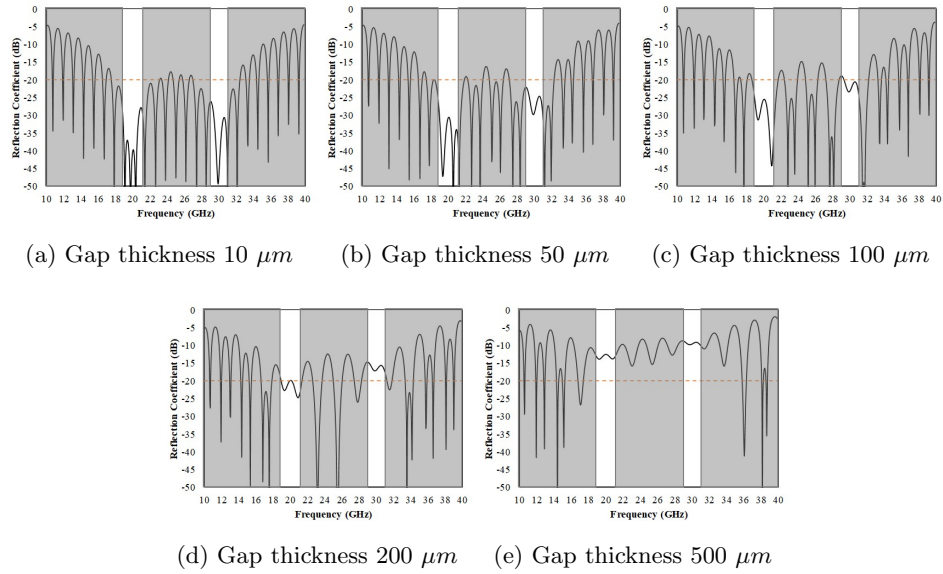


Figure 3.34: Reflection coefficient (S_{11}) under the assumption of normal incidence for the structure depicted in Fig. 3.32. The gap thickness is varied from 10 to 500 μm , while the gap relative electric permittivity is fixed to 2.

$\epsilon'_{\text{gap}} = 4$ by varying gap thickness

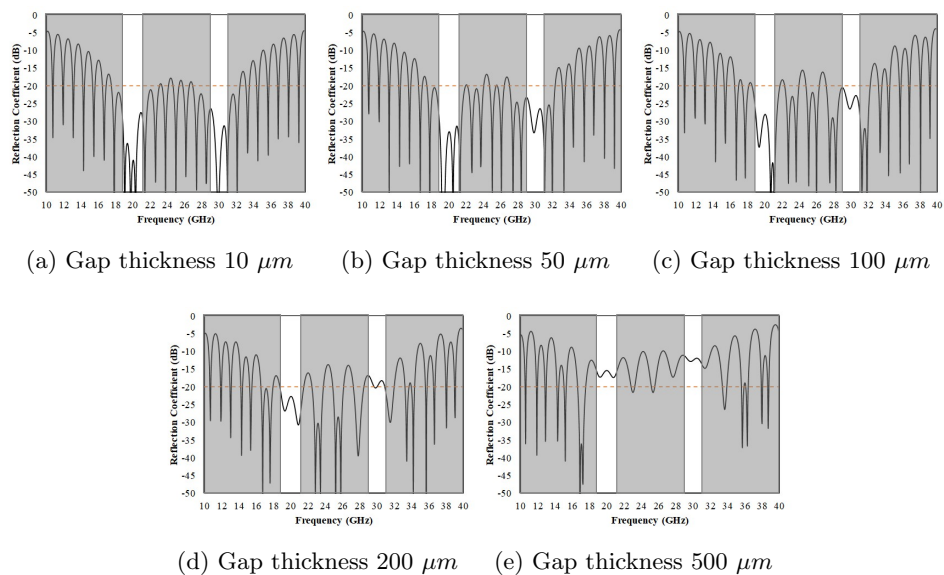


Figure 3.35: Reflection coefficient (S_{11}) under the assumption of normal incidence for the structure depicted in Fig. 3.32. The gap thickness is varied from 10 to $500 \mu m$, while the gap relative electric permittivity is fixed to 4.

$\epsilon'_{\text{gap}} = 6$ by varying gap thickness

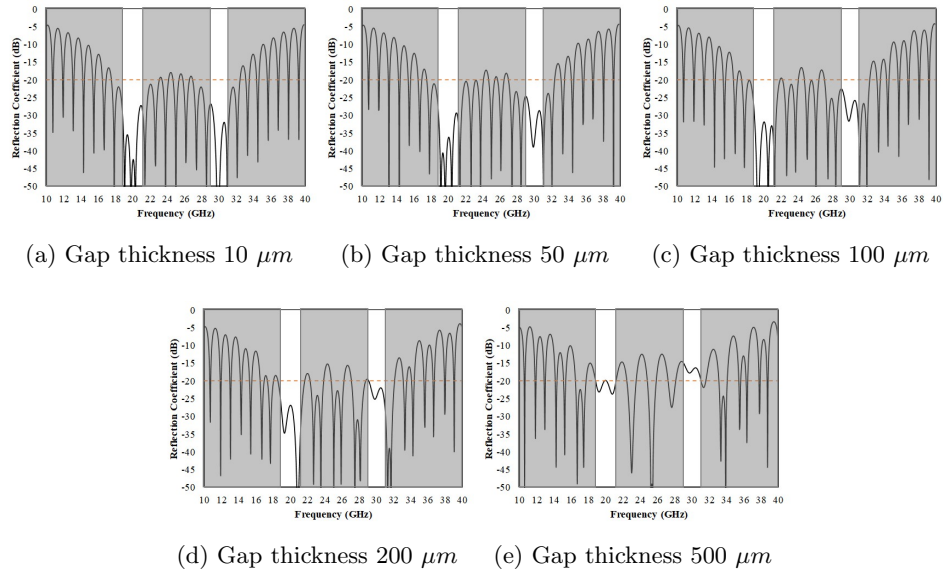


Figure 3.36: Reflection coefficient (S_{11}) under the assumption of normal incidence for the structure depicted in Fig. 3.32. The gap thickness is varied from 10 to 500 μm , while the gap relative electric permittivity is fixed to 6.

$\epsilon'_{\text{gap}} = 8$ by varying gap thickness

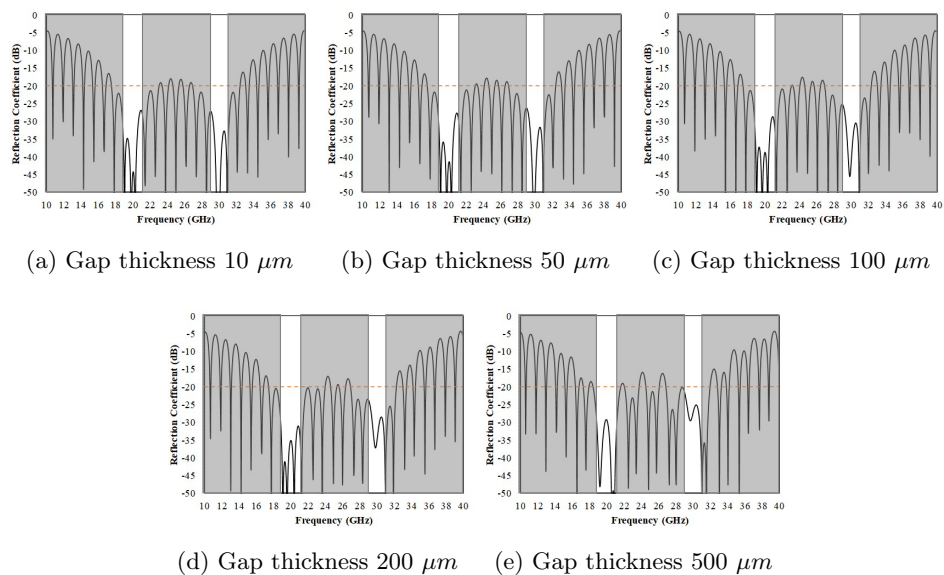


Figure 3.37: Reflection coefficient (S_{11}) under the assumption of normal incidence for the structure depicted in Fig. 3.32. The gap thickness is varied from 10 to $500 \mu m$, while the gap relative electric permittivity is fixed to 8.

$\epsilon'_{\text{gap}} = 9$ by varying gap thickness

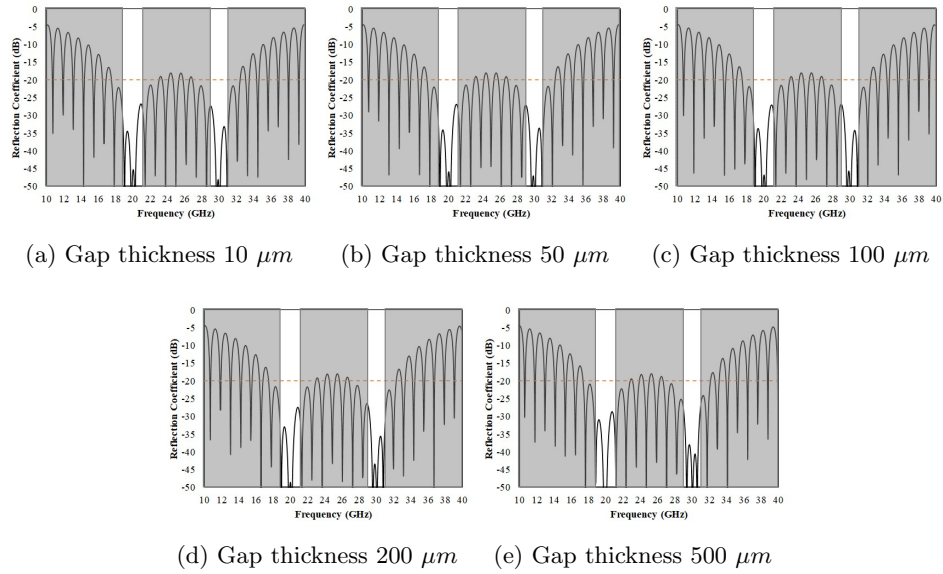


Figure 3.38: Reflection coefficient (S_{11}) under the assumption of normal incidence for the structure depicted in Fig. 3.32. The gap thickness is varied from 10 to 500 μm , while the gap relative electric permittivity is fixed to 9.

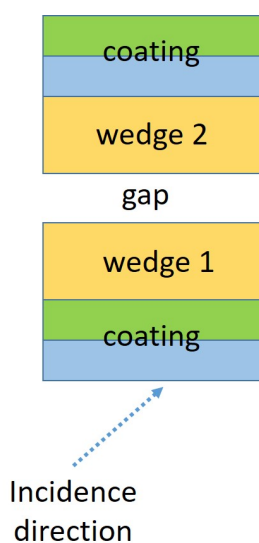


Figure 3.39: Parallel-interface structure in case of oblique incidence.

3.6.2 Oblique incidence

As said previously, this oblique incidence analysis should provide some clues on the performance of the up-down RP superstrate in the worst case of Fig. 3.31b, where the max incidence angle is about 12.5° . So, in the following subsection, several incidence angles will be analyzed, in a range going from 5° to 30° . Of course, 30° is considered as an extreme case, since in our structure such a value will never be touched.

Fig. 3.40 and 3.41, refer, respectively, to a gap permittivity of 1 and 3. Each set of plots presents the variation of the gap thickness in the horizontal direction [e.g. moving through plots (a)-(b)-(c)], and the variation of the incidence angle in the vertical direction [e.g. moving through plots (a)-(d)-(g)-(j)].

As it is possible to notice from Fig. 3.40 and 3.41 is that if the gap thickness increases or if the incidence angle increases, the reflection coefficient at the bands of interest (the bands of no interest are covered by grey boxes, so those ones of interest are within the blank spaces) becomes worse, but, for a small gap thickness, it remains good.

Analysis of a realistic up-down Risley prism system

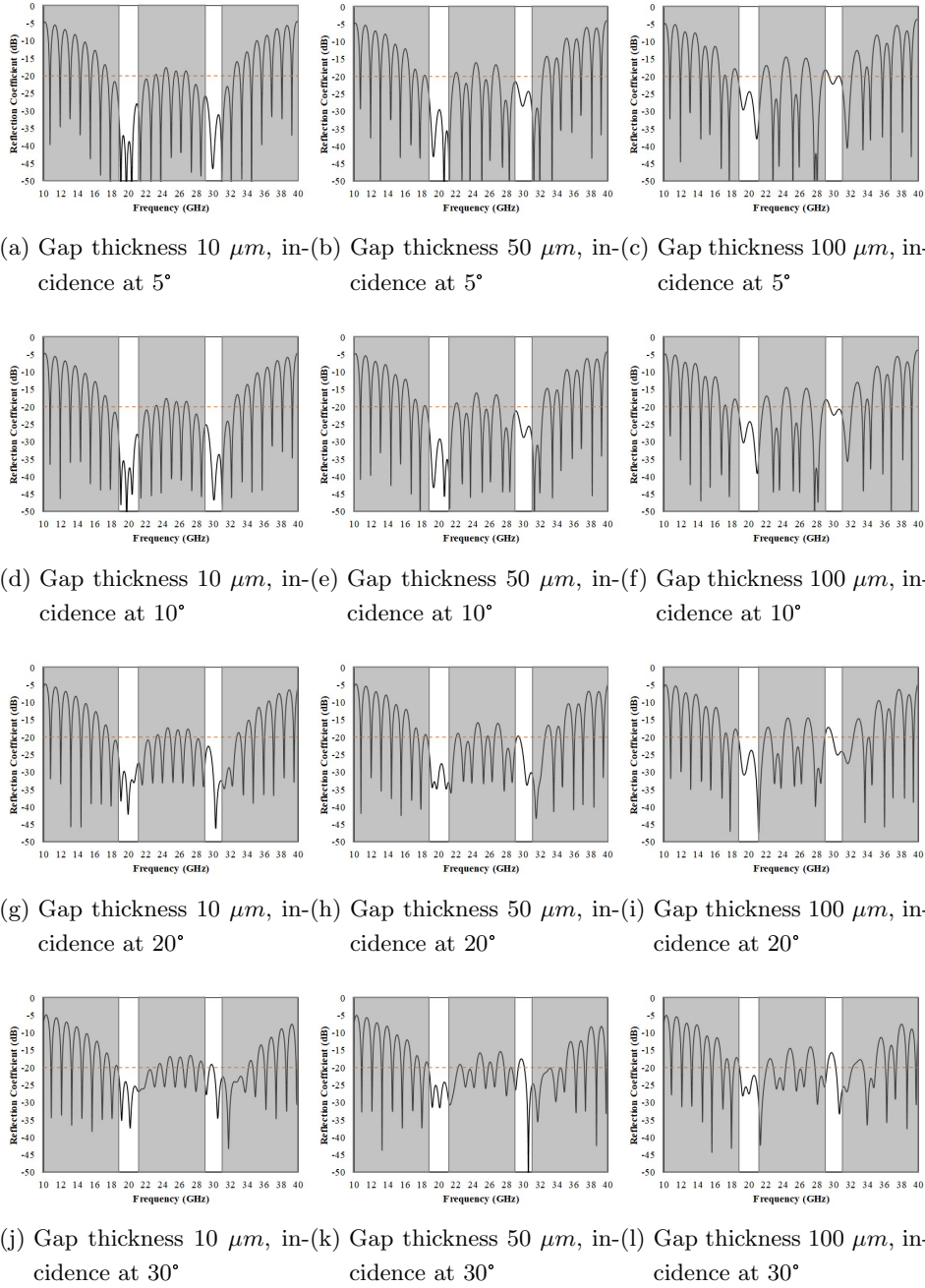


Figure 3.40: Reflection coefficient (S_{11}) under the assumption of oblique incidence for the structure depicted in Fig. 3.39. The gap thickness is varied from 10 to $100 \mu m$, while the gap relative electric permittivity is fixed to 1. The incidence angle is varied from 5° to 30° .

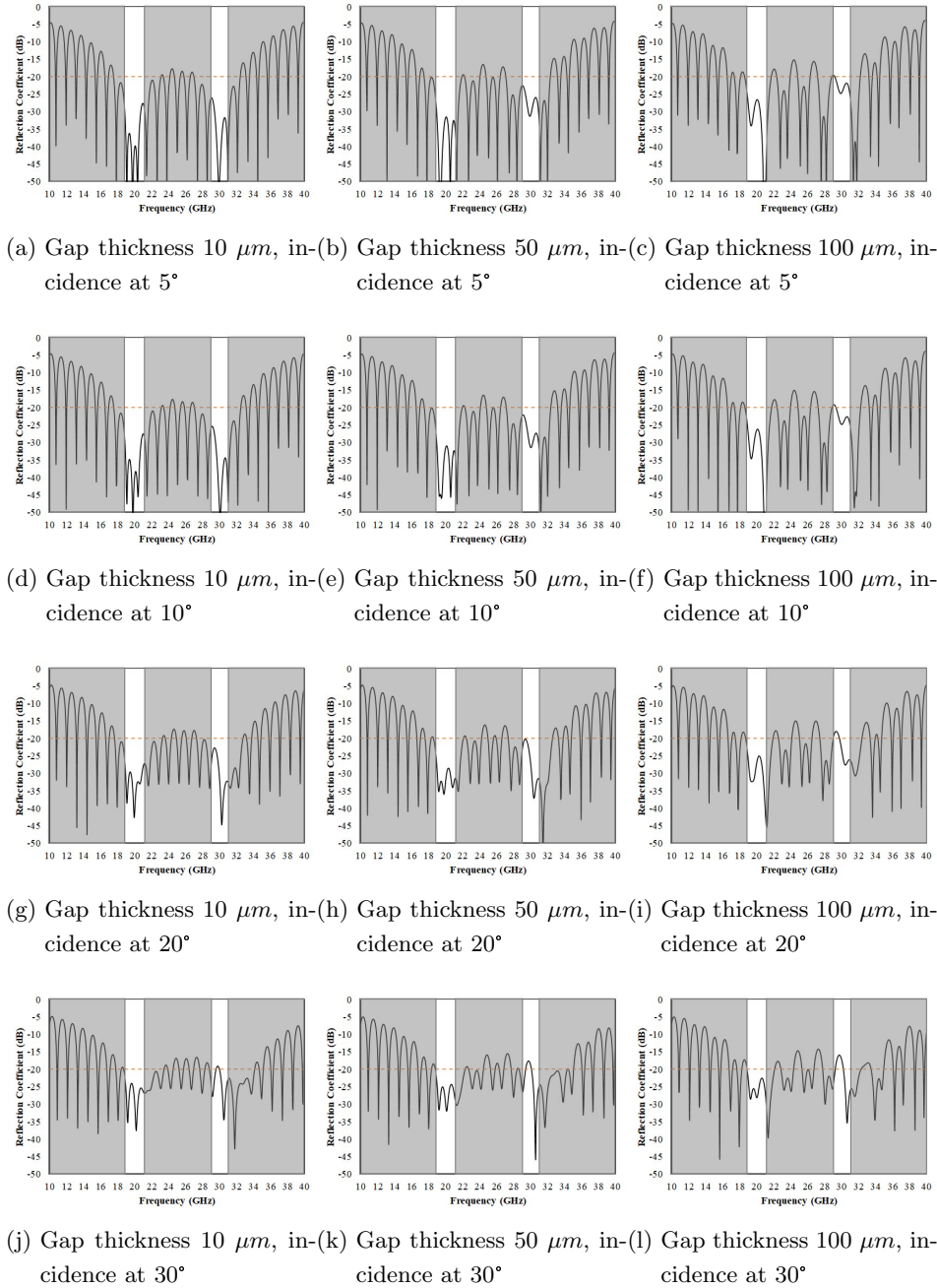


Figure 3.41: Reflection coefficient (S_{11}) under the assumption of oblique incidence for the structure depicted in Fig. 3.39. The gap thickness is varied from 10 to $100 \mu\text{m}$, while the gap relative electric permittivity is fixed to 3 . The incidence angle is varied from 5° to 30° .

3.6.3 Comments

The results presented in Subsecs. 3.6.1 and 3.6.2 have revealed the problems of the up-down RP configuration, suffering from the detrimental effects of the gap between the two wedges. It was shown that even a gap thickness as large as $200 \mu m$ destroys the performance of the structure. Unfortunately, it is not that easy to fabricate so thin gaps, but even in case it were possible, please remember that the structure should be mounted on moving and often vibrating platforms. So, due to vibrations and platform motions, that gap thickness is inevitably about to change, having bad effects on the antenna radiation performance, because of the reflection these changes would induce.

The analysis carried out so far helped understand the limits of the up-down RP topology, which despite its elegance, may cause several problems. Ultimately, such issues force to choose not the up-down RP but the classical RP topology. We remind that the classical RP configuration is the one with a prism (or wedge) at the bottom and another one at the top, as depicted in Fig. 3.23 on page 168. In this case, matching coatings are required on both air-dielectric interfaces on each wedge, having a total of 4 coatings to be applied.

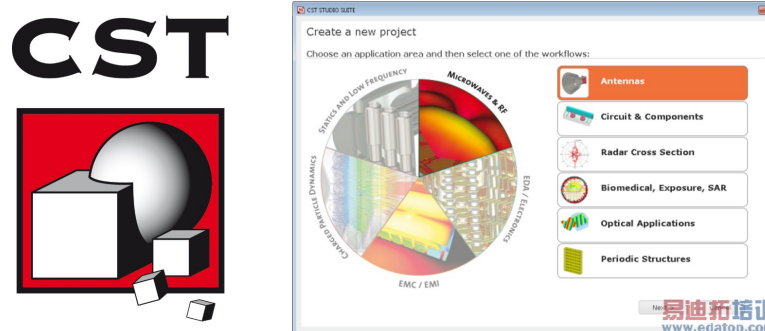


Figure 3.42: Simulation software used for the full-wave validation of the dual-band anti-reflection coating.

3.7 Full-wave validation of the dual-band anti-reflection coating

In Sec. 3.2, a dielectric wedge was proved to deviate the beam produced by a flat-panel array antenna. Because of the discontinuities at the air-dielectric interfaces, a dual-band anti-reflection coating made up of two quarter-wave layers was designed analytically in Sec. 3.4. Subsequently, a scanning architecture, based on Risley Prism (RP) topologies, providing elevation-and-azimuth beam squint, was presented in Sec. 3.5 and approximately evaluated on MATLAB by means of parallel-interface reflection/refraction theory, in a realistic scenario (Sec. 3.6). Since the operation of the RP structure is simply based on two identical dielectric wedges, a full-wave analysis of the single-wedge is presented here, with the aim of testing the functionality of the anti-reflection coating. The software used for the full-wave simulations is CST [22] (Fig. 3.42), providing time-domain and frequency-domain analyses, useful to analyze radiative structures (e.g. antennas) and closed structures (e.g. waveguides). If the full system had to be analyzed, having a real antenna size with 417 mm main diagonal (Fig. 3.30), a dielectric wedge of 417 mm diameter should be simulated. But, because of the high-memory and computational effort required to simulate such a big structure, a reduced-size antenna, and consequently a smaller wedge, was analyzed, as shown in Fig. 3.43. The aim of this full-wave validation is not to have an overall performance of the full antenna system, but to prove that the analytical results in terms of the coating's anti-reflectivity are confirmed. Thus, simulating a smaller structure will not have any bad effect on the scope of

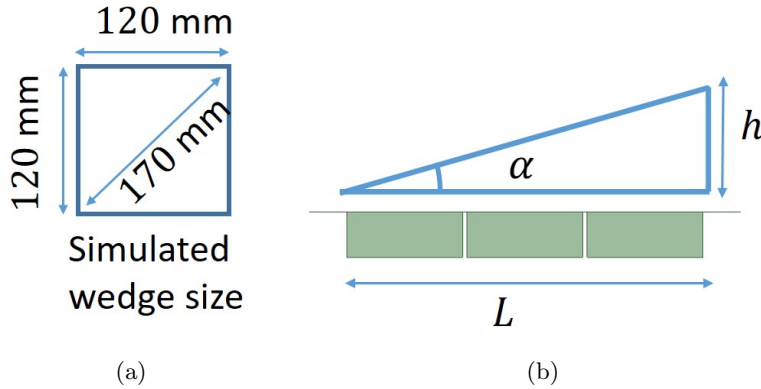


Figure 3.43: Simulated wedge size: (a) top view, (b) side view.

the work.

3.7.1 Simulation workflow

To analyze the dielectric wedge in a realistic scenario, first a planar wave front has to be created to imping on the wedge. To do that, CST provides a plane-wave excitation. However, a few attempts demonstrated that this tool was not adequate to compute the reflection coefficient of the wedge, neither the gain of the antenna. Plane-wave excitations are better for the computation of the field amplitude at some specific points in space or for radar-cross-section computations. In principle, the electric field amplitude may be used to compute the reflection coefficient as it is usually calculated in textbooks. However, in the case of the simulated wedge depicted in Fig. 3.44, there are several non-parallel interfaces, which yield multiple reflected or refracted waves and in very different directions. The theory of refraction described in textbooks is founded on parallel-interface assumption, which yields only one direction of wave propagation in the transmission side and one in the reflection side. In a situation like this, with a wedge with non-planar interfaces, this methodology will inevitably be less accurate.

Another way to create a locally planar wavefront is to simulate a flat-panel array antenna with all elements excited in phase. In this case, the radiated wave, detaches from the array aperture in planar wave fronts and goes on propagating through the wedge structure and is then radiated in the far field. In this case, it is possible to compute power reflection or transmission coefficients, as well as the gain of the antenna.

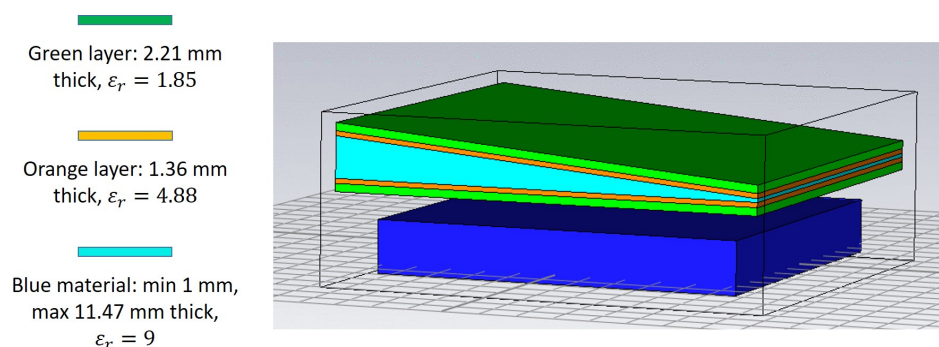


Figure 3.44: Wedge with coating layers modelled on CST.

The steps of this simulation are summarized in Fig. 3.45 and can be distinguished in three parts:

1. Array antenna simulation. A 10×10 array of horn antennas with in-phase excitations is simulated by using the time-domain simulation of CST, applying radiation boundary condition. The overall array fits within the wedge contour.
2. Equivalent source export. The equivalent source associated to the array antenna is exported (i.e. the near-field distribution at the radiation boundary box is computed and exported). In this way, the total array is just simulated once.
3. Wedge simulation. The equivalent source of the array, providing a locally planar wavefront, is imported in the CST model of the wedge. So, the wedge can then be analyzed in a more realistic scenario.

As clear from Fig. 3.45, the wedge yields a beam deviation of around 10° in agreement with the expectations. The simulated wedge is exactly the same as the one analyzed in Sec. 3.6. Its relative electric permittivity is 9 and the coating layer parameters are listed in Table 3.8 on page 161.

3.7.2 Full-wave extraction of the reflection coefficient

The most difficult part of the simulation was to find a way to calculate the reflection coefficient of the coated wedge. This procedure is depicted in Fig. 3.46 and can be described, again, in three steps:

Full-wave validation of the dual-band anti-reflection coating

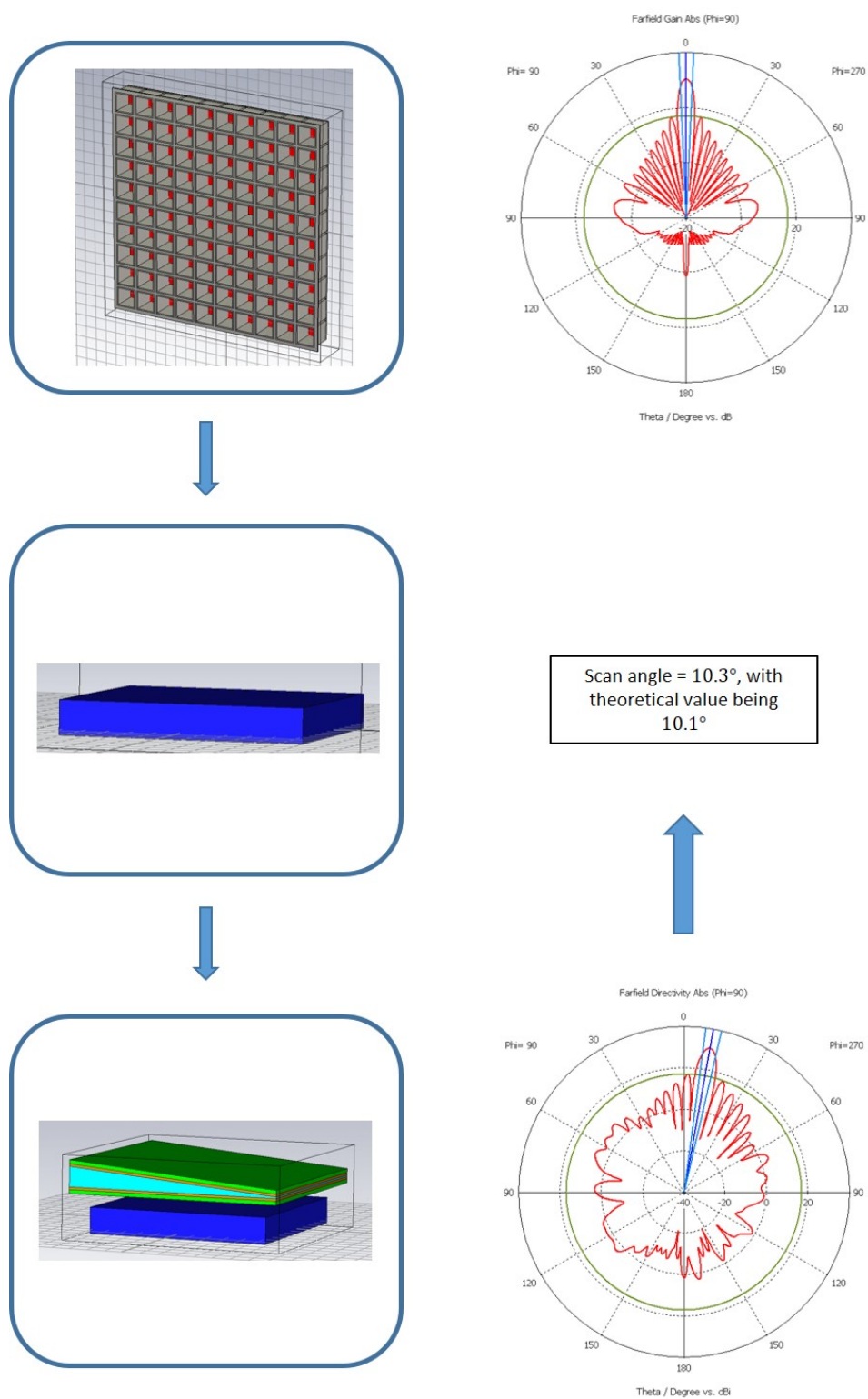


Figure 3.45: Simulation workflow carried out on CST. Radiation patterns computed at 30 GHz

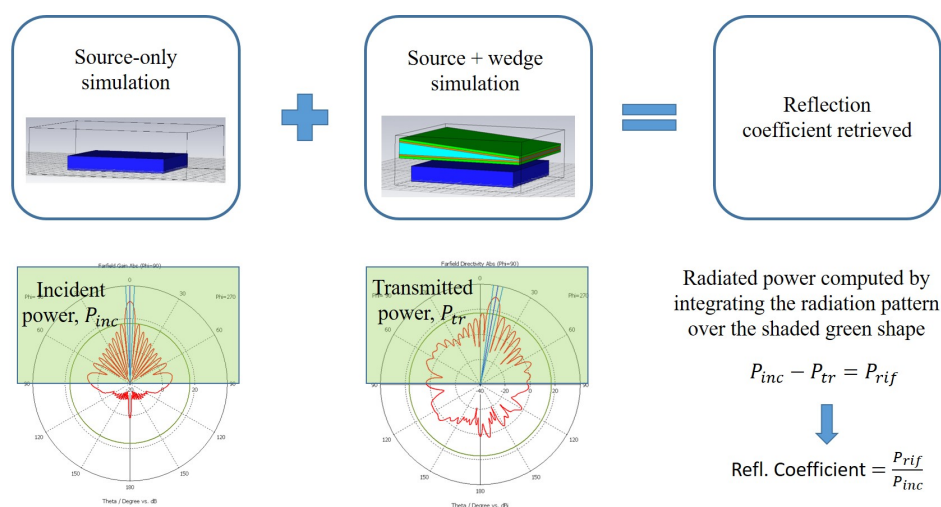


Figure 3.46: Workflow of the reflection coefficient computation on CST.

1. Incident power calculation. The power radiated towards the upper hemisphere in the case of the source-only model is computed by performing an integration of the Poynting vector on a surface of the upper hemisphere. This integration is automatically performed in CST.
2. Transmitted power calculation. The power which is transmitted after the wedge and radiated in the upper hemisphere is computed in the model of the source in presence of the wedge. The computation is, again, automatically carried out by CST.
3. Reflection coefficient calculation. The incident power is, of course, the sum of the reflected and the transmitted power. Indeed, since the incident power of the source-only model is the same, what is scattered back by the wedge is not transmitted through. At this point, the difference between the incident power (in the absence of the wedge) and the power transmitted in presence of the wedge results to be the reflected power. Then, the reflection coefficient can be retrieved by dividing the reflected power by the incident power.

The reflection coefficient computed with this methodology is reported in Fig. 3.47. The behavior of the reflection coefficient follows somehow the behavior obtained on MATLAB simulations, using the parallel-interface approximation and the transmission-matrix theory. In the bands of interest, around 20 and 30 GHz, the reflection coefficient is quite good.

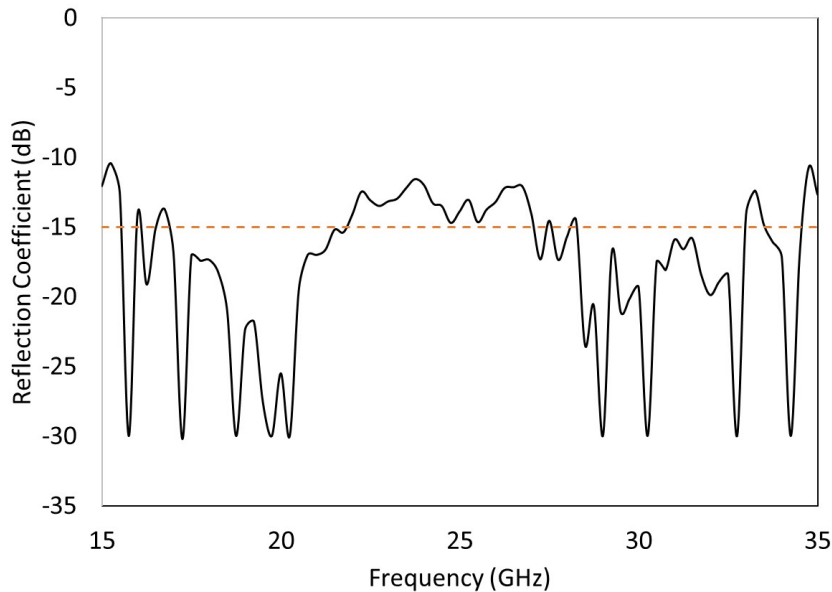


Figure 3.47: Reflection coefficient retrieved from CST simulations. The frequency step used in this simulation was 0.25 GHz.

3.8 Future work

Once the coating has been designed and validated through theoretical and full-wave analyses, a prototype and testing of the coated wedge is the closing step.

The manufacturing of the two dielectric wedges making up the RP configuration is, in principle, not a problem. It is sufficient to fabricate a dielectric cylinder and properly cut it through the right diagonal plane dividing the cylinder into two identical parts. Furthermore, several dielectric materials can be manufactured with various dielectric constants and are sometimes available on the shelf. The cost of the production of a few pieces, however, can be quite high. Major problems arise as for the synthesis of the anti-reflection coatings. In fact, every coating is composed of two dielectric layers with specific dielectric constant and specific thickness. It is very difficult to find so precise values of permittivities and thicknesses on the shelf. There are usually standard values of dielectric constants and the choices are quite limited for the application under exam. Nevertheless, an emerging technology that is driving a revolution in the field of prototyping is 3D printing, due to its very high flexibility and very limited prototypization costs.



Figure 3.48: 3D printing technology: a commercial 3D printer [23] (a) and a variety of 3D-printed objects [24] (b).

Nowadays, several 3D printers (Fig. 3.48a) are commercially available and provide a very big flexibility in terms of construction of different geometries (Fig. 3.48b) and possibility to synthesize a large variety of dielectric constants. For e.g., the University of Pavia, owns a fused-deposition modelling (FDM) 3D printer allowing to synthesize any dielectric constant (within a certain range) just by playing with the percentage of material in-fill. The construction of a 3D-printed object takes place by depositing trace by trace and layer by layer a plastic material. FDM works on an “additive” principle by laying down material in layers; a plastic filament or metal wire is unwound from a coil and supplies material to produce a part.

The in-fill percentage is the fraction of the dielectric material out of the total volume. In practice, the 3D-printed object consists of a frame of interlaced traces of plastic material; the remaining unfilled areas are permeated by air. A lower percentage of in-fill has the effect of reducing the fraction of plastic material in favor of air; in this way, the effective electric permittivity of the material can be reduced to any value between air and the plastic material. It is proven that there is a sort of linear dependency law between the in-fill percentage and effective permittivity [25]–[27]; and we have applied this sort of law to have a rough estimation of the possible materials to be used and related in-fill percentage to synthesize our desired coating layers.

Seeking for sufficiently high electric permittivities to realize the dielectric constant of the wedge, we found out a variety of filaments with relative dielectric permittivities comprised between 3 and 10 which would allow to manufacture all layers of our anti-reflection coating, as well as the wedge.

PREPERM® filaments for 3D printing		
Dimensions: Ø 1.75 mm		
Weight: 0.75 kg		
Product	ϵ_r	$\tan \delta$
PREPERM® 3D ABS ϵ_r 3.0	3.0	0.004
PREPERM® 3D ABS ϵ_r 4.0	4.0	0.004
PREPERM® 3D ABS ϵ_r 4.5	4.5	0.004
PREPERM® 3D ABS ϵ_r 5.5	5.5	0.004
PREPERM® 3D ABS ϵ_r 6.5	6.5	0.004
PREPERM® 3D ABS ϵ_r 7.5	7.5	0.004
PREPERM® 3D ABS ϵ_r 10.0	10.0	0.004




Figure 3.49: Premix Preperm low-loss filaments for 3D printing.

These filaments we found, produced by Premix Preperm, are reported in Fig. 3.49. They are high-frequency and low-loss materials which lend themselves to applications like dielectric lenses or superstrates. By making some rough calculations of in-fill percentage, we came up with three possible solutions to be implemented for the manufacturing of the coating layers and wedge prototypes. As shown in Fig. 3.50, we can choose among:

- A. Only the filament with relative electric permittivity $\epsilon_r = 10$ is used to print all dielectrics, in particular: the wedge, with in-fill of $\sim 90\%$; the “orange” coating layer (Fig. 3.44) with $\sim 45\%$ of in-fill; and the “green” layer with $\sim 10\%$ of in-fill.
- B. Two different filaments with $\epsilon_r = 10$ and $\epsilon_r = 5.5$ are used to print all dielectrics, in particular: the wedge is made from the filament with $\epsilon_r = 10$, with in-fill of $\sim 90\%$; the “orange” coating layer and the “green” one are made from the filament of $\epsilon_r = 5.5$, with $\sim 85\%$ and $\sim 20\%$ of in-fill, respectively.
- C. Three different filaments with $\epsilon_r = 10$, $\epsilon_r = 5.5$, and $\epsilon_r = 3$ are used each for printing each single dielectric, in particular: the wedge is made from a filament of $\epsilon_r = 10$, with $\sim 90\%$ of in-fill; the “orange” coating layer is made from a filament of $\epsilon_r = 5.5$, with $\sim 85\%$ of in-fill; and the “green” layer is made from a filament of $\epsilon_r = 3$, with $\sim 40\%$ of in-fill.

Solution A is the most convenient in terms of manufacturing simplicity, because only a filament is employed for all three dielectric materials, but





	Solution A (1 fil.)	Solution B (2 fil.)	Solution C (3 fil.)
 Green layer: 2.21 mm thick, $\epsilon_r = 1.85$	Fil. $\epsilon' = 10$ Infill 10% 	Fil. $\epsilon' = 5.5$ Infill 20%	Fil. $\epsilon' = 3$ Infill 40%
 Orange layer: 1.36 mm thick, $\epsilon_r = 4.88$	Fil. $\epsilon' = 10$ Infill 45%	Fil. $\epsilon' = 5.5$ Infill 85%	Fil. $\epsilon' = 5.5$ Infill 85%
 Blue material: min 1 mm, max 11.47 mm thick, $\epsilon_r = 9$	Fil. $\epsilon' = 10$ Infill 90%	Fil. $\epsilon' = 10$ Infill 90%	Fil. $\epsilon' = 10$ Infill 90%

Figure 3.50: Possible filament choices for 3D printing the anti-reflection coating. Solution A only employs 1 filament; solution B employs 2 different filaments; and solution C employs 3 different filaments. The in-fill percentage for the synthesis of each coating layer depends on the permittivity of the chosen filament.

it implies a very low in-fill percentage for the “green” coating layer, which would make the material structure little robust and tending to mechanical deformation. Conversely, solution C is the most convenient in terms in-fill percentage, with good in-fills for all dielectrics, but it is also the most complex, having to deal with three different filaments needing to be properly glued one on top of each other (this process may have some bad impact on the tightness of the various material discontinuities). Furthermore, when the 3D printer has to change filament, the deposition accuracy may be a little altered. Consequently, to manufacture a possible prototype with 3D printing technology, solution B seems to be the best compromise.

3.9 Conclusions

The problem of keyhole in azimuth-over-elevation mechanically steered antennas was investigated in this chapter and a solution was proposed to overcome this issue which limits the operational capability of such a kind of systems. A dielectric-based superstrate, based on two wedge-shaped low-loss materials (vertically spaced), was proposed to be placed above a planar array antenna. It allowed, through simple rotations of the wedges over the azimuth plane only, to introduce an additional degree of beam scanning about the zenith axis, thus overcoming the keyhole issue. Each wedge's top and bottom surfaces were covered with anti-reflection coatings to accomplish maximum transmission through the dielectric layers. The design and analysis of such coatings were carried out through a completely analytical procedure, subsequently validated by means of a commercial simulation tool. Results showed the possibility to effectively obtain beam steering in agreement with theoretical expectations. Eventually, 3D printing was mentioned to be a possible manufacturing technology allowing to make a low-cost prototype of the proposed structure.

References

- [1] Bryce Space and Technology, *State of the satellite industry report*, “<https://www.sia.org/annual-state-of-the-satellite-industry-reports/2017-sia-state-of-satellite-industry-report/>”, Jun. 2017.
- [2] H. Zhou, M. Jong, and G. Lo, “Evolution of satellite communication antennas on mobile ground terminals”, *International Journal of Antennas and Propagation*, vol. 2015, no. Article ID 436250, 2015.
- [3] R. E. Sheriff and Y. F. Hu, *Mobile Satellite Communication Networks*. Ltd, New York, NY, U.S.A.: John Wiley & Sons, 2001.
- [4] V. Weerackody and E. G. Cuevas, “Technical challenges and performance of satellite communications on-the-move systems”, *Johns Hopkins APL Technical Digest*, vol. 30, no. 2, pp. 113–121, 2011.
- [5] A. C. Densmore, V. Jamnejad, and K. E. Woo, “Satellite-tracking millimeter wave reflector antenna system for mobile satellite tracking”, US RE37218E, 2001.
- [6] D. J. Legare and D. M. Hummel, “Antenna for compact satellite terminal”, US 7859479B2, 2010.
- [7] G. R. Dunlop, P. J. Ellis, and N. V. Afzulpurkar, “The satellite tracking keyhole problem: A parallel mechanism mount solution”, *Transactions of the Institution of Professional Engineers New Zealand: Electrical/Mechanical/Chemical Engineering*, vol. 20, no. 1, Nov. 1993.
- [8] Q. Luo and S. Gao, “Smart antennas for satellite communications on the move”, in *2017 International Workshop on Antenna Technology: Small Antennas, Innovative Structures, and Applications (iWAT)*, Mar. 2017, pp. 260–263.
- [9] J. Navarro, “Ultra-small aperture terminals for satcom on-the-move applications”, in *2017 IEEE MTT-S International Microwave Symposium (IMS)*, Jun. 2017, pp. 1152–1154.
- [10] K. Y. Kapusuz, Y. Şen, M. Bulut, İ. Karadede, and U. Oğuz, “Low-profile scalable phased array antenna at ku-band for mobile satellite communications”, in *2016 IEEE International Symposium on Phased Array Systems and Technology (PAST)*, Oct. 2016, pp. 1–4.

-
- [11] M. C. Viganó, D. L. del Río, and S. Vaccaro, “Sparse array antennas for satellite mobile terminals”, in *The 8th European Conference on Antennas and Propagation (EuCAP 2014)*, Apr. 2014, pp. 3132–3136.
- [12] L. Josefsson and P. Persson, *Conformal Array Antenna Theory and Design*. IEEE Press Wiley-Interscience, 2006.
- [13] B. O. Zhu, J. M. Zhao, and Y. J. Feng, “Active impedance metasurface with full 360° reflection phase tuning”, *Scientific Reports*, vol. 3, no. 3059, 2013.
- [14] A. Ourir, S. N. Burokur, and A. D. Lustrac, “Phase-varying metamaterial for compact steerable directive antennas”, *Electronics Letters*, vol. 43, no. 9, pp. 493–494, 2007.
- [15] N. Gagnon and A. Petosa, “Using rotatable planar phase shifting surfaces to steer a high-gain beam”, *IEEE Transactions on Antennas and Propagation*, vol. 61, no. 6, pp. 3086–3092, Jun. 2013.
- [16] M. Born and E. Wolf, *Principles of Optics*, Third Revised Edition. Oxford Pergamon Press, 1965.
- [17] Ansys HFSS (2015), computer software, *3d electromagnetic field simulator for rf and wireless design*, “<http://www.ansys.com/products/electronics/ansys-hfss>”, (accessed April 2017).
- [18] S. J. Orfanidis, *Electromagnetic Waves and Antennas*. Piscataway, NJ, U.S.A.: Rutgers University, 2016.
- [19] G. Conciauro and L. Perregrini, *Fondamenti di Onde Elettromagnetiche*. Milan, Italy: Mc Graw-Hill Education, 2003.
- [20] B. J. Tame and N. A. Stutzke, “Steerable risley prism antennas with low side lobes in the ka band”, in *2010 IEEE International Conference on Wireless Information Technology and Systems*, Aug. 2010, pp. 1–4.
- [21] M. Ostaszewski, S. Harford, N. Doughty, C. Hoffman, M. Sanchez, D. Gutow, and R. Pierce, “Risley prism beam pointer”, *Proc. SPIE*, vol. 6304, 2006.
- [22] CST Studio Suite (2017), computer software, *3d electromagnetic field simulator for rf and wireless design*, “<https://www.cst.com/solutions/markets/microwaves-rf/>”, (accessed August 2018).

-
- [23] Commercial 3D printer, *Jumpstart 3d printer fully assembled*, “<https://www.matterhackers.com/store/printer-kits/jumpstart-3d-printer>”, Dec. 2017.
- [24] 3D-printed objects, *Cosa si può creare con una stampante 3d?*, “<https://techboom.it/cosa-si-puo-creare-stampante-3d/>”, Dec. 2017.
- [25] E. Massoni, L. Silvestri, M. Bozzi, L. Perregrini, G. Alaimo, S. Marconi, and F. Auricchio, “Characterization of 3d-printed dielectric substrates with different infill for microwave applications”, in *2016 IEEE MTT-S International Microwave Workshop Series on Advanced Materials and Processes for RF and THz Applications (IMWS-AMP)*, Jul. 2016, pp. 1–4.
- [26] P. Ransom, Z. Larimore, S. Jensen, and M. S. Mirotznik, “Fabrication of wideband antireflective coatings using fused deposition modelling”, *Electronics Letters*, vol. 52, no. 5, pp. 352–354, 2016.
- [27] B. Biernacki, S. Zhang, and W. Whittow, “3d printed substrates with graded dielectric properties and their application to patch antennas”, in *2016 Loughborough Antennas Propagation Conference (LAPC)*, Nov. 2016, pp. 1–5.

Chapter 4

An Error Model Analysis for ESA Monopulse Tracking Antennas

This chapter is devoted to an interesting activity conducted in the last year of the Ph.D. in a 6-month period spent at the European Space Operations Centre (ESOC), located in Darmstadt, Germany. The aim of the activity was to study some problems encountered in almost all ESA tracking ground stations belonging to the tracking network called ESTRACK. These problems are related to unexpected discrepancies between the actual position of a satellite (or a target) and the estimated position acquired by means of the antenna tracking receivers. Although they are very tiny errors for short-range missions, they may have detrimental consequences on deep-space missions, with possible loss of the spacecraft. The work done at ESOC aimed at understanding and developing an error model to characterize all microwave components making part of the tracking chain, and hopefully identify the possible sources of the errors encountered in the measurement campaigns. This activity was the fruit of a collaboration with Prof. Angel Mediavilla Sánchez, from Universidad de Cantabria, who has actively worked for ESA tracking antennas for a long time and provided me with some fundamental material. Furthermore, some of the results (figures, graphs, and tables) presented here were worked out in cooperation with Gabriele Ceccato from the University of Pavia. The fruit of the work was MATLAB code developed on purpose, implementing a model of the monopulse tracking chain. Since

this activity was the last one of this Ph.D., this chapter only presents some initial results. Refinement of the model and proper interpretation of the results is mandatory before publishing on this quite complex topic. For this reason, it is possible some publication will follow in the near future, but after the time this thesis is written. The next sections present an introduction on ESA tracking problem, with a summary of some operational ground stations. The monopulse technology all ground stations are based on will be described, with particular attention to the multi-mode monopulse, employed almost in all ESTRACK stations. The fundamental microwave components of the monopulse chain, such as mode couplers, hybrid junctions, and 3 dB/90° couplers will also be described and characterized in order to realize possible non-idealities which may impair the tracking information. A mathematical model of the receiving monopulse chain will be shown and a MATLAB code to simulate realistic target misalignment and tracking information retrieval will be used to identify the possible sources of errors. Specific non-idealities will be introduced in some parts of the chain, in the form of phase shifters and gain factors to model phase and gain unbalances.

4.1 Tracking

Tracking is a very famous topic, dating back to the world war times, where the first RADARs were born to localize the approaching enemies from a long distance. However, tracking is not only limited to RADAR applications, but also to point-to-point communications between relatively moving platforms. Especially in satellite communications, tracking is of great importance to properly maintain a constant link with the spacecraft from antennas located on the ground and also to acquire satellite orbital information. More importantly, deep-space missions have a strict requirement on antenna pointing accuracy, making necessary to automatically follow the spacecraft's relative motions and maintain the target always within the antenna beam. In such applications, antennas on the ground are usually very large (tens of meters in diameter) in order to focus the energy on very tiny beams directed towards the spacecrafts. Given so narrow beams, it is extremely likely to move the beam out of the spacecraft and lose any communication with it, unless a proper automatic tracking system is used.

There are two major types of tracking:

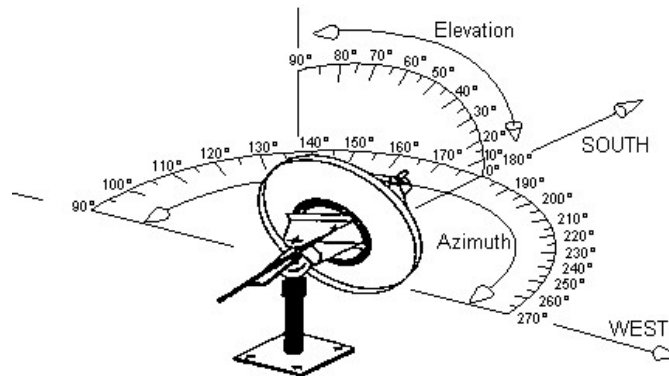


Figure 4.1: Azimuth and elevation [1]

- Program-track. The target's position is known from its orbital parameters, so the antenna on the ground is pointed according to the expected target ephemeris.
- Auto-track. The target's position is precisely determined based on a feed-back tracking system acquiring and updating the current measurement of the target.

The most accurate way of tracking a spacecraft is by using auto-track antennas. Actually, program track is also adopted but only in the initial acquisition phase, to have a rough pointing. Then, the position measurement is refined later by the auto-track system. An auto-track system is based on a feed-back logic: the target position is measured, the measurement gives an information on the target misalignment with respect to the antenna boresight and a tracking error drives the antenna servo system which is in charge of re-pointing the antenna to align its boresight to the target direction. The antenna continuously moves to maintain the target in the centre of the beam. The antenna servo system is commonly based on an azimuth/elevation mount (Fig. 4.1), i.e. there are two gimbals, one controlling the elevation inclination of the antenna and another one controlling its azimuth rotation.

4.2 Monopulse Tracking

Tracking in satellite applications (and not only) means acquisition of two pieces of information:

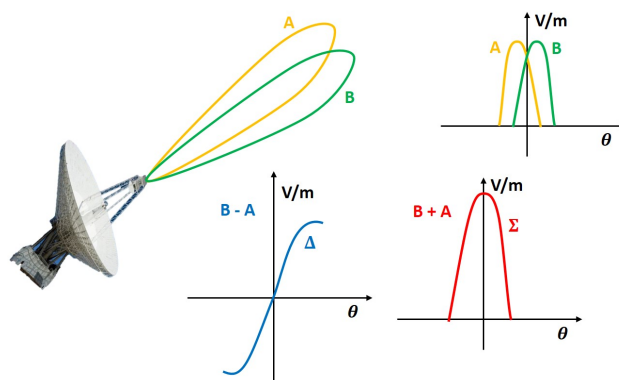


Figure 4.2: Monopulse principle.

- Range. It is the distance between the target and the antenna.
- Angular position. It represents the direction of the target and is usually expressed in polar coordinates, such as azimuth and elevation.

In this chapter, the range measurements will not be treated and the attention is only focused on angular measurements. There are three major ways of measuring the direction of a target, namely *conical scan*, *delta-DOR*, and *monopulse*. Since ESA systems are based on this last technology, the other two ones will not be subject of this work.

The term *monopulse* stems from *mono-*, meaning “one” from Greek, and *pulse*, from Latin “pulsus”. It is a technology which allows to retrieve the target angular position by receiving just one pulse (hence the name monopulse), even though more pulses are usually employed to improve the accuracy of the measurement. The idea behind the monopulse is simple. Let’s consider an antenna which is able to produce two identical beams A and B reciprocally slightly tilted, as shown in Fig. 4.2, such that at the antenna boresight ($\theta = 0$) they have the same amplitude. What happens if beam A is added to beam B? The result would be a unique taller and larger beam, called *sum* beam or Σ , shown in the red curve. Now, what if beam A is subtracted from beam B? In this case, at $\theta = 0$, the resulting point is zero and the curve assumes the shape of a symmetrical (about the origin) and monotonically increasing function of θ , at least in a small angular range about the origin. This resulting beam is called *difference* beam or Δ . Its meaning is quite clear: it is a sort of target misalignment error function. In fact, if the antenna points exactly at the target (target at boresight)

$\Delta = 0$, meaning that the misalignment error is zero; if the antenna is not well pointed at the target, $\Delta \neq 0$, with 0° -phase for positive misalignment angles and 180° -phase for negative misalignment angles. The monopulse *difference* signal gives a good estimate of the target misalignment about the antenna boresight and the amplitude of the difference signal is proportional to the misalignment. Thus, the difference signal tells how many degrees or how quickly the antenna has to rotate to re-establish boresight pointing at the satellite.

What about the *sum* signal? What is it intended for? Its main function is data link, e.g. telemetry, telecommands, and range measurements. But, in the tracking receiver, it is extremely important. Its role is usually disregarded, but it is actually fundamental for a proper operation of the tracking system. In fact, the tracking receiver should yield an angular error function which is independent of the signal strength or the target's distance. If the misalignment error depended upon the spacecraft's range, closer spacecrafts with smaller misalignments would produce the same difference signals as farther spacecrafts with larger misalignments (because the strength of the difference signal is inversely proportional to the target distance and proportional to the misalignment). To clarify this concept, consider a spacecraft transmitting a signal received by a monopulse antenna on the ground, under the assumption of small misalignments. The field amplitude received by the antenna through the sum beam will be substantially independent of the misalignment (sum beam is flat around boresight) and inversely proportional to the target distance d (due to propagation attenuation law), whilst the difference signal will be proportional to the misalignment angle θ_e and inversely proportional to the target distance. So, the field amplitude received through the sum beam Σ and the difference beam Δ can be expressed as:

$$\Sigma \sim \frac{K_s}{d} \quad (4.1a)$$

$$\Delta \sim K_d \frac{\theta_e}{d} \quad (4.1b)$$

where K_s and K_d are proportionality constants. If, now, the ratio of Δ to Σ is taken, a good misalignment error signal ϵ is obtained:

$$\epsilon = \frac{\Delta}{\Sigma} = K\theta_e \quad (4.2)$$

where, again, K is a proportionality constant. Actually, the error function is not directly proportional to the misalignment but only in a small range of

values about the origin. In general, a monopulse system operates within the 3 dB beamwidth of the sum beam, so in regions where the error function slope starts decreasing. In general, the error function has a tangent-like behavior. That's why in any monopulse tracking receiver, a proper calibration function is needed to associate a certain error signal reading to a specific misalignment angle. Another important aspect to consider is phase. The difference signal phase (0° or 180°) tells whether the target is misaligned in the positive or in the negative side about the boresight axis. But how is such phase retrieved? Phase is normally measured relatively to another signal normally used as a reference. Traditionally, in communications systems, the phase is aligned with a locally generated reference signal (output of the local oscillator). In a monopulse chain, the phase of the difference signal is compared with the phase of the sum signal. So, the difference signal is downconverted and processed using the sum signal phase as a reference. In a monopulse chain, phase and amplitude relationships between the sum and the difference channels are, then, very very important, more than fundamental for a proper operation of the tracking receiver. Any unbalance caused by differences in the cable lengths or phase shifts introduced by imperfect microwave components or amplitude unbalances due to amplifiers or power dividers or directional couplers can severely impair the tracking information generated by the monopulse receiver.

4.2.1 4-horn monopulse

A monopulse receiver cannot work without an antenna which should be able to generate a proper Δ beam.

A simple way to make a Δ radiation pattern is a system of 4 horn antennas located as shown in Fig. 4.3. If all 4 horns are excited in phase, the Σ beam is produced; if the 2 upper horns A and B (in phase with each other) are excited in phase opposition with respect to the 2 lower horns C and D (in phase with each other), a difference beam in elevation is produced ΔEL ; instead, if the 2 left-hand horns A and C are excited both in phase opposition with respect to the 2 right-hand horns B and D, a difference beam in azimuth is produced ΔEL . That is what the combining network in Fig. 4.3 is trying to do. Such a system is very simple and with 3 channels both azimuth and elevation error signals are produced. A 4-horn configuration may be used at the feed of a large reflector in such a way that

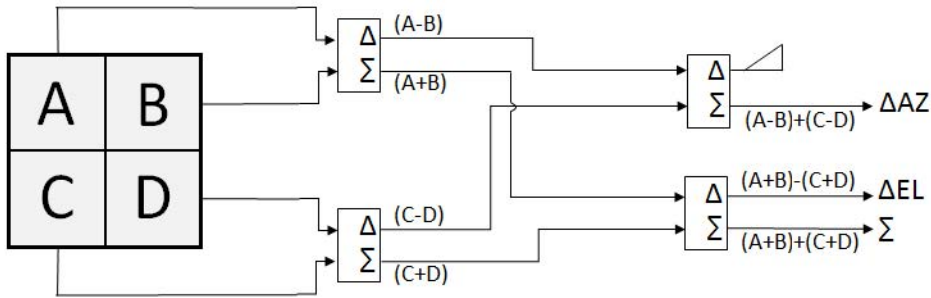


Figure 4.3: 4 horn monopulse topology.

the horns are displaced around the focal point so that the equivalent phase centers are all placed at the focus of the reflector. However, for satellite communications, the 4 horn monopulse gives poor flexibility and large space occupation, because the comparators are quite big [2].

4.3 Multi-mode monopulse

In satellite communications, a commonly used tracking technique is the multimode monopulse [3]. In this case, the feed of the reflector is a single conical horn excited in a certain number of high-order modes. The conical horn is attached to a circular waveguide, where all such modes are extracted by means of mode couplers¹ [4]. Since the focus of this work is on multimode monopulse, it is important to understand how it works in detail, starting out with a description of the circular waveguide modes and their radiation characteristics [5].

4.3.1 Circular waveguide modes

The fundamental mode which can propagate through a circular waveguide is the TE_{11} , which is a degenerate mode splitting up into two orthogonal modes, namely the TE_{11}^s and the TE_{11}^c (s stands for *sine* and c for *cosine*; it is just a nomenclature to distinguish the each degenerate mode). The first higher order mode is the TM_{01} , followed by the degenerate TE_{21}^s and TE_{21}^c modes. The subsequent mode is the TE_{01} followed by all other modes which

¹Mode couplers are devices capable of extracting (or injecting) a specific propagation mode from a waveguide. The extraction of the mode is carried out by means of slot-coupling or multi-hole coupling techniques, with resonant or travelling-wave methods.

are not interesting for the purpose of this work. Their amplitude is shown in Fig. 4.4 and their field vectors are depicted in Fig. 4.5. For the purpose of this work, it is important to look at the characteristics of the field in a region close to the waveguide centre, because the radiation features of these modes resemble those of the modes propagating in the waveguide.

Near the origin, the TE_{11}^s is practically constant and vertically polarized, while the TE_{11}^c is horizontally polarized. This mode produces a radiation pattern which can be used as a Σ beam. If both degenerate modes are used, through the sum beam it is possible to receive a circular polarization.

Near the origin, the TM_{01} has a null at the origin (which translates into a null at boresight, in the far field) and its electric field is radially polarized. This mode may be used to produce a Δ beam. This mode, in conjunction with the TE_{11} , can be used to retrieve the tracking information on azimuth and elevation, provided that the incident electric field is circularly polarized.

Near the origin, the TE_{21}^s has a null at the origin, is vertically polarized moving along the y axis and is horizontally polarized along the x axis. Its degenerate twin, the TE_{21}^c , is complementarily polarized: along y , its polarization is horizontal; along x , it is vertical. Due to this reason, if both TE_{21}^s and TE_{21}^c are adopted, full tracking capability in all-polarization scenarios (incident circular or incident linear polarization) can be obtained.

Last, near the origin, the TE_{01} has, again, a null at the origin and is rotationally polarized, i.e. its polarization is orthogonal to the one generated by the TM_{01} . For this property, if these two modes are used at the same time, full-tracking in all-polarization scenarios can be achieved.

4.3.2 Radiation features of the circular waveguide modes

The radiation characteristics of the modes resemble the features of the electromagnetic field of the modes propagating inside the waveguide.

In the following paragraphs, the expressions for the electric fields radiated in the far field by such modes are presented.

TE₁₁

The electric field of the TE_{11}^s in a polar coordinate system where the z axis coincides with the waveguide axis and θ and ϕ are measured in the usual

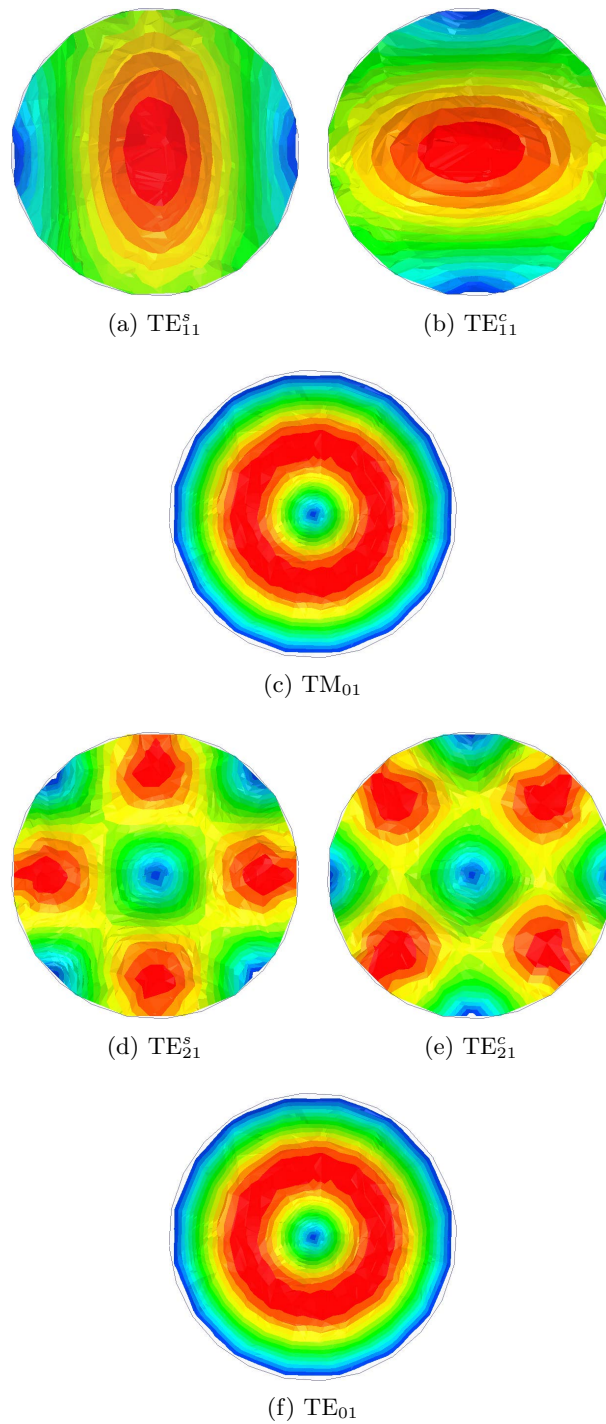


Figure 4.4: Amplitude of the first-order modes of a circular waveguide.

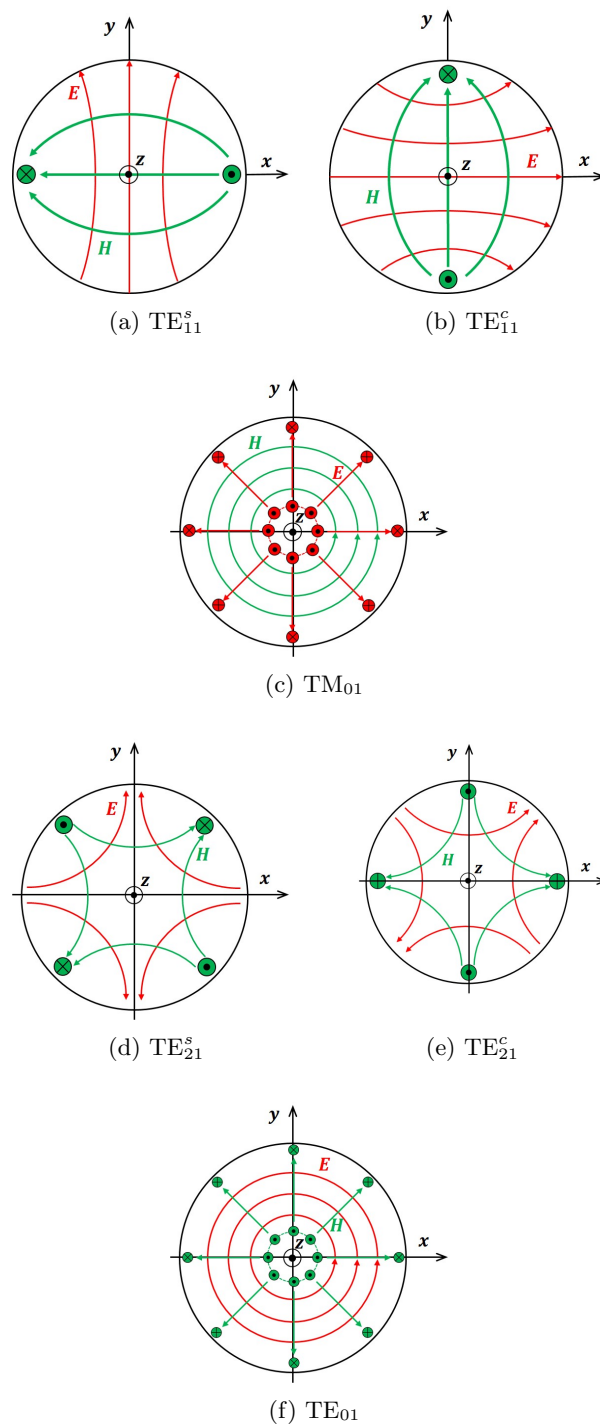


Figure 4.5: Field vectors of the first-order modes of a circular waveguide.

way² is expressed by the following relationships [6].

$$\left\{ \begin{array}{l} E_{\theta} = \frac{J_1(ka \sin \theta)}{ka \sin \theta} \frac{\sin \phi}{\tau'_{11} \sqrt{1 - \left(\frac{1}{\tau'_{11}}\right)^2}} \\ E_{\phi} = \frac{J'_1(ka \sin \theta)}{1 - \left(\frac{ka \sin \theta}{\tau'_{11}}\right)^2} \frac{\cos \phi}{\tau'_{11} \sqrt{1 - \left(\frac{1}{\tau'_{11}}\right)^2}} \end{array} \right. \quad (4.3)$$

where τ'_{11} is the first zero of the derivative of the first-order Bessel function of the first kind J'_1 .

The electric field of the TE_{11}^c mode is just the 90° rotation of the TE_{11}^c mode.

TM₀₁

The electric field of the TM_{01}^s is given by:

$$\left\{ \begin{array}{l} E_{\theta} = \frac{1 + \cos \theta}{2} \frac{J_1(ka \sin \theta)}{\tau_{11}^2 - (ka \sin \theta)^2} \\ E_{\phi} = 0 \end{array} \right. \quad (4.4)$$

TE₂₁

The electric field of the TE_{21}^c is given by:

$$\left\{ \begin{array}{l} E_{\theta} = \frac{J_2(ka \sin \theta)}{ka \sin \theta} \frac{2 \sin 2\phi}{\tau'_{21} \sqrt{1 - \left(\frac{2}{\tau'_{21}}\right)^2}} \\ E_{\phi} = \frac{J'_2(ka \sin \theta)}{1 - \left(\frac{ka \sin \theta}{\tau'_{21}}\right)^2} \frac{\cos 2\phi}{\tau'_{21} \sqrt{1 - \left(\frac{2}{\tau'_{21}}\right)^2}} \end{array} \right. \quad (4.5)$$

TE₀₁

The electric field of the TE_{01} is given by:

$$\left\{ \begin{array}{l} E_{\theta} = 0 \\ E_{\phi} = \frac{1 + \cos \theta}{2} \frac{J_1(ka \sin \theta)}{\tau_{11}^2 - (ka \sin \theta)^2} \end{array} \right. \quad (4.6)$$

² θ is the angle between the look direction and the z axis, while ϕ is the the angle between the x axis and the projection of the look direction onto the xy plane. In this case x and y are the same as those depicted in Fig. 4.5.

4.3.3 Approximate expressions around boresight

In satellite communications, the antenna beamwidths are usually very narrow. ESTRACK antennas are large in terms of wavelength, so it is useful to make some approximations of the radiated fields due to the high-order modes of the circular waveguide. Thanks to these approximation, it will be possible to immediately understand the mechanism behind the multi-mode monopulse.

Such analysis was carried out in total independence of the published literature. I searched for textbooks or papers describing in detail how multi-mode monopulse works, with no much success. I apologize if I did not find possible important authors who treated this topic before.

Approximations of Bessel functions

Bessel function can, naturally, be approximated around the origin. In particular, the following expressions hold:

$$J_0(x) \simeq 1 - \frac{x^2}{4} + o(x^4) \quad (4.7a)$$

$$J_1(x) \simeq \frac{x}{2} + o(x^3) \quad (4.7b)$$

$$J_2(x) \simeq \frac{x^2}{8} + o(x^4) \quad (4.7c)$$

As a consequence, their derivatives can be approximated as:

$$J'_0(x) \simeq -\frac{x}{2} + o(x^3) \quad (4.8a)$$

$$J'_1(x) \simeq \frac{1}{2} + o(x^2) \quad (4.8b)$$

$$J'_2(x) \simeq \frac{x}{4} + o(x^3) \quad (4.8c)$$

where $o(x^n)$ (called *little "o"* of x^n) is a term whose infinitesimal behavior is similar to x^n .

Approximation of TE₁₁

Gathering all constant terms in Eq. 4.3 under a unique constant, say K_{11} , and using the approximate expression 4.7b and 4.8b, the radiated field of

the TE_{11}^s around the boresight ($\theta \rightarrow 0$) is given by:

$$\begin{cases} E_\theta \simeq K_{11} \sin \phi \\ E_\phi \simeq K_{11} \cos \phi \end{cases} \quad (4.9)$$

Approximation of TM_{01}

Gathering all constant terms in Eq. 4.4 under a unique constant, say K_{m01} , approximating $\cos \theta \simeq 1$ and using the expression 4.7b, the radiated field of the TM_{01} around the boresight is given by:

$$\begin{cases} E_\theta \simeq K_{m01} \theta \\ E_\phi \simeq 0 \end{cases} \quad (4.10)$$

Approximation of TE_{21}

Gathering all constant terms in Eq. 4.6 under a unique constant, say K_{21} , approximating $\sin \theta \simeq \theta$ and using the approximate expression 4.7c and 4.8c, the radiated field of the TE_{21}^c around the boresight is given by:

$$\begin{cases} E_\theta \simeq K_{21} \theta \sin 2\phi \\ E_\phi \simeq K_{21} \theta \cos 2\phi \end{cases} \quad (4.11)$$

Approximation of TE_{01}

Gathering all constant terms in Eq. 4.6 under a unique constant, say K_{e01} , approximating $\cos \theta \simeq 1$ and using the expression 4.7b, the radiated field of the TE_{01} around the boresight is given by:

$$\begin{cases} E_\theta \simeq 0 \\ E_\phi \simeq K_{e01} \theta \end{cases} \quad (4.12)$$

Approximated fields in cartesian coordinates

A monopulse receiver outputs two pieces of misalignment information, namely azimuth and elevation error signals Δ_{AZ} , Δ_{EL} . Actually, the monopulse difference signals are not exactly azimuth and elevation misalignments, but they are rather elevation and cross-elevation misalignments, as shown in Fig. 4.6. In particular, \overline{OB} is the boresight axis. The elevation angle θ_{el} is the angle $E\hat{O}B$, while the cross-elevation angle θ_{xe} is the angle $A\hat{O}B$. In the next sections, these angles are also intuitively called vertical misalignment θ_V and horizontal misalignment θ_H . The true azimuth and elevation

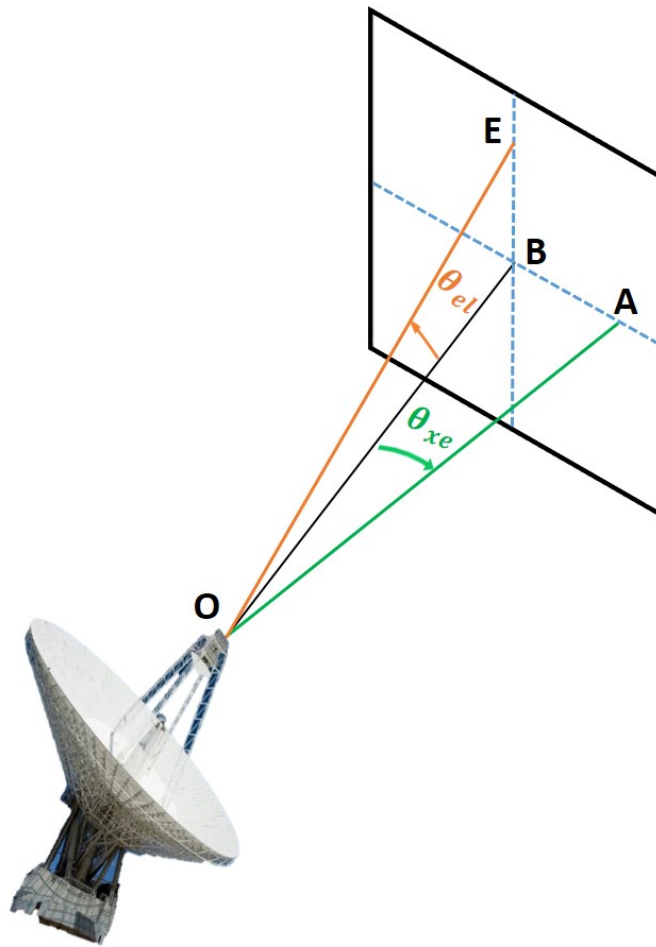


Figure 4.6: Elevation and cross-elevation misalignments.

angles (referred to the antenna elevation/azimuth reference system) are retrieved through mathematical transformations applied on the elevation and cross-elevation angles.

Since the monopulse outputs are related to vertical and horizontal misalignments, it is more convenient to express all the fields radiated by the modes in cartesian coordinates XY . The polar-coordinate expressions of the high-order-mode fields (around boresight) can be also written as:

$$\vec{E}_{11}^s \simeq K_{11} (\hat{\theta} \sin \phi + \hat{\phi} \cos \phi) \quad (4.13a)$$

$$\vec{E}_{11}^c \simeq K_{11} (\hat{\theta} \cos \phi - \hat{\phi} \sin \phi) \quad (4.13b)$$

$$\vec{E}_{m01} \simeq K_{m01} \theta \hat{\theta} \quad (4.13c)$$

$$\vec{E}_{21}^s \simeq K_{21} \theta (-\hat{\theta} \cos 2\phi + \hat{\phi} \sin 2\phi) \quad (4.13d)$$

$$\vec{E}_{21}^c \simeq K_{21} \theta (\hat{\theta} \sin 2\phi + \hat{\phi} \cos 2\phi) \quad (4.13e)$$

$$\vec{E}_{m01} \simeq K_{e01} \theta \hat{\phi} \quad (4.13f)$$

where the expressions for the other degenerate modes have also been added. Now, remembering the polar-to-cartesian transformation [7], it is possible to write:

$$\hat{\theta} = \hat{x} \cos \theta \cos \phi + \hat{y} \cos \theta \sin \phi - \hat{z} \sin \phi \quad (4.14a)$$

$$\hat{\phi} = -\hat{x} \sin \phi + \hat{y} \cos \phi \quad (4.14b)$$

which, around boresight ($\theta \rightarrow 0$), become

$$\hat{\theta} = \hat{x} \cos \phi + \hat{y} \sin \phi \quad (4.15a)$$

$$\hat{\phi} = -\hat{x} \sin \phi + \hat{y} \cos \phi \quad (4.15b)$$

Using Eqs. 4.15, it is possible to express all fields in cartesian coordinates as described in detail in the following paragraphs.

TE₁₁ in cartesian coordinates

Re-writing the E-vector of Eq. 4.13a by using expressions 4.15, we obtain

$$\begin{aligned} \vec{E}_{11}^s &\simeq K_{11} [\sin \phi (\hat{x} \cos \phi + \hat{y} \sin \phi) + \cos \phi (-\hat{x} \sin \phi + \hat{y} \cos \phi)] \\ &= K_{11} [\hat{x} (\sin \phi \cos \phi - \sin \phi \cos \phi) + \hat{y} (\sin^2 \phi + \cos^2 \phi)] \\ &= K_{11} \hat{y} \end{aligned} \quad (4.16)$$

In the same way, it can be shown that

$$\vec{E}_{11}^c \simeq K_{11} \hat{x} \quad (4.17)$$

TM₀₁ and TE₀₁ in cartesian coordinates

Re-writing the E-vector of Eq. 4.13c by using expressions 4.15, we obtain

$$\vec{E}_{m01} \simeq K_{m01} \theta (\hat{x} \cos \phi + \hat{y} \sin \phi) \quad (4.18)$$

In the same way, it can be shown that

$$\vec{E}_{e11} \simeq K_{e01} \theta (-\hat{x} \sin \phi + \hat{y} \cos \phi) \quad (4.19)$$

TE₂₁ in cartesian coordinates

Re-writing the E-vector of Eq. 4.13d by using expressions 4.15, we obtain

$$\begin{aligned} \vec{E}_{21}^s &\simeq K_{21} \theta [-(\hat{x} \cos \phi + \hat{y} \sin \phi) \cos 2\phi + (-\hat{x} \sin \phi + \hat{y} \cos \phi) \sin 2\phi] \\ &= K_{21} \theta [-\hat{x} (\cos 2\phi \cos \phi + \sin 2\phi \sin \phi) + \hat{y} (\sin 2\phi \cos \phi - \cos 2\phi \sin \phi)] \\ &= K_{21} \theta (-\hat{x} \cos \phi + \hat{y} \sin \phi) \end{aligned} \quad (4.20)$$

where trivial trigonometric identities have been used³. Similarly, the TE₂₁^c mode can be expressed as:

$$\vec{E}_{21}^c = K_{21} \theta (\hat{x} \sin \phi + \hat{y} \cos \phi) \quad (4.21)$$

4.3.4 Tracking information extraction

Consider an incident electric field \vec{E}_{inc} which is received by the antenna from a certain direction that is different from the boresight and tilted by an angle θ_V in elevation and θ_H in cross-elevation, shown in Fig. 4.7. Observing Fig. 4.7, we can see some interesting relationships between the angles. These are only angle-related considerations, thus for this purpose, the length of z_p does not matter. For simplicity of calculations, let's pose $z_p = 1$. In

3

$$\cos \alpha \cos \beta + \sin \alpha \sin \beta = \cos(\alpha - \beta)$$

$$\sin \alpha \cos \beta - \cos \alpha \sin \beta = \sin(\alpha - \beta)$$

For these identities,

$$\cos 2\phi \cos \phi + \sin 2\phi \sin \phi = \cos(2\phi - \phi) \equiv \cos \phi$$

$$\sin 2\phi \cos \phi - \cos 2\phi \sin \phi = \sin(2\phi - \phi) \equiv \sin \phi$$

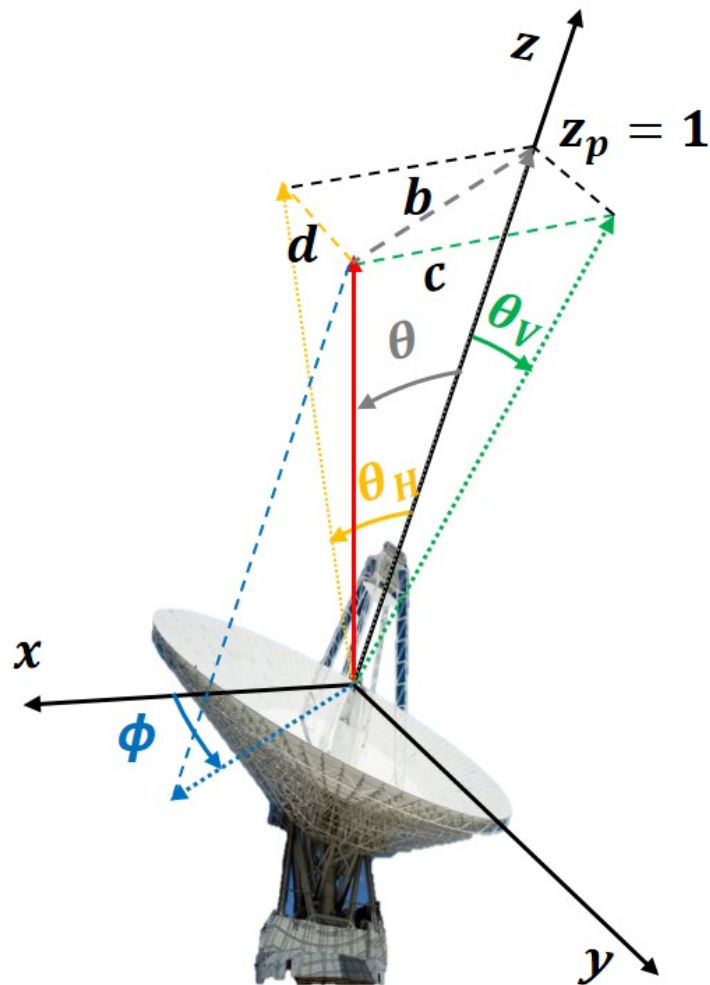


Figure 4.7: Definition of vertical (or elevation) misalignment angle θ_V and horizontal (or cross-elevation) misalignment angle θ_H .

particular, looking at the figure, we can say that:

$$b = z_p \tan \theta = \tan \theta \quad (4.22)$$

$$c = z_p \tan \theta_H = \tan \theta_H \quad (4.23)$$

$$d = z_p \tan \theta_V = \tan \theta_V \quad (4.24)$$

Furthermore, we can observe that:

$$\tan \theta_H \equiv c = b \cos \phi = \tan \theta \cos \phi \quad (4.25)$$

$$\tan \theta_V \equiv d = b \sin \phi = \tan \theta \sin \phi \quad (4.26)$$

For small angles around boresight ($\theta \rightarrow 0$, but also $\theta_H \rightarrow 0$ and $\theta_V \rightarrow 0$):

$$\theta_H \simeq \theta \cos \phi \quad (4.27a)$$

$$\theta_V \simeq \theta \sin \phi \quad (4.27b)$$

Very interestingly, through Eqs. 4.27, we can re-write the expressions of the E-field vectors radiated by the circular waveguide modes (small-angle approximation):

$$\vec{E}_{11}^s \simeq K_{11} \hat{y} \quad (4.28a)$$

$$\vec{E}_{11}^c \simeq K_{11} \hat{x} \quad (4.28b)$$

$$\vec{E}_{m01} \simeq K_{m01} (\hat{x}\theta_H + \hat{y}\theta_V) \quad (4.28c)$$

$$\vec{E}_{21}^s \simeq K_{21} (-\hat{x}\theta_H + \hat{y}\theta_V) \quad (4.28d)$$

$$\vec{E}_{21}^c \simeq K_{21} (\hat{x}\theta_V + \hat{y}\theta_H) \quad (4.28e)$$

$$\vec{E}_{m01} \simeq K_{e01} (-\hat{x}\theta_V + \hat{y}\theta_H) \quad (4.28f)$$

From the relationships 4.28, we can observe that the vertical and the horizontal misalignment information is carried by each one of the mode polarizations. It means that, for instance, if a vertically polarized field impinges on the antenna, the TM_{01} mode will carry the elevation misalignment information, while the TE_{01} mode will carry the cross-elevation misalignment information. Similarly, the TE_{21}^s mode will carry the elevation misalignment information, while the TE_{21}^c mode will carry the cross-elevation misalignment information. For these reasons, it is now very clear why multimode monopulse antennas normally adopt the TE_{21}^s - TE_{21}^c mode combination or the TM_{01} - TE_{01} mode combination; because with such combinations it is possible to track both in elevation and in azimuth.

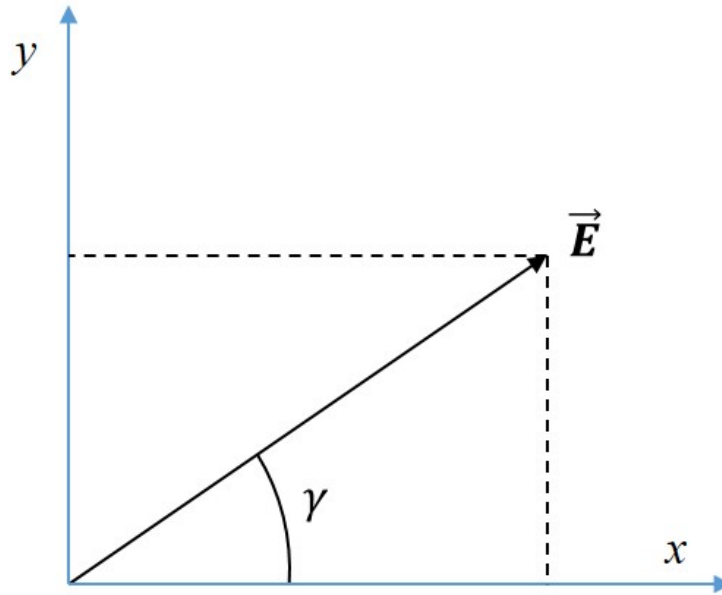


Figure 4.8: Linearly polarized incident electric field.

But, let's try to develop a systematic theory to describe the tracking error extraction by also considering the polarization of the incident field. The polarization of the incident field can be assumed to be either linear (as shown in Fig. 4.8), with the E-field vector forming an angle γ with respect to the x axis, left-hand circular (LHCP) or right-hand circular (RHCP). As already discussed, in multimode monopulse architecture, the degenerate mode TE_{11} is used to make the Σ beam, while a possible combination of either TM_{01} - TE_{01} or TE_{21}^s - TE_{21}^c is used to extract the Δ signals, namely the vertical difference signal Δ_V and the horizontal difference signal Δ_H . The two different combinations will be treated hereafter, although other cross-combinations are possible such as TM_{01} - TE_{21}^c and TE_{21}^s - TE_{01} . The following discussion is intended to hold for small-angles around boresight, in the range where a satellite monopulse system normally operates.

The incident field

In case of **linear polarization**, the received incident field can be expressed as:

$$\vec{E}_{\text{inc}} = E_0 (\hat{x} \cos \gamma + \hat{y} \sin \gamma) e^{-j\psi} \quad (4.29)$$

where E_0 is the amplitude of the incident field⁴, γ is the polarization angle, and ψ is the phase of the received E-field.

In case of **left-hand circular polarization (LHCP)**, the received incident field can be expressed as [7]:

$$\vec{E}_{\text{inc}} = \frac{E_0}{\sqrt{2}} (j \hat{x} + \hat{y}) e^{-j\psi} \quad (4.30)$$

and in case of **right-hand circular polarization (RHCP)**, the received incident field can be expressed as:

$$\vec{E}_{\text{inc}} = \frac{E_0}{\sqrt{2}} (-j \hat{x} + \hat{y}) e^{-j\psi} \quad (4.31)$$

The TE₁₁ as Σ signal

The fundamental degenerate mode was shown to make a very good Σ beam. In fact, it satisfies the most important requirement: being misalignment-angle-independent. The signal received through the degenerate mode TE₁₁ can be seen as the scalar product of the incident field and the mode polarization. Since the system normally operates in circular polarization, too, a *septum polarizer* is used to separate the LHCP from the RHCP.

The septum polarizer. This component, shown in Fig. 4.9, is commonly used to separate two orthogonal polarizations incident at one physical port and inject them in two separate physical output ports. If one of the input polarisation is properly phase-shifted with respect to the other, at the output ports the RHCP and LHCP polarizations can be separated. The scattering matrix, using the port notation in Fig. 4.9 is:

$$\frac{1}{\sqrt{2}} \begin{pmatrix} 0 & 0 & 1 & 1 \\ 0 & 0 & -j & j \\ 1 & -j & 0 & 0 \\ 1 & j & 0 & 0 \end{pmatrix} \quad (4.32)$$

⁴Be aware that the amplitude of the incident field depends on the distance from the transmitter, the gain and the transmitted power. But, as shown in Sec. 4.2, since the amplitude of the difference signal will be divided by the amplitude of the sum signal, all terms which are common in the two signals (like the distance from the source or the transmitted power) will be cancelled. This allows us to neglect all these terms.

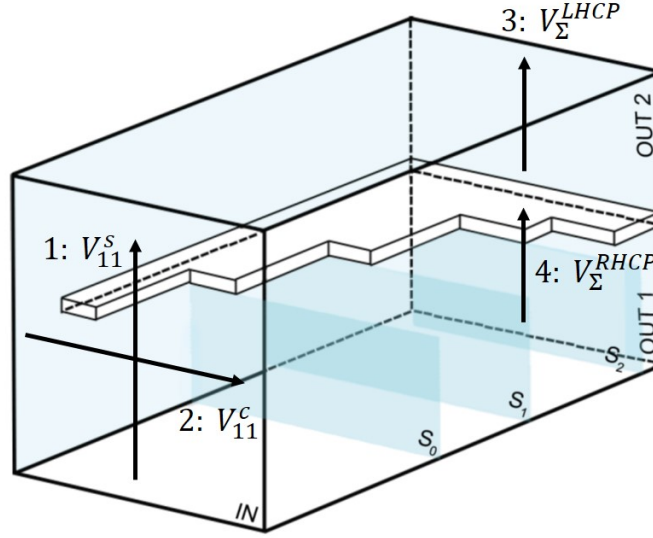


Figure 4.9: A septum polariser.

In case of **linear polarization**, the signals (labeled as “V”) received through the TE₁₁ modes, taking Eq. 4.29 into account, are:

$$V_{11}^s \simeq K_{11} E_0 \sin \gamma e^{-j\psi} \quad (4.33a)$$

$$V_{11}^c \simeq K_{11} E_0 \cos \gamma e^{-j\psi} \quad (4.33b)$$

If V_{11}^s and V_{11}^c are used at the input of the septum, the result at the output, using the septum’s scattering matrix, is:

$$\begin{aligned} V_{\Sigma}^{LHCP} &= \frac{1}{\sqrt{2}} (V_{11}^s - jV_{11}^c) \simeq \frac{1}{\sqrt{2}} K_{11} E_0 (\sin \gamma - j \cos \gamma) e^{-j\psi} = \\ &= \frac{-j}{\sqrt{2}} K_{11} E_0 e^{j\gamma} e^{-j\psi} = \frac{1}{\sqrt{2}} K_{11} E_0 e^{j(\gamma-\pi/2)} e^{-j\psi} \end{aligned} \quad (4.34)$$

$$V_{\Sigma}^{RHCP} = \frac{1}{\sqrt{2}} (V_{11}^s + jV_{11}^c) \simeq \frac{1}{\sqrt{2}} K_{11} E_0 e^{-j(\gamma-\pi/2)} e^{-j\psi}$$

In case of **LHCP polarization**, the signals received through the TE₁₁ modes, taking Eqs. 4.30, 4.28a, and 4.28b into account, are:

$$V_{11}^s \simeq K_{11} \frac{E_0}{\sqrt{2}} e^{-j\psi} \quad (4.35a)$$

$$V_{11}^c \simeq j K_{11} \frac{E_0}{\sqrt{2}} e^{-j\psi} \quad (4.35b)$$

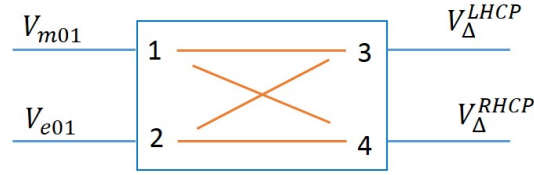


Figure 4.10: 3 dB/90° coupler in case of TM_{01} - TE_{01} mode combination.

If V_{11}^s and V_{11}^c are used at the input of the septum, the result at the output, using the septum's scattering matrix, is:

$$\begin{aligned} V_{\Sigma}^{\text{LHCP}} &= \frac{1}{\sqrt{2}} (V_{11}^s - jV_{11}^c) \simeq \frac{1}{\sqrt{2}} \simeq K_{11} \frac{E_0}{\sqrt{2}} (1 + 1) e^{-j\psi} = \\ &= K_{11} E_0 e^{-j\psi} \end{aligned} \quad (4.36)$$

$$V_{\Sigma}^{\text{RHCP}} = \frac{1}{\sqrt{2}} (V_{11}^s + jV_{11}^c) \simeq 0$$

In case of **RHCP polarization**, the signals received through the TE_{11} modes, taking Eqs. 4.31, 4.28a, and 4.28b into account, are:

$$V_{11}^s \simeq K_{11} \frac{E_0}{\sqrt{2}} e^{-j\psi} \quad (4.37a)$$

$$V_{11}^c \simeq -j K_{11} \frac{E_0}{\sqrt{2}} e^{-j\psi} \quad (4.37b)$$

If V_{11}^s and V_{11}^c are used at the input of the septum, the result at the output, using the septum's scattering matrix, is:

$$V_{\Sigma}^{\text{LHCP}} = \frac{1}{\sqrt{2}} (V_{11}^s - jV_{11}^c) \simeq \frac{1}{\sqrt{2}} \simeq K_{11} \frac{E_0}{\sqrt{2}} (1 - 1) e^{-j\psi} = 0 \quad (4.38)$$

$$V_{\Sigma}^{\text{RHCP}} = \frac{1}{\sqrt{2}} (V_{11}^s + jV_{11}^c) \simeq K_{11} E_0 e^{-j\psi}$$

The TM_{01} - TE_{01} as Δ signals

The signal received through these modes can be seen as the scalar product of the incident field and the mode polarization. Since the system normally operates in circular polarization, too, in this case a 3 dB/90° coupler is used to separate the LHCP from the RHCP.

The 3 dB/90° coupler. This component is a 4-port microwave device. The scattering matrix, using the port notation in Fig. 4.10 is:

$$\frac{1}{\sqrt{2}} \begin{pmatrix} 0 & 0 & 1 & j \\ 0 & 0 & j & 1 \\ 1 & j & 0 & 0 \\ j & 1 & 0 & 0 \end{pmatrix} \quad (4.39)$$

In case of **linear polarization**, the signals (labeled as “V”) received through the TM₀₁ and TE₀₁ modes, taking Eq. 4.29, 4.28c, and 4.28f into account, are:

$$V_{m01} \simeq K_{m01} E_0 (\theta_H \cos \gamma + \theta_V \sin \gamma) e^{-j\psi} \quad (4.40a)$$

$$V_{e01} \simeq K_{e01} E_0 (-\theta_V \cos \gamma + \theta_H \sin \gamma) e^{-j\psi} \quad (4.40b)$$

where it is possible that $K_{m01} \equiv \simeq K_{e01} = K_{me}$. If V_{m01} and V_{e01} are used at the input of the coupler, the result at the output, using the coupler’s scattering matrix, is:

$$\begin{aligned} V_{\Delta}^{\text{LHCP}} &= \frac{1}{\sqrt{2}} (V_{m01} + jV_{e01}) \\ &\simeq \frac{1}{\sqrt{2}} K_{me} E_0 [(\theta_H \cos \gamma + \theta_V \sin \gamma) + j(-\theta_V \cos \gamma + \theta_H \sin \gamma)] e^{-j\psi} \\ &= \frac{1}{\sqrt{2}} K_{me} E_0 [\theta_H (\cos \gamma + j \sin \gamma) - j\theta_V (\cos \gamma + j \sin \gamma)] e^{-j\psi} \\ &= \frac{1}{\sqrt{2}} K_{me} E_0 [\theta_H e^{j\gamma} + \theta_V e^{j(\gamma-\pi/2)}] e^{-j\psi} \\ V_{\Delta}^{\text{RHCP}} &= \frac{1}{\sqrt{2}} (jV_{m01} + V_{e01}) \\ &\simeq \frac{1}{\sqrt{2}} K_{me} E_0 [\theta_H e^{-j(\gamma-\pi/2)} - \theta_V e^{-j\gamma}] e^{-j\psi} \end{aligned} \quad (4.41)$$

In case of **LHCP polarization**, the signals received through the TM₀₁ and TE₀₁ modes, taking Eq. 4.30, 4.28c, and 4.28f into account, are:

$$V_{m01} \simeq \frac{E_0}{\sqrt{2}} K_{me} (j\theta_H + \theta_V) e^{-j\psi} \quad (4.42a)$$

$$V_{e01} \simeq \frac{E_0}{\sqrt{2}} K_{me} (-j\theta_V + \theta_H) e^{-j\psi} \quad (4.42b)$$

If V_{m01} and V_{e01} are used at the input of the coupler, the result at the output, using the coupler's scattering matrix, is:

$$\begin{aligned}
 V_{\Delta}^{\text{LHCP}} &= \frac{1}{\sqrt{2}} (V_{m01} + jV_{e01}) \\
 &\simeq \frac{K_{\text{me}} E_0}{\sqrt{2} \sqrt{2}} (j\theta_H + \theta_V + \theta_V + j\theta_H) e^{-j\psi} \\
 &= \frac{K_{\text{me}} E_0}{2} (2\theta_V + 2j\theta_H) e^{-j\psi} = K_{\text{me}} E_0 (\theta_V + j\theta_H) e^{-j\psi}
 \end{aligned} \tag{4.43}$$

$$V_{\Delta}^{\text{RHCP}} = \frac{1}{\sqrt{2}} (jV_{m01} + V_{e01}) = 0$$

In case of **RHCP polarization**, the signals received through the TM_{01} and TE_{01} modes, taking Eq. 4.31, 4.28c, and 4.28f into account, are:

$$V_{m01} \simeq \frac{E_0}{\sqrt{2}} K_{\text{me}} (-j\theta_H + \theta_V) e^{-j\psi} \tag{4.44a}$$

$$V_{e01} \simeq \frac{E_0}{\sqrt{2}} K_{\text{me}} (j\theta_V + \theta_H) e^{-j\psi} \tag{4.44b}$$

If V_{m01} and V_{e01} are used at the input of the coupler, the result at the output, using the coupler's scattering matrix, is:

$$\begin{aligned}
 V_{\Delta}^{\text{LHCP}} &= \frac{1}{\sqrt{2}} (V_{m01} + jV_{e01}) \simeq 0 \\
 V_{\Delta}^{\text{RHCP}} &= \frac{1}{\sqrt{2}} (jV_{m01} + V_{e01}) = \\
 &\simeq K_{\text{me}} E_0 (j\theta_V + \theta_H) e^{-j\psi}
 \end{aligned} \tag{4.45}$$

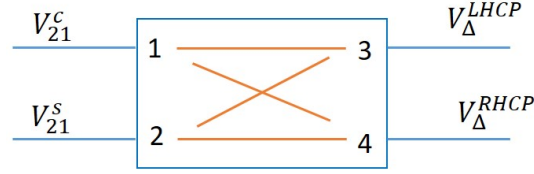
The TE_{21}^s - TE_{21}^c as Δ signals

The signal received through the degenerate mode TE_{21} can be seen as the scalar product of the incident field and the mode polarization. Since the system normally operates in circular polarization, too, in this case a $3 \text{ dB}/90^\circ$ coupler is used to separate the LHCP from the RHCP.

In case of **linear polarization**, the signals (labeled as "V") received through the TE_{21}^s and TE_{21}^c modes, taking Eq. 4.29, 4.28d, and 4.28e into account, are:

$$V_{21}^s \simeq K_{21} E_0 (-\theta_H \cos \gamma + \theta_V \sin \gamma) e^{-j\psi} \tag{4.46a}$$

$$V_{21}^c \simeq K_{21} E_0 (\theta_V \cos \gamma + \theta_H \sin \gamma) e^{-j\psi} \tag{4.46b}$$


 Figure 4.11: 3 dB/90° coupler in case of TE_{21}^s - TE_{21}^c mode combination.

If V_{21}^s and V_{21}^c are used at the input of the coupler, the result at the output, using the coupler's scattering matrix 4.39, is:

$$\begin{aligned}
 V_{\Delta}^{LHCP} &= \frac{1}{\sqrt{2}} (V_{21}^c + jV_{21}^s) \\
 &\simeq \frac{1}{\sqrt{2}} K_{21} E_0 [(\theta_V \cos \gamma + \theta_H \sin \gamma) + j(-\theta_H \cos \gamma + \theta_V \sin \gamma)] e^{-j\psi} \\
 &= \frac{1}{\sqrt{2}} K_{21} E_0 [-j\theta_H (\cos \gamma + j \sin \gamma) + \theta_V (\cos \gamma + j \sin \gamma)] e^{-j\psi} \\
 &= \frac{1}{\sqrt{2}} K_{21} E_0 [\theta_H e^{j(\gamma-\pi/2)} + \theta_V e^{j\gamma}] e^{-j\psi} \\
 V_{\Delta}^{RHCP} &= \frac{1}{\sqrt{2}} (jV_{21}^c + V_{21}^s) \\
 &\simeq \frac{1}{\sqrt{2}} K_{21} E_0 [-\theta_H e^{-j\gamma} + \theta_V e^{-j(\gamma-\pi/2)}] e^{-j\psi}
 \end{aligned} \tag{4.47}$$

In case of **LHCP polarization**, the signals received through the TE_{21} modes, taking Eq. 4.30, 4.28d, and 4.28e into account, are:

$$V_{21}^s \simeq K_{21} \frac{E_0}{\sqrt{2}} (-j\theta_H + \theta_V) e^{-j\psi} \tag{4.48a}$$

$$V_{21}^c \simeq K_{21} \frac{E_0}{\sqrt{2}} (j\theta_V + \theta_H) e^{-j\psi} \tag{4.48b}$$

If V_{21}^c and V_{21}^s are used at the input of the coupler, the result at the output,

using the coupler's scattering matrix, is:

$$\begin{aligned} V_{\Delta}^{\text{LHCP}} &= \frac{1}{\sqrt{2}} (V_{21}^c + j V_{21}^s) \\ &\simeq \frac{K_{21}}{\sqrt{2}} \frac{E_0}{\sqrt{2}} (2j\theta_V + 2\theta_H) = K_{21} E_0 (j\theta_V + \theta_H) e^{-j\psi} \end{aligned} \quad (4.49)$$

$$\begin{aligned} V_{\Delta}^{\text{RHCP}} &= \frac{1}{\sqrt{2}} (j V_{21}^c + V_{21}^s) \\ &\simeq \frac{K_{21} E_0}{2} (-\theta_V + j\theta_H - j\theta_H + \theta_V) = 0 \end{aligned}$$

In case of **RHCP polarization**, the signals received through the TE₂₁ modes, taking Eq. 4.31, 4.28d, and 4.28e into account, are:

$$V_{21}^s \simeq K_{21} \frac{E_0}{\sqrt{2}} (j\theta_H + \theta_V) e^{-j\psi} \quad (4.50a)$$

$$V_{21}^c \simeq K_{21} \frac{E_0}{\sqrt{2}} (-j\theta_V + \theta_H) e^{-j\psi} \quad (4.50b)$$

If V_{21}^c and V_{21}^s are used at the input of the coupler, the result at the output, using the coupler's scattering matrix, is:

$$\begin{aligned} V_{\Delta}^{\text{LHCP}} &= \frac{1}{\sqrt{2}} (V_{21}^c + j V_{21}^s) \\ &\simeq \frac{K_{21} E_0}{2} (-j\theta_V + \theta_H - \theta_H + j\theta_V) e^{-j\psi} = 0 \end{aligned} \quad (4.51)$$

$$\begin{aligned} V_{\Delta}^{\text{RHCP}} &= \frac{1}{\sqrt{2}} (j V_{21}^c + V_{21}^s) \\ &\simeq K_{21} E_0 (\theta_V + j\theta_H) e^{-j\psi} \end{aligned}$$

The magic behind monopulse

After having calculated the received signals in three different polarization cases (linear, LHCP, and RHCP) and in the most used mode combinations, now it is time to understand how the tracking information can be retrieved.

Here comes the magic behind multimode monopulse. In particular, in all the examined polarizations, it is very easy to notice an interesting relationship between the Σ (or sum) signal at the output of the septum polarizer

and the Δ (or difference) signals at the outputs of the 3 dB/90° coupler: the elevation (θ_V) and the cross-elevation (θ_H) tracking information carried by the difference modes are in phase-quadrature at the output of the coupler⁵; furthermore, they have a specific phase relationship with the Σ signal, i.e. one of the two misalignment angles is in phase with the Σ signal. To assess that, it is better to take an example.

Example 4.3.1. Let's assume to have a monopulse chain where the TE_{11} mode is used as Σ (it is always the case) and the TE_{21} degenerate modes are used as Δ signals; the incident field is supposed to be linearly polarized. In case of linear polarization, both outputs of the septum (LH and RH ports) and both outputs of the coupler (LH and RH ports) carry the same power. Thus, either the LH or the RH ports can be used to extract the tracking information. For this example, let's use the LH channels. The LH output of the septum carries the signal (see Eq. 4.34)

$$V_{\Sigma}^{\text{LHCP}} \simeq \frac{1}{\sqrt{2}} K_{11} E_0 e^{j(\gamma-\pi/2)} e^{-j\psi}$$

while the LH output of the 3 dB/90° coupler carries the signal (see Eq. 4.49)

$$V_{\Delta}^{\text{LHCP}} \simeq \frac{1}{\sqrt{2}} K_{21} E_0 [\theta_H e^{j(\gamma-\pi/2)} + \theta_V e^{j\gamma}] e^{-j\psi}$$

Evidently, in this example, the elevation misalignment θ_V is in phase with the Σ channel, while the cross-elevation misalignment θ_H is in phase quadrature! The last step to extract the monopulse signals, which will eventually be used by the servo system to drive the antenna motors, is to normalize the difference channels by the amplitude of the sum channel (to get a monopulse error signal being independent of the satellite's distance) and use an IQ demodulator (in-phase/quadrature-phase demodulator), triggered with the phase of the sum signal, to separate the elevation from the cross-elevation misalignment information, as shown in Fig. 4.12.

The result shown in Example 4.3.1 proves the phase relationships between the difference and sum signals, showing that to extract the monopulse tracking misalignment angles, it is sufficient an IQ demodulator triggered with the phase of the sum signal and an automatic gain control (AGC) to

⁵E.g. take Expression 4.51. As one may notice, the RH Δ signal highlights a specific quadrature phase relationship between θ_V and θ_H .

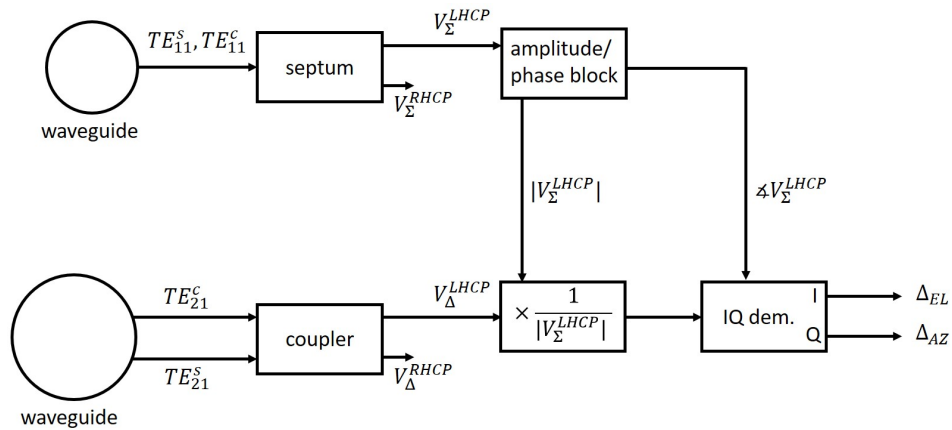


Figure 4.12: Tracking extraction based on Example 4.3.1.

normalize by the amplitude of the sum signal. The same chain architecture can be applied to all other mode combinations and polarization cases; sometimes, you only have to exchange θ_V and θ_H or to apply a change of sign, but the mutual phase relationships are unaltered.

A comment. The approximations done in the previous discussion only hold in a narrow range of angles around the antenna boresight; but a monopulse system is normally used until the -3 dB beamwidth of the sum radiation pattern, that is in regions where the relationship between the actual misalignment and the monopulse error voltages is not linear but an increasing monotone function having a tangent-like behavior (see Fig. 4.2). This is not a problem because monopulse systems commonly apply a calibration function on the error voltages to extract the actual misalignment angles, and the antenna tracks the satellites (or the targets) without any problem within the 3 dB beamwidth.

Another comment. Sometimes, in practical monopulse antennas, there are some isolated cases where the antenna is in locked condition (it is tracking something) but the target is completely in another position. This occurs because both the sum and the difference beams have several sidelobes and there are some regions where a sidelobe of the sum beam overlaps with some sidelobes of the difference beams having a shape that resemble the monopulse beams. In these cases, the antenna starts tracking an idle target (non-existing in that position), of course being completely wrong about the actual target position.

4.4 Tracking in ESTRACK stations

The core Estrack network comprises seven stations in seven countries. The ESTRACK Core Network, see Fig. 4.13, consists of 6 stations that host 8 terminals. These consist of three Deep Space Stations at Cebreros (Spain) with terminal CEB-1, Malargue (Argentina), with terminal MLG-1, New Norcia (Western Australia), with terminal NNO-1 and NNO-2 and the NE stations in Kiruna (Sweden) with terminals KIR-1 and KIR-2, Kourou (French Guiana) with terminal KRU-1, Redu (Belgium) with terminal RED-1 and Santa Maria of the Azores (Portugal) with terminal SMA-1. In addition, ESTRACK owns a small X-band terminal, which is installed in Malindi (Kenya) as MAL-X. These terminals are continuously maintained, upgraded or put into a safe state in relation to the evolution of the ESA Mission Model.

An overview of ESTRACK stations with related information on frequency bands, monopulse mode combinations, antenna dimensions, feed types, and microwave components in the monopulse chain is reported in Tables 4.1 and 4.2.



Figure 4.13: ESTRACK ground stations in the world.

Table 4.1: ESTRACK Station Overview.

Station	Terminal	Band	Diameter	HPBW	Feed Manufacturer
		GHz	m	mdeg	
Kiruna	KIR-1	S 2200-2300	15	600	Astrium (Airbus)
	KIR-1	X 7600-8500	15	160	Astrium (Airbus)
	KIR-2	S 2200-2300	13	650	Datron
	KIR-2	X 7600-8500	13	190	Datron
Redu	RED-1	S 2200-2300	15	600	Astrium (Airbus)
Kourou	KRU-1	S 2200-2300	15	600	Astrium (Airbus)
	KRU-1	X 8025-8500	15	160	Astrium (Airbus)
	KRU-1 XAA	X 8025-8500	1.3	1500	Astrium (Airbus)
New Norcia	NNO-1	S 2200-2300	35	280	Mirad
	NNO-1	X 8400-8500	35	74	Mirad
	NNO-2 NB	S 2200-2300	4.5	1900	Mirad
	NNO-2 NB	X 8050-8500	4.5	480	Mirad
	NNO-2 WB	X 8050-8500	0.7	3300	Mirad
Cebreros	CEB-1	X 8400-8500	35	Na	Mirad
	CEB-1	K 25500-27000	35	20	Mirad
	CEB-1	K 31800-32300	35	Na	Mirad
Malargue	MLG-1	X 8400-8500	35	Na	Mirad
	MLG-1	K 25500-27000	35	20	Mirad
	MLG-1	K 31800-32300	35	Na	Mirad
Santa Maria	SMA-1	S 2200-2300	5.5	1700	Indra
	SMA-1	X 8025-8400	5.5	500	amercani
Malindi	MAL-X	X 8050-8500	2	1200	Orbit
Svalbard	SG-54	S 2200-2300	6.4	1000	ESA Microwave
	SG-54	K 25500-27000	6.4	100	ESA Microwave

Table 4.2: ESTRACK Terminal feed and combining network components.

Terminal	Band	Mode		Feed		Combining Network		
		Sum	Delta	Sum	Tracking			
KIR-1	S	TE_{11}	$TE_{01}-TM_{01}$	Corrugated	Corrugated	COAX	$3dB/180deg$ hybrid	$3dB/90deg$ hybrid
KIR-1	X	TE_{11}	TE_{21}	Dielectric rod	Dielectric rod	COAX	$3dB/90deg$ hybrid	
KIR-2	S	TE_{11}	$TE_{01}-TM_{01}$	4 dipoles	4 dipoles	COAX	$3dB/90deg$ hybrid	hybrid polariser
KIR-2	X	TE_{11}	TE_{21}	Corrugated	Corrugated	COAX	$3dB/90deg$ hybrid	hybrid polariser
RED-1	S	TE_{11}	$TE_{01}-TM_{01}$	Corrugated	Corrugated	COAX	$3dB/180deg$ hybrid	$3dB/90deg$ hybrid
KRU-1	S	TE_{11}	$TE_{01}-TM_{01}$	Corrugated	Corrugated	COAX	$3dB/180deg$ hybrid	$3dB/90deg$ hybrid
KRU-1	X	TE_{11}	TE_{21}	Dielectric rod	Dielectric rod	COAX	$3dB/90deg$ hybrid	
KRU-1 XAA	X	TE_{11}	TE_{21}	Corrugated	Corrugated	COAX	$3dB/90deg$ hybrid	
NNO-2 NB	S	TE_{11}	TE_{21}	Corrugated	4 pins cavity	COAX	$3dB/90deg$ hybrid	$3dB/180deg$ hybrid
NNO-2 NB	X	TE_{11}	TEM	Corrugated	8 pins cavity	WG	$3dB/180deg$ hybrid	$3dB/90deg$ hybrid
NNO-2 WB	X	TE_{11}	TE_{21}	Corrugated	8 pins cavity	WG	$3dB/180deg$ hybrid	$3dB/90deg$ hybrid
CEB-1	K	TE_{11}	TE_{21}	Corrugated	Corrugated	WG	$3dB/180deg$ hybrid	$3dB/90deg$ hybrid
MLG-1	K	TE_{11}	TE_{21}	Corrugated	Corrugated	WG	$3dB/180deg$ hybrid	$3dB/90deg$ hybrid
SMA-1	S	TE_{11}	$TE_{01}-TM_{01}$	4 dipoles	4 dipoles	WG	$3dB/90deg$ hybrid	OTM
MAL-X	X	TE_{11}	TE_{21}	Dielectric rod	8 pins cavity	COAX	$3dB$ splitter	$3dB/180deg$ hybrid
SG-54	S	TE_{11}	TEM	Corrugated	Corrugated	COAX	OTM	$3dB/180deg$ hybrid
SG-54	S	TE_{11}	TM_{01}	Corrugated	Corrugated	COAX	OTM with integrated TM_{01} -mode coupler	$3dB/180deg$ hybrid

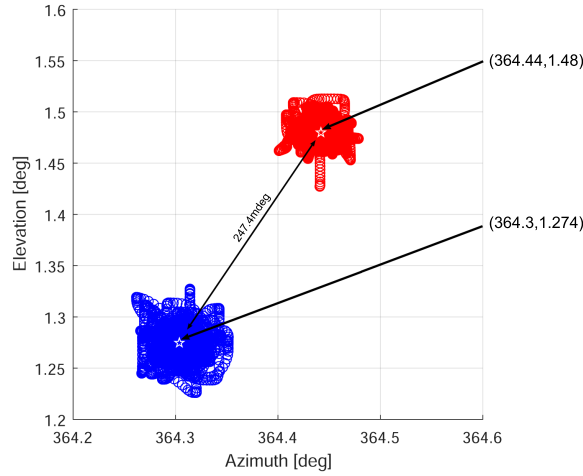


Figure 4.14: Pointing error of NNO-2 antenna.

4.4.1 Tracking problems

Some measurements have been performed with the NNO-2 terminal in X-Band that uses a symmetrical 8-way mode coupler⁶ and the KRU-1 in S-Band that uses a 2-way mode coupler. The following results show pointing errors of the station with New Norcia's calibration tower, 400 m far. From a physical point of view, the antenna performs corrections thanks to autotrack and maintains the target centred in the boresight, in case of errors (due to wind gusts or other sources of error) the antenna continues to move, trying to keep the target in the NULL of the Δ signal. From Fig. 4.14, it is evident that the antenna pointing is centered around the mean value which is the location of the calibration tower's feeds (two horns for LHCP and RHCP each) with an offset of about 250 mdeg which corresponds to about 10% of the half power beam width that could be almost negligible, but since NNO-2 is used in combination with the bigger NNO-1, practically passing the tracking information to the NNO-1 terminal whose HPBW is about 280 mdeg, the error is not that negligible anymore. In the case of KRU-1 the calibration tower is 5.5 km far from the antenna. As shown in Fig. 4.15, errors are larger and, from the shape traced by the antenna, it seems that there is an offset between the estimated position using LHCP or RHCP. It is possible to see that switching between the two circular polarisations,

⁶This 8-way mode coupler has 4 fingers to extract the TE_{21}^c mode and another 4 fingers to extract the TE_{21}^s mode. For further information on mode couplers, see Appendix B.

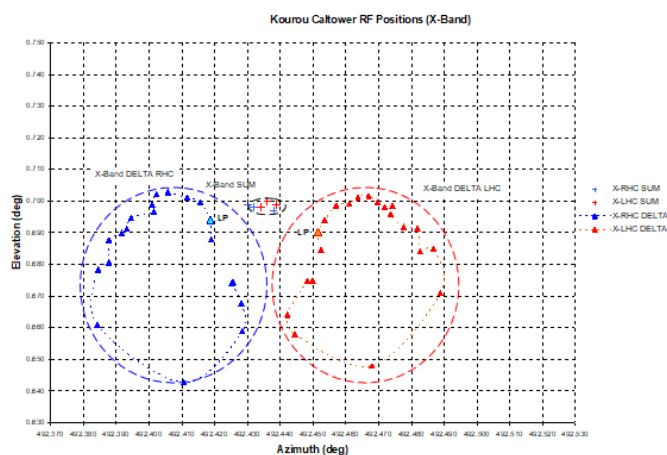


Figure 4.15: Pointing error of KRU-1 antenna.

there is an angular shift of about 90° . This error seems to appear in every ESTRACK station, regardless of the type of mode couplers used. The scope of this work is to identify possible sources of errors that may cause the problems highlighted in ESA measurements.

4.5 A MATLAB error model

To simulate the behaviour of a tracking system, a MATLAB tool has been developed. This tool simulates in a theoretical way the receiving chain using different combinations of modes to generate error signals. The results presented in this section were obtained in cooperation with Gabriele Ceccato, from the University of Pavia.

To assess a possible source of the problems in ESTRACK stations, the monopulse chains of several antenna architectures were investigated and modeled on MATLAB. First, an ideal monopulse chain was simulated assuming all components in perfect amplitude and phase balance. Afterwards, phase and amplitude factors were added in the monopulse chain to see the effect of their introduction.

To be concise, only an example will be presented here, just to show the methodology adopted and the results obtained.

An 8-way mode coupler architecture to extract the two degenerate modes TE_{21} is modeled here. This monopulse architecture is the one employed in ESA NNO-2 terminal. As shown in Fig. 4.16, the two TE_{21} degenerate

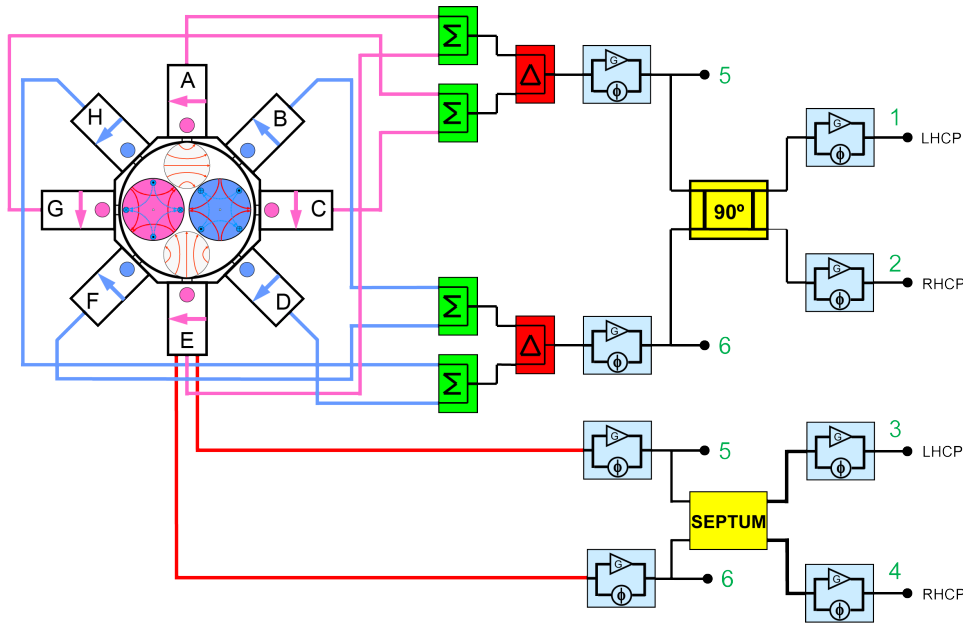


Figure 4.16: Model of an 8-way mode coupler monopulse architecture, with addition of phase and amplitude factors.

modes are extracted by means of the 8-way mode coupler. The signals picked by each finger are combined by means of power combiners (labeled as “ Σ ” blocks) and magic tees (labeled as “ Δ ” blocks) to properly reconstruct the signal carried by the TE_{21}^s and the TE_{21}^c modes. These two signals are then combined by using a 3 dB/90° coupler (labeled as “90°” block) to separate LHCP from RHCP channels. The TE_{11} mode, instead, is extracted at the termination of the waveguide. Its two degenerate orthogonal modes, TE_{11}^s and TE_{11}^c , are injected into a septum polarizer that separates the LHCP from the RHCP channels. In some parts of the chain, gain and phase blocks have also been introduced to simulate unbalances between the various channels. Unbalances in the input branches of the couplers as well as at their output branches can be analyzed with this model. Even if it is not shown in Fig. 4.16, after these microwave blocks, the difference channels are normalized in amplitude by the amplitude of the sum signal and the phase their phased is also aligned with that of the sum signal. Eventually, the in-phase and the quadrature-phase components are extracted and the elevation and cross-elevation error information is retrieved.

The construction of the signals received by each mode of the waveguide was done by considering a certain target’s misalignment, given in terms

of θ_V and θ_H (vertical and horizontal misalignments), and calculating the corresponding mode signals by using the analytical radiation patterns of the waveguide modes, presented in Sec. 4.3. In this way, the simulation is representative of a truly realistic scenario.

Prof. Angel Mediavilla Sánchez, from the University of Cantabris, provided some simulated scattering matrices of the mode coupler, obtained by full-wave simulations of multi-hole travelling wave couplers. Their scattering parameters are shown in Fig. 4.17 and highlight a very good coupling of the TE_{21} mode at the output branches of the mode couplers and practically zero coupling of the TE_{11} mode. In fact, as desired, the TE_{11} mode is unaffected by the mode coupler and travels until the end of the circular waveguide. The use of simulated mode couplers allows for a more realistic analysis of the monopulse chain.

4.6 Results of the error simulations

The MATLAB model was used to simulate phase and amplitude imbalances which may degrade the performance of the monopulse tracking receiver. In this section, some results are presented relatively to the NNO-2 scheme shown in Fig. 4.16.

Phase imbalances are introduced by putting some phase shifters in the branches of the monopulse channels. Amplitude imbalances, instead, are added by introducing some gain factors.

In real monopulse systems, phase imbalances can be due to: differences in cable lengths or in the lengths of the branches of the combining network and differences in the phase shifts introduced by the hybrid junctions or the couplers. Amplitude imbalances can be due to different coupling coefficients in the branches of the mode couplers or imperfect gain tuning in the AGCs and amplifiers used in the monopulse chain.

The MATLAB model was run by considering the case of a target located in the boresight axis and a target misaligned by a constant θ angle with respect to the boresight and by varying the ϕ angle (of course, setting a θ - ϕ couple of angles corresponds to a couple of θ_V - θ_H angles).

Assuming all ideal components in the monopulse chain, the slopes of the error signal versus the target vertical and horizontal misalignment angles are reported in Fig. 4.18, for both LHCP and RHCP polarizations of the

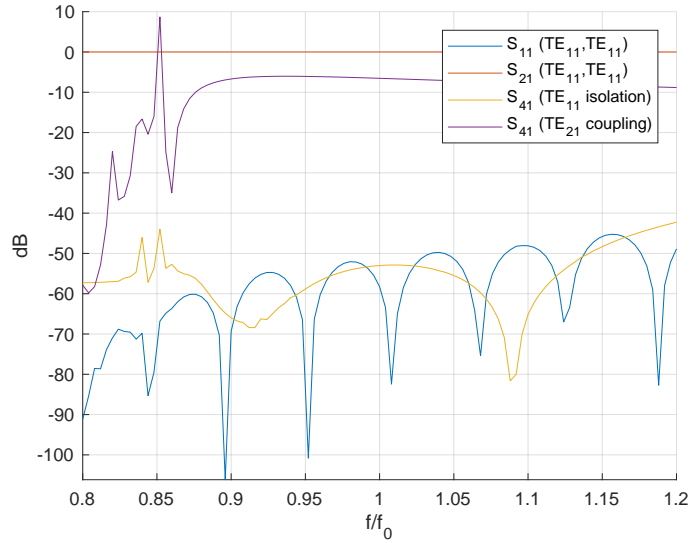


Figure 4.17: Simulated scattering parameters of a mode coupler with 4 output rectangular waveguides to extract a TE_{21} mode; another 4 rectangular waveguides extract the orthogonal mode. Port 1, 2 and 4 represent here physical ports. Port 1 is the input of circular waveguide; port 2 is the output of the circular waveguide (after the mode coupler); and port 4 is one of the 4 output rectangular waveguide branches of the mode coupler. The brown uppermost curve represents the transmission coefficient of the TE_{11} mode between the input and output of the circular waveguide. The second purple upper curve is the coupling between the TE_{21} mode in the circular waveguide and the TE_{10} mode in the output rectangular waveguide. The second lowermost orange curve is the coupling of the TE_{11} mode to the output of the mode coupler branches. Finally, the lowermost blue curve is the reflection coefficient of the TE_{11} mode at the input of the circular waveguide.

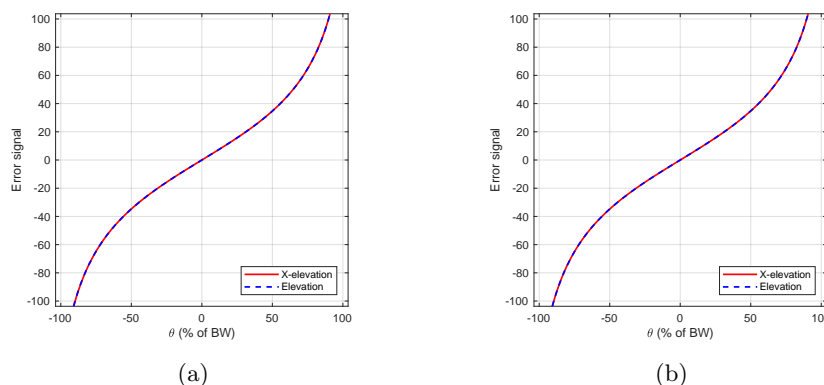


Figure 4.18: Slope of the monopulse error function in case of (a) left-hand and (b) right-hand circular polarization of the incident field.

incident electric field. These slopes were used as calibration function for the extraction of the misalignment angles. Assuming perfectly balanced channels, i.e. all phase shifters and gain factors in Fig. 4.16 are, respectively, set to 0° and 1, the *sum* and *difference* signal patterns for LHCP and RHCP are depicted in Fig. 4.19. Of course, in case of LHCP, only the red curve carries meaningful tracking information, because the RHCP channel carries no signal. Viceversa holds in case of RHCP.

By using the simulated mode coupler scattering matrices, in case of perfectly balanced system, the estimated target misalignments compared with the actual ones are depicted in Fig. 4.20 for LHCP and RHCP. In particular, the coloured circles represent actual target misalignment, set as inputs to the MATLAB code, while the coloured crosses represent the computed estimates of the misalignment after running the MATLAB code based on our model. It is clear that, after a proper calibration, the estimates perfectly overlap with the actual values, revealing that the system is properly operating.

After the simulation of the ideal situation, an amplitude imbalance of 0.1 (linear scale) between the branches of the mode coupler was introduced in the model of Fig. 4.16. In this non-ideal case, Fig. 4.21 shows *sum* and *difference* signal patterns as function of the target misalignment. It is possible to notice, now, a slight shift of the null pattern with respect to the bore-sight. And, the LHCP and RHCP patterns seems to be slightly different. This difference appears more evident if the misalignment estimate graphs

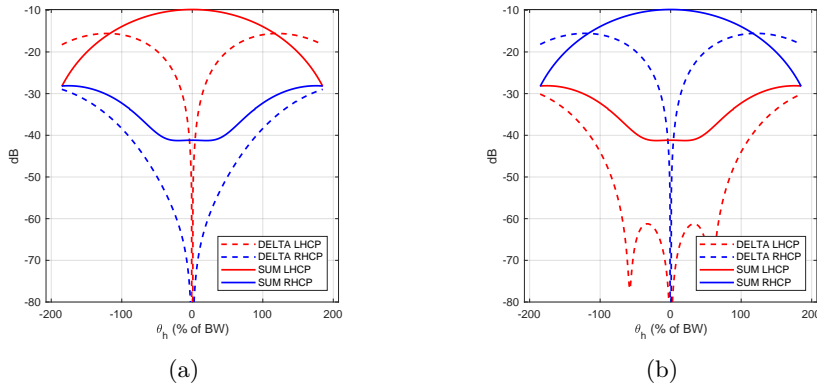


Figure 4.19: Patterns of the *sum* and *difference* signals for (a) left-hand and (b) right-hand circular polarization of the incident field, in the balanced case.

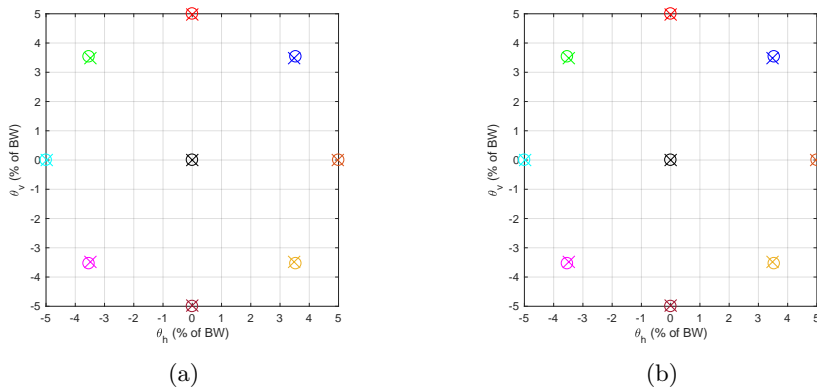


Figure 4.20: Misalignment estimates (coloured cross symbols) compared with actual target misalignments (coloured circles) assuming a constant θ and a varying ϕ misalignment. LHCP (a) and RHCP (b), in the balanced case.

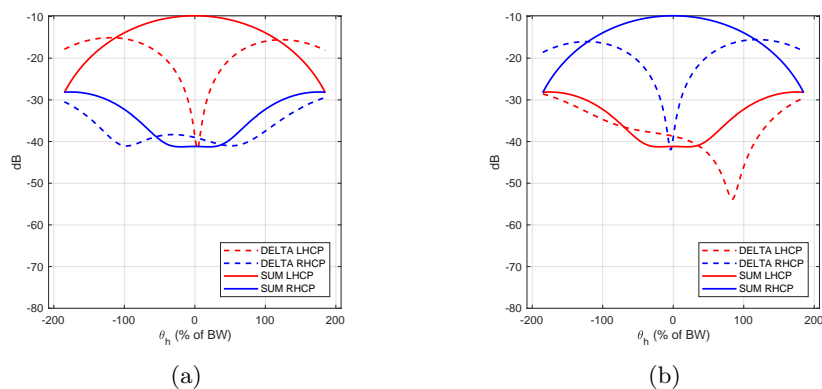


Figure 4.21: Patterns of the *sum* and *difference* signals for (a) left-hand and (b) right-hand circular polarization of the incident field, in the unbalances case.

are inspected, as depicted in Fig. 4.22. There is an evident shift between the RHCP and the LHCP. In particular, the target seems to be located in wrong position, even if the target actual position is centered in the boresight. This result resembles the one obtained in ESA measurement campaign, referring to Fig. 4.15, confirming that a possible amplitude imbalance may be a source of the tracking performance degradation, and especially of the difference between the RHCP and the LHCP estimated misalignments. The model allows also to consider phase unbalances which are not reported for brevity.

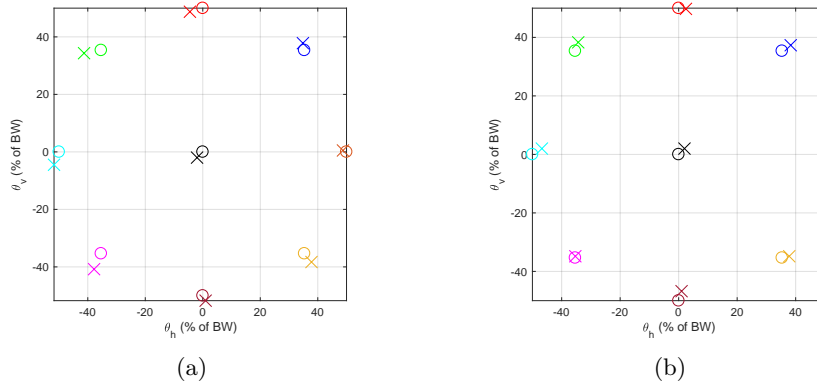


Figure 4.22: Misalignment estimates (coloured cross symbols) compared with actual target misalignments (coloured circles) assuming a constant θ and a varying ϕ misalignment. LHCP (a) and RHCP (b), in the unbalanced case.

4.7 Conclusions

ESA tracking ground stations (ESTRACK) extract the elevation and azimuth target misalignment information through a single feed, exploiting the propagation of high order modes. This kind of technology is called multi-mode monopulse and, typically, suffers from small errors of angular position estimation leading to misinterpretation of the correct position of a spacecraft. This is not a severe problem for short- and medium-range missions, but in case of deep-space missions, tracking problems may cause the loss of the spacecraft. ESA stations exhibit a shift of the estimated misalignment angles when switching from right-hand circular polarization (RHCP) and left-hand circular polarization (LHCP) tracking channel, even when the satellite is exactly located on the antenna boresight. A MATLAB tool has been developed to simulate a tracking chain, modelling each component of the tracking chain with its ideal and simulated scattering matrices. Some scattering matrices of the mode couplers have been provided by prof. Angel Mediavilla, University of Cantabria, who often collaborates with the European Space Agency on the development of multi-mode couplers.

First, the tracking information extraction process was fully understood and the radiation characteristics of all modes in the feed were analytically described. Afterwards, a MATLAB tool, designed on purpose was used to simulate in a realistic way an antenna architecture already belonging to ESTRACK network.

Results have demonstrated how non-idealities of mode couplers and asymmetries of modes extraction may have a significant impact on the tracking receiver performance. It was demonstrated that unbalances in amplitude and/or phase between SUM and DELTA channels are possible causes of pointing errors in ESA antennas. This work gave a significant contribute to understand the critical issues that must be taken into account in the design of multi-modal monopulse systems, showing the importance of fulfilling particular requirements on the tracking chain's components.

References

- [1] Nova Elettronica, *What is azimuth and elevation*, “<http://blog.novaeletronica.com.br/en/como-apontar-antena-para-satelite-usando-o-google-maps/>”, (accessed August 2018).
- [2] B. M. Chotaliya and S. Polara, “The comparison of two monopulse tracking systems: Four - horn and multimode (based on the simulation results of hfss)”, *International Journal of Computer Trends and Technology (IJCTT)*, vol. 4, no. 9, Sep. 2013.
- [3] Y. He, C. She, X. Tang, and B. Li, “Design of a te21-mode coupler for antenna feeds”, in *2010 International Conference on Microwave and Millimeter Wave Technology*, May 2010.
- [4] K. Goudey, Y. Choung, and L. Brians, “Theory and design of a ku-band te21-mode coupler”, *IEEE Transactions on Microwave Theory and Techniques*, pp. 1862–1866, 1982.
- [5] R. E. Collin, *Foundation for Microwave Engineering and Applications*. Mc. Graw Hill, 1966.
- [6] J. Nateghi, L. Mohammady, and E. Jedari, “Analysis of the te21 mode monopulse tracking technique in leo satellite systems”, in *2008 Fourth Advanced International Conference on Telecommunications*, Jun. 2008, pp. 42–45.
- [7] G. Conciauro and L. Perregrini, *Fondamenti di Onde Elettromagnetiche*. Milan, Italy: Mc Graw-Hill Education, 2003.

Appendix A

Dual band coating calculations

This appendix extends in detail the calculations of the parameters of the dual-band coating presented in Sec. 3.4. In particular, the objective was to calculate the indexes of refraction (n_1, n_2 , Fig. 3.17 on page 157) of the two quarter-wavelength dielectric layers composing the coating.

After making some first considerations, the mathematical problem to solve in Sec. 3.4 was the following:

$$\rho_2 = \rho_0 \tag{A.1a}$$

$$2C \rho_2 = \rho_1 + \rho_0 \rho_1 \rho_2 \tag{A.1b}$$

with

$$C = \cos\left(\pi \frac{\Delta f}{2 f_0}\right)$$

$$\Delta f = f_2 - f_1$$

where f_1 and f_2 are the specified reflection-less frequencies and f_0 is:

$$f_0 = \frac{f_1 + f_2}{2}$$

ρ_i is the simple reflection coefficient of i^{th} interface, so:

$$\left\{ \begin{array}{l} \rho_0 = \frac{n_0 - n_1}{n_0 + n_1} \\ \rho_1 = \frac{n_1 - n_2}{n_1 + n_2} \\ \rho_2 = \frac{n_2 - n}{n_2 + n} \end{array} \right. \tag{A.2}$$

Now, plugging the expressions A.2 into Eq. A.1a, we have:

$$\begin{aligned}\rho_2 &= \rho_0; \\ \frac{n_2 - n}{n_2 + n} &= \frac{n_0 - n_1}{n_0 + n_1}; \\ (n_2 - n)(n_0 + n_1) &= (n_0 - n_1)(n_2 + n); \\ \cancel{n_2 n_0} + n_2 n_1 - n n_0 - \cancel{n n_1} &= \cancel{n_0 n_2} + n_0 n - n_1 n_2 - \cancel{n_1 n}\end{aligned}$$

obtaining a beautiful relation between n_2 and n_1 :

$$n_1 n_2 = n n_0 \quad (\text{A.3})$$

Substituting $\rho_2 = \rho_0$ into the Eq. A.1b,

$$\begin{aligned}2C \rho_0 &= \rho_1(1 + \rho_0^2); \\ 2C \frac{n_0 - n_1}{n_0 + n_1} &= \frac{n_1 - n_2}{n_1 + n_2} \left[1 + \left(\frac{n_0 - n_1}{n_0 + n_1} \right)^2 \right]; \\ 2C(n_0 - n_1)(n_1 + n_2)(n_0 + n_1) &= (n_1 - n_2)[(n_0 + n_1)^2 + (n_0 - n_1)^2]; \\ 2C(n_0^2 - n_1^2)(n_1 + n_2) &= 2(n_1 - n_2)(n_0^2 + n_1^2); \\ (C + 1)n_1^4 + [(C - 1)n_0(n - n_0)]n_1^2 - (C + 1)nn_0^3 &= 0\end{aligned}$$

From the relationships above, we can obtain n_1 as:

$$n_1 = \sqrt{\frac{(1 - C)n_0(n - n_0) \pm \sqrt{[(C - 1)n_0(n - n_0)]^2 + 4(C + 1)^2 nn_0^3}}{2(C + 1)}} \quad (\text{A.4})$$

where (remember) $C = \cos\left(\pi \frac{f_2 - f_1}{2f_0}\right)$. Of course, from Eq. A.4 and Eq. A.3, the value of n_1 can be used to obtain:

$$n_2 = \frac{nn_0}{n_1} \quad (\text{A.5})$$

When calculating n_1 , pay attention to the sign of the argument of the square root which must, obviously, be positive. After some reasoning, we have found out that the $-$ sign leads to an impossible solution, provided that $n > n_0$ (which is our case, since n is the lens and n_0 is air). Instead, with the $+$ sign, Eq. A.4 always has a solution and it is given by:

$$n_1 = \sqrt{\frac{(1 - C)n_0(n - n_0) + \sqrt{[(C - 1)n_0(n - n_0)]^2 + 4(C + 1)^2 nn_0^3}}{2(C + 1)}} \quad (\text{A.6})$$

The condition for having physical solutions for n_1 and n_2 is that the solution of Eq. A.6 is ≥ 1 and $n_2 \geq 1$. Since $n_2 = n n_0/n_1$, n_1 must also be $\leq n n_0$. So, the condition for having a physical solution to the problem of finding a dual band matching coating is that

$$1 \leq n_1 \leq n n_0 \quad (\text{A.7})$$

(in our case, $n_0 = 1$). Let's address the first inequality $n_1 \geq 1$. This occurs if and only if:

$$\sqrt{\frac{(1-C)n_0(n-n_0) + \sqrt{[(C-1)n_0(n-n_0)]^2 + 4(C+1)^2 n n_0^3}}{2(C+1)}} \geq 1$$

We observe that

$$\begin{aligned} \sqrt{[(C-1)n_0(n-n_0)]^2 + 4(C+1)^2 n n_0^3} &\geq \sqrt{4(C+1)^2 n n_0^3} = \\ &= 2(C+1)\sqrt{n n_0^3} \geq 2(C+1) \end{aligned}$$

Since C is a cosine function, always limited between -1 and 1 , $(1-C) \geq 0$, so

$$(1-C)n_0(n-n_0) \geq 0$$

and we have

$$\begin{aligned} \sqrt{\frac{(1-C)n_0(n-n_0) + \sqrt{[(C-1)n_0(n-n_0)]^2 + 4(C+1)^2 n n_0^3}}{2(C+1)}} &\geq \\ \geq \sqrt{(1-C)n_0(n-n_0) + 2(C+1)} &\geq \sqrt{\frac{2(C+1)}{2(C+1)}} = 1 \end{aligned}$$

So, the left-hand side of inequality A.7 is always accomplished. As far as the second inequality is concerned, i.e. $n_1 \leq n n_0$, we have to impose that

$$\sqrt{\frac{(1-C)n_0(n-n_0) + \sqrt{[(C-1)n_0(n-n_0)]^2 + 4(C+1)^2 n n_0^3}}{2(C+1)}} \leq n n_0$$

which, after some algebra, leads to the following inequality

$$\sqrt{[(C-1)n_0(n-n_0)]^2 + 4(C+1)^2 n n_0^3} \leq 2n^2 n_0^2 (C+1) + (C-1)n_0(n-n_0)$$

If we pose

$$g(n) = 2n^2 n_0^2 (C+1) + (C-1)n_0(n-n_0) \quad (\text{A.8})$$

$$= 2n_0^2 (C+1)n^2 + (C-1)n_0 n - (C-1)n_0^2 \quad (\text{A.9})$$

we can calculate the discriminant of this second order expression $\Delta = (C - 1)n_0^2[1 + 8n_0^2(C + 1)]$. Since $-1 < C < 1$, $\Delta < 0$. Moreover, in our case, $f_2 - f_1$ is always $< f_0$ because, otherwise, we would exploit the periodic behavior of quarter-wave layers. This always means that $0 < C < 1$. Since $g(n)$ is always positive (its discriminant is negative), we can directly study the inequality

$$[(C - 1)n_0(n - n_0)]^2 + 4(C + 1)^2nn_0^3 \leq [2n^2n_0^2(C + 1) + (C - 1)n_0(n - n_0)]^2$$

which eventually leads to

$$(C + 1)n_0n^3 + (C - 1)n^2 - n_0(C - 1)n - 1 \geq 0$$

Which, of course, is pretty complicated to study analytically. Let's pose

$$P(n) = (C + 1)n_0n^3 + (C - 1)n^2 - n_0(C - 1)n - 1$$

then, we observe that $P(1) = 2n_0 + C - 2 > 0$. Now, if we prove that $P(n)$ is a steadily increasing function, then $P(n)$ will always be positive and, consequently, we will have eventually proved that $n_1 < nn_0$ to have physical solutions to our problem. Working on $P(n)$, its derivative is

$$P'(n) = 3(C + 1)n_0n^2 - 2(1 - C)n + n_0(1 - C)$$

We observe that

$$3(C + 1)n_0n^2 > 3n_0n > 3n$$

and, since $2(1 - C)n < 2n$,

$$-2(1 - C)n > -2n$$

So, we have, observing that $n_0(1 - C) > 0$:

$$P'(n) > 3n - 2n + 0 = n > 0$$

which tells us that $P(n)$ is, indeed, a steadily increasing function of n and that is, consequently, positive for every $n \geq 1$. This confirms the right-hand side of inequality A.7, i.e. $n_1 < nn_0$.

To sum up, in light of all previous analyses, it is possible to design a reflectionless dual band coating by using two quarter-wavelength dielectric layers, provided that the layers are quarter-wave at the arithmetic mean frequency between the two design frequencies. The indexes of refraction of the two dielectric slabs are given by Eq. A.6 and Eq. A.5; the thickness of the two slabs is simply $\lambda_i/4$ at the centre frequency f_0 , with λ_i being the wavelength inside each dielectric slab.

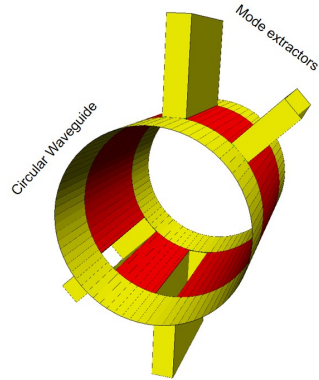
Appendix B

Mode couplers

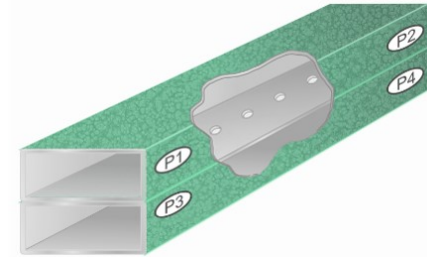
Mode couplers are used to extract waveguide modes in multi-mode feed-horn antennas. There are techniques making use of slots cut along the waveguide walls [Fig. B.1(a)]. These are narrow-band solutions; the slots are usually distributed symmetrically around the waveguide or asymmetrically. Other techniques make use of multiple holes running along the waveguide wall (Fig. B.1b); they exhibit a wider operational bandwidth. In both techniques, the signal which is “sniffed” from the waveguide is guided through a conventional rectangular waveguide on its fundamental TE_{10} mode; in this way, it becomes pretty simple to further process the signals by means of traditional microwave circuits. If multiple ports are used to extract the mode, their signals have to be properly recombined to maximize the constructive interference. This can be done with hybrid junctions, magic-T junctions, hybrid couplers, etc.

B.1 Positioning of the mode-coupler ports

The positioning of the mode-coupler ports is fundamental to effectively pick the electromagnetic field from the waveguide. Multi-hole directional couplers are commonly used whenever wide bandwidth and high coupling coefficients are required. A standard configuration is made up of a rectangular waveguide whose side wall touches the feed waveguide wall. A series of holes is cut in the rectangular waveguide’s side wall to allow for magnetic coupling with the feed waveguide. In order to maximize the coupling efficiency and bandwidth, the holes should be properly sized and spaced (variable sizes and spaces are possible), depending on the particular mode which is intended



(a) Courtesy of Angel Mediavilla Sánchez and Antonio Tazón Puente



(b) Courtesy of SpinningSpark

Figure B.1: Examples of waveguide mode extraction: (a) single-slot coupler; (b) multi-hole coupler.

to be coupled and depending on the modes to be rejected. However, the purpose of this section is to understand what is the best geometrical distribution of mode coupler ports to have coupling with specific feed waveguide modes. Thus, the attention is hereafter focus on a simplified single-slot coupling technique, with a slot being (simplistically) a rectangular waveguide aperture. Let's consider the magnetic field of a TE_{11} mode inside a circular waveguide, as depicted in Fig. B.2. In order to have magnetic coupling, a rectangular slot may be placed in the wall of non-zero magnetic field, as shown in Fig. B.3a, even though a multi-hole coupling (Fig. B.3b) is preferable for having broad band and high coupling coefficient.

If the orthogonal TE_{11} mode has to be extracted, the coupling port should be placed at 90° -angle with respect to the other TE_{11} mode, as depicted in Fig. B.4. Of course a diametrically opposite slot would also couple to this mode.

B.2 Coupling to higher order modes

The mode coupling scheme introduced in the previous section for the TE_{11} modes is not commonly adopted. Indeed, the scope of that section was only to understand the principle of mode extraction. In the reality, mode extraction is usually performed on higher-order waveguide modes, while the

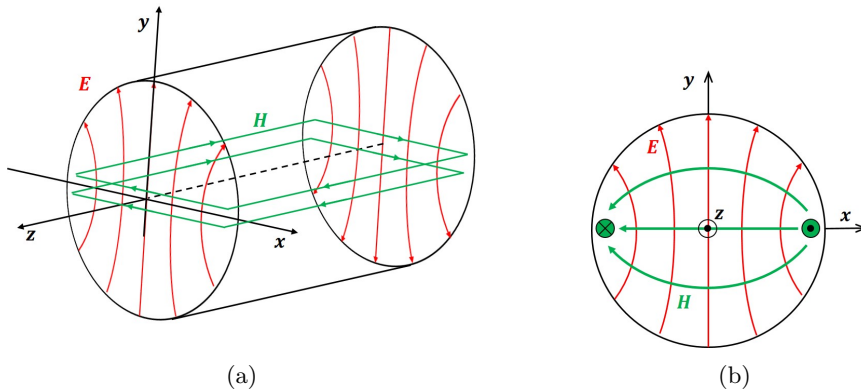
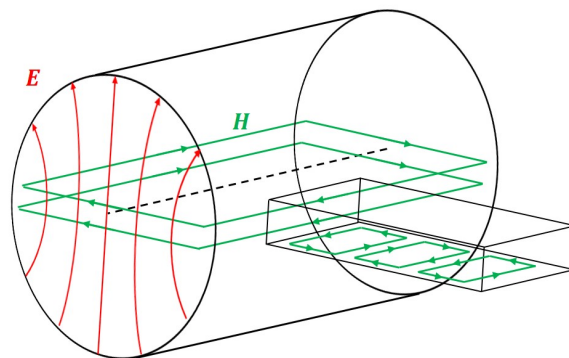


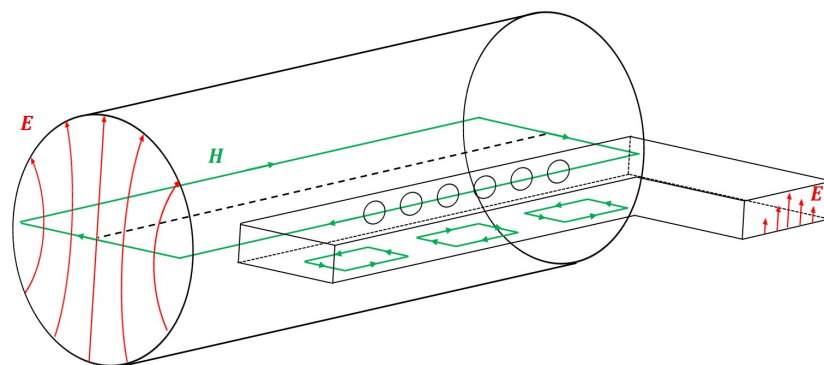
Figure B.2: Representation of the TE_{11} electric and magnetic fields inside a circular waveguide; the black dot inside the green circle represents vectors that are coming out of the plane towards the user, while the black cross represents vectors going into the plane.

fundamental mode is extracted at the end of the waveguide, where the size of the waveguide is reduced to reject all higher modes. In this section, magnetic mode extraction schemes are proposed for some of the most used higher-order modes used for tracking purposes. The problem is always the same: where is it possible to place coupling ports? The solution to this problem is found by (again) looking at the electric and magnetic field lines inside the waveguide for the desired mode. The coupling ports can be, then, placed in positions that maximize magnetic coupling. Fig. B.5 shows the electric and magnetic fields of a TE_{21} mode. Fig B.6 shows the possible locations of the ports to have a good magnetic coupling to both TE_{21} degenerate modes.

Mode couplers for TM_{01} and TE_{01} modes are also based on this maximization of the magnetic coupling efficiency. Slot (or finger) positions depend on the mode magnetic field configuration. In case of TM_{01} , the magnetic field is rotationally symmetric and forms closed circles around the waveguide centre (Fig. 4.5c). In this case transversal slots (or travelling wave mode couplers) can be used. In case of TE_{01} , the magnetic field is radial in the cross section and forms closed paths running axially through the waveguide wall and back through the waveguide central axis (Fig. 4.5f). In this case, axial slots (or, again, travelling wave mode couplers) can be used.



(a) Simplistic aperture coupling



(b) Multi-hole coupling

Figure B.3: Scheme of magnetic coupling from a TE_{11} circular waveguide mode to a TE_{10} rectangular waveguide mode.

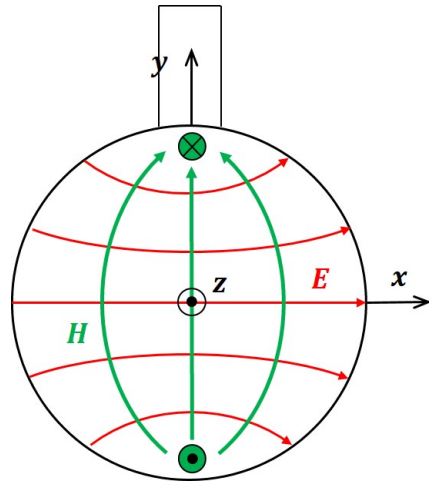


Figure B.4: Scheme of magnetic coupling from an orthogonal degenerate TE_{11} circular waveguide mode to a TE_{10} rectangular waveguide mode.

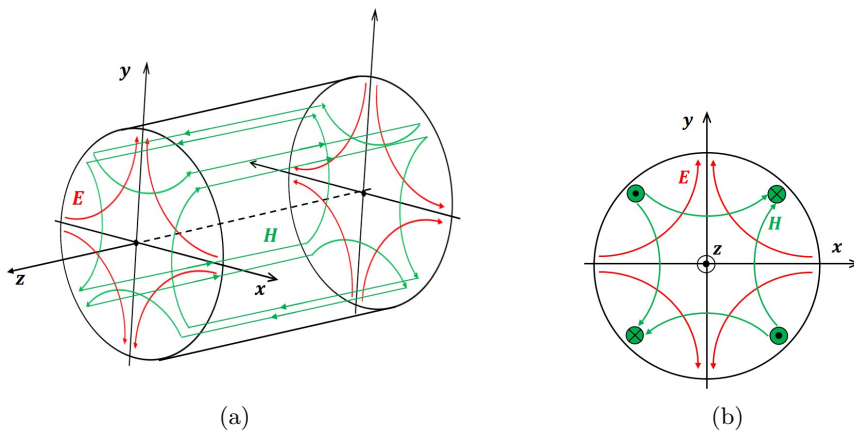
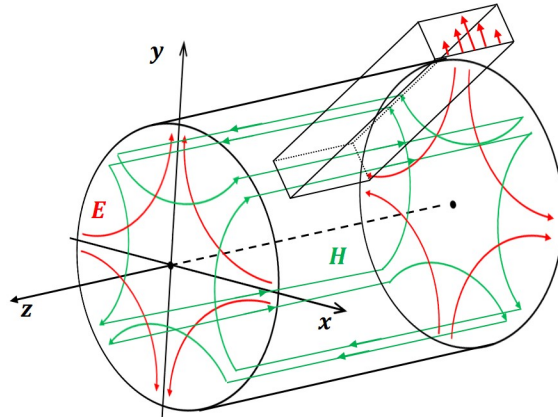
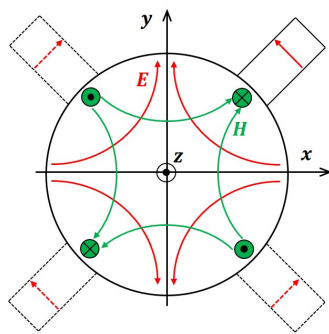


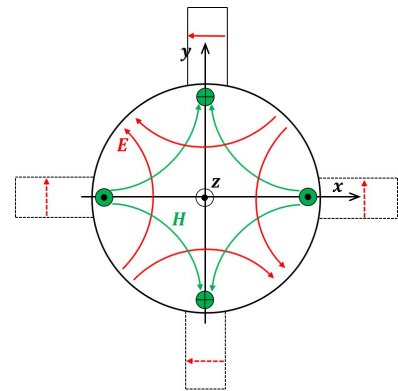
Figure B.5: Representation of the TE_{21} electric and magnetic fields inside a circular waveguide; the black dot inside the green circle represents vectors that are coming out of the plane towards the user, while the black cross represents vectors going into the plane.



(a) Example of good location of magnetically coupled port



(b) Possible port locations for the TE_{21} mode



(c) Possible port locations for the orthogonal TE_{21} mode

Figure B.6: Scheme of magnetic coupling from a TE_{21} circular waveguide mode to a TE_{10} rectangular waveguide mode.

Conclusion

All chapters of this thesis presented various technological solutions of beam steering issues ranging from the field of radar detection to the field of communication systems. They can be all grouped under the same topic which was subject of this Ph.D.: *advanced techniques for steerable antennas*. The proposed solutions were conceived starting from a well-defined idea and were developed through a balanced approach making extensive use of analytical electromagnetic theory and commercial software simulations for validation of the theory.

The first topic addressed was the design of a multi-array-antenna system for radar surveillance and tracking of space debris. A complete procedure to define the optimal phased-array-lattice geometrical parameters, given some rectangular pyramidal scan specifications, was developed. Analytical expressions for the three array parameters were computed, in contrast to purely graphical techniques relying on iterative optimization procedures. The effects of the array main lobe beamwidth and the single element pattern were also included in the formulation, and mutual coupling as well as aperture truncation were investigated through full-wave simulations. The element excitation phase errors were studied through a Monte Carlo analysis for an extreme-case scenario. The results obtained were published in conference and journal papers [1]–[5] and will be used by ESA as design guidelines for a European space debris radar architecture which will allow for the detection, size estimation, and monitoring of space debris objects. The data will be used to generate a European catalogue of debris objects with daily updated trajectories and orbital parameters, a fundamental database to rapidly send out warning messages to the operative satellite population for actuating collision avoidance maneuvers in short times.

In the second chapter, the general architecture of a mechanically scanned beam-wave-guide antenna for standoff target imaging was designed and pre-

liminarily analyzed. The proposed system was intended to operate at mm-wave frequencies, and in particular at 100 GHz. The architecture was based on a confocal gregorian reflector antenna, with a main ellipsoidal reflector illuminated after a set of mirrors used to magnify the beam and scan it through the use of a movable flat reflector. The system promises to reach fast scan speed as long as an array of receivers is used. An initial target scene, also called field of view (FoV), with the same size as a human being was intended to be covered by scanning the beam throughout it. However, covering such a large FoV proved to be quite critical because of significant system performance degradation, in terms of beam aberration and moving focal point, for large rotations of the mirror. In terms of power budget, the system under analysis proved to perform quite well both with very good scatterers and with very bad scatterers, leading to pretty good expected levels of received signals.

The third problem addressed was the keyhole in azimuth-over-elevation mechanically steered antennas where a solution was proposed to overcome this issue. A dielectric-based superstrate, based on two wedge-shaped low-loss materials (vertically spaced), was proposed to be placed above a planar array antenna. It allowed, through simple rotations of the wedges over the azimuth plane only, to introduce an additional degree of beam scanning about the zenith axis, thus overcoming the keyhole issue. Each wedge's top and bottom surfaces were covered with anti-reflection coatings to accomplish maximum transmission through the dielectric layers. The design and analysis of such coatings were carried out through a completely analytical procedure, subsequently validated by means of a commercial simulation tool. Results showed the possibility to effectively obtain beam steering in agreement with theoretical expectations. Eventually, 3D printing was mentioned to be a possible manufacturing technology allowing to make a low-cost prototype of the proposed structure.

The last topic studied in this thesis was the measured unexpected misalignment error in multi-mode monopulse antennas. Large-reflector ground stations exhibit a shift of the estimated misalignment angles when switching from right-hand circular polarization (RHCP) and left-hand circular polarization (LHCP) tracking channel, even when the satellite is exactly located on the antenna boresight. A MATLAB tool was developed on purpose to simulate a tracking chain, modelling each component of the tracking chain

with its ideal and simulated scattering matrices, where specific non-idealities were introduced. Results showed how non-idealities of mode couplers and asymmetries of modes extraction may have a detrimental impact on the tracking receiver performance.

Summary of the Ph.D. activities

In the framework of this Philosophy Doctorate, I attended several conferences on electrical and microwave engineering, as well as tens of technical seminars, four Ph.D. schools, and a university course; I published 4 conference papers and 3 journal articles; I gave teaching support for some electromagnetic and electronic courses delivered by the University of Pavia; I spent a research period of 6 months abroad at the European Space Agency; and I was co-chair of the IEEE Student Branch of Pavia from 2015 to 2018, organizing several technical seminars, scientific events and an engineering career day.

Conferences

1. EuMW 2017 (Nuremberg, Germany). European Microwave Week, October 8-13, 2017.
2. IMWS-AMP 2017 (Pavia, Italy). International Microwave Workshop Series on Advanced Materials and Processes, September 20-22, 2017.
3. EuMW 2016 (London, UK). European Microwave Week, October 3-7, 2016.
4. RINEM 2016 (Parma, Italy). Riunione Nazionale per l'Elettromagnetismo, September 12-14, 2016.
5. EuCAP 2016 (Davos, Switzerland). European Conference of Antennas and Propagation, April 10-15, 2016.

Courses and seminars

1. “Radar Fundamentals”, University of Pavia, 2016.
2. “High performance technologies for (bio)imaging”, short course, by Prof. Gustavo Marrero Callico, October 20-27, 2015.
3. “Designing Wearable Systems in the Internet of Things”, seminar, by Prof. David Atienza Alonso, 2017.
4. “Modern Navigation”, short course, by Prof. Kiril Alexiev, March 8-10, 2017.
5. Attendance to over 30 technical seminars delivered by the *Ph.D. School of Electronics, Computer Science and Electrical Engineering*, University of Pavia, from 2015 to 2018.

Ph.D. schools

1. “Ladybird Guide to Spacecraft Communications” Ph.D. school, ESEC, Redu, Belgium, March 6-9, 2018.
2. “International Summer School on Microwave Systems for the IoT”, University of Pavia, Pavia, Italy, September 7-9, 2016.
3. “Ph.D. Summer School of Phased Array Radars, TU Delft”, The Netherlands, July 2-8, 2016.
4. “Ph.D. School of Languages, Problems and Methods of Scientific Communication”, University of Pavia, Pavia, Italy, February 1-May 5, 2016.

List of publications

1. **Giuseppe Siciliano**, “Aperture Truncation and Excitation Error Analysis for a Space Debris Radar Antenna Array,” in *XII Riunione Nazionale per l'Elettromagnetismo (RINEM)*, Cagliari, Italy, September 03-06, 2018.
2. Enrico Massoni, **Giuseppe Siciliano**, Maurizio Bozzi, and Luca Perregrini, “Enhanced Cavity Sensor in SIW Technology for Material

- Characterization,” *IEEE Microwave and Wireless Components Letters*, accepted for publication, August 2018.
3. **Giuseppe Siciliano**, Magdalena Mendijur, Piermario Besso, Marco Pasian, and Luca Perregrini, “Time-Space Optimization of Uniform Array Lattices for Space Debris Radars,” *IEEE Transactions on Antennas and Propagation*, vol. 66, no. 5, pp. 2673-2677, May 2018.
 4. Fabio Dell’Acqua and **Giuseppe Siciliano**, “Technical Education on Aerospace and Remote Sensing, a Brief Global Overview”, *IEEE Geoscience and Remote Sensing Magazine*, March 2018.
 5. **Giuseppe Siciliano**, Magdalena Mendijur, Piermario Besso, Marco Pasian, and Luca Perregrini, “Effects of Finite Aperture and Random Phase Errors for a Space Debris Radar Antenna Array,” in *European Microwave Week (EuMW) 2017*, October 8-13, 2017.
 6. **Giuseppe Siciliano**, Magdalena Mendijur, Piermario Besso, Marco Pasian, and Luca Perregrini, “Lattice Optimization for a Multi-Array Antenna System Aimed at Space Debris Surveillance,” in *XI Riunione Nazionale per l’Elettromagnetismo (RINEM)*, Parma, Italy, September 12-14, 2016.
 7. **Giuseppe Siciliano**, Magdalena Mendijur, Piermario Besso, Marco Pasian, and Luca Perregrini, “A Multi-Array Antenna System with Optimal Lattice for Rectangular Pyramidal Scanning of Space Debris,” in *European Conference of Antennas and Propagation (EuCAP)*, Davos, Switzerland, April 10-15, 2016.

Teaching activities

- Student tutor of the university course entitled “Electromagnetic Fields and Circuits I,” taught by Prof. Luca Perregrini, University of Pavia, from 2015 to 2018.
- Held practical classes for the course of “Electromagnetic Fields and Circuits II,” taught by Prof. Marco Bressan, University of Pavia, in 2016 and 2017.

-
- Held practical classes for the course of “Microwave Measurements,” taught by Prof. Luca Perregrini, University of Pavia, in 2016 and 2017.
 - Held practical lectures for the course of “Electromagnetic Fields and Circuits I,” taught by Prof. Luca Perregrini, University of Pavia, in 2016 and 2017.
 - Student tutor of the university course entitled “Electronics I,” taught by Prof. Sabina Merlo, University of Pavia, in 2018.
 - Co-advisor of a Bachelor Thesis project entitled “Evaluation of the Radiation Pattern of Candidate Elementary Radiators in Planar Array Antennas for the Detection of Space Debris,” thesis defense, Mr. Yacer Tamo, University of Pavia, 2016.
 - Co-advisor of a Master Thesis project entitled “Reflector Antenna System at 300 GHz for a Mechanically Scanned Active Terahertz Imager,” thesis defense, Mr. Fabio Mirko Fasolo, University of Pavia, 2017.
 - Co-advisor of a Master Thesis project entitled “Characterisation of ESTRACK monopulse autotrack systems and possible source of under-performances,” thesis defense, Mr. Gabriele Ceccato, University of Pavia, 2018.

IEEE Student Branch activities

- “Job o’ Clock” initiative: it was an opportunity for some Italian companies (in the field of Electronics and Computer Science) to deliver a 10-minute technical and career-oriented talk to an audience of bachelor and master students. Organized in November 2016.
- “Poster Week” initiative: call for posters on research or thesis reports to allow the engineering community of my Department to share ideas, projects, and lab experiences. The 3 best posters were granted awards. Organized in November 2016 and November 2017.
- Distinguished Talks initiative: researchers and teachers from important European universities and institutions were invited to deliver

technical seminars to participant Ph.D. students. Organized from November 2016 to July 2018.

Experience abroad

I was visiting scientist at the European Space Operations Centre (ESOC), Darmstadt, Germany, from October 2017 to March 2018. I focused on:

- Beam steering techniques for moving antenna terminals for Satellite Communications on-the-move (SOTM), at Ka band.
- Monopulse tracking RF subsystems of some ground station antennas belonging to ESA tracking network (ESTRACK).

Acknowledgements

I would like to thank my supervisor Prof. Luca Perregrini for constantly supporting me throughout my Ph.D., for guiding me through the tools that a researcher should always know: spirit of initiative, creativity, and methodologic rigours.

I thank Prof. Marco Pasian and Prof. Bozzi for sharing with me some fundamental parts of this work, giving me precious advice.

I thank Engs. Piermario Besso, Fabio Pelorossi, and Filippo Concaro for being my supervisors during my experience at ESOC.

I thank my master thesis student, Gabriele Ceccato, who made me proud of his work at ESOC, worked hard with me and gave fundamental contributions to my thesis, as well.

Last but not least, I thank my wife, my father, my mother, my brother, and all my friends for encouraging me to pursue my researches.